ELECTRONIC STRUCTURE OF TRANSITION METAL IONS AND CLUSTERS

By

W. M. C. Sameera

Submitted in fulfilment of the requirements for
the Degree of Doctor of Philosophy

Department of Chemistry
Faculty of Physical Sciences
University of Glasgow

September 2009

Declaration

The work presented in this thesis has not been submitted in fulfilment of any other degree or professional qualification.

A number of results presented here have appeared in the following publications:

- The role of substrate in unmasking oxyl character in oxomanganese complexes: the key to selectivity?, W. M. C. Sameera, J. E. McGrady, *Dalton Trans.*, 2008, 6141.
- On the oxidation of alkyl and aryl sulfides by $[(Me_3TACN)Mn(V)O(OH)_2]^+$: A density functional study, A. E. Anastasi, P. H. Walton, J. R. L. Smith, W. M. C. Sameera, J. E. McGrady, *Inorg. Chim. Acta*, 2008, **361**, 1079.

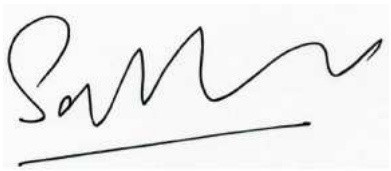

W. M. C. Sameera

30. 09. 2009

“All things appear and disappear because of the concurrence of causes and conditions. Nothing ever exists entirely alone; everything is in relation to everything else.”

- Lord Buddha

Abstract

This thesis uses density functional theory (DFT) to explore the electronic structure and reaction mechanisms of open-shell transition metal ions and clusters. The early part of the thesis (Chapters 2 and 3) is devoted to high-valent metal-oxo species, both mono- and bimetallic, while Chapter 4 describes some aspects of copper-catalysed carbon-carbon bond formation. Finally, Chapter 5 highlights the role of DFT in computing magnetic and spectroscopic properties of exchange-coupled iron clusters. Whilst the chemistry contained in the thesis is rather diverse, the underlying theme of open-shell transition metal ions is common to all chapters. Moreover, we are primarily concerned with the ways in which interactions between two or more adjacent open-shells (either two metals or a metal and a ligand radical) control structure and reactivity.

After a brief introduction to relevant theoretical aspects in Chapter 1, we use Chapter 2 to establish a link between the electronic structure of the high-valent Mn(V)=O porphyrin monomer species and their ability to perform oxidation reactions. The reaction profiles for oxidation of a range of substrates depend critically on the electronic structure of the isolated oxidant. Where the electronic ground state is genuinely best described as Mn(V)=O, the interaction between oxidant and substrate is repulsive at large separations, only becoming attractive when the incoming nucleophile approaches close enough to drive an electron out of oxide pπ manifold. In contrast, where the ground state is better described as an oxyl radical form, Mn(IV)-$O^{\cdot+}$, the oxidation occurs in sequential one-electron steps, the first of which is barrierless. In Chapter 3, we extend these ideas to bimetallic systems, where the presence of two high-valent manganese centres allows the system to oxidise water. Specifically, we focus on two model systems which have been shown to oxidise water, a Mn-porphyrin-based system synthesised by Naruta and a Mn-based system reported by McKenzie where the ligands contain a mixture of pyridine and carboxylate donors. In both cases, we again find that the emergence of oxyl radical character is the key to the reaction chemistry. However, the radical character is ‘masked’ in the electronic ground states, either by transfer of an

electron from the porphyrin ring (Naruta) or by formation of a di-μ-oxo bridge (McKenzie system).

In Chapter 4 we turn our attention to copper chemistry, and the role of copper complexes in catalysing atom transfer radical additions (Kharasch additions). In this reaction, the copper cycles between Cu(I) and Cu(II) oxidation states, and the result is the formation of a new C-C bonds. This Chapter makes extensive use of hybrid QM/MM techniques to model the environment of the copper centre in the target polypyrazolylborate-copper complexes ($Tp^{x}Cu$). Finally, in Chapter 5 we consider the electronic structure, magnetic and spectroscopic properties of a pair of exchange-coupled Fe_3 clusters, $[Fe_3(\mu_3\text{-}O)(\mu\text{-}4\text{-}O_2N\text{-}pz)_6X_3]^{2-}$ (where pz = pyrazolato, X = Cl, Br). Our primary goal was to establish how well broken-symmetry DFT is able to reproduce the observed Mössbauer spectroscopic parameters, which are extensively used to identify the chemical environments of iron species and, in the case of mixed-valence clusters, to establish the degree of delocalisation of the additional electrons. In recent years DFT has proved able to compute these parameters with encouraging accuracy, but it is not clear to what extent the known deficiencies in broken-symmetry wavefunctions will compromise this ability. Our work suggests that neither the isomer shift nor the quadrupole splitting are strongly influenced by the nature of the coupling between the metal ions, suggesting that broken-symmetry solutions can be used as a basis for computing these parameters in more complex clusters.

Acknowledgements

I would like to express my sincere gratitude to my supervisor, Prof. John E. McGrady, for his guidance, support and encouragement towards interesting research projects, and for giving me the freedom to pursue it. It is a pleasure to thank our collaborators, Prof. Raphael Raptis (University of Puerto Rico), Prof. Christine McKenzie (University of Southern), Prof. Feliu Maseras (Institute of Chemical Research of Catalonia) and Prof. Pedro J. Pérez (Universidad of Huelva), whose contribution has immensely benefited me in assorted ways. I would like to acknowledge national service for computational chemistry software (NSCCS) for enabling me to access their computational chemistry resources.

I gratefully acknowledge Pulasthika Bethmini (University of Glasgow) and Nihal Dharmapriya (Ceylon Shipping Corporation) for their valuable comments and suggestions for preparation of this thesis. I am grateful to present and past members of the computational chemistry group in the Glasgow University, particularly Dr. Hans M. Senn, Dr. Dimitrios A. Pantazis, Dr. Ekaterina Zueva and Tobias Krämer for interesting science discussions and the pleasure working together in the beam line.

Contents

List of Figures

List of Tables

To my wife Bethmini …

Introductory comments

This thesis presents an account of research that has been conducted in the Department of Chemistry, University of Glasgow, over the period October 2006 to September 2009, and was financially supported by the WestCHEM graduate school. The aim of this thesis has been to relate the electronic structure of transition metal clusters to function, either in the context of mechanism or magnetochemistry. The major theme of the thesis is oxidation chemistry, and Chapters 2 and Chapter 3 give a detailed account of our work in this area. The work in Chapters 4 and 5 covers rather different subject matter – the mechanism of the Cu-catalysed Kharasch reaction and the computation of spectroscopic parameters of an exchange-coupled Fe_3 clusters, respectively. Thus the chemistry described in this thesis is very diverse, and a detailed introduction of the relevant experimental and computational literature will be presented at the start of each individual chapter. The purpose of this brief chapter is to introduce the subject matter to be covered in the thesis, and to give an overview of the key ideas that we explore.

The electronic structure of transition metal ions and clusters continues to be one of the main themes of inorganic chemistry, largely because of the interest in the preparation of model complexes which in some way mimic the naturally occurring biological processes. Our ultimate goal is to understand the detailed electronic structure of model systems and relate it to functions such as reactivity, magnetism and spectroscopy. The emergence of density functional theory over the past two decades means that these properties can now be computed with something approaching chemical accuracy. Thus theory can provide both qualitative and quantitative insights. In the majority of cases described in this thesis, the size of the system of interest precludes chemical accuracy, and our focus is on establishing underlying general mechanistic principles. This thesis consists of five chapters; **Chapter 1** focuses on the fundamental aspects of the electronic structure theory as applied to the calculation of molecular properties of

transition metal complexes and clusters. The first section of this introduces some fundamental quantum mechanical concepts. Following a brief description of Hartree-Fock theory, electron correlation and post Hartree-Fock methods, the foundations of DFT and their realisation in the framework of the Kohn–Sham construction are described. Finally, the computational methods that we have used for this work are briefly introduced.

In **Chapter 2**, we explore the link between the distribution of electron density in the low-lying electronic states of the formally Mn(V)-oxo porphyrin monomer complexes, (OH)(Porp)Mn(O) and $[(H_2O)(Porp)Mn(O)]^+$, and their ability to act as effective oxidants for substrates such as Me_2S, CH_4 and C_2H_4. The fundamental requirement for a rapid reaction appears to be the formation of active metal oxyl radical species [Mn(IV)-$O^{\cdot+}$], and the rate determining step of two-electron oxidation reactions is therefore highly dependent on the distribution of electron density in the low-lying electronic states of the Mn(V)-oxo porphyrin complexes. Where this oxyl character is present in the ground state, the reaction is essentially barrierless. In cases where the oxyl character is 'masked' by transfer of electrons from the metal or other ligands to the oxygen centre, an energetic penalty is required to 'unmask' the oxyl character. The size of this barrier depends on the electronic structure of the metal complex but also on the spatial properties of the orbitals on the incoming nucleophile. The shapes of the potential energy surfaces are also markedly dependent on the density functional used: the percentage of Hartree-Fock exchange in the functional has a dramatic impact not just on the multiplicity of the ground state, but on the electron density distribution within the most important triplet state. The contents of this chapter have been published in two papers; 'The role of substrate in unmasking oxyl character in oxomanganese complexes: the key to selectivity?', W. M. C. Sameera and J. E. McGrady, *Dalton Trans.*, **2008**, 6141; and 'On the oxidation of alkyl and aryl sulfides by $[(Me_3TACN)Mn(V)O(OH)_2]^+$: A density functional study', A. E. Anastasi, P. H. Walton, J. R. L. Smith, W. M. C. Sameera and J. E. McGrady, *Inorg. Chim. Acta*, **2008**, 361, 1079.

The focus on oxidation reactions continues in **Chapter 3**, where we explore possible mechanisms for water oxidation catalysis. The splitting of water by photosynthetic

organisms is one of the most remarkable phenomena in nature, where the oxygen evolving centre (OEC), a tetramanganese cluster found in the Photosystem II (PSII), is central to the catalytic process. However, the detailed chemical steps involved in the oxygen evolution process and precisely how such highly active species avoid oxidative damage to the surrounding protein environment remain a mystery. In developing our understanding of the photosynthetic water oxidation, synthetic oxygen evolving complexes (small molecular mimics of the OEC) play a key role because they provide a relatively well-defined chemical environment. In this chapter we use DFT to explore two specific examples of Mn-based biomimetic water oxidation catalysts, a $Mn(III)_2$-porphyrin complex synthesised by Naruta and co-workers and a $Mn(II)_2$-mcbpen species synthesised by McKenzie and co-workers. Both of these systems have been shown to oxidise water, and both contain binuclear manganese cores. Their electronic structure presents a significant challenge to theory because the problems of dealing with open-shell Mn(IV)-oxyl radical species is compounded by the coupling between two metal centres, where ferromagnetic (F) or anti-ferromagnetic (AF) coupling leads to a large number of different spin states. Detailed potential energy profiles for the oxygen evolution for these systems were developed by considering the potential energy surfaces connecting the most stable electronic states. Our DFT calculations confirmed that the formation of metal-oxyl radical intermediate is the common denominator for the O-O bond formation in both Naruta and McKenzie systems. The implications of this work may guide the design of catalytically novel and chemically significant second-generation water oxidation catalysts. The academic interest in understanding the photosynthesis process is also critical and our findings offered insight into oxidative formation of molecular oxygen at biomimatic metal clusters. This chapter is in preparation for publishing as 'Biomimetic water oxidation: Some clues from computational chemistry', W. M. C. Sameera, C. J. McKenzie and J. E. McGrady.

The theme of metal-based redox catalysis continues into **Chapter 4**, where we explore the structure-function relationships in atom transfer radical addition (ATRA) reactions catalysed by polypyrazolylborate-copper family of complexes (Tp^xCu). This work was conducted during a 3-month research visit to Prof Feliu Maseras' group at the Institute

of Chemical Research of Catalonia (ICIQ) and was done in collaboration with Prof. Pedro J. Pérez, Universidad of Huelva. The Kharasch addition reaction, the addition of a polyhalogenated saturated hydrocarbon to an alkene, is an efficient route to carbon-carbon bond formation. In the present study, we use DFT in conjunction with QM/MM approaches to explore the electronic structure of the Tp^xCu family of complexes and the detailed chemical steps involved in ATRA of CCl_4 to C_2H_4. The intrinsic tuneability of Tp^x ligands provides an ideal platform for establishing structure/function relationships, and also for opening up new synthetic pathways.

In **Chapter 5**, we move away from catalysis and focus instead on the magnetic and spectroscopic properties of a family of all-ferric Fe_3 clusters, $[Fe_3(\mu_3\text{-}O)(\mu\text{-}4\text{-}O_2N\text{-}pz)_6X_3]^{2-}$ clusters (X = Cl, Br). This work was performed in collaboration with Prof. Raphael Raptis, University of Puerto Rico. The ultimate goal of this project is to understand the nature of the mixed valency (localised or delocalised) in reduced ferric/ferrous clusters. One of the key tools in this programme is Mössbauer spectroscopy which can, in principle, distinguish Fe(II) and Fe(III) centres. Our goal here was to compute Mössbauer parameters (isomer shift and quadrupole splitting) for two exchange coupled $[Fe_3(\mu_3\text{-}O)(\mu\text{-}4\text{-}O_2N\text{-}pz)_6X_3]^{2-}$ complexes for a variety of electronic configurations (both high-spin and broken-symmetry states) in order to evaluate different model electronic structures against experiments. Much work has been done on monomers, but it is not clear how well suited the broken-symmetry wavefunctions typically used for clusters are as a basis for computing these parameters. Another objective here is to establish how accurately DFT can compute exchange coupling constants (*J*) in these exchange-coupled systems. This chapter is in preparation for submission as: 'Electronic structure of pyrazolate-supported $Fe_3(\mu_3\text{-}O)$ complexes: Prediction of Mössbauer parameters and exchange coupling constants using broken-symmetry DFT', W. M. C. Sameera, John. E. McGrady, Ekaterina M. Zueva, Dalice Piñero, Radovan Herchel, Yannis Sanakis and Raphael G. Raptis. *Eur. J. Inorg. Chem.*

Chapter 1

Electronic Structure Theory

1.1 Introduction

One of the most important goals of chemistry and physics in the past century has been to understand and predict the properties of many-particle systems using the quantum mechanical laws of the nature. The behaviour of such systems is governed by the non-relativistic and time-independent Schrödinger equation;[1,2]

$$\hat{H}|\psi\rangle = E|\psi\rangle \tag{1.1}$$

where $\hat{H}$ is the Hamiltonian operator, ψ is a time-independent wavefunction, and E is the observable energy. The Hamiltonian operator $\hat{H}$ of the Equation (1.1) for molecular systems can be described as a sum of kinetic energy and potential energy operators;

$$\hat{H} = \hat{T}_{\mathrm{e}} + \hat{T}_{\mathrm{n}} + \hat{V}_{\mathrm{ne}} + \hat{V}_{\mathrm{ee}} + \hat{V}_{\mathrm{nn}} \tag{1.2}$$

The first two terms of the above equation represent the kinetic energy operator of electrons ($\hat{T}_{\mathrm{e}}$) and nuclei ($\hat{T}_{\mathrm{n}}$), while the third term is the nuclear-electron Coulomb attraction between the *M* nuclei and *N* electrons ($\hat{V}_{\mathrm{ne}}$). The last two expressions are the

Coulomb repulsion in electron-electron ($\hat{V}_{ee}$) and nuclear-nuclear ($\hat{V}_{nn}$) operators. Then the Hamiltonian operator $\hat{H}$ for a molecular system with *M* nuclei and *N* electrons can be written as (in *atomic units*),[3,4]

$$\hat{H} = -\frac{1}{2}\sum_{i=1}^{N}\nabla_i^2 - \frac{1}{2}\sum_{A=1}^{M}\frac{1}{M_A}\nabla_A^2 - \sum_{i=1}^{N}\sum_{A=1}^{M}\frac{Z_A}{r_{iA}} + \sum_{i=1}^{N}\sum_{j>i}^{N}\frac{1}{r_{ij}} + \sum_{A=1}^{M}\sum_{B>A}^{M}\frac{Z_A Z_B}{R_{AB}} \tag{1.3}$$

where M_A mass, Z_A is atomic number of nuclei A, $r_{iA} = |r_i - R_A|$, $r_{ij} = |r_i - r_j|$, and $R_{AB} = |R_A - R_B|$.

The observable energy E of the Schrödinger equation can be obtained as an expectation value of the Hamiltonian $\hat{H}$;

$$E = \langle \hat{H} \rangle = \frac{\int \psi^* \hat{H} \psi \, d\tau}{\int \psi^* \psi \, d\tau} \tag{1.4}$$

or in Dirac notation;

$$E = \langle \hat{H} \rangle = \frac{\langle \psi | \hat{H} | \psi \rangle}{\langle \psi | \psi \rangle} \tag{1.5}$$

The solution of the Schrödinger equation includes 3*N* spatial variables and *N* spin variables of electrons and 3*M* spatial variable of the nuclei (ignoring nuclear spin), and therefore finding an exact solution is impossible even for small molecules. One way to circumvent the complete solution is to construct approximations. Such approximate methods have been most successful in explaining a large range of chemical and physical phenomena ranging from bonding, mechanisms in chemistry, magnetism, conductivity, and etc.

1.2 The Born–Oppenheimer approximation

The first approximation generally made and of central importance in quantum chemistry is to separate the movement of the electrons and the nuclei. This separation is known as the *Born–Oppenheimer approximation*,[5] which is based on the fact that the mass of a proton (^{1}H) is much higher than that of an electron (m_p:m_e ~ 1:1836), and therefore the nuclei of the system move much more slowly than the electron(s). As a result, the nuclei of the system can be considered to be fixed in space (i.e. kinetic energy of the nucleus becomes zero), and the electrons are considered to be moving in the field generated by these nuclei plus the other electrons. Then the total Hamiltonian operator can be simplified to the electronic Hamiltonian $\hat{H}_e$, which contains only the kinetic and potential energy terms that act upon the electrons;

$$\hat{H}_e = \hat{T}_e + \hat{V}_{ne} + \hat{V}_{ee} \tag{1.6}$$

$$\hat{H}_e = -\frac{1}{2}\sum_{i=1}^{N}\nabla_i^2 - \sum_{i=1}^{N}\sum_{A=1}^{M}\frac{Z_A}{r_{iA}} + \sum_{i=1}^{N}\sum_{j>i}^{N}\frac{1}{r_{ij}} \tag{1.7}$$

Solution of the Schrödinger equation with the above electronic Hamiltonian $\hat{H}_e$ gives rise to E_e and Ψ_e;

$$\hat{H}_e\Psi_e\left(X_1, X_2, ..., X_N \middle| R_1, R_2, ..., R_M\right) = E_e\Psi_e\left(X_1, X_2, ..., X_N \middle| R_1, R_2, ..., R_M\right) \tag{1.8}$$

where X_i denotes the three spatial degrees of freedom (r_i) and the spin degrees of freedom for the i^{th} electron. The above differential equation (1.8) can be solved at any nuclear configuration $R_1, R_2, ..., R_M$ for the exact eigenstates $\Psi_0(X|\mathrm{R}), \Psi_1(X|\mathrm{R}), ...(X = X_1, X_2, X_3, ..., X_N)$ with energies $E_0, E_1, E_2, ...$ that represent the ground state and the electronically excited states of the system. However, solving the Schrödinger equation described above is still computationally demanding.

Moreover, this can only be applied for small systems, and further approximations are needed if it is to be applied to large systems such as transition metal clusters.

1.3 Antisymmetry principle

The approximate wave function describing a single electron is known as an orbital, and is a function of spatial position and spin,

$$\chi(\bar{x}) \quad \text{with} \quad \bar{x} = (\bar{r}, \sigma) \tag{1.9}$$

where $\bar{r}$ is the spatial coordinate and σ is the spin function. A common procedure is to divide each orbital into a spatial and a spin dependent part,

$$\chi(\bar{x}) = \begin{cases} \psi(\bar{r}) \cdot \sigma_+ \\ \quad or \\ \psi(\bar{r}) \cdot \sigma_- \end{cases} \tag{1.10}$$

where $\sigma_+ = \alpha$ or $\sigma_- = \beta$. The spatial (molecular or atomic) orbitals are assumed to form an *orthonormal basis*;

$$\left\langle \psi_i(\bar{r}) \middle| \psi_j(\bar{r}) \right\rangle = \delta_{ij} \tag{1.11}$$

The symbol δ_{ij} is called the *Kronecker delta*, which is equal to 1 whenever the two indices *i* and *j* are equal, and equal to 0 when *i* and *j* are not equal. The spin functions are orthonormal,

$$\langle \alpha | \alpha \rangle = 1; \qquad \langle \beta | \beta \rangle = 1; \qquad \langle \alpha | \beta \rangle = 0; \qquad \langle \beta | \alpha \rangle = 0;$$

where the alpha spin α is referred to as “spin-up”, while the beta spin β is called “spin-down”. The Pauli exclusion principle states that no two electrons can occupy the same spin orbital (χ), which means that two electrons may have identical spatial orbitals, but they must differ in the spin function. This implies that the wave functions for many-electron system must satisfy the *antisymmetry principle*.[6] For a two-particle case;

$$\Psi(\bar{x}_1,\bar{x}_2) = -\Psi(\bar{x}_2,\bar{x}_1) \tag{1.12}$$

A mathematical function that follows this antisymmetric property is a determinant, and a generalized *N*-electron wave function can be represented by the *Slater determinant* (SD).[7,8]

$$\Psi_{SD}(\bar{x}_1,\bar{x}_2,\ldots,\bar{x}_N) = \frac{1}{\sqrt{N!}}\begin{vmatrix} \chi_1(\bar{x}_1) & \chi_2(\bar{x}_1) & \ldots. & \chi_N(\bar{x}_1) \\ \chi_1(\bar{x}_2) & \chi_2(\bar{x}_2) & \ldots. & \chi_N(\bar{x}_2) \\ \vdots & \vdots & \ddots & \vdots \\ \chi_1(\bar{x}_N) & \chi_2(\bar{x}_N) & \ldots. & \chi_N(\bar{x}_N) \end{vmatrix} \tag{1.13}$$

1.4 Hartree–Fock theory

The Hartree-Fock (HF) theory is the foundation to much of the electronic structure theory, which postulates that each electron's motion can be described by a single-particle function (orbital), which does not depend explicitly on the instantaneous motions of the other electrons.[9,10] The ubiquity of orbital concepts in chemistry is a testimony to the predictive power and intuitive appeal of Hartree-Fock theory. As long as we are content to consider molecules near their equilibrium geometry, Hartree-Fock theory often provides a good starting point for more elaborate theoretical methods which are better approximations to the electronic Schrödinger equation (Equation 1.8). The Hartree-Fock theory was developed to solve the electronic Schrödinger equation that results from the time-independent aspect after invoking the Born-Oppenheimer approximation.

The Hamiltonian described by the Equation (1.7) prevents an exact solution because of the electron–electron interaction term. If we ignore this term, the Hamiltonian would be simply a sum of one-particle contributions and its eigenfunctions would be products of single-electron wave functions Φ_r (i.e. orbitals) the so-called Hartree Product (HP).

$$\Psi_{\mathrm{HP}}(\bar{r}_1,\bar{r}_2,.....,\bar{r}_N) = \Phi_1(\bar{r}_1)\Phi_2(\bar{r}_2)...\Phi_{\mathrm{N}}(\bar{r}_{\mathrm{N}}) \tag{1.14}$$

It is important to note that the above Hartree product fails to satisfy the antisymmetry principle, and therefore the appropriate form for a system of non-interacting electrons is a single *Slater determinant*. Moreover, the electrons can be described by an antisymmetrised product, which is equivalent to the assumption that each electron moves independently of all the others except that it feels the Coulomb repulsion due to the average positions of all electrons (i.e. independent particle model). The single determinant described above that gives rise to the lowest energy can be obtained by using the *variational principle*.[11] The variation theorem is a fundamental approach in quantum chemical methods, and this principal states that the approximate value for the energy that is calculated with a trial wave function (Ψ_{trial}) cannot be lower than the true energy of the system E_0;

$$E_0 \leq \frac{\left\langle \Psi_{trial} \middle| \hat{H} \middle| \Psi_{trial} \right\rangle}{\left\langle \Psi_{trial} \middle| \Psi_{trial} \right\rangle} \tag{1.15}$$

This approach provides a criterion for the optimisation of trial wave functions. Since the energy calculated from a trial wave function is lower bounded by the true energy, a better wavefunction can be obtained by varying the parameters in terms of which Ψ_{trial} is expressed until the expectation value for the energy is minimised. This approach reduces the N-particle problem to a set of one-particle eigenvalue problems the so-called Hartree-Fock equations;

$$\hat{f}_i \Psi_i = \varepsilon_i \Psi_i \tag{1.16}$$

where Ψ_i is an eigenfunction of the one particle Hamiltonian $\left(\hat{f}_i\right)$, the *Fock operator*, and the corresponding energy is ε_i. The *Fock-operator* for each electron can be defined as;

$$\hat{f}_i = -\frac{1}{2}\nabla_i^2 - \sum_{A=1}^{M}\frac{Z_A}{r_{iA}} + \sum_{j}^{N}\left[\hat{J}_i(j) - \hat{K}_i(j)\right] \tag{1.17}$$

where $\hat{J}_i(j)$ is the Coulomb operator which represents the electrostatic interaction of two electrons (charge clouds), while $\hat{K}_i(j)$ is the exchange operator, which represents the non-classical self-repulsion. These operators can be defined as;

$$\hat{J}_i\left|\Psi_j(2)\right\rangle = \left\langle \Psi_i(1)\left|\frac{1}{r_{12}}\right|\Psi_i(1)\right\rangle \left|\Psi_j(2)\right\rangle \tag{1.18}$$

and

$$\hat{K}_i\left|\Psi_j(2)\right\rangle = \left\langle \Psi_i(1)\left|\frac{1}{r_{12}}\right|\Psi_j(1)\right\rangle \left|\Psi_i(2)\right\rangle \tag{1.19}$$

The Hartree-Fock equations are usually solved by introducing a finite set of *M* known basis functions, and each molecular orbital is expanded in terms of these basis functions. This linear combination of atomic orbitals (Φ_a) procedure gives rise to molecular orbitals (Ψ_i) expressed in terms of atomic components.

$$\Psi_i = \sum_{\alpha=1}^{M} C_{\alpha i}\Phi_\alpha \tag{1.20}$$

The Hartree-Fock equation (1.16) can then be written as the *Roothan-Hall* equations;

$$\hat{f}_i \sum_{\alpha=1}^{M} C_{\alpha i} \Phi_\alpha = \varepsilon_i \sum_{\alpha=1}^{M} C_{\alpha i} \Phi_\alpha \tag{1.21}$$

Further, these *M* equations can be collectively represented by matrix equations,

$$\mathbf{F}C = \mathbf{C}S\boldsymbol{\varepsilon} \tag{1.22}$$

where ε is a diagonal matrix of the orbital energies ε_i, and S is the overlap matrix, $S_{\alpha\beta} = \left\langle \Phi_\alpha \middle| \Phi_\beta \right\rangle$. The **F** matrix contains Fock matrix elements, $F_{\alpha\beta} = \left\langle \Phi_\alpha \middle| \hat{f} \middle| \Phi_\beta \right\rangle$, and **C** is a $M \times M$ matrix of expansion coefficients $C_{\alpha i}$. The Hartree-Fock equations can be solved numerically (exact Hartree-Fock), or they can be solved in the space spanned by a set of basis functions (Hartree-Fock-Roothan equations). The orbital Ψ_i is obtained by solving the eigenvalue equation with the corresponding operator $\hat{f}_i$. This $\hat{f}_i$ depends on the orbitals of all the other electrons, and therefore an iterative procedure has to be followed for the solution of HF equations. For this reason, Hartree-Fock is called a self consistent field (SCF) approach. The SCF method can be started by making an initial guess for the orbitals, then the average potential of the system can be calculated; using this value, a new set of orbitals are obtained by solving the HF equation. This procedure continues until self-consistence is satisfied.

1.5 Post Hartree-Fock methods

The Hartree-Fock approach considers the average effect of electron-electron repulsions but not the explicit effects (i.e. correlation effects are not counted). As a result, the calculated energy of a system is above the exact value, and the difference between the exact energy and Hartree-Fock energy is defined as the correlation energy;[12,13]

$$E_C = E_{exact} - E_{HF} < 0 \quad (1.23)$$

The correlation energy arises from the electron–electron interactions that are not covered by the mean-field approach provided in the Hartree-Fock treatment. Thus, addition of electronic correlation of a system significantly improves the computed energy. However, correlation energy treatments are computationally demanding. The current post Hartree-Fock approaches consider the Hartree-Fock method as the starting point, and attempt to improve the correlation energy. The following section describes the commonly used post Hartree-Fock methods.

Configuration interaction (CI) method: The configuration interaction (CI) method is a theoretically elegant approach,[14] which would in the limit of full basis set, yield the physically correct energy. The CI method begins from the HF wave functions, and new determinants are included by promoting electrons from the occupied orbitals to the unoccupied orbitals. These new determinants are defined as singly (S), doubly (D), triply (T), and quadruply (Q) excited determinants depending on how many electrons have been promoted to the unoccupied orbitals of the reference determinant;

$$\Psi_{\mathrm{CI}} = c_0 \Psi_{HF} + \sum_S c_S \Psi_S + \sum_D c_D \Psi_D + \sum_T c_T \Psi_T + \ldots\ldots \quad (1.24)$$

The expansion coefficients c_i are then determined variationally to yield the final CI function. The full configuration interaction (FCI) calculations includes all possible excitations, and gives an exact solution in the presence of a very large basis set, where the difference between the HF energy and FCI energy corresponds to the correlation energy of the system. However, FCI calculations are computationally demanding, and therefore only possible for a system with a few atoms. The computational cost can be minimised by reducing the order of the excitations. The doubly (CISD) or triply (CIST) excited determinants are commonly used with frozen-core approximation, where the

inner core electrons are omitted for the CI treatment. Substantial cost of the CI method has encouraged the development of several related methods.

Multi-configurational self-consistent field (MCSCF) method: The Multi-configurational self-consistent field (MCSCF) method writes the wavefunction as a linear combination of configuration state functions and varies not only the expansion coefficients c_i but also the molecular orbitals.[15-18] The optimum MCSCF orbitals can be obtained by an iterative process somewhat similar to that of the SCF approach. The most commonly used MCSF method is called the complete active space self consistent field (CASSCF) approach, which includes all possible determinants that can be formed by distributing a set of active electrons among a set of active orbitals. The CASSCF method separates the orbitals into active and inactive space. Further, the active space is denoted as the CAS(*n*,*m*), where *n* is the number of electrons and *m* is the number of active orbitals. After that, a full expansion for the CI can be obtained by considering the defined active space. Due to the computational cost of the CASSCF approach, the size of the active space is minimized by including only a minimum number of orbitals for the CASSCF treatment. However, selecting an active space is a significant challenge as this active space may yield inaccurate results.

Perturbation methods: The idea of perturbation methods is that the problem under investigation only differs slightly from a problem which has already been solved exactly or approximately.[18] This is defined mathematically by considering a Hamiltonian operator, which consists of two parts, namely the reference $\hat{H}_0$ and the perturbation $\hat{H}'$. Perturbation methods can be used for adding corrections to solutions, which employ an independent particle model. In order to apply perturbation theory to find the correlation energy, the unperturbed Hamiltonian must be selected. The most common choice is to take the sum of the single particle Fock operators as the unperturbed Hamiltonian, and the difference between the full Hamiltonian and the HF Hamiltonian as the perturbation.

This approach is called Møller–Plesset (MP) perturbation method.[19,20] The main limitation of perturbation methods is the assumption that the zero-order wave function is a reasonable approximation to the real wave function. The poorer the HF wave function describes the system, the larger are the correction terms, and therefore more terms must be added to achieve a given level of accuracy.

Coupled Cluster method: Coupled cluster theory (CC) is one of the most common approach in quantum chemistry to include electronic correlation.[15-18,21,22] The basic idea of CC methods is to include all corrections of a given type, S, D or T for instance, to infinite order. This method is different from the perturbation methods like MP described in the previous section, where MP theory add all type of corrections (S, D, T) to the reference wave function up to a given order. The wave function of the coupled cluster theory is written as an exponential ansatz,

$$\left|\Psi\right\rangle = e^{\hat{T}} \left|\Phi_0\right\rangle \tag{1.25}$$

where Φ_0 is a Slater determinant, and is usually constructed from HF molecular orbitals. The $\hat{T}$ is the excitation operator acting on $\left|\Phi_0\right\rangle$, which produces a linear combination of excited Slater determinants. Moreover, the cluster operator can be written in the form,

$$\hat{T} = \hat{T}_1 + \hat{T}_2 + \hat{T}_3 + ... \tag{1.26}$$

where the $\hat{T}_1$ operator is for all the singlet excitations, $\hat{T}_2$ is for all double excitations and so forth. Further, $\hat{T}_1$ and $\hat{T}_2$ excitation operators can be expressed as;

$$\hat{T}_1 = \sum_i \sum_r t_a^r \hat{a}_a \hat{a}_r^\dagger \tag{1.27}$$

$$\hat{T}_2 = \frac{1}{4}\sum_{a,b}\sum_{r,s} t_{ab}^{rs}\, \hat{a}_a\, \hat{a}_b\, \hat{a}_r^{\dagger}\, \hat{a}_s^{\dagger} \tag{1.28}$$

In the above formulae, $a_r^{\dagger}$ and $\hat{a}$ denote the creation and annihilation operators respectively, and *a*, *b* stand for occupied and *r*, *s* for unoccupied orbitals. The one-particle excitation operator and two-particle excitation operator $\hat{T}_1$ and $\hat{T}_2$ convert the reference function $|\Phi_0\rangle$ into a linear combination of the singly- and doubly-excited Slater determinants respectively. Solving for the unknown coefficients t_a^r and t_{ab}^{rs} is necessary for finding the approximate solution $|\Psi\rangle$. Taking into consideration the structure of $\hat{T}$, the exponential operator $e^{\hat{T}}$ may be expanded in a Taylor series;

$$e^{\hat{T}} = 1 + \hat{T} + \frac{\hat{T}^2}{2!} + \frac{\hat{T}^3}{3!} + \cdots = 1 + \hat{T}_1 + \hat{T}_2 + \frac{\hat{T}_1^2}{2!} + \hat{T}_1\hat{T}_2 + \frac{\hat{T}_2^2}{2!} + \cdots \tag{1.29}$$

However, this series is finite in practice because the number of molecular orbitals is finite, as is number of excitations. In order to simplify the task of finding the coefficients $t_{ab\ldots}^{ij\ldots}$, the expansion of excitation operators is terminated at the second or slightly higher excitations. With the coupled cluster wavefunctions, the Schrödinger equation becomes;

$$\hat{H}\, e^{\hat{T}} |\Phi_0\rangle = E\, e^{\hat{T}} |\Phi_0\rangle \tag{1.30}$$

Multiplying from the left by Φ_0^* and integrating the above equation yield;

$$\begin{aligned} \langle \Phi_0 |\, \hat{H}\, e^{\hat{T}} |\Phi_0\rangle &= E_{cc} \left\langle \Phi_0 \middle| e^{\hat{T}}\, \Phi_0 \right\rangle \\ &= E_{cc} \left\langle \Phi_0 \middle| \left(1 + \hat{T}_1 + \hat{T}_2 + \cdots\right) \Phi_0 \right\rangle \end{aligned} \tag{1.40}$$

Then,

$$E_{cc} = \langle \Phi_0 |\, \hat{H}\, e^{\hat{T}} |\Phi_0\rangle \tag{1.41}$$

Abbreviations of the coupled cluster methods begin with the letter CC followed by S for single excitations, D for double excitations, T for triple excitations, and Q for quadrupole excitations. It is important to note that the most popular CCSD(T) method calculates the S and D excitations with CC method, while the triplet excitations are calculated by using perturbation theory. For many applications sufficient accuracy may be obtained with CCSD, whereas more complicated coupled-cluster methods such as CCSDT and CCSDTQ are used only for high-accuracy calculations of small molecules.[23-25]

1.6 Foundations of DFT

The basic idea of DFT is that the energy of a system composed of fixed nuclei and mobile electrons can be expressed as a functional of the electron density.[26-30] This approach allows an exact description of the interacting many-particle systems in terms of an effective non-interacting particle system. The effective potential in this non-interacting particle system (the Kohn-Sham system) can be shown to be completely determined by the electron density $\rho(r)$ of the interacting system. The DFT formalism takes the electron density instead of wave function to describe the electronic structure, and reduces the number of dimensions to three, regardless of how many electrons are present in the system, and therefore significantly enhance the computational cost. The foundations of DFT are the two Hohenberg–Kohn theorems.[30,31] The first theorem states that 'the external potential $V_{ext}(r)$ (to within a constant) is a unique functional of $\rho(r)$; since in turn $V_{ext}(r)$ fixes $\hat{H}$ we see that the full many particle ground state is a unique functional of $\rho(r)$'. Then the ground state energy (E_0) of the system and all other electronic properties of the system can be calculated from the ground state density ρ_0.

$\rho_0 \Rightarrow \{N, Z_A, R_A\} \Rightarrow \hat{H} \Rightarrow \Psi_0 \Rightarrow E_0$ and all other properties.

Since the ground state energy (E_0) is a functional of the ground state electron density,

$$E_0[\rho] = T[\rho_0] + E_{ee}[\rho_0] + E_{Ne}[\rho_0] \tag{1.42}$$

where $T[\rho_0]$ is kinetic energy, $E_{ee}[\rho_0]$ is the electron-electron interaction, and $E_{Ne}[\rho_0]$ is the nucleus-electron attraction. Further, $E_{Ne}[\rho_0]$ can be written as;

$$E_{Ne}[\rho_0] = \int \rho_0(\vec{r}) V_{Ne}\, d\vec{r} \tag{1.43}$$

The first two terms of the Equation 1.42 are collectively known as the Hohenberg-Kohn functional $F_{HK}[\rho]$, where ρ is some arbitrary density;

$$F_{HK}[\rho] = T[\rho] + E_{ee}[\rho] \tag{1.44}$$

The $F_{HK}[\rho]$ holds the functionals of the kinetic energy and the electron-electron interaction; explicit forms of both these functionals, however, are unknown. The electron-electron interaction term $E_{ee}[\rho]$ of the Hohenberg-Kohn functional can be written as,

$$E_{ee}[\rho] = J[\rho] + E_{ncl}[\rho] \tag{1.45}$$

where $J[\rho]$ represents the repulsion between the electron density and itself, and is non-zero even for one-electron systems, and $E_{ncl}[\rho]$ is the non-classical contribution to the electron-electron interactions containing all the effects of self-interaction correlation, exchange and Coulomb correlation. However, finding explicit expressions for $T[\rho]$ and $E_{ncl}[\rho]$ is a significant challenge for DFT. Then we can apply the variational principle to a trial density, $\tilde{\rho}$, using the second Hohenberg-Kohn theorem. This theorem states

that $F_{HK}[\rho]$, the functional that delivers the ground state energy of the system, delivers the lowest energy if and only if the input density is the true ground state density ρ_0,

$$E_0 \leq E[\tilde{\rho}] = T[\tilde{\rho}] + E_{Ne}[\tilde{\rho}] + E_{ee}[\tilde{\rho}] \tag{1.46}$$

where $\tilde{\rho}$ is the trial electron density which satisfies the boundary conditions such as $\tilde{\rho}(\vec{r}) \geq 0$ and $\int \tilde{\rho}(\vec{r})d\vec{r} = N$. Then, the ground state density and ground state energy can be obtained as;

$$E_0 = \min_{\rho \to N} \left(F[\rho] + \int \rho(\vec{r}) V_{Ne} \, d\vec{r} \right) \tag{1.47}$$

Kohn and Sham introduced the concept of a 'non-interacting' reference system built from a set of orbitals such that the major part of the kinetic energy can be computed with a reasonable level of accuracy. Since the exact wave functions of non-interacting fermions are Slater determinants, it is possible to introduce a non-interacting reference system, where the corresponding Hamiltonian consists of an effective local potential $V_S(\vec{r})$. It is important to note that this Hamiltonian does not hold any electron-electron interactions;

$$\hat{H}_S = -\frac{1}{2}\sum_i^N \nabla_i^2 + \sum_i^N V_S(\vec{r}_i) \tag{1.48}$$

The ground state wave function of this system is represented by a Slater determinant, and the spin orbitals are determined by;

$$\hat{f}^{KS}\varphi_i = \varepsilon_i \varphi_i \tag{1.49}$$

where the one-electron Kohn-Sham operator $\hat{f}^{KS}$ is defined as,

$$\hat{f}^{KS} = -\frac{1}{2}\nabla^2 + V_S(\vec{r}) \tag{1.50}$$

and the resulting orbitals are called the *Kohn-Sham orbitals*. Moreover, the summation of the moduli of the squared orbitals φ_i is equal to the ground state density of the real system of interacting electrons.

$$\rho_S(\vec{r}) = \sum_i^N \sum_s \left|\varphi_i(\vec{r},s)\right|^2 = \rho_0(\vec{r}) \tag{1.51}$$

The kinetic energy of a non-interacting system is not equal to the real kinetic energy of the corresponding interacting system. Kohn and Sham therefore introduced the following separation of the functional;

$$F[\rho(\vec{r})] = T_S[\rho(\vec{r})] + J[\rho(\vec{r})] + E_{XC}[\rho(\vec{r})] \tag{1.52}$$

where E_{XC} is the exchange-correlation energy, and which can be defined as;

$$E_{XC}[\rho] \equiv (T[\rho] - T_S[\rho]) + (E_{ee}[\rho] - J[\rho]) = T_C[\rho] + E_{ncl}[\rho] \tag{1.53}$$

In principle, the exchange and correlation energy $E_{XC}[\rho]$ functional holds all the unknown components. The T_C of the above equation is the so-called residual part of the true kinetic energy. The total energy of the interacting (real) system can be written as;

$$E[\rho(\vec{r})] = -\frac{1}{2}\sum_i^N \langle\varphi_i|\nabla^2|\varphi_i\rangle + \frac{1}{2}\sum_i^N\sum_j^N \iint |\varphi_i(r_1)|^2 \frac{1}{r_{12}} \left|\varphi_j(\vec{r}_2)\right|^2 d\vec{r}_1 d\vec{r}_2 + E_{XC}[\rho(\vec{r})] -$$

$$\sum_i^N \int \sum_A^M \frac{Z_A}{r_{1A}} \left|\varphi_i(\vec{r}_1)\right|^2 d\vec{r}_1 \tag{1.54}$$

Then the variation theorem can be applied to find the orbitals (φ_i) that minimize the energy. The resulting equations are,

$$\left[-\frac{1}{2}\nabla^2+\left(\int\frac{\rho(\vec{r}_2)}{r_{12}}d\vec{r}_2+V_{XC}(\vec{r}_1)-\sum_A^M\frac{Z_A}{r_{1A}}\right)\right]\varphi_i=\left(-\frac{1}{2}\nabla^2+V_{eff}(\vec{r}_1)\right)\varphi_i=\varepsilon_i\varphi_i \qquad (1.55)$$

and this equation is comparable to the one particle equation for the non-interacting model [Equation 1.50]. Then,

$$V_S(\vec{r})\equiv V_{eff}(\vec{r})=\left(\int\frac{\rho(\vec{r}_2)}{r_{12}}d\vec{r}_2+V_{XC}(\vec{r}_1)-\sum_A^M\frac{Z_A}{r_{1A}}\right) \qquad (1.56)$$

where V_{XC} is defined as the functional derivative of E_{XC} with respect to ρ;

$$V_{XC}\equiv\frac{\delta E_{XC}}{\delta\rho} \qquad (1.57)$$

The Kohn-Sham one-electron equations (1.55) can be solved iteratively (in the same way as the HF equations). The accuracy of the calculated energy, however, depends on the chosen exchange–correlation functional.

1.6.1 Exchange–correlation functionals

1.6.1.1 The local density approximation

The local-density approximation (LDA) method simplifies the exchange-correlation

(XC) energy functional in DFT,[27,28,30,31] where the energy of the system is obtained from a purely local integral over the density;

$$E_{XC}[\rho] = \int (\varepsilon_X[\rho(r)] + \varepsilon_C[\rho(r)])\, \rho(r) dr \quad (1.58)$$

The above equation contains the local exchange $\varepsilon_X[\rho(r)]$ and correlation terms $\varepsilon_C[\rho(r)]$ separately, where these exchange–correlation functionals depend only on the scalar value of the electron density at a given point in space. The Dirac-Slater exchange energy functional[32,33] can be written as;

$$\varepsilon_X[\rho(r)] = -\frac{3}{2}\left(\frac{3}{\pi}\rho(r)\right)^{\frac{1}{3}} \quad (1.59)$$

where the exchange energy depends on the local density. However, the expressions for local correlation functionals are more complicated. These functionals have been parameterised to reproduce the highly accurate Monte Carlo results obtained for the homogeneous electron gas.[34] The combination of the Slater local exchange functional described above [Equation (1.59)] and the Vosko, Wilk and Nusair local correlation functional is often referred to as the SVWN[35] or LDA (local density approximation) functional. In general, LDA based methods give rise to good predicted molecular geometries, and a reasonable description of molecular electronic structure and thermochemistry. In contrast, calculated bond energies are usually overestimated with large deviations compared to experiment. The LDA model of density functional theory is exact only for systems with constant electron density throughout space, and has been used in a wide variety of applications for calculations on solids.

1.6.1.2 Gradient-corrected functionals

The LDA by itself does not contain sufficient accuracy for chemical applications.

Therefore, it is necessary to include terms that explicitly take into account the spatial variation of the density, and this is the formulation of functionals within the generalised gradient approximation (GGA).[36] The GGA functionals contains functions of the scalar density in the integrand of Equation (1.59) and also functions of the gradient of the density. The fundamental basis to include the gradient terms is that the energy functional is expected to vary rapidly near the nuclei but slowly far from the nuclei. The most popular exchange functionals proposed by Becke (B) is given below,[37] which is a sum of the local exchange described in Equation (1.59) and a correction term that depends on the gradient of the density, and this functional was designed to reproduce the correct long-range behaviour of the Coulomb potential;

$$\varepsilon_X[\rho] = -\sum_\sigma \rho_\sigma^{\frac{1}{3}} \left(\frac{3}{2}\left(\frac{3}{4\pi}\right)^{\frac{1}{3}} + \frac{\beta\, x_\sigma^2}{\left(1 + 6\,\beta\, x_\sigma\, sinh^{-1} x_\sigma\right)} \right) \tag{1.60}$$

where the σ represents up-spin and down-spin, and x_σ is given by $|\nabla\rho_\sigma| / \rho_\sigma^{4/3}$. The parameter β was considered as 0.0042 to reproduce exchange energy of for a rare gas atoms. Many other gradient-corrected exchange functionals have been developed by considering the physical properties to which the parameters have been adjusted, and the physical constraints that have been applied to the nature of the solutions such as long-range cancellation of self-interaction. With respect to the correlation functionals, P86 is a popular GGA correlation functional[38] which holds one empirical parameter fitted for the Ne atom. This was modified later by Perdew and Wang (PW91).[39,40] Another widely used GGA correlation functional is LYP proposed by Lee, Yang and Parr.[41-43] It has empirical parameters fitted to the He atom and its overall performance may originate from an efficient handling of self-interaction error in many-electron system. Typical combinations (exchange and correlation functionals) in common use are BLYP, BP86 and BPW91, and these GGA functionals increase the accuracy of calculated energies compared to the LDA approach.

1.6.1.3 Kinetic energy density functionals

The kinetic energy density functionals include further functions of the density at each point in space such as the Laplacian of the total density (the densities of spin-up and spin-down electrons) and the sum of the kinetic energy densities of the Kohn–Sham orbitals.[44] The former term corresponds to the next term in the Taylor expansion of the density around a given point.

$$\varepsilon[\rho] = \varepsilon\left[\rho_\sigma, \nabla\rho_\sigma, \nabla^2\rho_\sigma, \sum_i^{occ}\left|\nabla\psi_{i\sigma}\right|^2\right] \tag{1.61}$$

An often used kinetic energy density functional (i.e. meta-GGA functional) is the TPSS functional developed by Tao, Perdew, Staroverov and Scuseria.[45] The TPSS functional is not fitted to experimental data, and therefore this functional is referred to as a 'non-empirical' functional. However, the extra complexity of these functionals does not yield a very large improvement in accuracy over GGA functionals.[29]

1.6.1.4 Hybrid density functionals

The Hartree–Fock method described in section 1.4 underestimates the calculated energies of a system of interest, whereas the local exchange and correlation functionals lead to significant overestimation of the computed energies.[29] Therefore, combination of the two may improve the calculated thermochemical properties. The hybrid density functionals calculate exchange–correlation energy using the Hartree–Fock type exchange energy of the Slater determinant formed from the Kohn–Sham orbitals, and the LDA exchange energy of the corresponding density.[46] This approach has been shown to give accurate results for a number of applications. Over the last few years, a number of hybrid density functionals have been developed, including the most popular B3LYP functional.[46-48] The B3LYP functional represents the exchange–correlation

energy as a combination of the local exchange–correlation energy, the HF exchange energy, and the gradient corrections to the exchange and correlation energies;

$$E_{XC} = E_{XC}^{LDA} + a_0\left(E_X^{HF} - E_X^{LDA}\right) + a_X\left(E_X^{GGA} - E_X^{LDA}\right) + a_C\left(E_C^{GGA} - E_C^{LDA}\right) \quad (1.62)$$

where the semi-empirical coefficients a_0, a_X and a_C control the relative amounts of HF exchange, GGA exchange, and GGA correlation from the various sources and they are determined empirically. The E_X^{GGA} and E_X^{LDA} generalized gradient approximations: the Becke 88 exchange functional and the correlation functional of Lee, Yang and Parr.[49,50] The E_C^{LDA} is the VWN local-density approximation to the correlation functional. Many other hybrid functionals have been developed and some of them have also been widely used. The most common hybrid functionals are based on GGA and local exchange–correlation functionals, others have been developed by considering the kinetic energy density functionals, e.g. a hybrid based on the TPSS functional, TPSSh, and the TPSSh0 functional is a 25% exchange version of TPSSh that yields improved energetics compared to TPSSh but is otherwise not well tested.[50] The pure functional of Perdew, Burke and Ernzerhof (PBE) was made into its hybrid form as the PBE1PBE or PBE0.[51] Truhlar and co-workers have developed a suite of meta-hybrid density functionals including M06, M06HF, M062X, M05, and M052X.[52-56] The half-and-half functionals namely BHandH and BHandHLYP are also well-known, where these functionals hold 50% exact exchange.[57]

1.6.1.5 Extended double hybrid functionals

In addition to mixing the HF-exchange into a given density functional, the extended hybrid functionals developed by Grimme and co-workers are composed of a fraction of the MP2 correlation energy calculated with hybrid DFT orbitals, and that can be expressed as;

$$E_{XC} = a\,E_X^{HF} + (1-a)E_X^{DFT} + (1-c)E_C^{DFT} + c\,E_C^{MP2} \tag{1.63}$$

They recommend the B88 exchange functional, the LYP correlation functional and the parameters a = 0.53 and c = 0.27, which gives rise to the B2PLYP functional.[58,59] The mPW2PLYP double hybrid functional is also well-known.[60,61]

1.7 Basis sets

A basis set in chemistry is a set of functions used to create the molecular orbitals. There are two common types of basis functions, namely *Slater type orbitals (STO)*[62] and *Gaussian type orbitals (GTO).*[63] The STOs can be described by the following function, which depends on spherical coordinates;

$$\Phi_i(\zeta,n,l,m;r,\theta,\varphi) = Nr^{n-1}e^{-\zeta r}Y_{lm}(\theta,\varphi) \tag{1.64}$$

where **N** is the normalisation constant, ζ is the 'exponent', and r,θ,φ are spherical coordinates, and Y_{lm} is the angular momentum part, which describes the shape of the orbitals. The *n*, *l*, and *m* are principal, angular momentum and magnetic quantum numbers respectively. The GTOs are more commonly utilised, where we can approximate the shape of the STO by taking a linear combination of primitive GTOs with different exponents and coefficients. A GTO can be expressed by the following function;

$$g(\alpha,l,m,n;x,y,z) = Ne^{-\alpha r^2}x^l\,y^m\,z^n \tag{1.65}$$

where α is the 'exponent', and *x*, *y*, and *z* are Cartesian coordinates. Gaussian primitives are usually obtained by quantum calculations on atoms, where the exponents are varied until the lowest total energy of the atom is achieved.

The minimal basis set is the smallest possible set, and contains only one STO per occupied atomic orbital in the ground state. The most popular minimal basis sets are the STO-*n*G, where *n* is the number of Gaussian primitives in the contraction.[64] The STO-3G holds three primitives per function, and this type of basis sets is known as single-zeta (SZ) basis sets. Further, more sophisticated basis sets such as double zeta (DZ), triple zeta (TZ), quadruple zeta (QZ) are also available.

It is well-known that the valence orbitals of atoms are more affected by the formation of bonds than the core (inner) orbitals, and therefore it is obvious to employ a more sophisticated basis set to describe the valence orbitals than the core orbitals. This idea prompted the development of split-valence (SV) basis sets, which can be expressed as *n*-*ij*G or n-*ijk*G, where *n* denotes number of primitives for the inner shells, and *ij* (DZ) or *ijk* (TZ) represent the number of primitives for contractions in the valence shell. A typical example is the 6-31G basis set, where the inner orbitals are described by six primitive GTOs, while the valence orbitals are described by two functions, the first of which consists of three primitive GTOs and the other one is uncontracted. The basis sets can be extended by adding other functions, where the most popular are polarization and diffuse functions. The polarization functions are simply functions having higher values of angular momentum (*l*) than that is present in occupied atomic orbitals for the corresponding atom. Polarization functions allow orbitals to distort from their original symmetry. Basis sets are also frequently augmented with diffuse functions, which are necessary for a correct description of anions, weak bonds, and excited electronic states.

Dunning's correlation consistent basis sets have been designed to overcome the high cost and reduced valence flexibility of atomic natural orbital (ANO) bases.[69-71] Further, they converge systematically to the complete basis set (CBS) limit using extrapolation techniques. For second-row atoms, the basis set structure is cc-pVNZ, where cc-p stands for 'correlation consistent polarized', V indicates that they are valence only basis sets, and N = D, T, Q, ... (D=double, T=triple, etc.). However, additional functions are usually added in the case of the third-row atoms, and the basis set structure is then cc-

pV(N+d)Z. These basis sets included diffuse or augmented functions for electronic excited-state calculations, electric field property calculations, and long-range interactions, such as Van der Waals forces.

In the case of relatively big systems, transition metal complexes and clusters for instance, a large number of basis functions are required and therefore computationally demanding. It is well-known that the core (inner) orbitals are in most cases not affected significantly by changes in chemical bonding, and therefore we can replace inner-shell electrons by analytical functions, the so-called effective core potentials (ECP) or pseudopotential,[65-68] which allow inner shells of electrons to be treated as some averaged potential rather than actual particles. The ECPs are described in the literature using parameters in the following expansion;

$$ECP(r) = \sum_{i=1}^{M} d_i r^{ni} \mathrm{e}^{-\xi_i r^2} \tag{1.66}$$

where M is the number of terms in the expansion, d_i is a coefficient for each term, r denotes the distance from the nucleus, n_i is a power of r for the i^{th} term, and ξ represents the exponent for the i^{th} term. This approach is computationally very efficient, in particular for transition metal ions and clusters.

1.8 Computational details

The calculations described in this thesis have been carried out with Gaussian03,[73] Gaussian09,[74] Jaguar 7.5v[75] and ORCA 2.6-35[76] programme packages. The method most commonly used for this work is DFT with hybrid functionals, in particular B3LYP.[46-48] Most calculations in this thesis have utilized SDD[77-79] or LanL2DZ[77,80-82] basis sets and associated effective core potential for transition metal ions. In the case of simple model systems, 6-31G* or TZVP basis sets were considered for all atoms

bonded to metal, and 6-31G or TZV basis set were employed for other systems.[83-86] A full descriptions of the computational methods are presented in detail in each chapter.

Chapter 2

The Role of Substrate in Unmasking Oxyl Character in Oxomanganese Complexes

2.1 Introduction

Macrocycle ligand-complexed transition metal species are found in a wide variety of biological and inorganic reactions, where the formation of active high-valent metal-oxo species has been suggested as the key step for the catalytic activity. Organic species generally posses low-spin ground states and their reactions proceed on a single potential energy surface, which is referred to as single-state reactivity (SSR) (Figure 2.1a).[87,88] However, organometallic systems may quite often involve (at least) two states and the ground state may not necessarily be the most reactive one. The phenomenon of two different multiplicities that determine the minimum-energy pathway of a reaction can be classified as two-state reactivity (TSR),[87,88] and is characterised by a crossing of two potential-energy surfaces of different multiplicities (Figure 2.1b). TSR is proposed as a fundamental concept in organometallic chemistry, in particular oxidation catalysis. The link between electronic structure and reactivity in iron-oxo compounds has been the subject of intense debate, largely because of the interest in unravelling the complex reactivity of cyctochrome P450.[87–96] The primary reactive species of P450 enzymes is

considered to be a (SH)(Porp)Fe(IV)O species,[87,88] and most of the issues of this field can be understood in terms of the reactivity of this system. The stable electronic configurations of (SH)(Porp)Fe(IV)O involves a close-lying pair of quartet and doublet spin states (Figure 2.2).

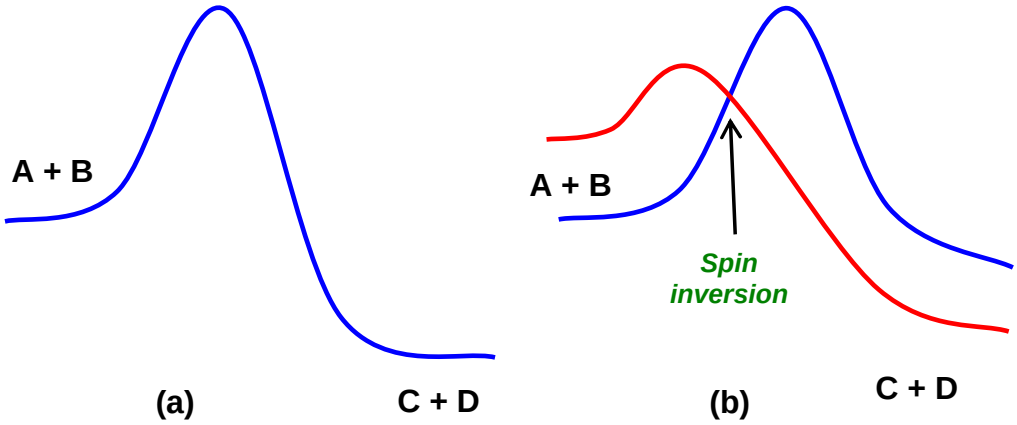

Figure 2.1 (a) A single spin surface connects reactants and products and (b) more than one spin surfaces connect reactants and products.

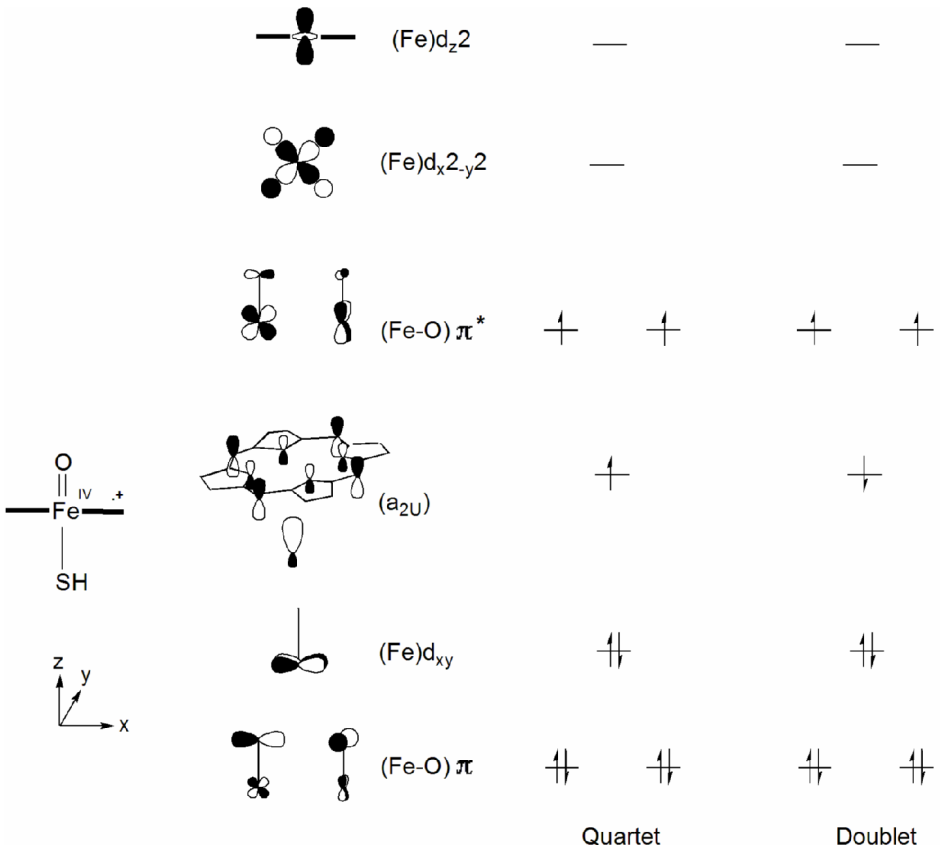

Figure 2.2 High-lying occupied and low-lying virtual orbitals, quartet and doublet electronic states of (SH)(Porp)Fe(IV)O complex.

Both quartet and doublet states contribute to the reactivity with different reaction barriers and sometimes also different reaction mechanisms, which are characteristics of TSR. The orbital manifold of (SH)(Porp)Fe(IV)O involves several close-lying orbitals, and therefore other states may also participate in the reactions and give rise to multi-state reactivity (MSR).[87-88] Since curve crossing between the high- and low-spin states constitutes a distinct mechanistic step along the reaction coordinates, spin-orbit coupling is an important factor for TSR and MSR.[97-102] Shaik and co-workers have shown how this complexity can be understood and used it to rationalise a number of previously puzzling kinetic observations associated with a number of reactions catalysed by P450 enzymes, namely C-H hydroxylation, epoxidation, benzene hydroxylation, and sulfoxidation.[87,88,103-105]

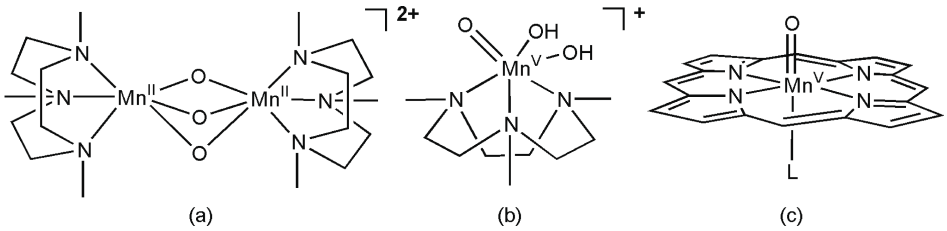

Figure 2.3 Structures of manganese-based oxidants (a) $[(Me_3TACN)Mn_2(\mu\text{-}O)_3]^{2+}$, (b) $[(Me_3TACN)Mn(O)(OH)_2]^{+}$ and (c) (L)(Porp)Mn(O).

In comparison to their iron analogues, high-valent manganese oxo systems are rather less well studied, although the recent interest in the chemistry of the oxygen evolving centre (OEC) has encouraged a number of researchers to explore this issue.[106–113] Manganese-based oxidants are increasingly becoming an important synthetic tool (Figure 2.3), and salen-based manganese complexes[114] have been used extensively in the oxidation of both alkenes and sulfides.[115-118] Manganese complexes of triazacyclononane (TACN) (Figure 2.3a) have also been used extensively in bleaching catalysis,[119-124] and have been shown to be catalytically competent for sulfide and sulfoxide oxidation.[125,126] The extensive oxidation chemistry based on iron porphyrin systems has also driven research into manganese species with porphyrin and corrole ligands.[127-135] Groves proposed the existence of Mn(V)=O porphyrin species as early as 1983,[136] and subsequent spectroscopic characterisation[137,138] has confirmed their

presence in solution. As for the iron analogues, the *trans* ligand in these complexes appears to play a major role in controlling the properties of the complexes, and Groves and Spiro have recently presented spectroscopic evidence for a *trans* dioxo Mn(V) species[139,140]. The presence of four manganese centres in the OEC suggest that multiple metal sites may be critical for effective multi-electron oxidation of substrates such as water, and indeed catalytic water oxidation has been reported for di-manganese porphyrin and corrole species.[141]

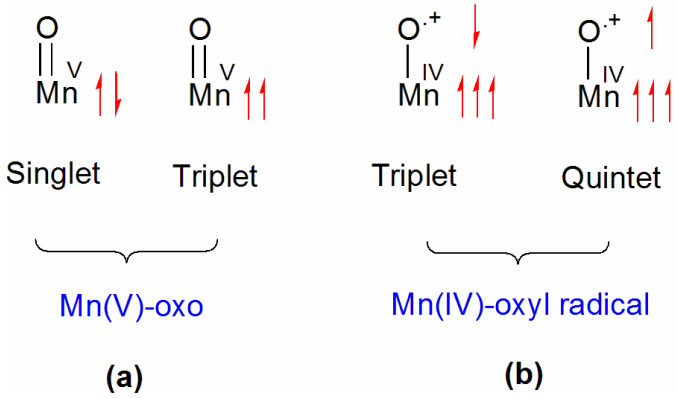

Figure 2.4 Possible spin states for the formal Mn(V)=O complexes.

The remarkable ability of the OEC to selectively oxidise water has encouraged a number of groups to explore the mechanism of O_2 evolution using theory.[142-150] In the context of the biological system itself, Siegbahn has argued that Mn(IV)-oxyl character [Mn(IV)-$O^{\cdot+}$], as distinct from the Mn(V)-oxo 'electromer' [Mn(V)=O], is a pre-requisite for effective O–O bond formation.[142-150] Irrespective of the precise nature of the active species, the endergonic nature of water oxidation suggests that it must be very potent: precisely how such a highly active species avoids oxidative damage to the surrounding protein environment remains a puzzle. A Mn(V) ion has two electrons in the 3*d*-orbitals, making up a low-spin singlet and a high-spin triplet state (Figure 2.4a), and these two electronic states hold Mn(V)=O character. If one of the bonding electron pairs between Mn and O splits, one electron goes to Mn, which becomes Mn(IV), and the other to O, which becomes an oxyl radical, and an alternative triplet state or a quintet state are formed (Figure 2.4b) (*vide infra*). Hybrid DFT calculations by Siegbahn and co-workers indicate that the active high-valent Mn-oxo species prefer

Mn(IV)-oxyl radical character in their ground state, and such species are active in water oxidation.[142-145] However, the inactive complexes that they investigated hold Mn(V)=O character in their ground state.[142-145]

The electronic structure of model systems including salen-,[151–163] porphyrin-[164-166] and corrole-based[167,168] manganese complexes and high-valent ruthenium species,[169] has also been extensively explored, and oxyl radical character again emerges as an important theme. In common with the iron analogues, the delicate balance between energy levels in these systems presents a significant challenge to theory,[158] and small changes in computational methodology can, in some cases, alter the qualitative mechanistic picture quite dramatically.

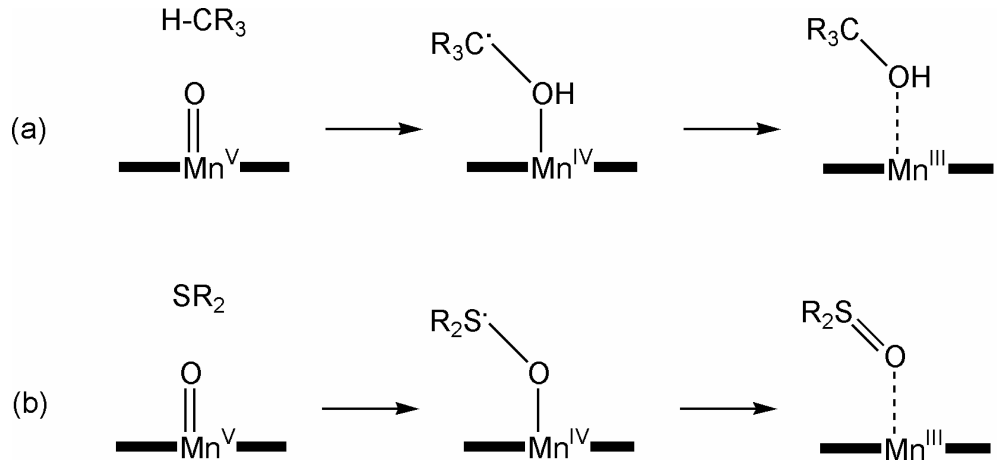

Figure 2.5 Rebound mechanisms for (a) hydrocarbon and (b) sulfide oxidation by high-valent Mn(V)=O species.

In a recent communication,[170] Eisenstein and co-workers used the electronic structure of the isolated manganese porphyrin complexes as a basis to explore the potential energy surface for the rebound mechanism (Figure 2.5a) for oxidation of a model hydrocarbon, toluene. In a similar vein, McGrady and co-workers have previously discussed the electronic structure of a triazacyclonanone complex, $[(TACN)Mn(O)(OH)_2]^+$, and its ability to act as a two electron oxidant towards sulfur-based nucleophiles [Figure 2.5b].[171] The key stationary points on the potential energy surfaces in these two cases are qualitatively very similar, with the oxidation clearly divided into two distinct one-

electron steps (Figure 2.5). In the case of $[(TACN)MnO(OH)_2]^+$, the first of these steps proved to be barrierless, offering an explanation for the rather limited influence of electron-donating or withdrawing substituents on the rate of sulfide oxidation (Hammett $\rho = -0.28$).

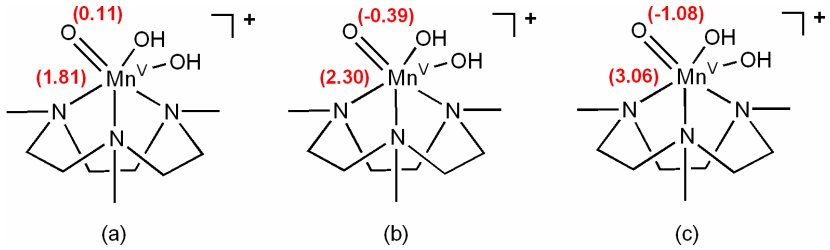

Figure 2.6 The electron density distribution in the optimised triplet electronic structure for $[(TACN)Mn(O)(OH)_2]^+$ complex with (a) BLYP (0% HF), (b) B3LYP (20% HF), and (c) BHandH (50% HF).

In contrast, Rajagopal and co-workers reported a much larger substituent effect in the oxidation of sulfides by the salen-complex (salen)Mn(V)O (Hammett $\rho = -1.86$).[172-176] We have noted above Siegbahn's proposal that oxyl radical character is critical for rapid water oxidation, and indeed the spin densities for the triplet ground state of $[(TACN)Mn(O)(OH)_2]^+$, [ρ(Mn) = 2.39, ρ(O) = -0.39], confirm the presence of significant minority-spin density at the oxygen center (Figure 2.6b). The electron density distribution in the triplet is, however, very sensitive to the amount of Hartree-Fock (HF) exchange included in the functional: for the pure BLYP functional, the oxyl radical character is negligible: ρ(Mn) = 1.81 and ρ(O) = 0.11 [Figure 2.6a], while for BHandHLYP (50% HF exchange), it is greatly enhanced: ρ(Mn) = 3.06 and ρ(O) = -1.08 (Figure 2.6c). Thus changing the percentage of HF exchange appears to map out a continuum linking the two forms, Mn(V)=O and Mn(IV)–$O^{\cdot+}$. Our spin densities calculated for $[(TACN)MnO(OH)_2]^+$ using the BLYP functional (Figure 2.6a) are rather similar to those reported by Eisenstein and co-workers for (Cl)(Porp)Mn(O)[170] (using the BP86 functional), where a small but significant barrier emerged in the first step of the rebound process (Figure 2.5a). It seems likely that these observations are connected, the presence or absence of a barrier may be intimately related not just to the multiplicity of the ground state, but also to the extent to which it displays oxyl radical character.

2.2 Objectives

In this chapter, we explore the link between the distribution of electron density in the low-lying electronic states of the formally Mn(V)-oxo porphyrin complexes, (OH)(Porp)Mn(O) and $[(H_2O)(Porp)Mn(O)]^+$ (Figure 2.3c), and then we show that the percentage of HF exchange in the functional has a dramatic impact not just on the multiplicity of the ground state, but on the electron density distribution within the most important triplet state, and that this in turn has a significant impact on the shape of the potential energy surface for the sulfide oxidation reaction with a model sulfide substrate, Me_2S. Critically, the first one-electron step is only barrierless when the ground-state triplet has oxyl radical character. In cases where oxyl radical character is 'masked' in the ground state, the interaction with an incoming nucleophile is repulsive at long separations because the pπ orbitals on oxygen are fully occupied. The interaction only becomes attractive when the nucleophile approaches closely enough to drive an electron out of the oxo pπ manifold, onto either the metal or the porphyrin ring. Further, we explore this issue by considering the two electron oxidation of CH_4 and C_2H_4 (epoxidation) catalysed by the $[(H_2O)(Porp)Mn(O)]^+$ complex. The active role of the incoming nucleophile in unmasking the oxyl radical character offers a potential explanation for the selectivity of formally Mn(V)=O oxidants, including the OEC.

2.3 Computational details

All calculations were carried out using density functional theory as implemented in the Gaussian03 and Gaussian09 packages[73,74]. Unless otherwise stated, the chosen functional was either the pure functional BLYP[176-178] or its hybrid, B3LYP[46-48], which incorporates 20% HF exchange. The SDD basis set[77-79] and associated effective core potential was used for Mn, 6-31G(d) for sulfur and for all atoms bonded to Mn (N, O), and 6-31G for carbon and hydrogen.[83,84] All geometry optimisations were full, with no restrictions, unless indicated explicitly in the text. Vibrational frequency calculations

were also performed in order to establish that the stationary points were minima or transition states, and the nature of the transition states was confirmed by relaxing the transition state geometry towards both the reactant and the product complexes.

2.4 Results and discussion

2.4.1 Limiting descriptions of the electronic structure of (L)(Porp)Mn(V)=O

Our starting point is a qualitative discussion of the limiting electron density distributions in the various spin-states of the formally Mn(V)-oxo porphyrin species, (L)(Porp)Mn(V)=O.

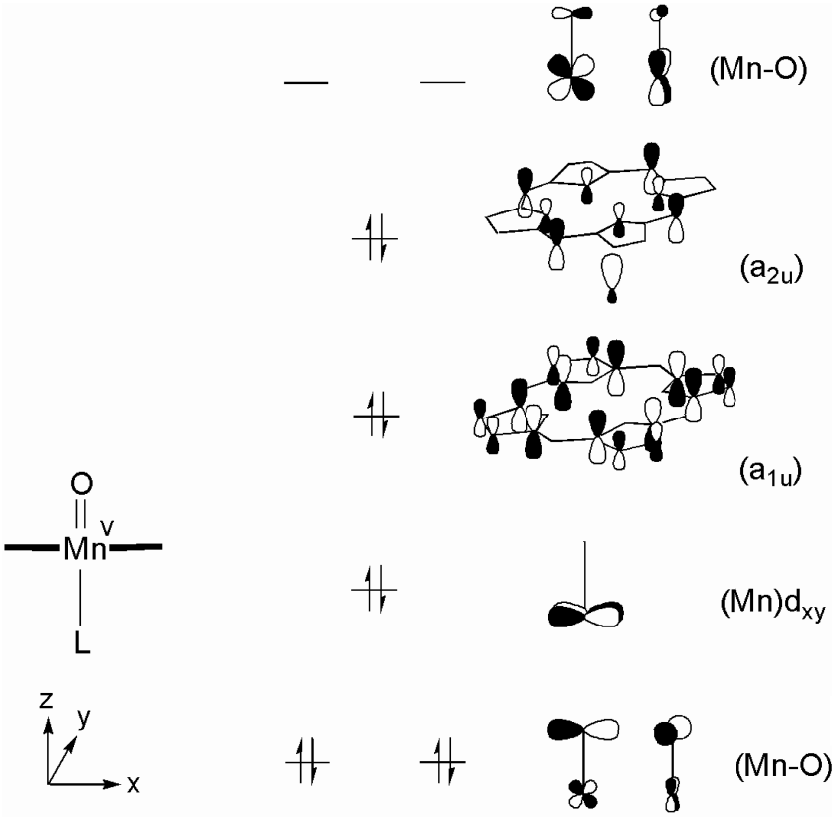

Figure 2.7 Key orbitals and the electronic structure of the singlet state (^{1}A) of (HO)(Porp)Mn(V)=O.

For a formally d^2 Mn(V)=O complex in an approximately octahedral environment, there are two ligand-field states, a singlet (^{1}A) and a triplet ($^3\Pi_{yz}$) are possible; in the former, the Mn–O non-bonding d_{xy} orbital is doubly occupied while in the latter, d_{xy} and one component of the degenerate two Mn–O π* {d_{xz}, d_{yz}} pair are singly occupied. The key orbitals and the electronic structure of the singlet state (^{1}A) of the (L)(Porp)Mn(V)=O are shown in Figure 2.7 and Kohn-Sham orbitals for the singlet state (^{1}A) of (OH)(Porp)Mn(V)=O are depicted in Figure 2.8. We base our nomenclature of states on Shaik's scheme[87,88] for the doublet and quartet states of the analogous iron system. Thus the label of the state is determined by the identity of the vacant orbital in the spin-α manifold: for example, d_{yz} for $^3\Pi_{yz}$. In the $^3\Pi_{yz}$ configuration shown in Figure 2.9, where the orbitals are separated into majority-spin (α) and minority-spin (β) manifolds. The accumulation of a spin density on the metal centre stabilizes the majority-spin manganese orbitals relative to their minority spin counterparts. In contrast, the splitting between majority- and minority-spin (β) components of the 'mainly O' Mn–O π orbitals is negligible simply because the oxygen atom carries less spin density.

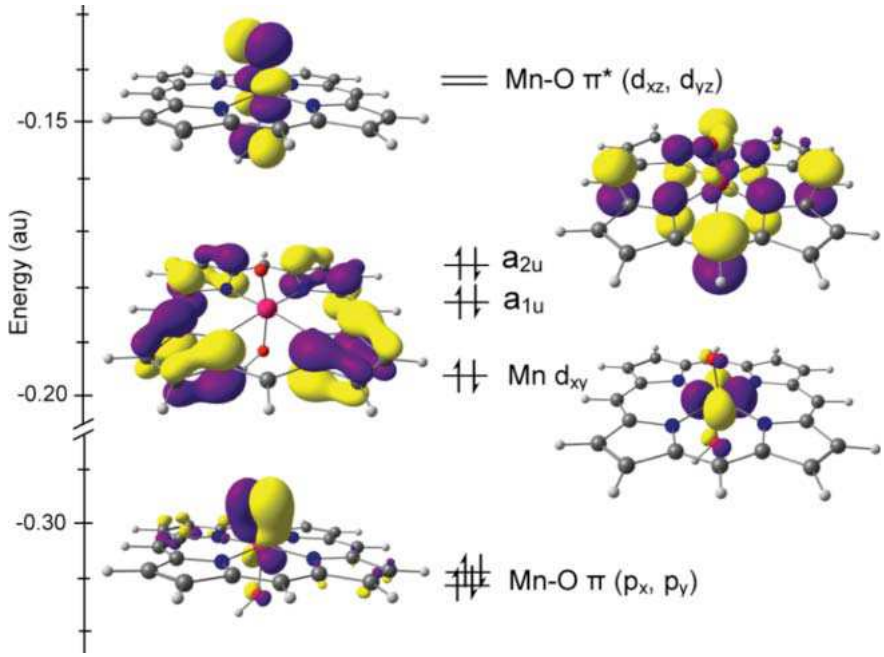

Figure 2.8 Kohn-Sham orbitals for the singlet state (^{1}A) of (L)(Porp)Mn(V)=O.

In the limit of complete localisation of the Mn–O π and π* orbitals on oxide or metal, respectively, we would anticipate net spin densities of 2.0 and 0.0 on metal and oxide,

with $<S^2>$ close to 2.0, the value for a pure triplet state. However, covalent mixing within the Mn–O π* orbital will share the majority-spin electrons between metal and oxide, introducing a finite positive spin density at the oxide. The spin-density distribution in a representative example of a $^3\Pi_{yz}$ state is shown in Figure 2.10a. The qualitative description of electron density distributions such as those of $^3\Pi_{yz}$ has been the source of some debate: Siegbahn has argued that this state is typical of Mn(V)=O species,[143-154] while Eisenstein has suggested that the emergence of spin density at the oxide implies some oxyl character.[170]

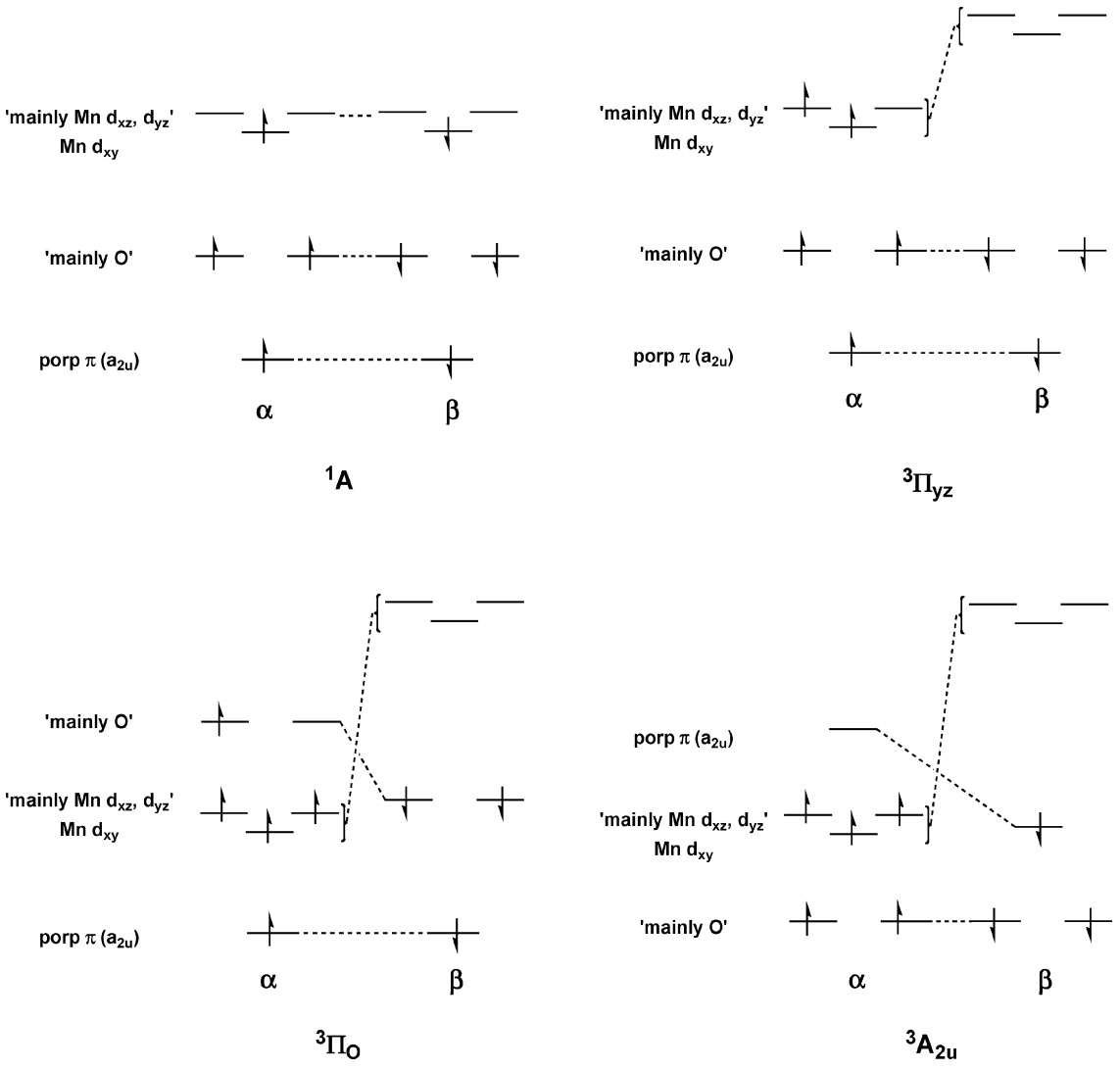

Figure 2.9 Schematic singlet and triplet electron density distributions for an (L)(Porp)Mn=O unit, where ^{1}A and $^3\Pi_{yz}$ represent 'normal' ligand field schemes, while $^3\Pi_O$ and $^3A_{2u}$ are 'inverted'.

It is important to emphasise that the accumulation of majority-spin density at the ligand is an entirely general phenomenon that occurs, to a greater or lesser extent, in all paramagnetic compounds. Thus although the extent of this spin redistribution will undoubtedly influence the real charge distribution on the Mn–O unit, it does not change the formal oxidation state of the metal so long as the singly occupied orbitals remain polarised towards the metal centre. We therefore regard electron density distributions such as $^3\Pi_{yz}$, with *majority* spin density at the oxygen centre, as being typical of Mn(V)=O 'metal radical' character, and quite distinct from the oxyl character that emerges in other triplets (*vide infra*).

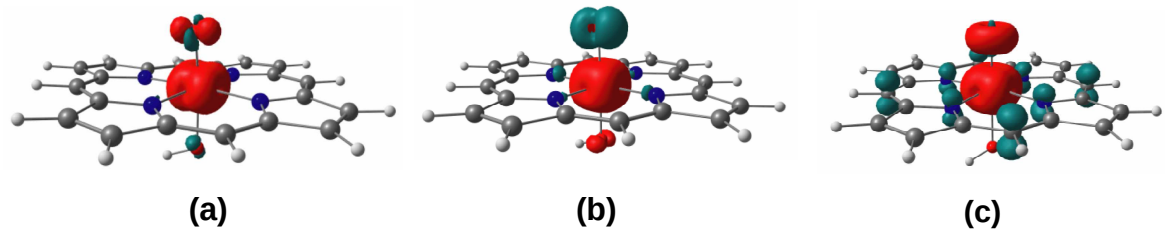

Figure 2.10 Spin density distributions in the three distinct triplet configurations, (a) $^3\Pi_{yz}$ {(HO)(Porp)Mn(O)/BLYP}, (b) $^3\Pi_O$ {(HO)(Porp)Mn(O)/B3LYP} and (c) $^3A_{2u}$ {[(H_2O)(Porp)Mn(O)]$^+$/B3LYP}.

The situation in $^3\Pi_{yz}$, where the metal-based orbitals lie above their ligand-based counterparts, is generally referred to as a 'normal' ligand field scheme. In cases where the metal is in a very high oxidation state and/or has a large number of unpaired electrons, this situation can be reversed in the majority-spin manifold, leading to a so-called 'inverted' scheme.[179] This is illustrated in Figure 2.9 for the second triplet state, $^3\Pi_O$, where the vacant majority-spin (α) Mn–O π* orbital now has dominant oxide character. The net result is that three spin-α orbitals on Mn are singly occupied, giving a formal oxidation state of Mn(IV). The localisation of the vacancy in the spin-α manifold onto the oxide leads to an excess of minority-spin (α) electrons and, in the limit of complete localisation of the orbitals, we would anticipate net spin densities of +3.0 on Mn and -1.0 on O, and an $\langle S^2 \rangle$ value approaching 3.0,[180,181] reflecting the strong spin contamination. A typical spin density plot illustrating $^3\Pi_O$ (oxyl radical) character is illustrated in Figure 2.10b. We regard the inverted scheme of $^3\Pi_O$, with its associated

accumulation of *minority*-spin (β) density on the oxide ligand, and $<S^2>$ value significantly higher than 2.0, as being indicative of 'oxyl' character. It is important to emphasise, however, that the distinction between the Mn(V)=O and Mn(IV)–$O^{\cdot +}$ limits, as defined by the $^3\Pi_{yz}$ and $^3\Pi_O$ configurations of Figure 2.9, rests solely on the dominant character of the vacant majority-spin (α) orbital: mainly Mn *d* in $^3\Pi_{yz}$, and mainly oxide π in $^3\Pi_O$. Given the relatively strong overlap between these two atomic orbitals, we should naturally anticipate a continuum of intermediate situations linking these two limiting forms. The potential for inverted ligand-field schemes is, of course, not limited to orbitals localised on the oxide.

The presence of high-lying porphyrin-based orbitals offers the possibility of an additional, quite distinct, triplet electron density distribution, $^3A_{2u}$. In this case, the majority-spin metal manifold falls below the porphyrin π* orbital (A_{2u} in idealised D_{4h} symmetry), and the vacancy in the majority-spin manifold (α) electron is localised on the porphyrin ring. We should again anticipate $<S^2>$ values approaching 3.0, with a total of +3.0 units of spin density delocalized over the Mn–O unit and -1.0 unit localised the porphyrin. A spin density plot for a representative example of a $^3A_{2u}$ state is shown in Figure 3.10c. Finally, we note that each of the inverted triplets, $^3\Pi_O$ and $^3A_{2u}$ can be described as containing an S = 3/2 Mn(IV) centre, antiferromagnetically coupled to an unpaired electron located on one of the ligands. Spin flips at the ligand therefore generate two quintet states, $^5\Pi_O$, and $^5A_{2u}$, where the coupling is ferromagnetic. In the limit of weak coupling, we anticipate that triplet and quintet states related by a simple spin-flip should have very similar energies.

2.4.2 Electronic structure of (HO)(Porp)Mn(O)

With a description of the limiting electron density distributions in hand, we are now in a position to interpret the electronic structure description that emerges from our calculations using DFT. Optimised structural parameters, net spin densities, $<S^2>$ values and relative energies of the various spin states accessible to a formally d^2

L(Porp)Mn(O) complex are summarised in Table 2.1. Values for the B3LYP functional are shown in plain text, those for the BLYP functional in italics. For the hydroxy complex, (HO)(Porp)Mn(O), calculations using the B3LYP functional clearly identify the triplet as the ground state, and the net spin densities [ρ(Mn) = 3.04, ρ(O) = -0.89] and $<S^2>$ value (2.92) are typical of the Mn(IV)–$O^{\cdot+}$ electron density distribution, $^3\Pi_O$ (Figure 10b). The quintet, $^5\Pi_O$ where the spin vectors on Mn and O are aligned ferromagnetically, lies only 2.8 kcal mol^{-1} higher in energy, and its structure is very similar to the triplet. The singlet state (^{1}A) lies a further 2.3 kcal mol^{-1} above the quintet, and the very short Mn–O bond reflects the depopulation of the Mn–O π* orbitals.

Table 2.1 Optimised bond lengths (Å), spin densities, $<S^2>$ values and relative energies (kcal mol^{-1}) of singlet, triplet and quintet states of (HO)(Porp)Mn(O) and $[(H_2O)(Porp)Mn(O)]^+$ B3LYP values are shown in plain text, BLYP in italics.

	Bond lengths		**Spin densities**				**$< S^2 >$**	**Relative energy**
	r(Mn-O)	**r(Mn-L)**	**ρ(Mn)**	**ρ(O)**	**ρ(L)**	**ρ(Porp)**		
(HO)(Porp)Mn(O)								
Singlet	1.55 (*1.59*)	1.82 (*1.85*)	0 (*0*)	0 (*0*)	0 (*0*)	0 (*0*)	0 (*0*)	+5.1 (*0.0*)
Triplet	1.78 (*1.66*)	1.85 (*1.90*)	3.04 (*2.17*)	-0.89 (*0.13*)	0.11 (*-0.09*)	-0.27 (*-0.22*)	2.92 (*2.17*)	0.0 (*+8.3*)
Quintet	1.84 (*1.79*)	1.84 (*1.92*)	2.86 (*2.59*)	1.09 (*0.96*)	0.13 (*0.23*)	-0.08 (*0.21*)	6.03 (*6.06*)	+2.8 (*+19.4*)
$[(H_2O)(Porp)Mn(O)]^+$								
Singlet	1.51 (*1.55*)	2.38 (*2.41*)	0 (*0*)	0 (*0*)	0 (*0*)	0 (*0*)	0 (*0*)	+9.8(*0.0*)
Triplet	1.64 (*1.63*)	2.27 (*2.28*)	2.48 (*2.31*)	0.66 (*0.26*)	0.01 (*0.02*)	-1.12 (*-0.55*)	3.08 (*2.51*)	0.0 (*+4.8*)
Quintet	1.64 (*1.67*)	2.27 (*2.30*)	2.45 (*2.41*)	0.66 (*0.69*)	0.00 (*0.00*)	0.88 (*0.89*)	6.08 (6.04)	0.0 (*+8.9*)

The BLYP functional, in contrast, gives a very different picture of the electronic structure. Most obviously, the relative energies of the spin states are reversed, with the singlet now lying lower than either the triplet or quintet. The tendency of HF exchange to stabilise states of higher multiplicity is well known,[186] so this change in order is not unexpected. The accumulated experimental evidence on (L)(Porp)Mn(V)=O species

suggests that they are diamagnetic,[137-140] in qualitative agreement with the results obtained with the BLYP rather than B3LYP functional. This conclusion must, however, be viewed with some caution in view of the close spacing of energy levels, the simplified nature of our model porphyrin ligand and the uncertainty regarding the identity of the axial ligand. More subtley, the absence of HF exchange causes a distinct change in the character of the triplet, which now has majority-spin density on both Mn (+2.17) and O (+0.13) and $<S^2>$ = 2.17, diagnostic of the $^3\Pi_{yz}$ Mn(V)=O state. The absence of HF exchange therefore induces a switch from an open-shell Mn(IV)–$O^{\cdot+}$ oxyl radical to a metal radical, Mn(V)=O, arrangement. The different character of the B3LYP and BLYP triplets is clearly reflected in a much shorter Mn–O bond length for the latter (1.66 Å *vs.* 1.78 Å). The quintet states, in contrast, have rather similar structures and spin densities at B3LYP and BLYP levels: both approach the Mn(IV)–$O^{\cdot+}$ ($^5\Pi_O$) limit, and the relatively large triplet–quintet splitting for BLYP reflects the fact that the two states have qualitatively different electron density distributions.

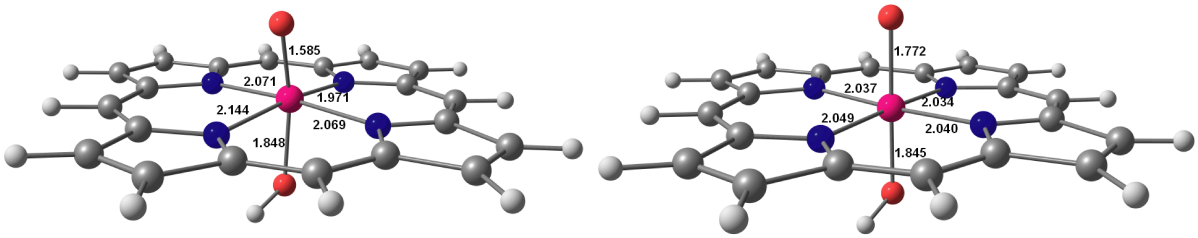

Figure 2.11 Optimised ground state structure for the (HO)(Porp)Mn(O) complex; (a) singlet ground state (^{1}A) with the BLYP (0% HF) functional and (b) triplet ground state ($^3\Pi_O$) with the B3LYP (20% HF) functional.

2.4.3 Electronic structure of $[(H_2O)(Porp)Mn(O)]^+$

In qualitative terms, protonation of the axial ligand should reduce the π-donor capabilities of the *trans* ligand, and so stabilise the orbitals localised in the Mn=O unit relative to their porphyrin-based analogues. This is indeed the case, and the stabilisation is sufficient that the triplet has porphyrin radical ($^3A_{2u}$) character (Figure 2.10c). An

$<S^2>$ value of 3.08 (B3LYP) along with the presence of majority-spin density on both Mn and O and minority-spin density on the porphyrin (ρ = -1.12) are characteristic of the $(H_2O)(Porp^{\cdot+})Mn(IV)=O$ limit. The orthogonality of the orbitals on the Mn=O and porphyrin units means that the quintet ($^5A_{2u}$) where the spins are aligned ferromagnetically, is almost identical, both structurally and energetically. The rather short Mn–O bond lengths of 1.64 Å in each case are indicative of substantial Mn(IV)=O multiple bond character, in contrast to the long $Mn(IV)–O^{\cdot+}$ bond length (1.78 Å) in the hydroxy case. The shift to the pure BLYP functional has a rather predictable influence on the overall energetics of the spin state equilibrium: the singlet is stabilised relative to the triplet and quintet, such that it becomes the ground state. For the triplet, the absence of HF exchange again reduces the open-shell character, such that it lies midway between the $(H_2O)(Porp)Mn(V)=O$ ($^3\Pi_{yz}$) and $(H_2O)(Porp^{\cdot+})Mn(IV)=O$ ($^3A_{2u}$) limits: $<S^2>$ = 2.51, ρ(Mn) =2.31, ρ(Porp) = -0.55.

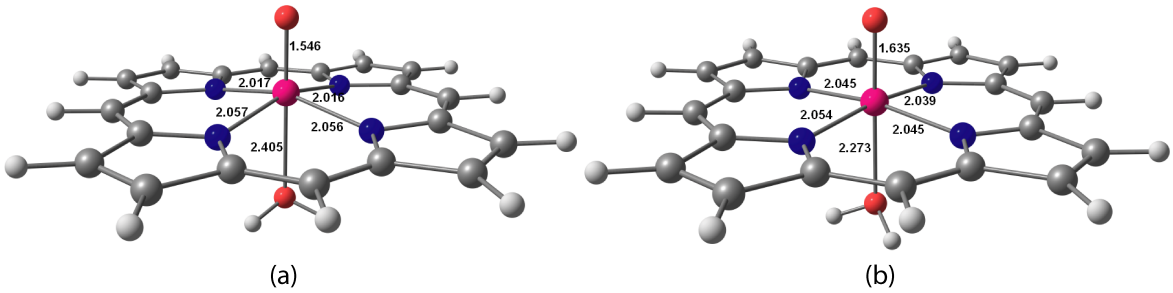

Figure 2.12 Optimised ground state structure for the $[(H_2O)(Porp)Mn(O)]^+$ complex; (a) singlet ground state (^1A) with the BLYP (0% HF) functional and (b) triplet ground state ($^3A_{2u}$) with the B3LYP (20% HF) functional.

In summary, our survey of the electronic structure shows that the electron density distribution in these formally Mn(V)=O complexes varies in a complex but predictable way as a function of both axial ligand and functional. The singlet state can be identified without ambiguity as a Mn(V)=O species with a short, strong Mn=O bond, regardless of the protonation state of the axial ligand (HO or H_2O) or the chosen functional.

Table 2.2 Exact exchange, $<S^2>$ values, key structural parameters, and triplet electronic structure of (HO)(Porp)Mn(V)=O and $[(H_2O)(Porp)Mn(V)=O]^+$ model complexes with a variety of DFT functionals.

DFT	Exact exchange (%)	$<S^2>$	r(Mn-O)	r(Mn-L)	Spin densities		
					ρ(Mn)	ρ(O)	ρ(Porp)
(HO)(Porp)MnO							
BP86	0	2.11	1.64	1.88	2.06	0.16	-0.15
BLYP	0	2.17	1.66	1.90	2.17	0.13	-0.22
PBEPBE	0	2.14	1.65	1.88	2.14	0.15	-0.19
BPW91	0	2.14	1.65	1.88	2.16	0.12	-0.20
OLYP	0	2.25	1.65	1.90	2.39	0.07	-0.32
B3LYP*	10	2.20	1.68	1.91	2.25	0.09	-0.26
O3LYP	11.6	2.85	1.74	1.85	3.01	-0.81	-0.33
B3LYP**	15	2.75	1.74	1.88	2.81	-0.68	-0.27
B3LYP	20	2.92	1.78	1.85	3.04	-0.89	-0.27
B3PW91	20	2.92	1.76	1.84	3.04	-0.86	-0.29
PBE1PBE	25	2.97	1.77	1.83	3.12	-0.92	-0.31
MPW1PW91	25	2.97	1.78	1.83	3.12	-0.92	-0.31
B1LYP	25	2.97	1.79	1.84	3.08	-0.92	-0.28
M05	28	3.01	1.78	1.85	3.19	-0.96	-0.34
BHandH	50	3.11	1.82	1.80	3.19	-1.10	-0.23
M052X	56	3.12	1.81	1.84	3.33	-1.07	-0.34
$[(H_2O)(Porp)MnO]^+$							
BP86	0	2.55	1.63	2.28	2.34	0.28	-0.60
BLYP	0	2.51	1.63	2.28	2.31	0.26	-0.55
PBEPBE	0	2.27	1.61	2.23	2.15	0.13	-0.26
BPW91	0	2.48	1.61	2.25	2.35	0.23	-0.56
OLYP	0	2.74	1.62	3.36	2.51	0.24	-0.73
B3LYP*	10	2.61	1.65	2.29	2.38	0.31	-0.67
O3LYP	11.6	3.03	1.62	2.34	2.59	0.54	-1.11
B3LYP**	15	2.73	1.66	2.30	2.34	0.35	-0.78
B3LYP	20	3.08	1.64	2.27	2.48	0.66	-1.12
B3PW91	20	3.10	1.63	2.25	2.53	0.64	-1.15
PBE1PBE	25	3.12	1.62	2.34	2.56	0.60	-1.15
MPW1PW91	25	3.12	1.62	2.24	2.55	0.62	-1.05
B1LYP	25	3.11	1.63	2.27	2.49	0.64	-1.12
M05	28	3.18	1.62	2.33	2.65	0.56	-1.20
BHandH	50	3.20	1.59	2.14	2.62	0.53	-1.15
M052X	56	3.19	1.60	2.24	2.70	0.43	-1.13

The electron density distribution in the triplet, in contrast, is highly dependent on functional, tending towards the metal radical {L(Porp)Mn(V)=O} limit for the BLYP functional but showing marked open-shell character for the hybrid B3LYP. The triplet electronic structure of (L)(Porp)Mn(V)=O systems with a variety of DFT functionals are summarised in Table 2.2, where hybrid and non-hybrid functionals give very different qualitative descriptions of spin density populations. The open-shell triplet can display dominant oxyl radical {L(Porp)Mn(IV)–$O^{\cdot+}$} or porphyrin radical {L($Porp^{\cdot+}$)Mn(IV)=O} character depending on axial ligand. Given the emphasis in the literature on 'oxyl' character as a requirement for effective water oxidation, it seems likely that these different limiting descriptions will give rise to oxidants with rather different characteristics.

2.4.4 Oxidation of Me_2S by (HO)(Porp)Mn(O)

This section describes the oxidation of the sulfide, Me_2S, with (HO)(Porp)Mn(O) system by defining a reaction coordinate involving the approach of the sulfur centre towards the oxo ligand. The computed potential surface (B3LYP) for oxidation of Me_2S by (HO)(Porp)Mn(O) is summarised in Figure 2.13a, where the S–O distance is defined as a one-dimensional reaction coordinate and varied from 3.5 to 1.4 Å. All other structural parameters were allowed to optimise freely, and reactants, intermediates and products are identified as **R**, **I** and **P**, respectively. The potential energy profiles are qualitatively identical to that of complex, $[(Me_3TACN)Mn(O)(OH)_2]^+$ reported by McGrady and co-workers.[171] At large S–O separations, the energies of the electronic states reflect those of the isolated manganese species discussed in the previous section: the triplet **(^{3}R)** lies below the quintet **(^{5}R)**. Moreover, the optimised structural parameters and net spin densities (summarised in Table 2.3) resemble the isolated reactants, with dominant oxyl radical ($^3\Pi_O$) character, (HO)(Porp)Mn(IV)–$O^{\cdot+}$. On the triplet surface, the interaction with the incoming nucleophile is attractive even at long separations, and a barrierless transfer of a majority spin (α) electron from sulfur to oxygen leads to a shallow minimum, ^{3}**I**, 2 kcal mol^{-1} below the entry channel. The

electronic properties of this intermediate [$<S^2>$ = 2.83, ρ(Mn) = 2.92, ρ(O)=-0.46, ρ(S)=-0.33] suggest that it should be formulated as a Mn(IV)–O–$S^{\cdot+}$ species, analogous to the 'rebound' intermediate shown in Figure 2.5.

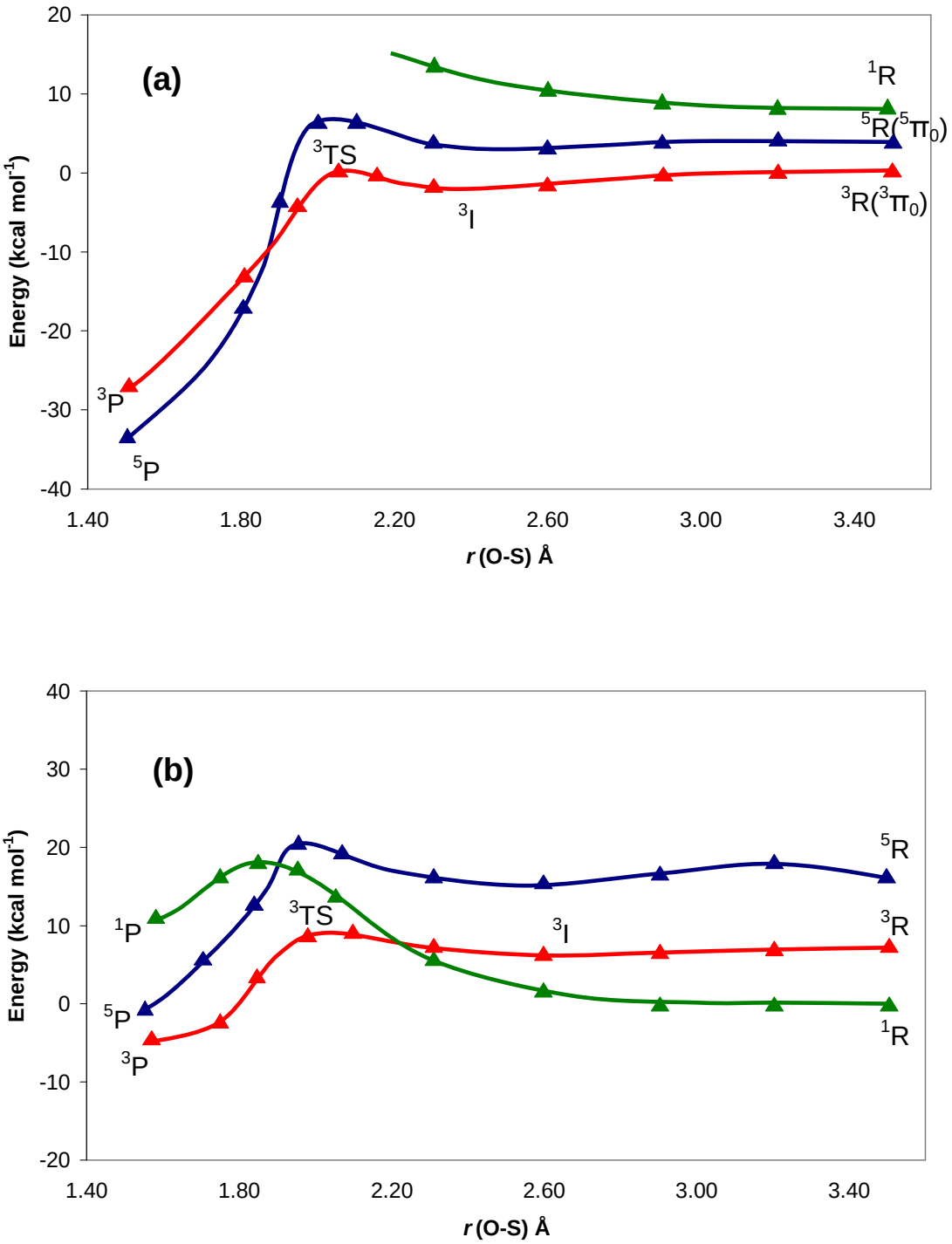

Figure 2.13 Singlet, triplet and quintet potential energy surfaces for oxidation of Me_2S by (HO)(Porp)Mn(O) with (a) B3LYP functional and (b) BLYP functional.

The oxyl radical character of the free reactant means that the electronic changes in the early stages of the reaction coordinate are localised almost entirely on the S–O unit, with the metal centre acting as a spectator. As a result, both the Mn–O bond length and the net spin density at the metal remain almost constant. Groves has previously noted the potential importance of changes in Mn–O bond length in controlling the kinetics of electron-transfer reactions for singlet and triplet ground states.[137-140] Our analysis suggests that such factors may be critical even in states with the same multiplicity. Although the singlet state remains above the triplet at all points in Figure 2.13b, a comparison of the long-range interaction with the nucleophile is instructive. In marked contrast to the triplet, the singlet curve is repulsive at large separations. This fundamental difference can be traced to the full occupancy of the pπ manifold of the oxide ligand in the singlet, as a result of which the nucleophile effectively 'bounces off'. In terms of the overall reaction, whilst a long-range repulsion, as observed for the singlet, implies a slower reaction, it also offers the possibility of substrate selectivity, as the shape of the repulsive wall will depend on the nucleophile. In contrast, where the long-range interaction is attractive, as is the case for the oxyl radical triplet, the rate will increase but there is less opportunity to discriminate between incoming nucleophiles.

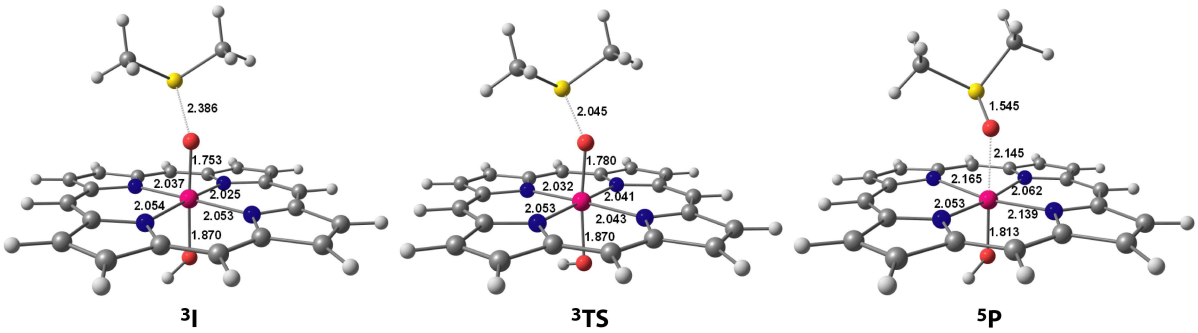

Figure 2.14 Optimised key stationary points of the potential energy surfaces for oxidation of Me_2S by (HO)(Porp)Mn(O) with B3LYP.

From the Mn(IV)–O–$S^{\cdot+}$ intermediate, ^{3}**I**, transfer of the minority-spin (β) electron from sulfur to the metal centre leads to the triplet product, ^{3}**P**, *via* a very low-lying transition state, ^{3}**TS**. In the triplet product, ^{3}**P**, the net spin density of 2.08 on manganese is typical of a low-spin Mn(III) complex. Given the weak-field nature of the sulfoxide ligand in

the product, it is unsurprising that the quintet surface drops below the triplet for the products, and the properties of ^{5}**P** are typical of a high-spin Mn(III) complex (Figure 2.14) . In the following sections, we discuss how changes in both functional and axial ligand can influence the nature of the potential energy surface.

Table 2.3 Optimised bond lengths (Å), spin densities, $<S^2>$ values and relative energies (kcal mol^{-1}) of various stationary points on the potential energy surface for the reaction of (HO)(Porp)Mn(O), and $[(H_2O)(Porp)Mn(O)]^+$ with Me_2S (B3LYP values are shown in plain text, BLYP in italics).

	Structural parameters		**Mulliken Spin density**				**$<S^2>$**	**Relative energy**
	r(O-S)	**r(Mn-O)**	**ρ(Mn)**	**ρ(O)**	**ρ(S)**	**ρ(Porp)**		
(HO)(Porp)MnO								
^{1}**R**	3.50 *(3.50)*	1.56 *(1.59)*	0 *(0)*	0 *(0)*	0 *(0)*	0 *(0)*	0 *(0)*	+7.6 *(0.00)*
^{3}**R**	3.50 *(3.50)*	1.78 *(1.67)*	3.01 *(2.27)*	-0.85*(0.09)*	-0.02 *(0.09)*	-0.27 *(-0.21)*	2.91 *(2.24)*	0.0 *(+7.1)*
^{5}**R**	3.50 *(3.50)*	1.84 *(1.77)*	2.88 *(2.59)*	1.07 *(0.81)*	0.02 *(0.19)*	-0.09 *(0.15)*	6.05 *(6.05)*	+4.1 *(+16.4)*
^{3}**I**	2.39 *(2.60)*	1.75 *(1.70)*	2.92*(2.43)*	-0.46 *(-0.09)*	-0.33 *(-0.23)*	-0.23 *(-0.16)*	2.83 *(2.37)*	-2.0 *(+6.4)*
^{3}**TS**	2.05 *(2.03)*	1.78 *(1.80)*	2.69 *(2.41)*	-0.17 *(0.00)*	-0.38 *(-0.26)*	-0.20 *(-0.16)*	2.57 *(2.32)*	-0.02 *(+9.2)*
^{3}**P**	1.51*(1.56)*	2.16 *(2.19)*	2.08 *(2.16)*	0.00 *(0.00)*	0.00 *(0.00)*	-0.13 *(-0.24)*	2.03 *(2.10)*	-27.1 *(-4.8)*
^{5}**P**	1.54 *(1.54)*	2.17 *(2.60)*	3.91 *(3.76)*	-0.01 *(0.00)*	0.00 *(0.23)*	0.09 *(-0.04)*	6.06 *(6.04)*	-32.7 *(-0.8)*
$[(H_2O)(Porp)MnO]^+$								
^{5}**R$_1$**	3.50	1.65	2.56	0.56	0.34	0.51	6.07	0.0
^{3}**R$_1$**	3.50	1.64	2.55	0.57	-0.34	-0.76	3.06	+0.1
^{3}**R$_2$**	3.50	1.66	2.95	-0.43	-0.29	-0.21	2.80	+5.3
^{3}**I**	2.27	1.68	2.84	-0.16	-0.52	-0.16	2.74	-7.3
^{3}**TS**	2.08	1.70	2.62	-0.04	-0.46	-0.14	2.52	-6.1
^{3}**P**	1.58	1.93	2.03	0.00	0.00	-0.04	2.01	-32.7
^{5}**P**	1.55	2.21	4.03	0.05	0.01	-0.13	6.05	-48.9

In all cases, the later stages of the reaction from the radical intermediate ^{3}**I** to the product, **P**, are very similar, involving a low barrier on the triplet surface and, in the case of B3LYP, a spin crossover to the quintet surface. The most interesting differences occur in the early stages of the reaction, where the O–S separation is large. We noted

above that the BLYP functional gives a fundamentally different picture of the electronic structure of (HO)(Porp)Mn(O): the singlet lies below the triplet, and the latter has dominant metal radical ($^3\Pi_{yz}$) as distinct from oxyl radical ($^3\Pi_O$) character. The absence of oxyl radical character in the triplet state translates into a qualitatively different potential energy surfaces for the reaction with Me_2S (Figure 2.13b). Most conspicuously, the singlet state lies lowest at large separations, and the interaction with the incoming nucleophile is again repulsive due to the fully occupied pπ manifold on the oxo ligand. A very shallow minimum corresponding to **^{3}I** (Figure 2.15) again emerges in the triplet curve, but in this case it occurs at rather longer O–S separations (2.60 Å *vs.* 2.39 Å for B3LYP) and lies only 0.7 kcal mol^{-1} below the entry channel (*vs.* 2 kcal mol^{-1} for B3LYP). Moreover, the net spin densities [ρ(Mn) = 2.43, ρ(O) = -0.09] remain very similar to those in the triplet ground state of the free reactant (Table 2.3), suggesting that long-range electron transfer from sulfur to oxygen is much less developed than was the case with the B3LYP functional.

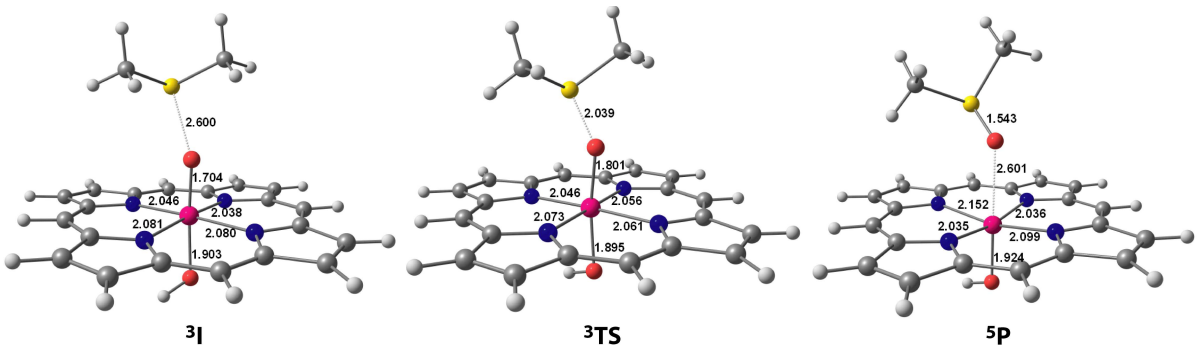

Figure 2.15 Optimised key stationary points of the potential energy surfaces for oxidation of Me_2S by (HO)(Porp)Mn(O) with BLYP.

The overall picture of the oxidation reaction is therefore fundamentally different from the BLYP functional: the system remains on the singlet surface to relatively short O–S separations (~ 2.3 Å), before crossing to the triplet curve, passing over a low barrier, and forming the product in its triplet ground state. The intermediate on the triplet surface is by-passed, and therefore the reaction is better viewed as a concerted two-electron transfer rather occurring in two sequential one-electron steps. Throughout the reaction, the unpaired electron density in the triplet remains buried on the metal centre,

with only small amounts delocalised out onto the oxo ligand. The majority and minority-spin electrons on the incoming nucleophile are not, therefore, strongly differentiated as they would be in the case of an oxyl radical. The overall barrier of 9.2 kcal mol^{-1} is in reasonable qualitative agreement with the kinetic data reported by Nam and co-workers for oxidation of sulfides.[139,140]

We have presented the B3LYP and BLYP surfaces side by side in this section to illustrate the very different pictures that can emerge from commonly used functionals. We noted in the first section that the singlet ground state predicted by the BLYP functional seems in better agreement with available spectroscopic data, and the barrier of 9.2 kcal mol^{-1} on the BLYP surface also seems to be rather more consistent with kinetic data than the essentially barrierless sequential reaction predicted by the B3LYP functional. At the opposite end of the potential energy surface, however, B3LYP predicts a high-spin (quintet) state for the product, while BLYP predicts a triplet. The majority of experimental data on Mn(III) porphyrins suggests a high-spin (quintet) ground state, although the presence of very low-lying triplet states has been noted.[182-186] It is probably unrealistic to expect any single functional to accurately describe both Mn(V)=O and Mn(III)–O limits with equal accuracy,[187] even if the ligand environment was modelled exactly, and therefore some imbalance seems inevitable. We simply wish to highlight here that choice of functional can have important implications, not just in quantitative terms but in the qualitative description of the reaction pathway.[188]

2.4.5 Oxidation of Me_2S by $[(H_2O)(Porp)Mn(O)]^+$

The potential energy surface (B3LYP) for oxidation of Me_2S by the protonated species, $[(H_2O)(Porp)Mn(O)]^+$ (Figure 2.16) shows very different features, all of which are connected to the different properties of the ground states discussed in the previous section. Although both (HO)(Porp)Mn(O) and $[(H_2O)(Porp)Mn(O)]^+$ have triplet ground states at the B3LYP level, their character is very different: the former has

dominant Mn(IV)–$O^{\cdot+}$ oxyl radical character ($^3\Pi_O$), while the latter has dominant ($Porp^{\cdot+}$)Mn(IV)=O character ($^3A_{2u}$). The consequences of this difference are most apparent at long separations (> 3.1 Å), where the interaction with the incoming nucleophile on the triplet surface is repulsive for the protonated species, due to the double occupancy of both components of the oxide pπ manifold in the $^3A_{2u}$ state.

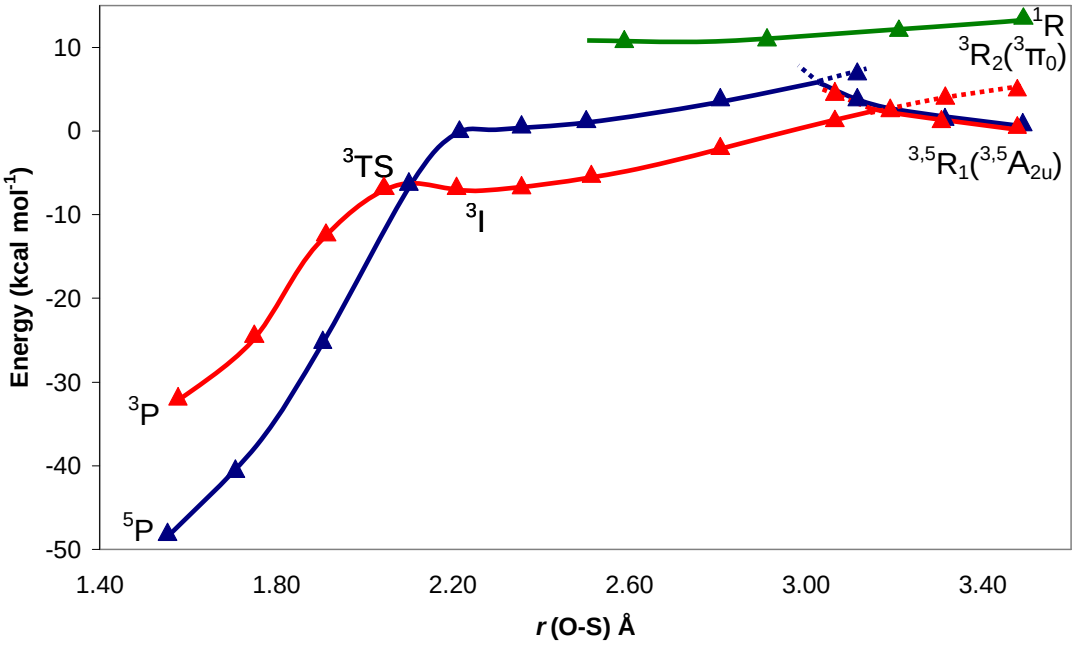

Figure 2.16 Singlet, triplet and quintet potential energy surfaces for the oxidation of Me_2S by $[(H_2O)(Porp)Mn(O)]^+$ (B3LYP).

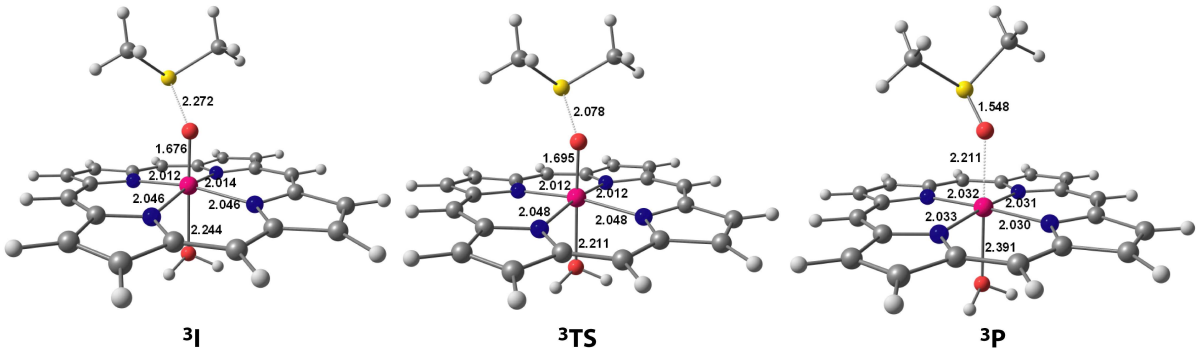

Figure 2.17 Optimised key stationary points of the potential energy surfaces for oxidation of Me_2S by $[(H_2O)(Porp)Mn(O)]^+$ with B3LYP.

In the region of r(O–S) = 3.1 Å there is a discontinuity in the triplet surface, which then becomes attractive, leading to the triplet intermediate **^{3}I** (Figure 2.17), which is qualitatively very similar to that for the hydroxy complex. Extrapolating the attractive segment of the curve back past the discontinuity to large S–O separations has allowed us to locate a second triplet state **(^{3}R$_2$)** where the electronic distribution is typical of an oxyl radical state, $^3\Pi_O$. Thus the discontinuity in the triplet surface marks the point where the oxyl radical character of the manganese species is 'unmasked' by the repulsive interactions between the lone pairs on the incoming nucleophile and the oxide ligand, which drive an electron into the vacancy in the porphyrin ring, opening up a route for electron transfer from sulfur to the oxide. The quintet differs from the triplet only in the nature of the coupling of metal- and ligand based electrons, and so we see a similar discontinuity in the quintet surface at somewhat shorter O–S separation. It is important to emphasise that Figure 2.16 represents a one dimensional scan through the potential energy surface, and so the discontinuity in the triplet surface does not represent a true transition state, but rather a lower bound to its energy. Thus there are abrupt changes in other structural parameters (primarily the Mn–O, Mn–N and C–C distances) that reflect the transfer of an electron from oxide to porphyrin. In terms of the dynamics of the reaction, this means that the incoming nucleophile will have to approach somewhat beyond the discontinuity before it can access the attractive channel of the triplet surface. We further investigate this issue by considering the two-electron oxidation of CH_4 and C_2H_4 catalysed by $[(H_2O)(Porp)Mn(O)]^+$ complex.

2.4.6 Oxidation of CH_4 by $[(H_2O)(Porp)Mn(O)]^+$

Iron-porphyrin complexes can catalyse C-H hydroxylation in cytochrome P450 enzymes.[87,88,189] Synthetic Mn-,[190,191] Ru-,[192,193] and Fe-based[194,195] model complexes are also well-known in C-H hydroxylation reactions. The generally accepted catalytic cycle (rebound mechanism) for the C-H bond oxidation is shown in Figure 2.18.[196-199] This mechanistic proposal consists of three steps; the first of which is oxidation of the (Porp)Mn(III) catalyst to a (Porp)Mn(V)O species, which initiates the C-H

hydroxylation process. Then H atom abstraction from the substrate C–H bond leads to a radical intermediate and OH-rebound by OH transfer to this radical.

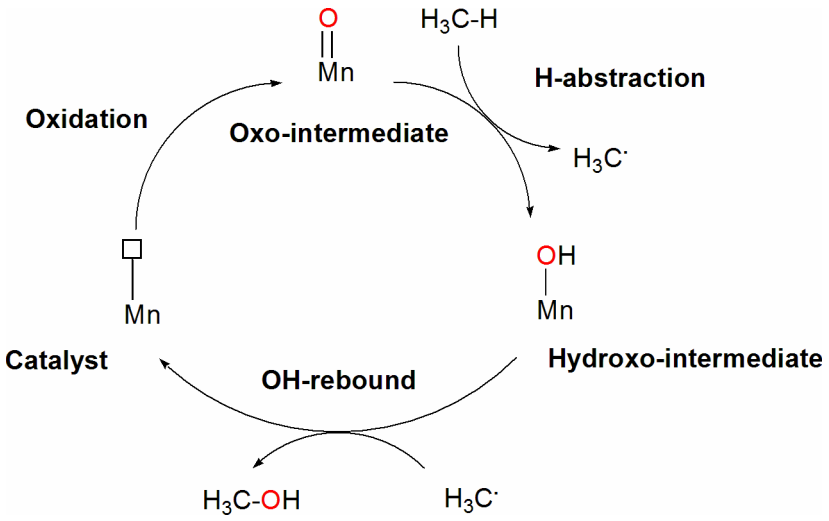

Figure 2.18 Rebound mechanism for oxidation of CH_4 by high-valent Mn-oxo species.

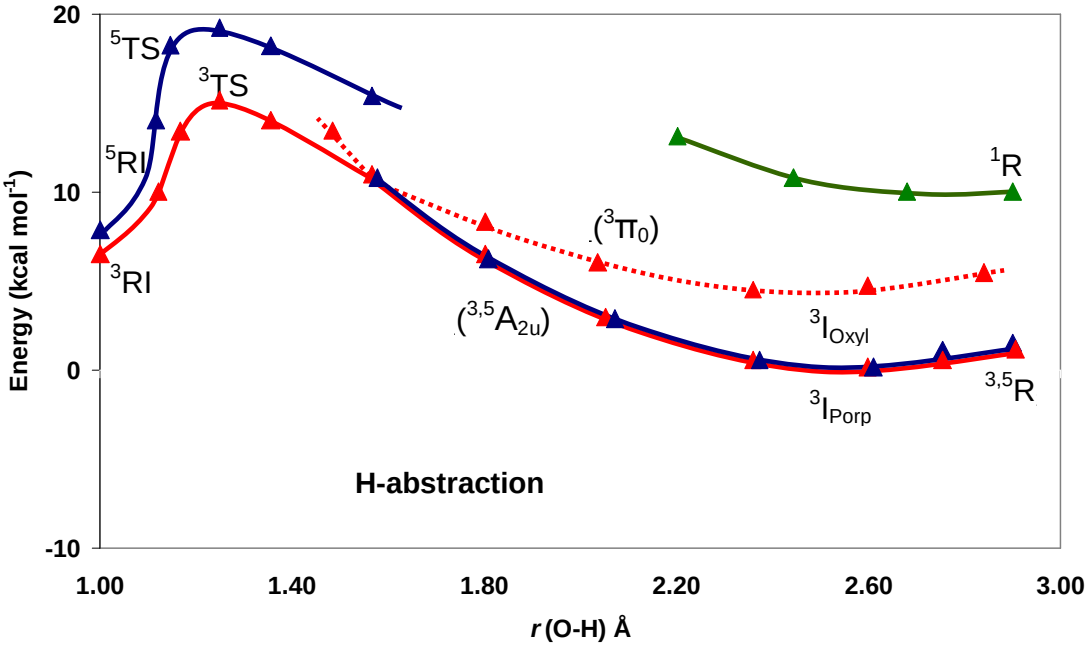

Figure 2.19 Singlet, triplet and quintet potential energy surfaces for the oxidation of CH_4 by $[(H_2O)(Porp)Mn(O)]^+$.

We have explored the potential energy profiles for oxidation of CH_4 with $[(H_2O)(Porp)Mn(O)]^+$ complex by defining a reaction coordinate involving the

approach of the H towards the oxo ligand. Calculated potential energy surfaces are depicted in Figure 2.19, which has a stable intermediate, $^{3}\mathbf{I_{Porp}}$, which lies 0.5 kcal mol^{-1} below the separated reactants $^{3}\mathbf{R}$ and CH_4 [r(O-H) = 3.5 Å]. This intermediate has dominant $(H_2O)(Porp^{\cdot+})Mn(IV)=O$ character [ρ(Porp) = -1.12], and therefore the oxyl radical character is 'masked'. A second intermediate, $^{3}\mathbf{I_{Oxyl}}$, has a spin density on Mn of 3.02 and on O of -0.82, indicating a dominant $Mn(IV)–O^{\cdot+}$ character ($^{3}\Pi_O$), and is 5 kcal mol^{-1} above the porphyrin radical intermediate **($^{3}\mathbf{I_{Porp}}$)**. However, the oxyl radical potential energy surface ($^{3}\Pi_O$) is repulsive at short-range separations because C–H bonding electrons are less diffuse than the lone pairs of Me_2S, and the discontinuity region for hydrocarbon oxidation occurs at shorter separations [r(O-H) ~ 1.6 Å], and therefore higher energy [~ 10.1 kcal mol^{-1}].

Table 2.4 Optimised bond lengths (Å), spin densities, $<S^2>$ values and relative energies (kcal mol^{-1}) of various stationary points on the potential energy surface for the reaction of $[(H_2O)(Porp)Mn(O)]^{+}$ with CH_4.

	Structural parameters		Mulliken Spin density				$<S^2>$	Relative energy
	r(O-H)	r(Mn-O)	ρ(Mn)	ρ(O)	ρ(C)	ρ(Porp)		
$^{1}\mathbf{R}$	3.50	1.55	---	---	---	---	0.00	+9.8
$^{3}\mathbf{R}$	3.50	1.63	2.48	0.66	0.00	-1.12	3.08	0.0
$^{5}\mathbf{R}$	3.50	1.64	2.47	0.65	0.00	0.89	6.07	+0.1
$^{3}\mathbf{I_{Porp}}$	2.69	1.64	2.46	0.65	0.00	-1.12	3.08	-0.5
$^{3}\mathbf{I_{Oxyl}}$	2.59	1.68	3.02	-0.82	-0.01	-0.20	2.84	+4.5
$^{3}\mathbf{TS}$	1.21	1.72	3.04	-0.35	-0.59	-0.17	2.91	+13.7
$^{5}\mathbf{TS}$	1.29	1.77	3.09	0.57	0.49	-0.09	6.10	+19.9
$^{3}\mathbf{RI}$	0.99	1.76	3.11	0.00	-1.06	-0.18	3.08	+8.1
$^{5}\mathbf{RI}$	0.99	1.77	3.18	0.05	1.00	-0.19	6.12	+8.4
$^{3}\mathbf{P}$	0.98	2.02	2.03	-0.01	-0.01	-0.09	2.16	-38.0
$^{5}\mathbf{P}$	0.97	2.31	4.05	0.03	0.00	-0.12	6.06	-58.4

The $^{3}\mathbf{I_{Oxyl}}$, and the corresponding radical intermediate, $^{3}\mathbf{RI}$, are separated by a transition state, $^{3}\mathbf{TS}$, where the O-H bond is significantly contracted (1.21 Å), while the Mn-O bond is further elongated to 1.72 Å (Figure 2.20). This smooth electron transfer

pathway gives rise to a barrier of 13.7 kcal mol^{-1}. The barrier on the quintet surface (^{5}**TS**) is further 6.2 kcal mol^{-1} higher in energy. The resulting ^{3}**RI** has a net spin density on Mn of 3.11, which confirms the d^3 configuration, and the excess of spin-β density is now localised on C (-1.06). This intermediate can therefore be described as a Mn(IV) species, antiferromagnetically coupled to a C radical. The corresponding quintet state, ^{5}**RI**, arising from ferromagnetic coupling of the metal- and ligand-based radicals have been located 0.3 kcal mol^{-1} above the ^{3}**RI**.

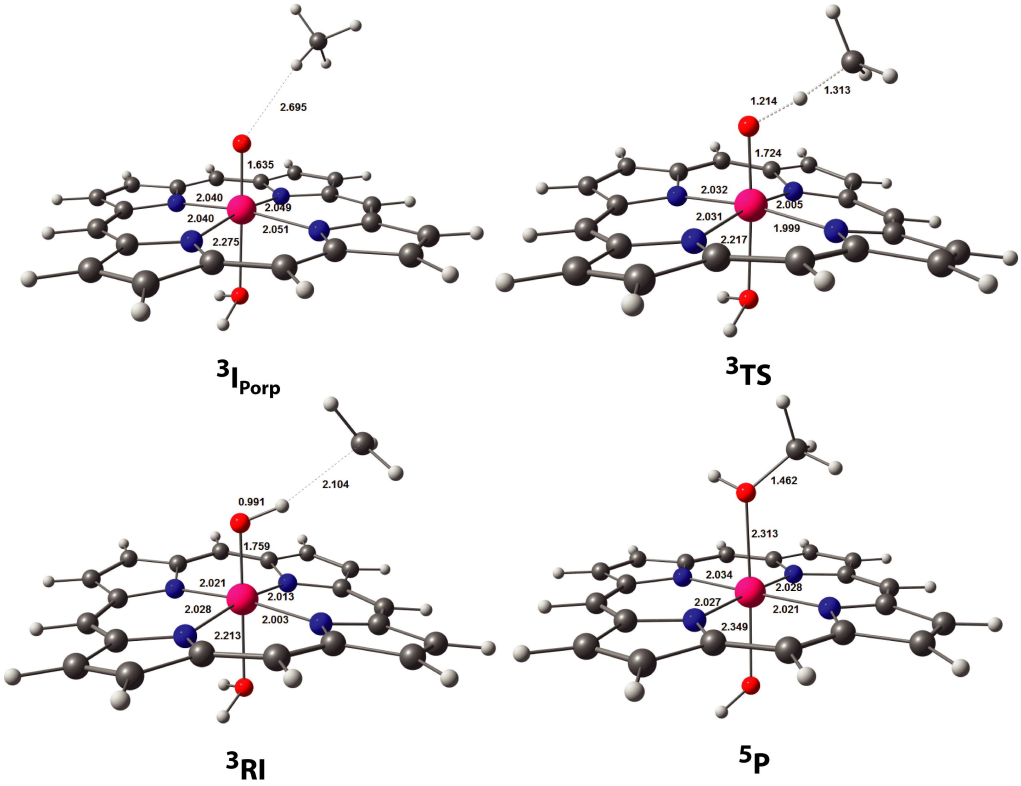

Figure 2.20 Optimised key stationary points of the potential energy surfaces for oxidation of CH_4 by $[(H_2O)(Porp)Mn(O)]^+$ with B3LYP.

The overall oxidation process leads to the highly exothermic (-58.4 kcal mol^{-1}) formation of a stable Mn(III)-CH_4OH product, ^{5}**P**, which has a quintet ground state, typical of high-spin Mn(III) (d^4) [ρ(Mn) = +4.05] (Figure 2.20). The corresponding triplet state of the product, ^{3}**P**, featuring a low-spin Mn(III) centre [ρ(Mn) = +2.03], has also been located, some 20.4 kcal mol^{-1} above the ^{5}**P**.

2.4.7 Epoxidation of C_2H_4 by $[(H_2O)(Porp)Mn(O)]^+$

Cytochrome P-450 enzymes catalyse a number of important metabolic reactions including epoxidation of alkenes,[87,88,200-202] where a high-valent Fe-oxo species is believed to be the active species for the catalytic activity.[87,88] The structurally well-characterised metal-oxo porphyrins of Ru,[203-205] Cr,[206-209] Fe[210-215] and Mn,[151-163,216-217] the simple active site model complexes for the cytochrome P-450 enzymes, have been identified as the active species in catalytic epoxidation. The development of synthetic metal-based oxidation catalysts for epoxidation reactions is industrially useful as well as provide possible insights into the mechanistic features of selective oxidation reactions by the cytochrome P-450 enzymes. The generally accepted mechanism for the epoxidation of olefins by the metal-porphyrin systems is given in Figure 2.21, where the oxidant **(OX)** provides an oxygen atom, which may transfer from the oxidant to the metal, and then to the alkene to form the epoxide.[218]

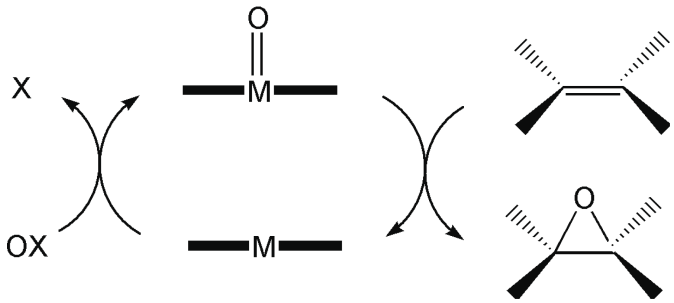

Figure 2.21 The catalytic cycle for the epoxidation of alkene by the metal-porphyrin species.

The mechanistic nature of epoxidation of alkene by the Mn-porphyrin species merits some discussions due to the lack of experimental evidence of intermediates and rate determining step. The oxidised form of the metal-porphyrin systems, in most cases high-valent metal-oxo species, leads to epoxidation *via* various reaction pathways depending on the oxidation potentials of the alkenes (Figure 2.22).[219]

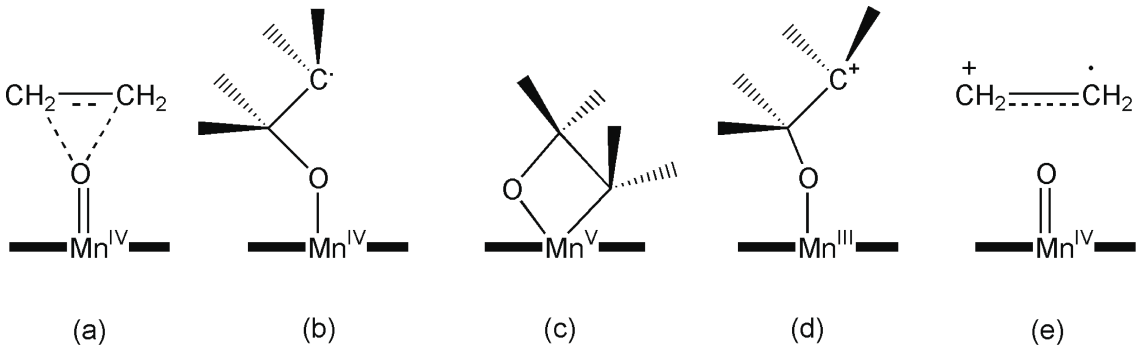

Figure 2.22 Proposed intermediates (a) a concerted insertion, (b) a carbon radical, (c) a metallaoxetane, (d) a carbocation, and (e) an alkene derived π-radical cation for the epoxidation of alkene by the high-valent Mn(V)-oxo porphyrin species as an example.

Experimental and theoretical work by Katsuki and Jacobsen led to elucidation of the mechanism based on high-valent Mn-oxo-salen species, where the isolated alkenes have been proposed to react in a concerted manner (Figure 2.22a), while the conjugated alkenes react in a stepwise radical process (Figure 2.22b). Both substrate classes may involve the reversible formation of a metallaoxetane (Figure 2.22c). Formation of a radical intermediate (Figure 2.22b) is supported by the observed formation of *trans* epoxides in the epoxidation of *cis* alkenes.[220-222] A recent computational study with DFT on the relevant Mn(V)-oxo porphyrin monomer systems by Randall and co-workers also supports the radical reaction pathway.[218] However, the detailed chemical steps and the nature of the rate-determining step involved in the epoxidation by the high-valent Mn-oxo porphyrin species are still unclear.

If we accept the radical intermediate as the key intermediate for the reaction (Figure 2.23), the olefin epoxidation by high-valent Mn(V)-oxo species may operate *via* a single electron rate determining path way, where the first electron transfer gives rise to a radical intermediate and the second electron transfer leads to oxygen atom transfer from the metal to the alkene. To explain this question, we have developed the full potential energy profile for epoxidation of ethylene by the $[(H_2O)(Porp)Mn(O)]^+$ monomer model complex.

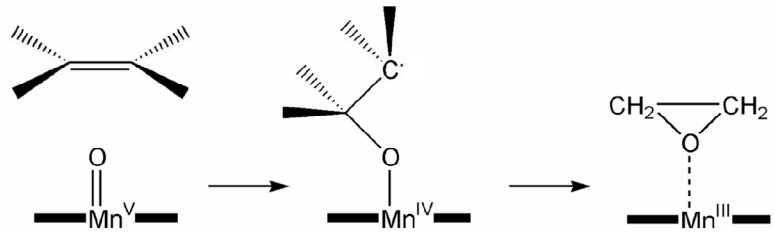

Figure 2.23 Mechanisms for olefin oxidation by high-valent Mn(V)=O species *via* a carbon radical intermediate.

The optimised structural parameters, spin densities, $<S^2>$ values and relative energies of the various stationary points on the potential energy surface for the reaction of $[(H_2O)(Porp)Mn(O)]^+$ with C_2H_4 are summarised in Table 2.5. The detailed potential energy surfaces are depicted in Figure 2.24, where the C-O distance is defined as a one-dimensional reaction coordinate in the region of 1.4–3.5 Å for the first C-O bond formation.

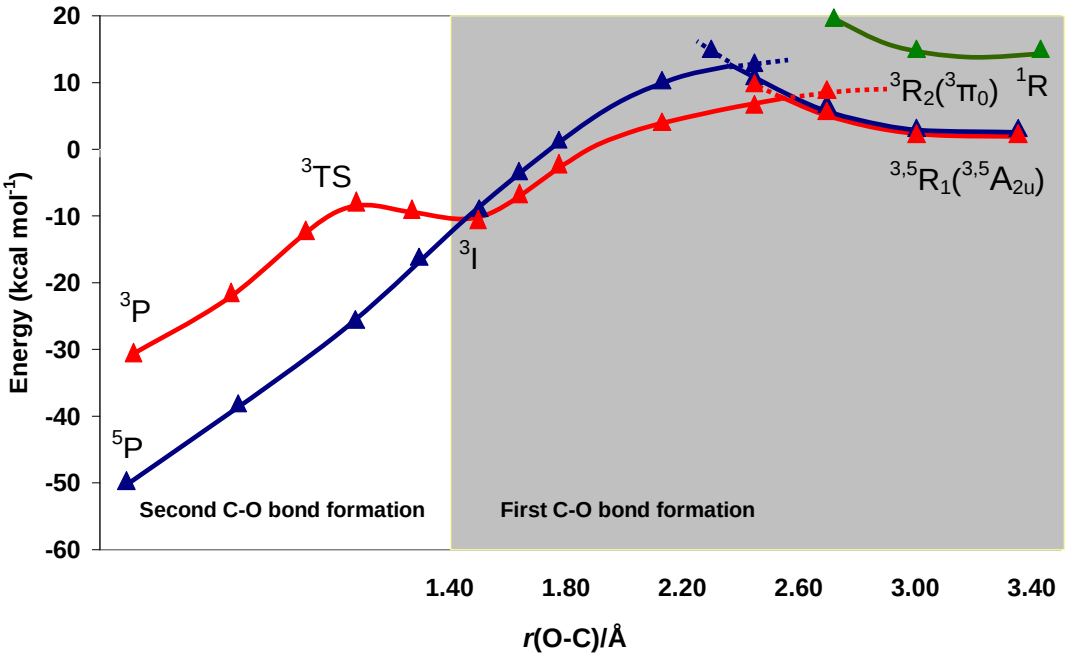

Figure 2.24 Singlet, triplet and quintet potential energy surfaces for the oxidation of C_2H_4 by $[(H_2O)(Porp)Mn(O)]^+$.

Table 2.5 Optimised bond lengths (Å), spin densities, $<S^2>$ values and relative energies (kcal mol^{-1}) of various stationary points on the potential energy surface for the reaction of $[(H_2O)(Porp)Mn(O)]^+$ with C_2H_4.

	r(Mn-O)	r(O-C)	Spin densities				$< S^2 >$	Relative energy
			ρ(Mn)	ρ(O)	ρ(Porp)	ρ(C)		
^{1}**R**	1.55	3.50	---	---	---	---	0.00	+7.9
^{3}**R$_1$**	1.66	3.50	2.47	0.64	-1.06	0.00	3.09	0.0
^{5}**R$_1$**	1.66	3.50	2.46	0.66	0.89	0.00	6.08	0.1
^{3}**RI**	1.76	1.51/2.46	2.93	0.08	-0.12	-1.02	3.03	-13.6
^{3}**TS**	1.82	1.49/2.15	2.46	0.24	-0.08	-0.73	2.60	-10.7
^{3}**P**	1.99	1.52	2.01	-0.01	0.01	0.01	2.01	-31.7
^{5}**P**	2.29	1.51	3.99	0.02	-0.06	0.00	6.01	-51.7

The alkene-complexed $[(H_2O)(Porp)Mn(V)O]^+$ system has dominant porphyrin radical character ($^3A_{2u}$ or $^5A_{2u}$) at long range separations (> 2.6 Å). Consequently, the resultant potential energy surfaces, $^3A_{2u}$ or $^5A_{2u}$, are repulsive because the oxyl radical character of the oxidant is clearly 'masked'. The discontinuity of potential surfaces occur in the region of *r*(O-C) ~ 2.6 Å, which is only 3.8 kcal mol^{-1} above the entry channel, and this region corresponds to the formation of oxyl radical character ($^3\Pi_0$) in the oxidant *via* electron density transfer from the oxide to the vacancy in the porphyrin ring. The presence of the active oxyl radical character leads to barrierless formation of the radical intermediate, **^{3}I**, 13.6 kcal mol^{-1} below the ground state of the reactant complex (Figure 2.25).

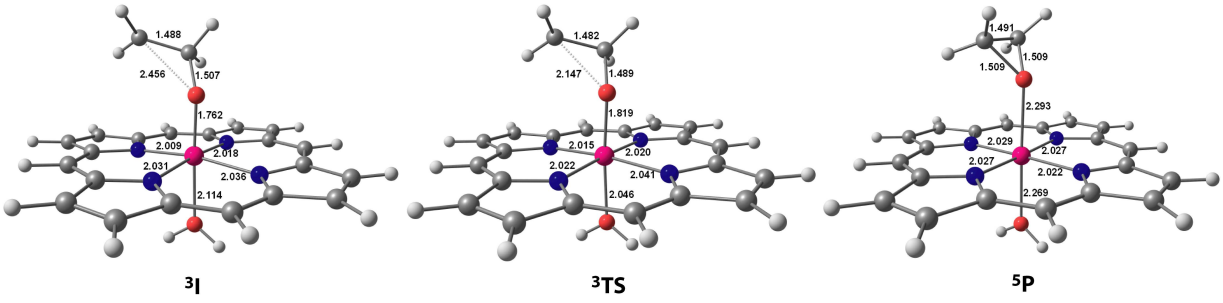

^{3}I ^{3}TS ^{5}P

Figure 2.26 Optimised key stationary points of the potential energy surfaces for oxidation of C_2H_4 by $[(H_2O)(Porp)Mn(O)]^+$ with B3LYP.

The net spin density on the *β*-C atom (radical intermediate) of -1.02 confirmed the presence of *β*-electron density on the radical carbon, which is antiferromagnetically coupled to the Mn centre, where the spin density on the metal of 2.93 is characteristic of a Mn(IV). The spin crossover from triplet to quintet occurs before the triplet transition state, ^{3}**TS**, and leads to the quintet product. The second electron transfer process is barrier less in this case because the spin crossover region is very near to the triplet radical intermediate. The spin density ρ(Mn) = 3.99 of the resultant quintet product complex confirmed the presence of the Jahn-Teller active high-spin Mn(III) ion (d^4), and the population of the metal d_{z^2} orbital leads to a longer Mn-O bond length (2.29 Å) (Figure 2.25). In summary, a detailed survey of the potential energy surface for the epoxidation of a C_2H_4 by $[(H_2O)(Porp)Mn(O)]^+$ system suggests that the 'unmasking' of the oxyl character *via* electron transfer from the oxo ligand to the porphyrin ring is rate determining, and this opens the active channel of the oxidation process.

2.5 Conclusions

Our survey of the electronic structure of the manganese porphyrin systems, (HO)(Porp)Mn(O) and $[(H_2O)(Porp)Mn(O)]^+$, reveals the impact of subtle redistribution of electron density between orbitals localised on metal, porphyrin and oxide ligands. Depending on axial ligand and chosen functional, it is possible to access three quite distinct electron density distributions, each of which is compatible with a triplet multiplicity: (L)(Porp)Mn(V)=O (metal radical), (L)(Porp)Mn(IV)–$O^{\cdot+}$ (oxyl radical) and (L)($Porp^{\cdot+}$)Mn(IV)=O. The inclusion of HF exchange in the functional favours the inverted ligand-field states containing a Mn(IV) centre and a oxyl radical. The nature of the triplet state has important implications for subsequent oxidation of model substrates, dimethyl sulfide and ethylene. When the oxyl radical character is already 'exposed' in the ground state of the isolated reactant [(HO)(Porp)Mn(O)/B3LYP], the reaction proceeds *via* sequential one-electron transfer steps separated by a sulfur-radical intermediate. The interaction with the incoming nucleophile is attractive even at very

long range, offering little opportunity for substrate discrimination. In the protonated analogue, $[(H_2O)(Porp)Mn(O)]^+$, the oxyl character is masked in the ground state by the transfer of an electron from the porphyrin ring, and, as a result, the long-range interaction with the nucleophile is repulsive. This point offers a possible mechanism for substrate discrimination: C–H bonding electrons are less diffuse than the lone pairs of Me_2S or indeed water, and so the discontinuity for hydrocarbon oxidation is likely to occur at shorter separations and therefore higher energies (Figure 2.26).

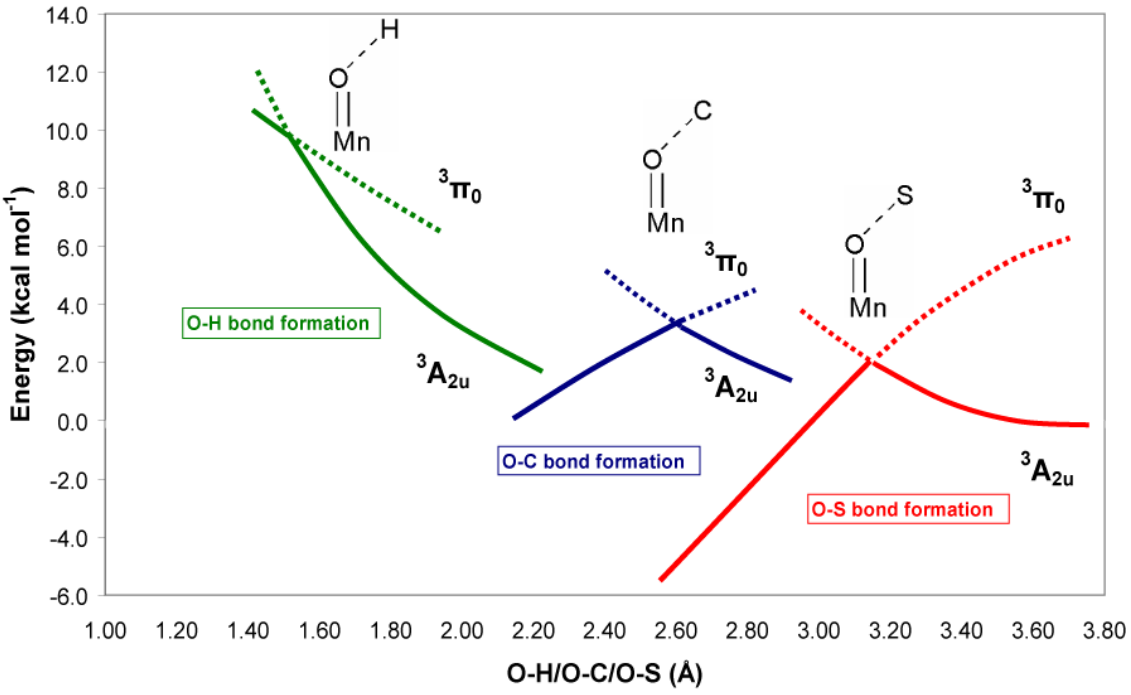

Figure 2.26 Discontinuity in the triplet surfaces (porphyrin radical and oxyl radical) for oxidation of Me_2S, CH_4 and ethylene by $[(H_2O)(Porp)Mn(O)]^+$ complex.

The approaching nucleophiles, Me_2S, C_2H_4 and CH_4 drive an electron from the oxo ligand into the vacancy in the porphyrin manifold at oxygen–substrate separations in the region of ~ 3.2 Å, ~2.6 Å and ~1.6 Å respectively (Figure 2.26), allowing the system to access the attractive region of the potential energy surface. The point at which the discontinuity occurs will depend critically not just on the relative energies of the limiting $^3\Pi_{yz}$ and $^3\Pi_O$ configurations, but also on the spatial properties of the orbitals on the incoming nucleophile: for the oxidation of CH_4 for instance, the donor H needs to

approach more closely to drive an electron into the porphyrin manifold, and therefore has higher energy.

The choice of functional also has a dramatic impact on the oxidation reaction: for the hydroxy species (HO)(Porp)Mn(O), a switch from B3LYP to BLYP changes the nature of the ground state (triplet to singlet) and, moreover, changes the electronic distribution in the triplet state, such that it approaches the metal radical {(HO)(Porp)Mn(V)=O} rather than oxyl radical {(HO)(Porp)Mn(IV)–$O^{\cdot+}$} limit. As a result, a long-range barrier emerges, and the process is better viewed as a concerted two electron oxidation. Our discussion has placed great emphasis on the shape of the long-range part of the potential energy surface, and in particular whether it is repulsive or attractive. The active role of substrate in unmasking the oxidising character of the Mn(V)=O unit offers the potential for discrimination that is one of the defining features of the oxygen evolving centre, and may represent a general framework for understanding structure-function relationships in water oxidation catalysts.

Chapter 3

Biomimetic Water Oxidation: Some Clues from Computational Chemistry

3.1 Introduction

DFT calculations on (L)(Porp)Mn(V)=O complexes described in the previous chapter confirmed that the rate determining step of two-electron oxidation reactions is highly dependent on the distribution of electron density in the low-lying electronic states of the Mn(V)-oxo porphyrin complexes and spatial properties of the orbitals on the incoming nucleophile. The fundamental requirement for a rapid reaction appears to be the formation of active metal oxyl radical species [Mn(IV)-$O^{\cdot+}$]. In order to further our understanding of oxidation catalysts, this chapter focuses on two specific examples of Mn-based biomimetic water oxidation catalysts, a $[\{(Porp)Mn(III)\}_2$-(μ-phe)$]^{2+}$ complex synthesised by Naruta and co-workers[223,224] and a $Mn(II)_2$-mcbpen species synthesised by McKenzie and co-workers[225,226] (Figure 3.1). Metal-based biomimetic metal clusters have been studied as simple active site model complexes for well-known electron transfer enzymes such as nitrogenase (iron-sulphur),[227-229] catalase (dimanganese),[230-233] methane monooxygenese (diiron),[234,235] ribonucleotide reductase (diiron),[234,235] tyrosinase (dicopper),[236,237] and photosystem II (tetramanganese).[238-242] The presence of

more than one metal centre in these biologically significant metal clusters generates multiple electronic states, which may play an important role in the catalytic activity. Therefore, a detailed understanding of the electronic and structural features of these biomimetic metal clusters will be a vital step towards understanding their functionality.

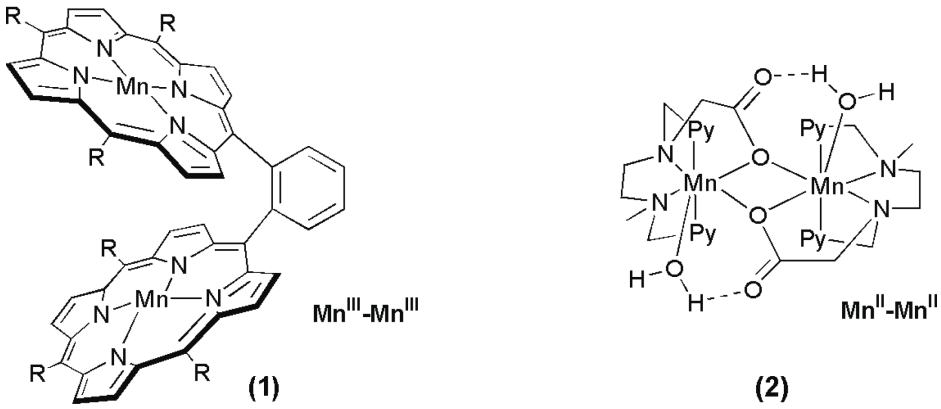

Figure 3.1 Oxygen evolving (a) $[\{(Porp)Mn(III)\}_2$-(μ-phe)$]^{2+}$ complex by Naruta and co-workers[223,224], and (b) $Mn(II)_2$-mcbpen complex by McKenzie and co-workers[225,226].

This chapter contains three sub-sections; we first present a brief review of current models for biological and biomimetic water oxidation catalysts. The next two sections describe the link between the electronic structure and detailed chemical steps involved in the oxygen evolution by Naruta and McKenzie systems.

3.1.1 Photosynthesis

Photosynthesis occurs in many organisms like higher green plants, algae and cyanobacteria, all of which convert the energy of sunlight into chemical energy in the form of carbohydrates and molecular oxygen through a sequence of chemical reactions.[243] Photosynthesis created an oxygen-rich atmosphere that has been critical for the development of higher life on the earth. The overall chemical reaction of oxygenic photosynthesis is given by Equation 3.1.

$$6CO_2 + 6H_2O \longrightarrow C_6H_{12}O_6 + 6O_2 \quad (1.1)$$

The splitting of water by photosynthetic organisms is one of the most remarkable phenomena of nature, where a large enzyme, Photosystem II (PSII),[242,243] performs light-induced water-splitting in higher green plants, algae and cyanobacteria (Figure 3.2). The PSII exists as a dimer of two almost identical monomers, each of which has protein subunits D1 and D2, many cofactors and one oxygen evolving centre (OEC).

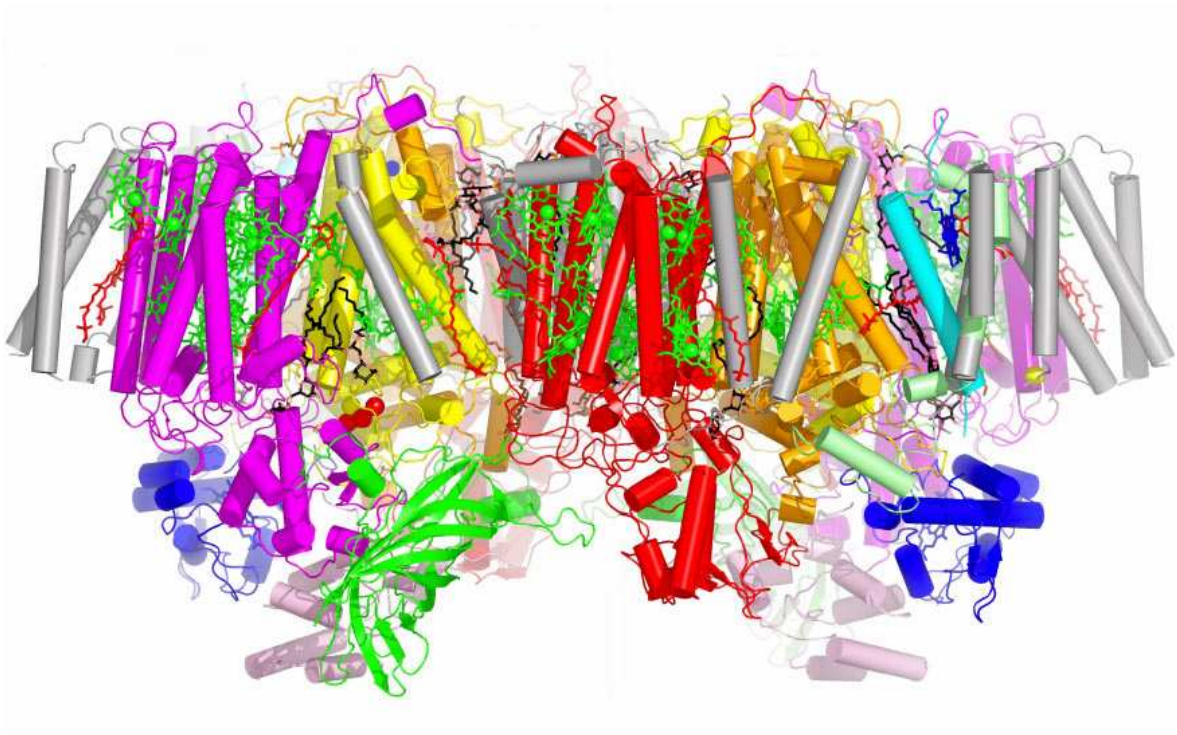

Figure 3.2 Protein subunits, chlorophylls (green), *β*-carotenes (orange), lipids (black), haems (blue), oxygen evolving centre (red spheres) of photosystem II (PSII).

Light absorption by chlorophyll and carotenoid containing proteins in the PSII supply energy for the electron transfer processes (Figure 3.3). This photonic energy initiates oxidation of P_{680} (chlorophyll, Chl) to $P_{680}^{\cdot+}$ and the ejected electron is transferred towards the final electron acceptor plastoquinone (Q_B) through Chl_{D1}, pheophytin ($Pheo_{D1}$), and Plastoquinone (Q_A). After accepting two electrons and undergoing protonation, Q_B is released to the membrane matrix. Then oxidation of water at the oxygen evolving centre (OEC),[238] a tetramanganese cluster found in Photosystem II,

provides electrons to reduce the $P_{680}^{\cdot+}$ radical cation through the redox active tyrosine (Y_z).

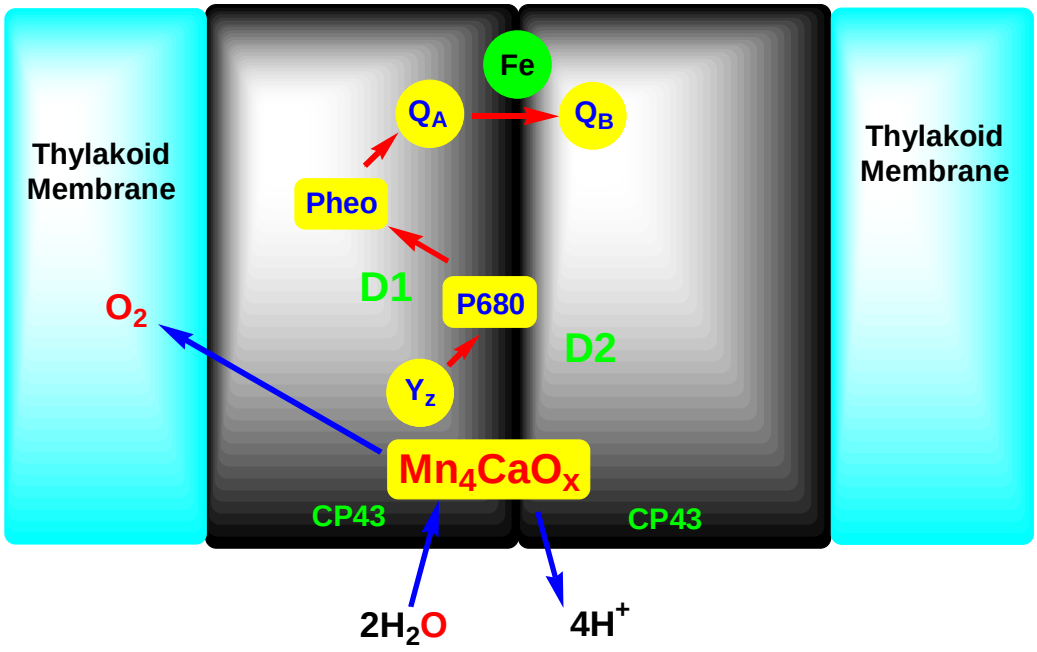

Figure 3.3 The main cofactors involved in electron transfer process of PSII. The arrows (red) show the electron transfer steps.

3.1.1.1 The oxygen evolving centre (OEC)

The OEC contains four manganese ions which has been shown to be essential for photosynthetic oxygen evolution.[238-243] Based on EXAFS (extended X-ray absorption fine structure) measurements, Yachandra and Sauer proposed several possible arrangements of the four Mn ions in the OEC,[244] including two or three di-μ-oxo-bridged Mn_2O_4 moieties (Figure 3.4). According to the recent crystallography of Ferreira and co-workers, the OEC is a cubane-like Mn_3CaO_4 cluster,[238] and each metal ion in this structure is connected by μ-oxo bridges (Figure 3.5), which is similar to the structure ***i*** (Figure 3.4) suggested by Yachandra and Sauer. Recent EXAFS and pulsed EPR (electron paramagnetic resonance) spectroscopic evidence confirmed the location of the Ca^{2+} ion within the OEC, which is an essential cofactor for oxygen evolution,[245-250] and removing the calcium ion from the OEC clearly blocks the water oxidation.[251-254]

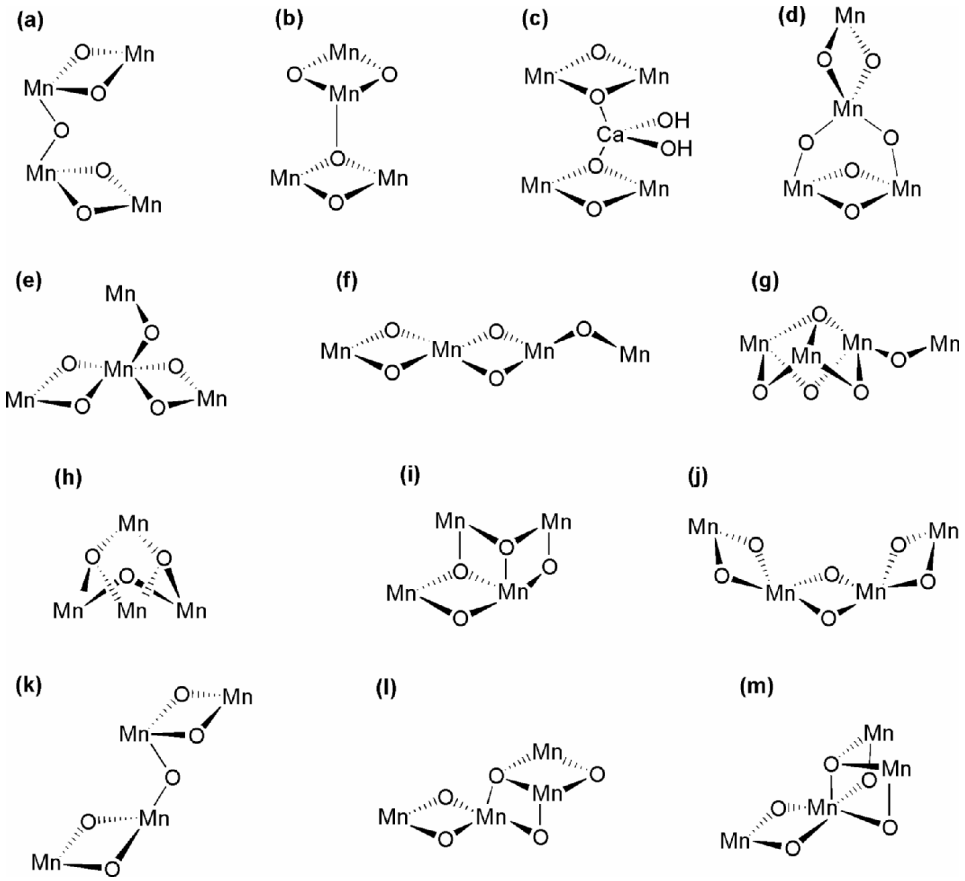

Figure 3.4 Possible arrangements of the four Mn ions in the OEC.[244]

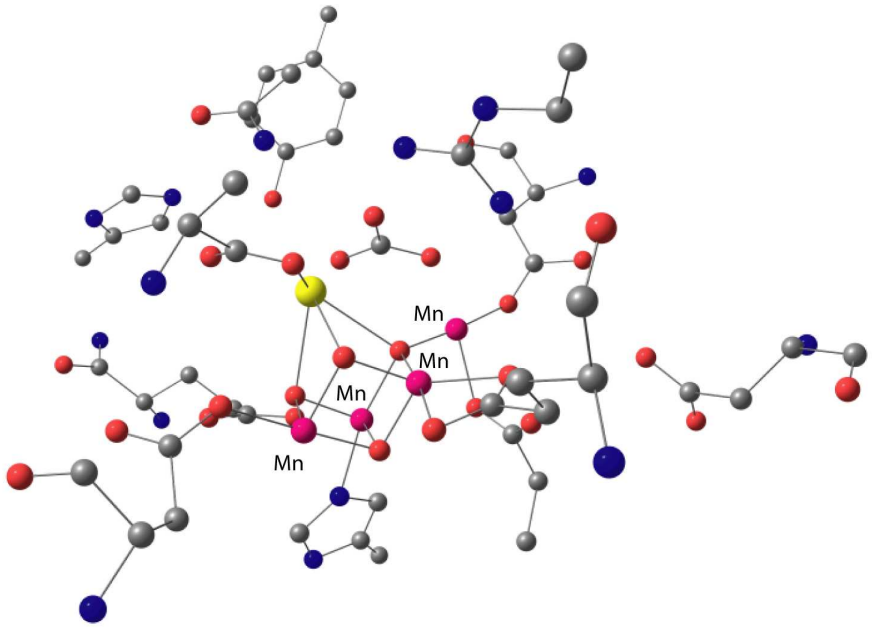

Figure 3.5 X-ray structure of the OEC with its surrounding ligands [Manganese (pink), calcium (yellow), oxygen (red), carbon (grey) and nitrogen (blue)].[238]

The calcium may be important as a substrate water binding site, and it may also influence proton transfer processes. A chloride ion bound to the OEC has been proposed to influence proton-transfer away from the OEC.[255] Recent spectroscopic evidence suggested that the chloride is not absolutely essential for water splitting, and chloride can be substituted by alternative anions such as Br^-, NO_3^-, NO_2^-, and I^-, without disrupting the water-splitting process.[254-259]

Water oxidation at the OEC is known to occur *via* four successive oxidations, which can be described by the Kok cycle (Figure 3.6).[260] This S state cycle transits from the most reduced S_0 state of the OEC through the S_1, S_2, S_3 and finally to the active S_4 state, and these transitions are induced by absorption of photons at the antenna pigments of the light harvesting proteins in the PSII. Then the O_2 evolution takes place during the spontaneous (light-independent) $S_4 \rightarrow S_0$ transition. However, many of the structural and mechanistic details of the Kok cycle remain unclear. Understanding the detailed electronic structure of the OEC during the S state cycle becomes critical in terms of establishing the oxygen evolving reaction pathway.

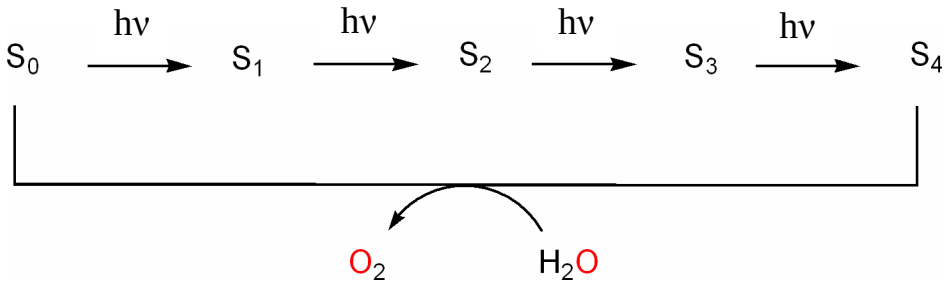

Figure 3.6 The Kok cycle (S state cycle).[260]

In general, removing electrons from the OEC gives rise to paramagnetic species, and therefore EPR has been an important tool. The first two oxidation steps of the Kok cycle have been extensively studied by spectroscopic methods, and Figure 3.7 summarises the electronic structure of the Mn_4 unit within the Mn_4CaO_4 cluster for the first three S states, where the both $S_0 \rightarrow S_1$ and $S_1 \rightarrow S_2$ transitions involved metal-based oxidations.[261-268]

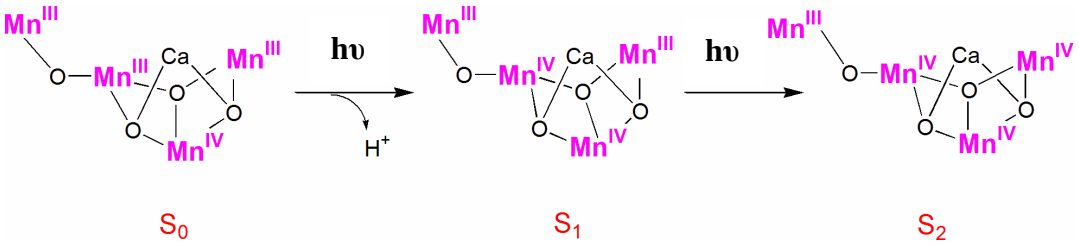

Figure 3.7 Electronic structure of the Mn_4 unit within the Mn_4CaO_x cluster for the first three S states S_0, S_1 and S_2.

Metal-based oxidation for both transitions would involve oxidation of Mn(III) to Mn(IV). However, the detailed chemical steps involved in the last two oxidations remain a mystery, and a number of proposals have been made by several authors.[269-273]

3.1.2 Proposed mechanisms of oxygen evolution at the OEC

Detailed knowledge of water-splitting in photosynthesis is very useful in terms of developing biomimetic artificial catalysts for large scale applications of water-splitting. Over the last two decades, a number of mechanisms have been proposed for photosynthetic water oxidation,[270-273] and the following section summarises the currently favoured mechanisms.

3.1.2.1 Coupling of two Mn-bridging oxo ligands: Butterfly or double pivot mechanism

The butterfly or double pivot mechanism was been proposed by Dismukes and Christou (Figure 3.8).[274] According to this proposal, the OEC has a cubane-like geometry composed of alternating metal and oxo units, and the O-O bond formation occurs *via* coupling of two Mn-bridging oxo ligands across the face of a cuboidal cluster during the $S_4 \rightarrow S_0$ transitions. This hypothesis is supported by the formation of O_2 from the Mn_4O_4 cuboidal model complexes (gas phase).[275] However, recent isotope exchange

measurements suggested that the μ-oxo groups in the Mn model complexes exchange much more slowly,[276] and therefore the butterfly or double pivot mechanism may be disfavoured for photosysnthetic water oxidation.

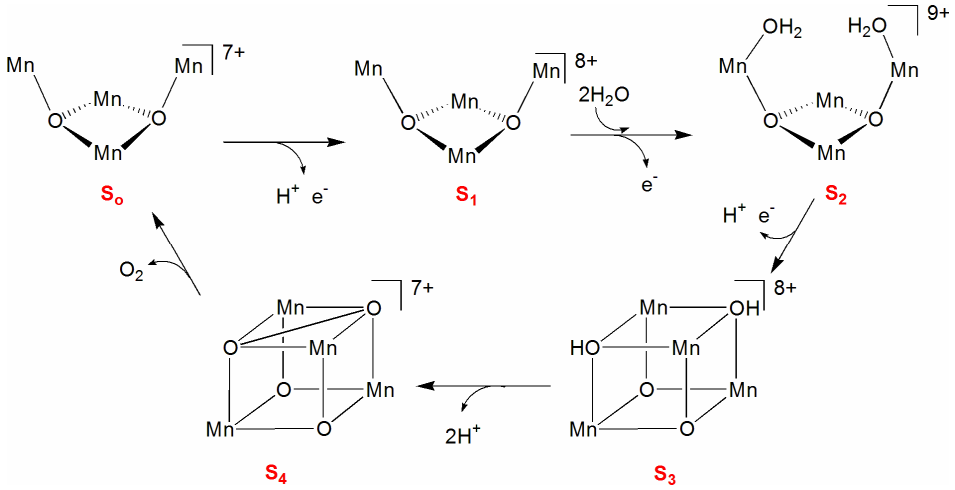

Figure 3.8 The butterfly or double pivot mechanism of Dismukes and Christou[274].

3.1.2.2 Attack of a terminally bound water or hydroxide upon a terminal Mn(V)=O

Wydrzynski and co-workers have studied water splitting at the OEC using rate exchange (k_{ex}) measurements of water molecules in the S-states.[277] They suggest that at least one substrate water molecule is bound to the OEC throughout the catalytic cycle, and a second water molecule may be bound at the S_2 state (Figure 3.9).[278] They found that H_2O exchange rates of the OEC are too fast to be consistent with manganese-μ-oxo exchange for some other metal-oxo model complexes,[279] and this finding implied that two substrate water molecules are bound as terminal ligands to the manganese cluster. Based on the above implications and considering the experimental evidence, Pecoraro and Brudvig have postulated that the calcium bound water or hydroxide may form the O-O bond by attacking the oxygen of a terminal Mn(V)=O species in the S_4 state[280-282] Mass spectrometry measurements by Hendry and Wydrzynski provided direct evidence from ^{18}O-exchange that calcium is involved in binding one of the substrate waters.[283]

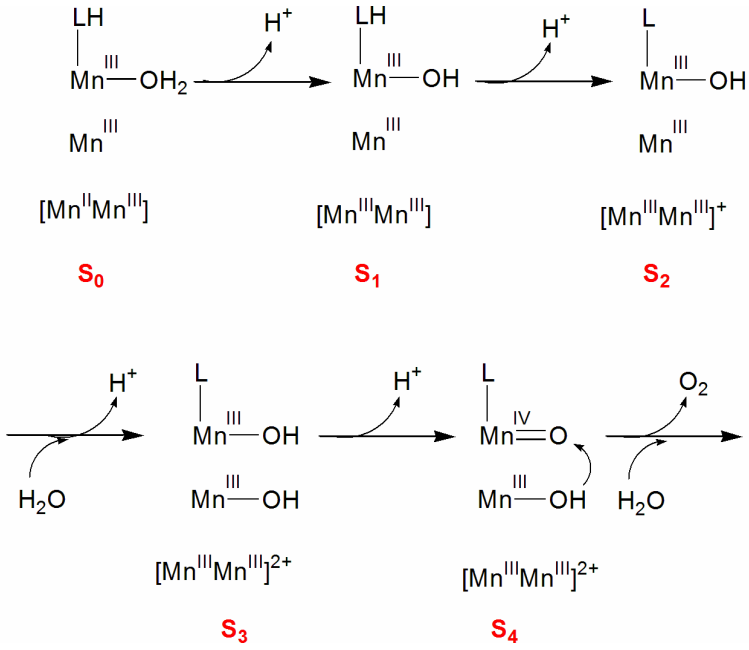

Figure 3.9 The O-O bond formation mechanistic proposal of Wydrzynski and co-workers.[277]

3.1.2.3 Tyrosine-Z (Y_Z) and the hydrogen abstraction model

Babcock and co-workers proposed that tyrosine-161 (Y_z) of the D1 subunit of PSII may be the redox active oxidant of the OEC.[284-287] The basis for this interpretation is spectroscopic evidence, where ENDOR (electron-nuclear double resonance) spectroscopy suggests that Y_Z is very close to the manganese cluster (at a distance of less than 5 Å),[288] while EPR spectroscopy indicated that the disordered hydrogen-bonding environment of Y_Z may allow the flexibility required for Y_Z to dispose of its acquired proton to bulk.[289-293] They noted that the O-H bond energy in the phenolic tyrosine side chain is quite similar to that of the manganese-based synthetic model compounds.[294,295] These findings suggested that the Y_Z radical may remove a hydrogen atom from water or hydroxide coordinated to high-valent manganese during the S state transition (Figure 3.10). Then, ligand-based oxidation at the $S_3 \rightarrow S_4$ transition gives rise to a peroxide species bound to manganese. This transition involves two reactions, the first of which is a hydrogen atom transfer ($Y_z^{\cdot}$ may abstract this hydrogen atom as in

the other transitions) giving rise to a Mn-bound oxyl radical, and the second reaction is an addition of the oxyl radical to the terminal oxo ligand of a second Mn ion.

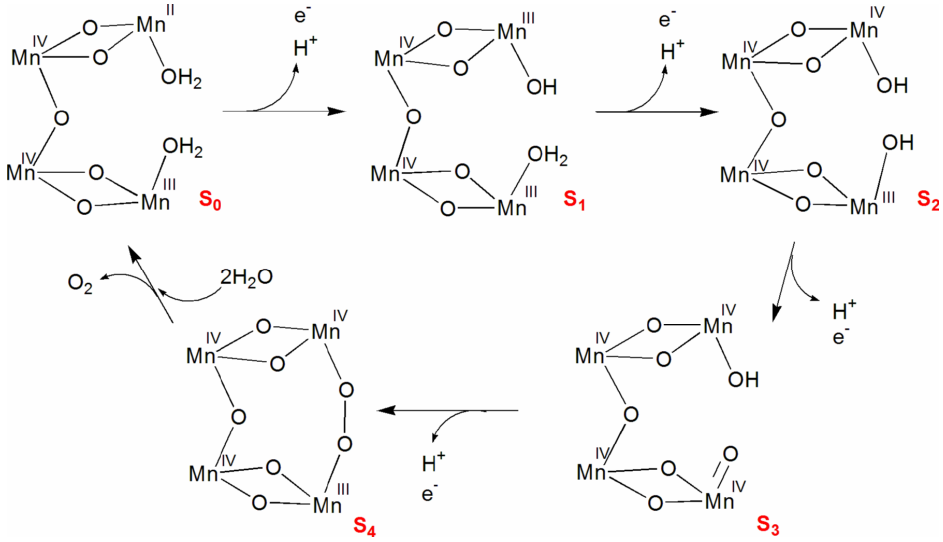

Figure 3.10 The O-O bond formation mechanistic proposal of Babcock and co-workers.[284]

3.1.2.4 Coupling reactions involving an oxyl radical

Some authors have proposed ligand-based oxidation for the last two transitions ($S_2 \rightarrow S_3$ and $S_3 \rightarrow S_4$) of the Kok cycle, and this idea inspired a number of proposals with radical-based reaction pathways. The general idea of this reaction scheme is the formation of fully deprotonated terminal oxo group at the later state of the Kok cycle, and this species is then involved in O-O bond formation through nucleophilic attack of bulk water molecule, a water/hydroxo bound to the Ca^{2+} ion or bridging oxygen between Ca^{2+} and Mn ions.

Yachandra and Co-workers: According to Yachandra and co-workers, the last two oxidation of the Kok cycle, $S_2 \rightarrow S_3$ and $S_3 \rightarrow S_4$, are centred on metal-bound oxygen atoms. Consequently, two oxyl radicals may be formed during these transitions.[296,297]

The second oxyl radical ($S_3 \rightarrow S_4$ transition) has been suggested to be a bridging or terminal oxygen. Then the resulting metal-oxyl radical species leads to O-O bond formation *via* a number of manganese-bridged μ-oxo species at the S_4 state (Figure 3.11). The overall picture of this mechanistic proposal has a precedent in the delicately balanced equilibrium between the bis(μ-oxo)dicopper(III) and the (μ-η^2:η^2 peroxo-dicopper(II) of dimeric copper chemistry proposed by Tolman and co-workers.[298]

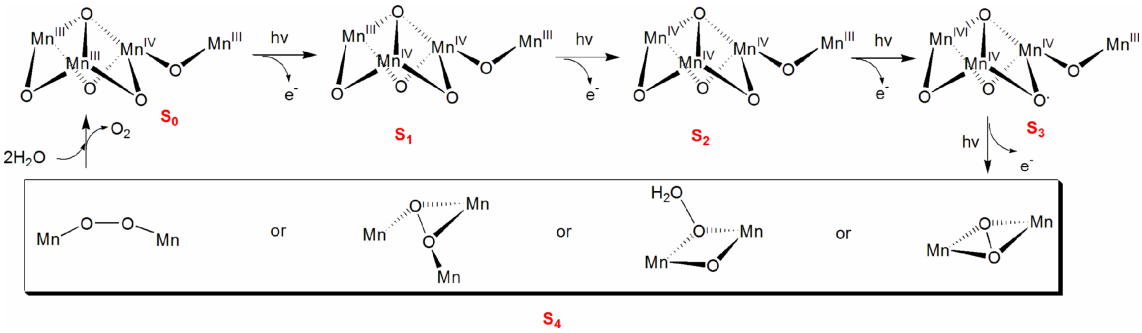

Figure 3.11 The O-O bond formation mechanism proposed by Yachandra and coworkers[296,297].

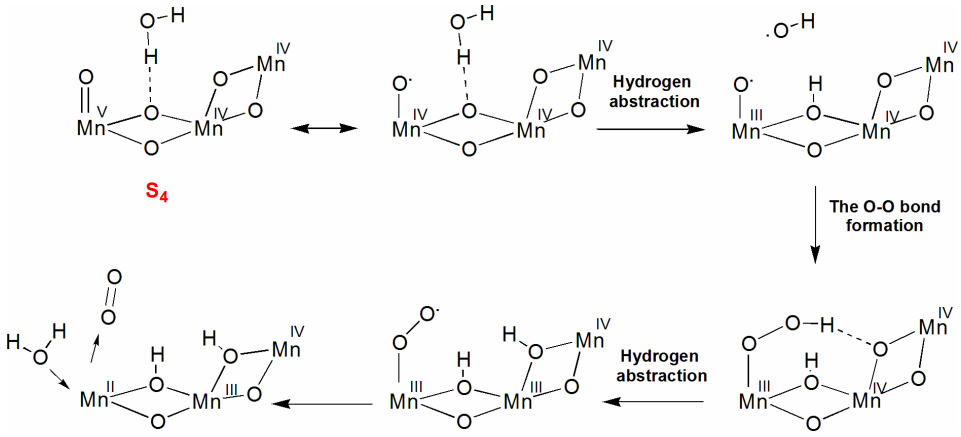

Figure 3.12 The O-O bond formation mechanism proposed by Dau and co-workers[299].

Dau and co-workers: Dau and co-workers suggested that the O-O bond is formed through the reaction of a hydroxyl radical with a terminal oxyl radical species at the S_4 state (Figure 3.12).[299] Further, a μ-oxide of the Mn_4CaO_4 may abstract a hydrogen atom from the substrate water molecules and the resulting hydroxyl radical may interact with the Mn(IV)-$O^{\cdot+}$ species to form the O-O bond. Then H atom abstraction by the second

Mn-μ-oxide moiety induces dioxygen loss. The overall picture of this mechanistic proposal suggested that the Mn-μ-oxide moieties act as bases for the O-O bond formation.

Messinger and Co-workers: Messinger and co-workers have proposed two possible mechanisms for the O-O bond formation.[300] In the first proposal, there are two substrate water molecules, namely W_{fast} and W_{slow}, bonded to the Ca and one of the Mn ions of the OEC respectively in the S_0 state (Figure 3.13). They assumed that the fast exchanging water molecule bound to the Ca ion (W_{fast}) may form a H-bond with the redox active tyrosine (Y_z). During the first oxidation, $S_0 \rightarrow S_1$, deprotonation of the Mn bound W_{slow} occurs and after single electron and a proton transfer processes, the $S_3 \rightarrow S_4$ transition involves H-atom abstraction from W_{slow}, leading to the formation of a Mn(V)=O species in the S_4 state. As a result, O-O bond formation may occur through a nucleophelic attack of W_{fast} (OH bound to Ca) onto the high-valent Mn-oxo species.

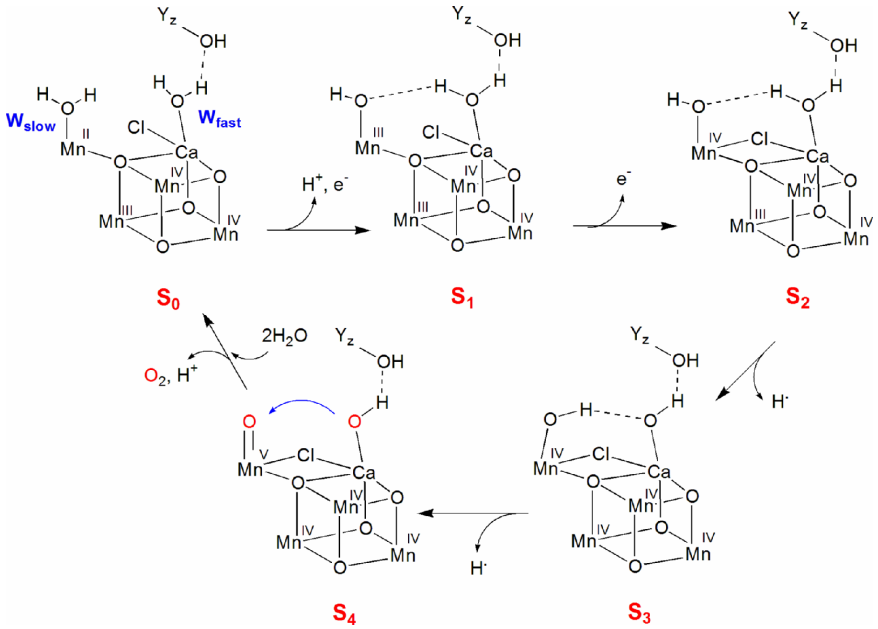

Figure 3.13 Nucleophilic attack of a Ca bound substrate water onto Mn(V)=O species (Messinger and Co-workers)[300].

The second proposal (Figure 3.14) included some modification to the first mechanism to be consistent with new experimental findings.[301-304] According to substrate exchange experiments, it seems most probable that a μ-OH bridge between Ca and Mn(III)

represents W_{slow} (substrate) in the S_0 state, and this bridge becomes deprotonated during the first oxidation $S_0 \rightarrow S_1$. This mechanistic proposal involves a ligand centred oxidation in the $S_2 \rightarrow S_3$ and $S_3 \rightarrow S_4$ transitions before the O-O bond formation, where they favoured a radical mechanism, in which the O-O bond is formed *via* a radical coupling of a terminal oxygen atom with a μ-oxide ligand of the cuboidal cluster.

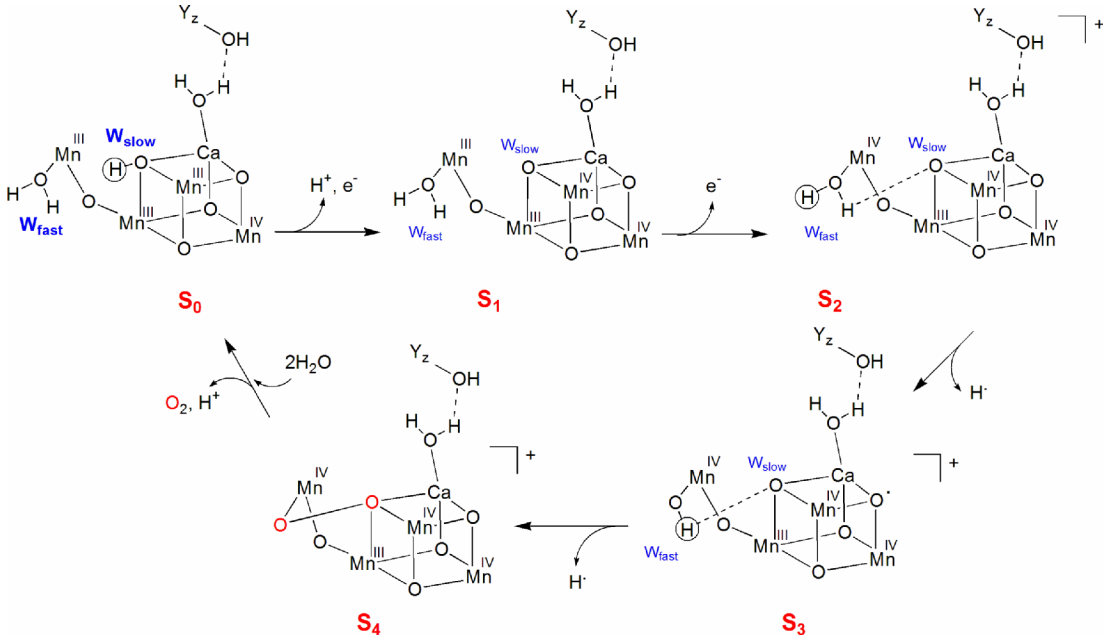

Figure 3.14 The O-O bond formation *via* a radical coupling of a terminal oxygen atom with a μ-oxide ligand of the cuboidal cluster (Messinger and Co-workers)[300].

Siegbahn and co-workers: Quantum chemical methods, in particular with DFT, have been shown to be useful in studying clusters featuring multiple electronic states, and the detailed chemical steps involved in the O-O bond formation. Siegbahn and co-workers applied DFT to explore the mechanism of water splitting at the OEC.[142-150] Further, they applied DFT to the electronic structure of the Mn_4CaO_4 cluster in the recent 3.5 Å resolution structure of the OEC. Their DFT results suggested that there are no major problems involved in oxidising the Mn ions of the OEC from Mn(III) to Mn(IV). However, the Mn(IV) oxidation state is not highly reactive towards production of O_2, and therefore achieving higher oxidation state such as Mn(V)=O may be critical.

On the other hand, not all the formally Mn(V)=O species are active in oxidation reactions.[142-145]

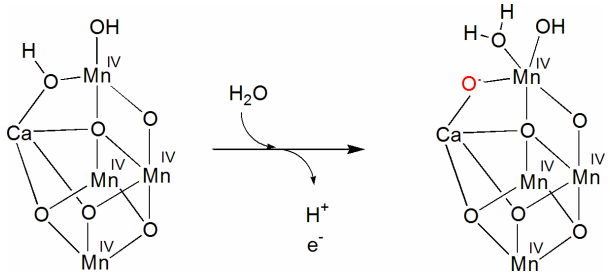

Figure 3.15 The $S_3 \rightarrow S_4$ transition of the S-state cycle (Siegbahn and co-workers).[142-145]

By considering the above issues, Siegbahn postulated that the formation of electron deficient metal-oxyl radical species [Mn(IV)-$O^{\cdot+}$], as distinct from the metal–oxo [Mn(V)=O] form, is possible (Figure 3.15). Then, a water molecule bound to the Ca^{2+} ion may interact with this Mn(IV)-oxyl radical to form the O-O bond. Moreover, their DFT calculation suggested that cross-over between states of different multiplicity (e.g. high-spin to low-spin states or *vice versa*) reduces the barrier for the O-O bond formation.[142-145] In this case, finding the minimum energy crossing points (MECP) is critical in terms of estimating an accurate barrier for the O-O bond formation.[305] The calculated barrier for the O-O bond formation for photosynthetic water-splitting is about 15 kcal mol^{-1}.[142-145]

Batista and co-workers: Batista and co-workers also investigated photosynthetic water splitting by using combined quantum mechanical/molecular mechanics (QM/MM) calculations.[306] They used the crystal structure of PSII with 3.5 Å resolution[238] to make their computational models. The DFT region of their models consisted of the Mn_4CaO_4 clusters and the directly ligating carboxylate groups containing residues, Cl^- and OH^- ions, while the molecular mechanics (MM) layer was described by the Amber MM force field parameters.[307] They validated their models for the possible S states through a direct comparison of simulated high-resolution EXAFS

with the spectroscopic data.[308-311] Similar to Siegbahn, their QM/MM calculations supported ligand based oxidation in the final oxidation step ($S_3 \rightarrow S_4$) of the Kok cycle, which gives rise to a metal oxyl radical electronic form, [Mn(IV)-$O^{\cdot+}$], before the O-O bond formation (Figure 3.16). This Mn(IV)-oxyl radical undergoes nucleophilic attack by a substrate water molecule initially coordinated to the calcium ion.

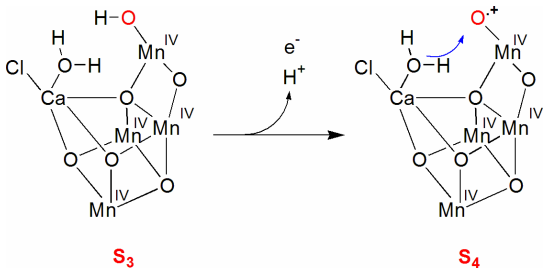

Figure 3.16 The $S_3 \rightarrow S_4$ transition of the OEC (Batista and co-workers).[306]

3.1.2.5 Summary of the proposed mechanism for the O-O bond formation

The literature on PSII is quite complex and it is possible to find some experimental evidence supporting all of the mechanistic proposals described in the previous section. The O–O bond formation described above can be collected into three categories, namely nucleophilic attack on Mn(V)=O or Mn(IV)-$O^{\cdot+}$ in the S_4 state, radical in the S_3 state ($S_3Y_z^{\cdot}$) and coupling of two oxo or hydroxo groups in the S_3 state (Figure 3.17).

(a) Nucleophilic attack in the S_4 state: The basic idea of this approach is to generate a terminal or bridging oxygen to Mn(V)=O or Mn(IV)-$O^{\cdot+}$ species (Figure 3.17a). Further, this active species is attacked by a nucleophilic bulk water molecule or a water/hydroxo bound to Ca or bridging between Ca and Mn. This mechanism requires the formation of a Mn(III)/Mn(IV) species during the $S_2 \rightarrow S_3$, transition, and another metal-based or ligand-based oxidation ($S_3 \rightarrow S_4$ transition) giving rise to Mn(IV)/Mn(V)=O or Mn(IV)/Mn(IV)-$O^{\cdot+}$ species respectively. The O-O bond

formation mechanisms proposed by Messinger (experimental studies) and Batista (computational studies) support for this approach.

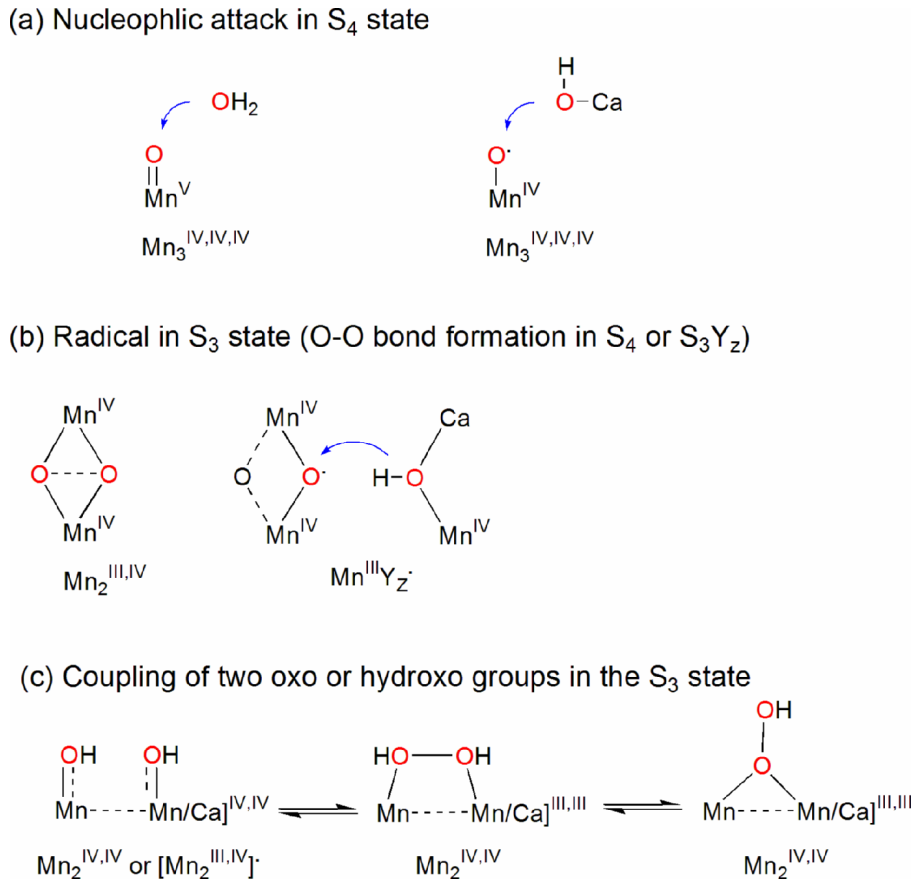

Figure 3.17 Suggested routes for O–O bond formation mechanism at the OEC; (a) nucleophilic attack in S_4 state, (b) radical in S_3 state ($S_3Y_z^{\cdot}$) and coupling of two oxo and (c) hydroxo groups in the S_3 state

(b) Radical mechanisms: The radical mechanism assumes the formation of a radical species at the S_3 state *via* a ligand-based oxidation. One of the principle components of this mechanism is the oxidation of a μ-oxo bridge during the $S_2 \rightarrow S_3$ transition, which gives rise to an oxyl radical. In general, two different options are proposed for the O bond formation; (1) during the $S_3 \rightarrow S_4$ transition the second (bridging) oxyl radical is formed and the O–O bond is created between two radicals at this S_4 state, (2) the O–O bond formation is triggered by the $S_3Y_Z^{\cdot}$ state formation. In that case a peroxidic intermediate may be formed between the oxygen radical and a water (hydroxo/oxo)

molecule bound to Ca and/or Mn, which can be oxidized by $Y_Z^{\cdot}$ and molecular oxygen is formed. The O-O bond formation mechanistic proposal by Yachandra is a good example for this category.

(c) O–O bond formation in the S_3 state: In this proposal, the O–O bond formation is favoured at the S_3 state that may include an oxyl radical and/or a Mn(IV,IV,IV,IV) state. Further, redox equilibrium between various forms of peroxide complexation is a common feature, and such species are assumed to be donating an electron to $Y_Z^{\cdot}$ and liberate O_2. A good example is the O-O bond formation mechanism proposed by Babcock.

Understanding the key features of the OEC, its surrounding, and proposed mechanisms for the S-state cycle that fit with the experimental and computational studies is critical in terms of developing computationally tractable models of the OEC and designing biomimetic water oxidation catalysts.

3.1.3 Functional models to the OEC

In the absence of definitive evidence to support the mechanism of O_2 formation at the OEC itself, studies of catalytically active synthetic metal-based water oxidation catalysts become critical. Current biomimetic oxygen evolving complexes are usually metal dimer systems, and these systems undergo oxidation in the presence of active oxidant or under electrochemical conditions. However, no visible light driven homogeneous water oxidation catalyst has been developed. Over the past decade, a few metal-based oxygen evolving complexes have been developed, and these biomimetic complexes are very useful in developing industrial catalysts for large scale applications

of water-splitting in the future. The following section is a summary of chemically significant and catalytically active metal-based oxygen evolving model complexes.

3.1.3.1 Oxygen evolving ruthenium family complexes

Until recently, a dinuclear ruthenium complex, $[(bpy)_2(H_2O)Ru(III)(\mu\text{-}O)Ru(III)(H_2O)(bpy)_2]^{4+}$, synthesised by Meyer and co-workers was one of the few well-defined biomimetic water oxidation catalysts (Figure 3.18a).[312,313]

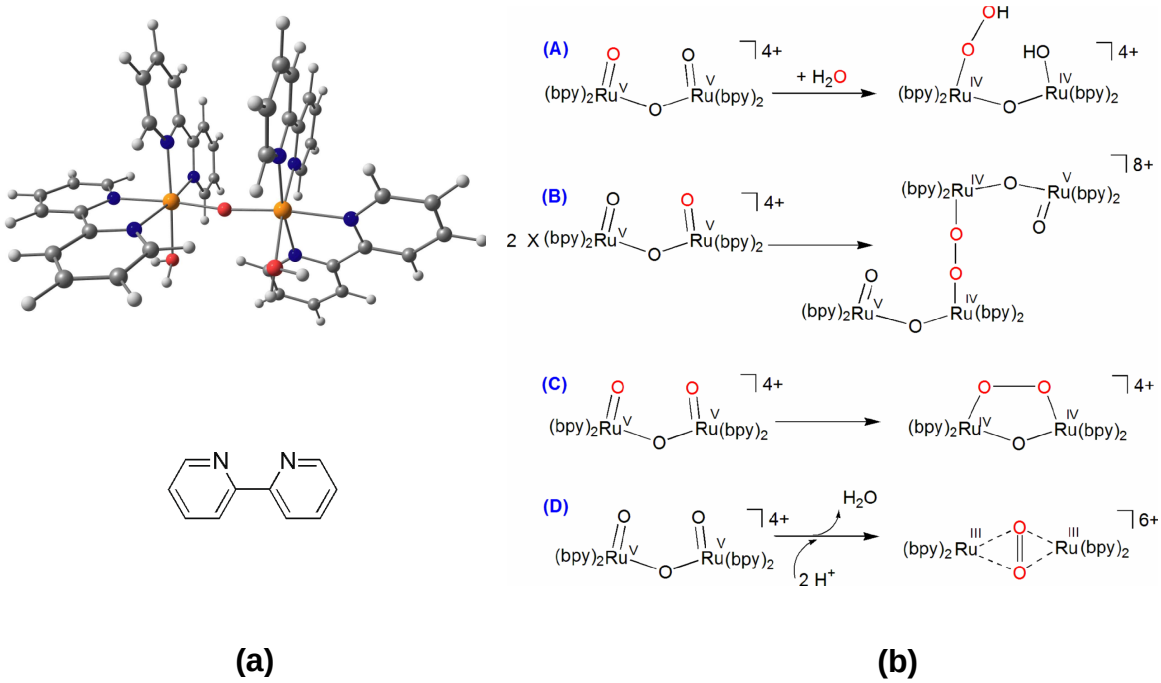

Figure 3.18 (a) The oxygen evolving $[(bpy)_2(H_2O)Ru(III)(\mu\text{-}O)Ru(III)(H_2O)(bpy)_2]^{4+}$ complex, (b) proposed mechanisms for the O-O bond formation.

This system has performed water-oxidation in the presence of primary oxidants such as Co(III),[314] Ce(IV)[315,316] or electrochemical oxidation.[317-319] Formation of a Ru(V,V) dimer complex has been proposed to be the active intermediate for the O-O bond formation.[320] Mixed-isotope experiments implied that the interaction between the single oxo group bound to Ru and a solvent water molecule is responsible for the O-O bond formation (Pathway A, Figure 3.18b).[321] However, the full reaction pathway for the

catalytic water oxidation by the above species is still under active discussion, and three other mechanistic proposals have been suggested for the O-O formation.[322] The detailed oxygen evolution mechanism was comprehensively studied by Baik and co-workers using DFT, where they have considered both reaction paths A and B in some detail (Figure 3.18b).[323] Their DFT calculations suggested that the fundamental basis for the catalytic activity of the oxygen evolving Ru_2 complex lies in the formation of active Ru(IV)-$O^{\cdot+}$ species rather than the Ru(V)=O form, and this radical species acts as a strong oxidant to cleave the H-OH bond. This computational work emphasises the potential importance of Ru(IV)-$O^{\cdot+}$ species as distinct from the Ru(V)=O form in oxygen evolution, where the calculated barrier for the O-O bond formation (mechanism A) is about 25 kcal mol^{-1}.

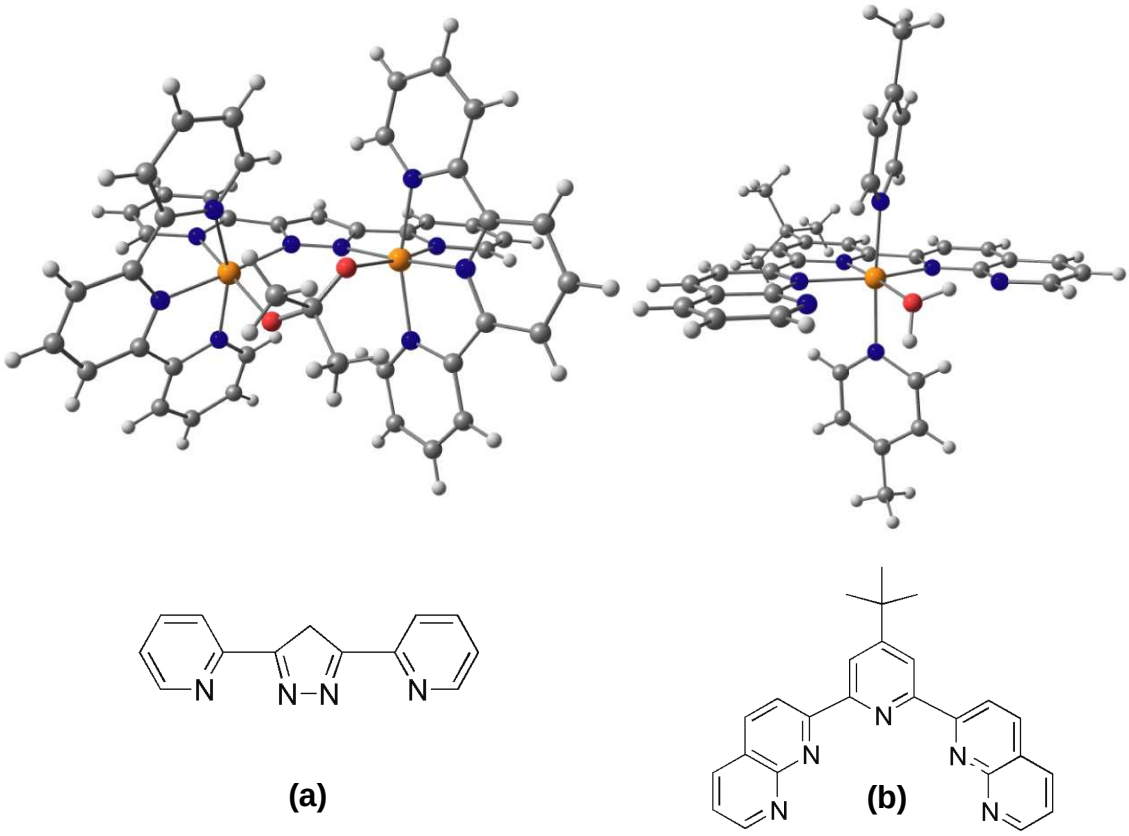

Figure 3.19 Oxygen evolving (a) $([Ru(II)_2(\mu\text{-}OAc)(bpp)(tpy)_2]^{2+}$ complex and (b) a mononuclear ruthenium system.

The second family of ruthenium-based oxygen evolving complexes, $[Ru(II)_2(\mu\text{-}OAc)(bpp)(tpy)_2]^{2+}$, was synthesised by Benet-Buchholz and co-workers (Figure 3.19a),[324-326] where bpp = 3,5-di(2-pyridyl)pyrazole and tpy = 2,2':6,2''-terpyridine.

This system has been shown to oxidise water at a faster rate than the first species in the presence of Ce(IV) as an oxidant. The third dinuclear ruthenium system is a $[Ru(II)_2(OH)_2(3,6\text{-}t\text{-}Bu_2quinone)_2(btpyan)]^{2+}$ complex, where btpyan = 1,8-bis {(2,2':6,2'')-terpyridyl}anthracene. This system was catalytically active in water-splitting under electrochemical oxidation.[327-329] However, unlike the first two species, this system is not catalytically active in the presence of a chemical oxidant. Thumel and co-workers have synthesized a Ru mononuclear water oxidation catalyst (Figure 3.19b),[330,331] which has been shown to evolve O_2 using Ce(IV) as an oxidant with good oxygen-evolving activity.

3.1.3.2 Oxygen evolving manganese complexes

In terms of developing large scale fuel cells in the future, Ru-based biomimetic water oxidation catalysts are not good as the industrial catalysts because the metal is rare, expensive and toxic. Mn-based water oxidation catalysts are important as industrial water oxidation catalyst as manganese is cheap and readily available. Over the past years a few catalytically active Mn-based water oxidation catalyst have been synthesised.

Cubane models: A few biomimetic tetramanganese complexes containing a $[Mn_4O_x]$ core have been reported. Dismukes and co-workers developed a cubane-like complex $L_6Mn_4O_4$ [L = diphenylphosphinate anion (Ph_2PO^{2-}], [332-334] and this system has been shown to release O_2 under gas phase conditions. The O-O bond formation may involve coupling of the two oxygen atoms across two corners of the cubane complex in a manner reminiscent of the 'double pivot mechanism' proposed for the oxygen evolution at the OEC.[374] The $[Mn_4O_2L_5]^{2+}$ 'butterfly' complex of Robin and co-workers released O_2 upon photo excitation of the Mn ← O charge transfer band,[335,336] but non-cuboidal Mn-based models containing $[Mn_2O]$, $[Mn_2O_2]$ and $[Mn_3O_3]$ cores failed to evolve O_2.[337-339]

[(terpy)(H_2O)Mn(IV)(μ-O)$_2$Mn(III)(H_2O)(terpy)]$^{3+}$ complex: Brudvig and co-workers have characterised a [(terpy)(H_2O)Mn(IV)(μ-O)$_2$Mn(III)(H_2O)(terpy)]$^{3+}$ complex, and this system was the first reported Mn-based homogeneous water-oxidation catalyst (Figure 3.20a).[340-342] Based on the experimental findings, this metal dimer has been proposed to carry out the four-electron oxidation of water through a high-valent [Mn(IV,V)] species (Figure 3.20b).

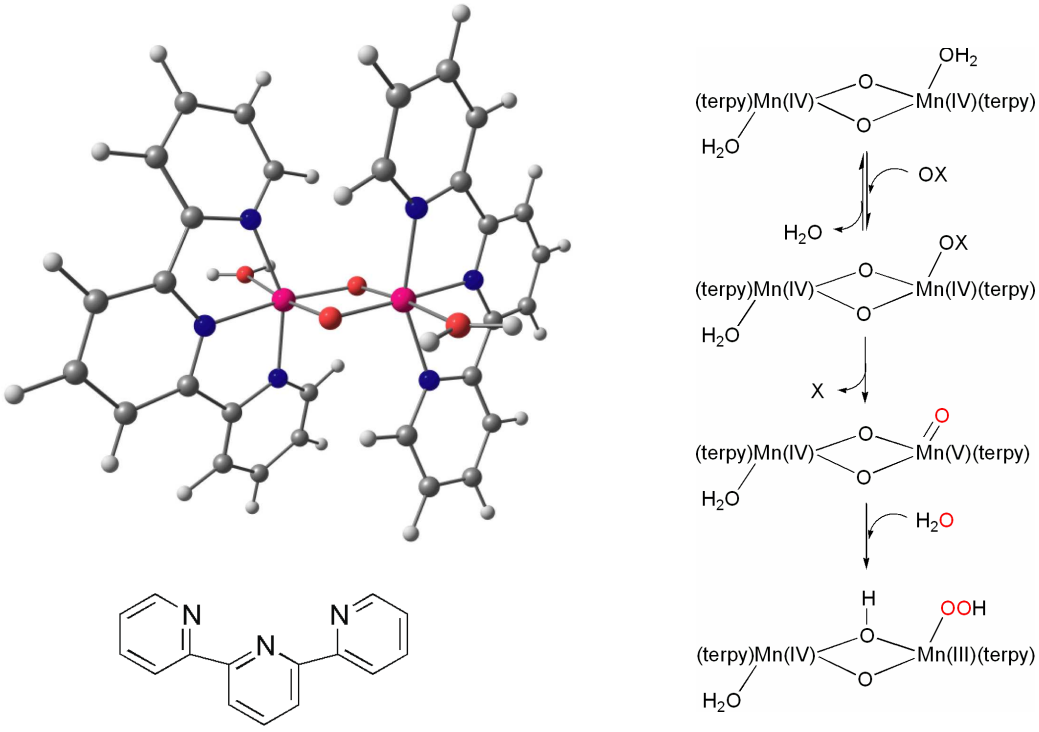

Figure 3.20 (a) Oxygen evolving [(terpy)(H_2O)Mn(III)(μ-O)$_2$Mn(III)(H_2O)(terpy)]$^{3+}$ complex and (b) proposed reaction pathway for the O-O bond formation.

The high-valent Mn-oxo of the active [Mn(IV,V)] complex undergoes nucleophilic attack by a water or a hydroxide ion in solution, a proposal reminiscent of the Ru-based complex (Figure 3.18b, mechamism A).[323] Due to strong structural correspondence between this biomimetic manganese dimer and the OEC, Brudvig argue that the O-O bond formation of the OEC may also proceed through a Mn(V)=O intermediate. However, some well characterised Mn(V)=O model complexes are not active in the O-

O bond formation.[142-145] Siegbahn and co-workers studied the nature of this highly oxidised [Mn(IV,V)] form of the above oxygen evolving dinuclear Mn system with DFT.[343] Their calculations suggested that the active state is in fact a Mn(IV)-$O^{\cdot+}$ rather than the Mn(V)=O form for O-O bond formation (Figure 3.21). Then reaction between the active metal-oxyl radical with a molecule of H_2O leads to O-O bond formation, with a calculated barrier for the O-O bond formation of 28 kcal mol^{-1} [142-145]. By considering the structural analogy between the bis-μ-oxo bridged Mn(III/IV) terpyridyl species and the OEC and comparing the DFT results with their previous work on models of the OEC,[142-150] Siegbahn concluded that the formation of the Mn(IV)-$O^{\cdot+}$ radical is the key component for the O-O bond formation in photosynthesis.

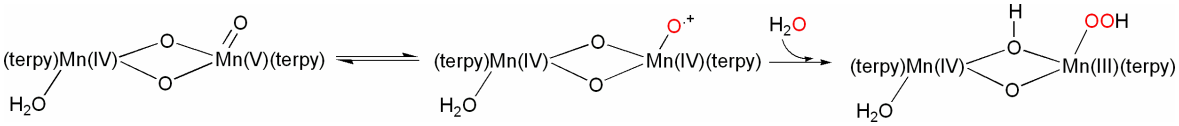

Figure 3.21 Possible O-O bond formation reaction based on DFT calculations.

Bis-porphyrin model: A $[\{(Porp)Mn(III)\}_2\text{-}(\mu\text{-phe})]^{2+}$ complex by Naruta and co-workers[223,224] is a well-known biomimetic water oxidation catalyst. The proposed reaction pathway for the oxygen evolution is depicted in Figure 3.22.

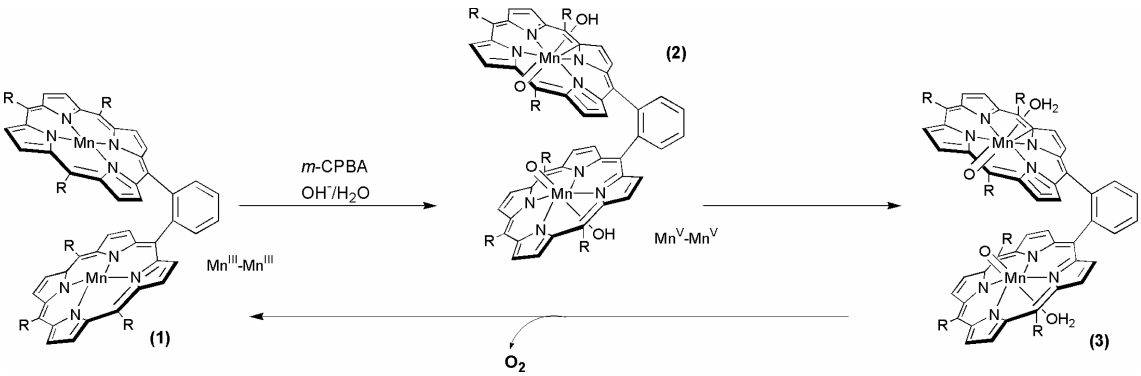

Figure 3.22 The $[\{(Porp)Mn(III)\}_2\text{-}(\mu\text{-phe})]^{2+}$ complex **(1)** and the proposed reaction pathway for the O_2 evolution.[223,224]

A stable dinuclear Mn(V)-oxo complex **(2)** is formed by reacting the $[\{(Porp)Mn(III)\}_2\text{-}(\mu\text{-phe})]^{2+}$ complex **(1)** with *m*-chlorobenzoic acid (*m*-CPBA) under strongly basic

conditions; labelling experiments suggest that the oxo and hydroxo axial ligands of **(2)** may derive from H_2O or OH^-. In the presence of a small amount of acid, O_2 is generated, presumably through a dinuclear Mn(V)-oxo-aqua species **(3)**. Naruta proposed that the O-O bond formation could occur either *via* coupling between the two Mn(V)=O groups or by attack of a Mn(V)=O aqua group on water.[224] This system is the subject of section two of this chapter.

$[Mn(II)_2(mcbpen)_2(H_2O)_2]^{2+}$ complex: McKenzie and co-workers have synthesized a catalytically active dimanganese complex $[Mn(II)_2(mcbpen)_2(H_2O)_2]^{2+}$, where mcbpen =N-methyl-N'-carboxymethyl-N,N'-bis(2-pyridylmethyl)ethane-1,2-diamine.[225,226] This system performs water oxidation in the presence of *tert*-butylhydroperoxide (TBHP) or cerium nitrate.[225,226] According to their proposed mechanism, the O-O bond is formed across the $Mn(IV)_2$-(μ-$O)_2$ unit through a μ-peroxo intermediate, but without forming an active Mn(IV)-$O^{\cdot+}$ species or highly oxidized Mn(V)=O form (Figure 3.23).

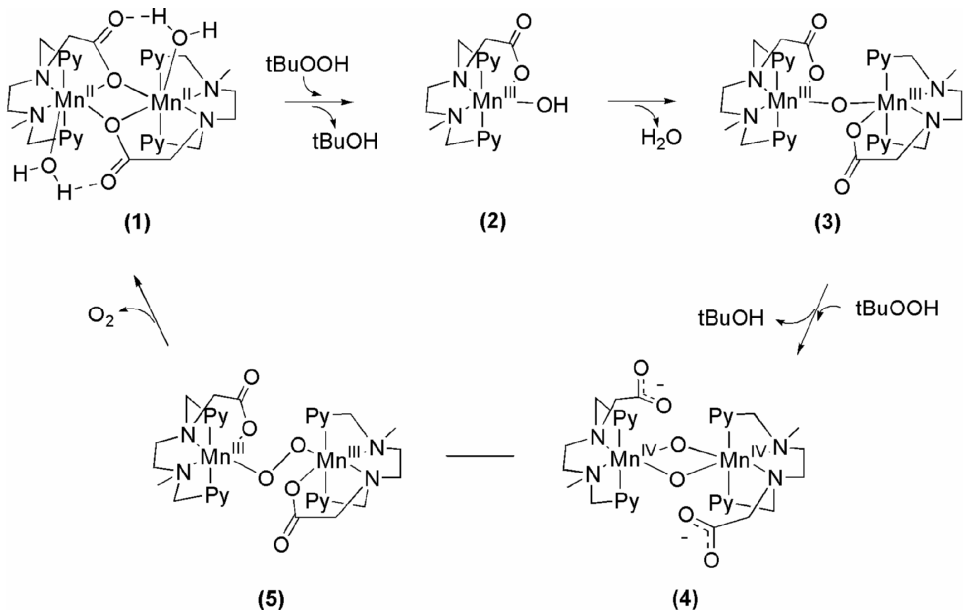

Figure 3.23 Proposed mechanism of water oxidation by $[Mn(II)_2(mcbpen)_2(H_2O)_2]^{2+}$ complex.

This proposed reaction pathway for the O-O bond formation is similar to that of the butterfly or double pivot mechanism for oxygen evolution at the OEC suggested by

Dismukes and Christou (Figure 3.8). However, based on the recent studies of μ-oxo exchange rates of the substrate waters in the OEC by Wydrzynski and co-workers, it seems unlikely that nucleophilic oxygen originates from brigdes.[279] A detailed survey of the mechanism of this reaction is presented in the third section of this chapter.

3.1.3.3 Heterogeneous oxygen evolving systems

In addition to the above homogeneous water oxidation catalysts, a number of less-well-defined systems such as oxides of metals (iridium, ruthenium, and manganese) are known to evolve oxygen under certain conditions, in particular with Ce(IV) or oxone oxidants.[344,345] Permanganate solutions are well-known to evolve oxygen when dissolved in water, where the MnO_4^- ion acts as the oxidant.[346] The 'ruthenium red', $[(NH_3)_5RuORu(NH_3)_4ORu(NH_3)_5]^{6+}$, is known as a highly active heterogeneous oxygen evolving system.[347-350] However, heterogeneous oxygen evolving systems are not reliable for large scale fuel cells to produce dioxygen.

3.2 Objectives

We aim to explore possible mechanisms for water oxidation by the Naruta and McKenzie systems [Figure 3.22 and Figure 3.23]. Their dinuclear Mn species are electronically complex because the problems of dealing with open-shell Mn(IV)-oxyl radical species is compounded by the coupling between two metal centres, where ferromagnetic (F) or anti-ferromagnetic (AF) coupling leads to a large number of different spin states. Detailed potential energy profiles for the oxygen evolution were developed by considering the potential energy surfaces connecting the most stable electronic state(s). The implications of this work may guide the design of catalytically novel and chemically significant second-generation water oxidation catalysts.

3.3 Computational details

All the gas phase optimisations were carried out using the Gaussian 03 programme[73] with the hybrid B3LYP[46-48] functional and the LanL2DZ basis set.[77,80-82] Vibrational frequency calculations were also performed in order to establish that the stationary points were minima or transition states. The anti-ferromagnetic spin states were obtained by using the broken symmetry approach,[351,352] where manual adjustments of the initial guess functions were made by examining Mulliken spin populations and frontier orbitals or using the Jaguar 7.5 programme.[75]

3.4 Results and discussion

3.4.1 Oxygen evolving $[\{(Porp)Mn(III)\}_2\text{-}(\mu\text{-phe})]^{2+}$ complex complex

This section describes how the $[\{(Porp)Mn(III)\}_2\text{-}(\mu\text{-phe})]^{2+}$ complex **(1)** (Figure 3.24), developed by Naruta and co-workers,[223,224] successively mimics the four-electron oxidation of water to evolve molecular oxygen. The proposed catalytic cycle for the water oxidation has been discussed in section 3.1.3.2. This catalyst can also mimic epoxidation of olefins, cyclooctene for instance,[353] like the cytochrome P-450 enzymes.[87,88] The active component for the catalytic oxidation of water or olefins has been proposed to be a high-valent Mn(V)-oxo species. The proposed key intermediates for the water oxidation (catalytic cycle) are depicted in Figure 3.24. First, oxidation of $[\{(Porp)Mn(III)\}_2\text{-}(\mu\text{-phe})]^{2+}$ complex **1** with *m*-CPBA as an oxidant yields a high-valent Mn-oxo complex **2**. On the basis of chemical and magnetic studies, Naruta proposed that the Mn centres of **2** are low-spin Mn(V) ions (d^2). When a small excess of trifluoromethanesulfonic acid (CF_3SO_3H) was added to the Mn(V)=O species **2**, dioxygen evolution was observed through a dinuclear Mn(V)-oxo-aqua system **3**.

Further, O_2 evolution was followed by mass spectrometry (MS), which confirmed quantitative incorporation of oxygen atoms from H_2O or OH^- in the solution.

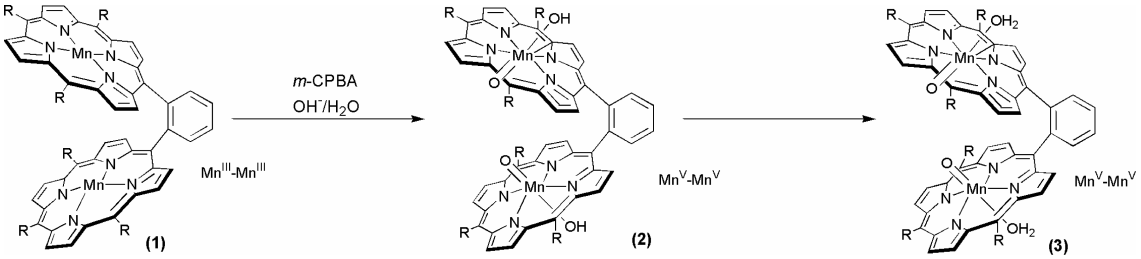

Figure 3.24 The key intermediates of the proposed mechanism for O_2 evolution.[223,224]

According to Naruta, O-O bond formation occurs by coupling either between the H_2O-Mn(V)=O units of **3** (direct mechanism) or by attack of the H_2O-Mn(V)=O group of **3** on water (two-step mechanism). However, the detailed chemical steps involved in the catalytic cycle of oxygen evolution have not been fully confirmed to date. Therefore, we applied DFT to explore the possible mechanisms for the catalytic water oxidation by using the available experimental evidence to provide a framework.

3.4.1.1 Electronic structure of [{(Porp)Mn(III)]$_2$}-(μ-phe)]$^{2+}$ complex

Our first goal was to understand the detailed spin density distributions of various spin states of key intermediates **1**, **2**, and **3**. We have considered two model complexes for the reactant complex **1**,[{(Porp)Mn(III)}$_2$-(μ-phe)]$^{2+}$ **(1_1)** and [{(H_2O)$_2$(Porp)Mn(III)]$_2$}-(μ-phe)]$^{2+}$ **(1_2)**, in both of which the mesityl groups have been replaced by H for simplicity (Figure 3.25). Both **1_1** and **1_2** complexes contain high-spin Mn(III) ions (S = 2) on the individual metal sites, and therefore two important spin states, namely an open-shell singlet (antiferromagnetic) and a nonet (ferromagnetic) are possible. The optimised structural parameters (Å), spin densities, $<S^2>$ values and relative energies of the optimised electronic states of **1_1** and **1_2** are depicted in Table 3.1. The ground state of both systems are broken-symmetry singlet electronic states with antiferromagnetically coupled high-spin Mn(III) ions [ρ(Mn) = $\pm$ 3.97 or $\pm$ 3.99]. The

energy difference between the stable singlet and the corresponding nonet state is negligible for the both systems, which indicates that the magnetic coupling of metal centres (S = 2) *via* the μ-phe bridge is weak.

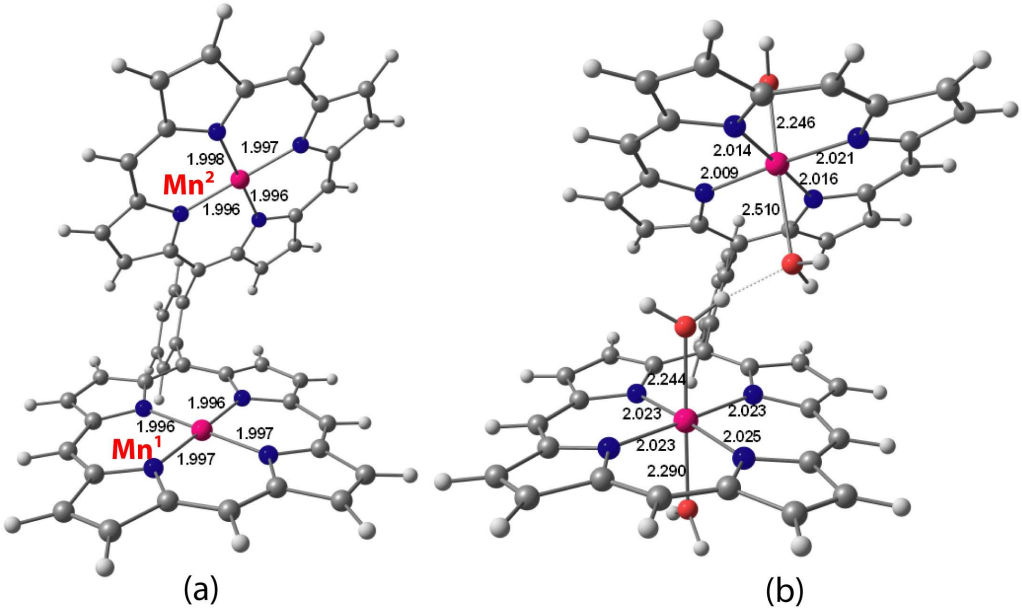

Figure 3.25 Optimised singlet electronic states of (a) $^{1}\mathbf{1}_{1}$ and (b) $^{1}\mathbf{1}_{2}$ complexes.

Table 3.1 Mulliken spin populations, bond lengths (Å), $<S^2>$ values and relative energies (kcal mol^{-1}) of the key electronic states for $\mathbf{1}_1$ and $\mathbf{1}_2$ complexes.

	Structural parameters		Mulliken Spin density				$<S^2>$	Relative energy
	r(Mn-Mn)	r(Mn-L)	ρ(Mn^1)	ρ(Mn^2)	ρ(Porp^1)	ρ(Porp^2)		
$^{1}\mathbf{1}_{1}$	7.18	----	-3.97	3.97	0.03	-0.03	4.11	0.0
$^{9}\mathbf{1}_{1}$	7.18	----	3.97	3.97	0.03	0.03	20.10	+0.1
$^{1}\mathbf{1}_{2}$	6.24	2.24-2.51	-3.99	3.99	0.04	-0.06	4.10	0.0
$^{9}\mathbf{1}_{2}$	6.24	2.24-2.50	3.99	3.99	-0.03	-0.06	20.10	+0.1

3.4.1.2 Electronic structure of [{(HO)(Porp)Mn(V)O}$_2$-(μ-phe)] complex

The detailed electronic structure of (HO)(Porp)Mn(V)O mononuclear system is discussed in the second chapter. Our DFT calculations (B3LYP) on this complex

confirmed the presence of a triplet ground state, where the net spin densities on Mn of +3.04 and O of -0.89 are characteristics of the Mn(IV)–$O^{\cdot+}$ spin density distribution ($^3\Pi_O$). The corresponding quintet state ($^5\Pi_O$) has spin vectors on Mn and O aligned ferromagnetically [ρ(Mn) = +2.86, ρ(O) = +1.09]. The dinuclear system [{(HO)(Porp)Mn(V)O}$_2$-(*μ*-phe)] **(2)** holds two (HO)(Porp)Mn(V)O mononuclear units connected through a *μ*-phe bridge. Therefore, the key electronic states of this dinuclear system can be considered as ferro- or antiferromagnetically coupled triplet or quintet states of (HO)(Porp)Mn(V)O units (Figure 3.26). Ferro- and antferromagnetic coupling of triplet spin density distribution ($^3\Pi_O$) of the individual (HO)(Porp)Mn(V)O units give rise to singlet a **(^{1}2$_1$)** and a quintet **(^{5}2)** electronic states respectively. Two other possible configurations, a singlet **(^{1}2$_2$)** and a nonet **(^{9}2)** can be formed *via* ferro- and antferromagnetic coupling of quintet spin density distribution ($^5\Pi_O$) of the monomer units. Calculated Mulliken spin populations, bond lengths (Å), $<S^2>$ values and relative energies of the key electronic states of the dimer are depicted in Table 3.2.

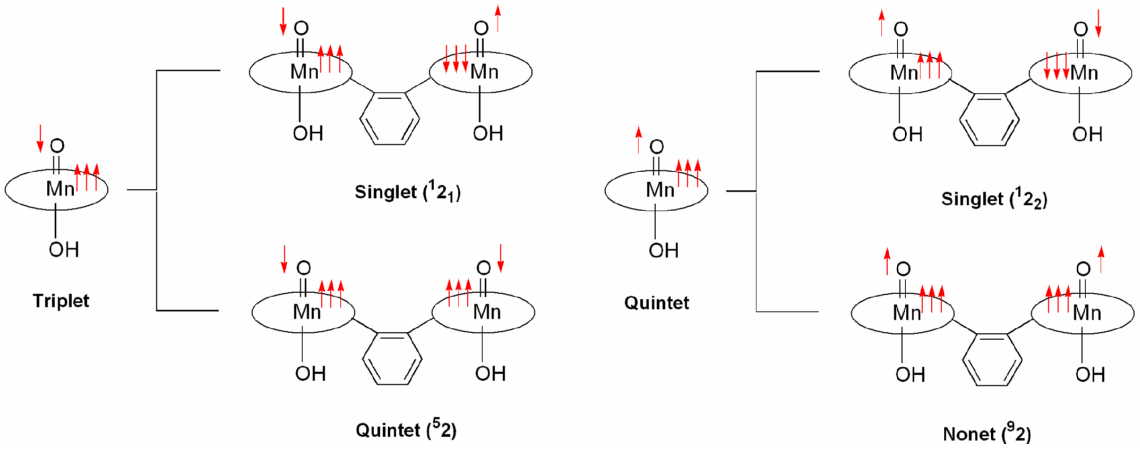

Figure 3.26 Coupling of the key electronic states of (HO)(Porp)Mn(V)O to generate spin states for [{(HO)(Porp)Mn(V)O}$_2$-(*μ*-phe)].

The ground state electronic structure of [{(HO)(Porp)Mn(V)O}$_2$-(*μ*-phe)] is an open-shell singlet, **^{1}2$_1$**, where spin densities on Mn^1 of +2.90, O^1 of -0.89, Mn^2 of -2.91 and O^2 of +0.89 indicate triplet Mn(IV)-oxyl character ($^3\Pi_O$) at the both Mn-oxo moieties, which are antiferromagneticaly coupled *via* the *μ*-phe bridge. The optimised structure and total spin density distribution of the ground state **^{1}2$_1$** are shown in Figure 3.27. The

corresponding high-spin quintet state $^{5}\mathbf{2}$ is structurally and energetically similar to the ground state $^{1}\mathbf{2_1}$ but two Mn sites are ferromagnetically coupled, and the triplet Mn(IV)-$O^{\cdot+}$ spin density distribution of $^{1}\mathbf{2}$ and $^{5}\mathbf{2}$ states yields relatively shorter Mn-O bond lengths (1.80 Å).

Table 3.2 Possible electronic states of [{(HO)(Porp)Mn(V)O}$_2$-(μ-phe)] and [{(H_2O)(Porp)Mn(V)O]$_2$-(μ-phe)]$^{2+}$ systems.

	Structural parameters		Mulliken Spin density						<S^2>	Relative Energy (kcal mol^{-1})
	r(MnO)	r(MnL)	ρ(Mn^1)	ρ(Mn^2)	ρ(O^1)	ρ(O^2)	ρ(Porp^1)	ρ(Porp^2)		
[{(HO)(Porp)Mn(V)O}$_2$-(μ-phe)]										
$^{1}\mathbf{2_1}$	1.80	1.85	2.90	-2.91	-0.89	0.89	-0.20	-0.20	3.9	0.0
$^{1}\mathbf{2_2}$	1.86	1.86	2.74	-2.73	1.14	-1.14	-0.05	0.05	4.1	+7.3
$^{5}\mathbf{2}$	1.80	1.85	2.90	2.90	-0.89	-0.89	-0.20	-0.20	7.9	+0.2
$^{9}\mathbf{2}$	1.86	1.84	2.73	2.73	1.14	1.14	-0.05	-0.05	20.1	+7.3
$^{1}\mathbf{2_{RKS}}$	1.57	1.82	-	-	-	-	-	-	0.0	+15.9
[{(H_2O)(Porp)Mn(V)O}$_2$-(μ-phe)]$^{2+}$										
$^{1}\mathbf{3_1}$	1.66	2.19	2.41	-2.41	0.70	-0.70	-1.02	1.02	4.10	0.0
$^{1}\mathbf{3_2}$	1.66	2.19	2.40	-2.40	0.70	-0.70	0.82	-0.82	4.10	0.0
$^{5}\mathbf{3}$	1.66	2.19	2.41	2.41	0.70	0.70	-1.07	-1.07	8.20	+0.5
$^{9}\mathbf{3}$	1.66	2.19	2.40	2.40	0.70	0.70	0.88	0.88	20.2	+0.6
$^{1}\mathbf{3_{RKS}}$	1.53	1.53	-	-	-	-	-	-	0.0	+29.0

The computed spin density distribution of the second antiferromagnetic open-shell singlet state $^{1}\mathbf{2_2}$ indicates that the spin vectors at the individual Mn-oxo sites are now parallel [ρ(Mn^1) = +2.74, ρ(O^1) = +1.14 and ρ(Mn^2) = -2.73, ρ(O^2) = -1.14], in agreement with quintet Mn(IV)-oxyl radical character ($^{5}\Pi_O$). The ferromagnetic nonet state $^{9}\mathbf{2}$ is structurally and energetically similar to the $^{1}\mathbf{2_2}$, and these two configurations are 7.3 kcal mol^{-1} above the ground state **($^{1}\mathbf{2_1}$)**. The closed-shell singlet state $^{1}\mathbf{2_{RKS}}$ is further 7.6 kcal mol^{-1} higher in energy, and which has much shorter Mn-O bond distances (1.57 Å). The most significant electronic feature of the proposed intermediate

2 is metal-oxyl radical [Mn(IV)-$O^{\cdot+}$] spin density distributions in the stable electronic states.

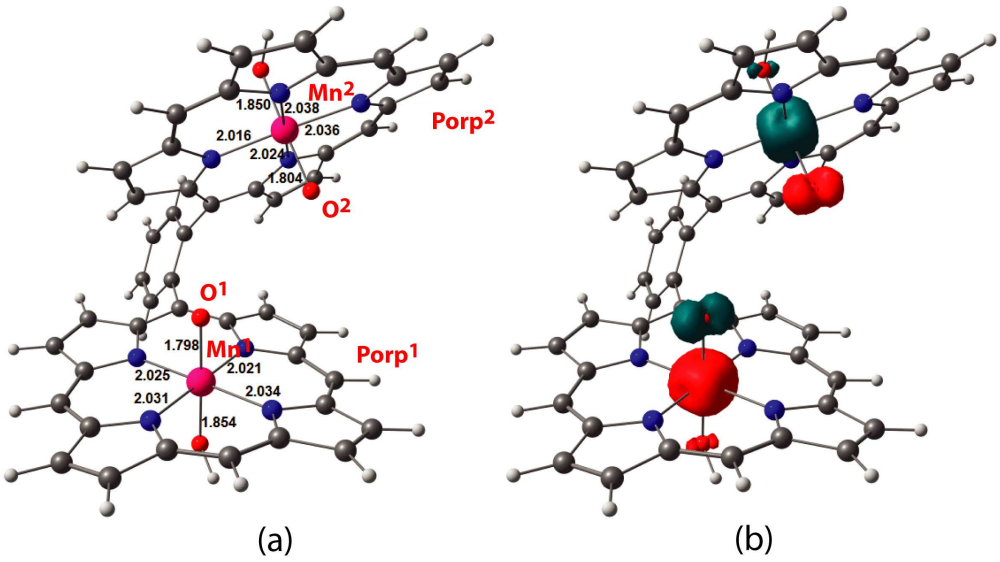

Figure 3.27 (a) Optimised structure with labelling of the fragments and (b) total spin density distribution of the singlet ground state **(^{1}2$_1$)**.

3.4.1.3 Electronic structure of [{(H_2O)(Porp)Mn(V)O}$_2$-(μ-phe)]$^{2+}$ complex

The proposed active species for the O-O bond formation, [{(H_2O)(Porp)Mn(III)}$_2$-(μ-phe)]$^{2+}$, has two [(H_2O)(Porp)Mn(V)O]$^+$ units, which are connected through the μ-phe bridge. The electronic structure of [(H_2O)(Porp)Mn(V)O]$^+$ mononuclear system has been comprehensively discussed in Chapter 2, and the key electronic property of this system is porphyrin-radical character in the energetically significant electronic states. The key electronic states of the corresponding dinuclear system, [{(H_2O)(Porp)Mn(III)}$_2$-(μ-phe)]$^{2+}$, are summarised in Figure 3.28, where we considered ferro- or antiferromagnetic coupling between triplet ($^3A_{2u}$) or quintet ($^5A_{2u}$) states of two [(H_2O)(Porp)Mn(V)O]$^+$ units. The ground state of this system, ^{1}**3$_1$**, has majority spin density on both Mn and O of each Mn-oxo unit [ρ(Mn) = +2.41, +0.70 (or -2.41, -0.70)] and minority spin on the porphyrin [-0.82 (or +0.82)] indicating triplet

porphyrin radical character ($^3A_{2u}$), where the spin vectors of the Mn-oxo unit and the porphyrin ring are aligned anti-parallel. The optimised structure and total spin density distribution of the ground state $^1\mathbf{3_1}$ are depicted in Figure 3.29.

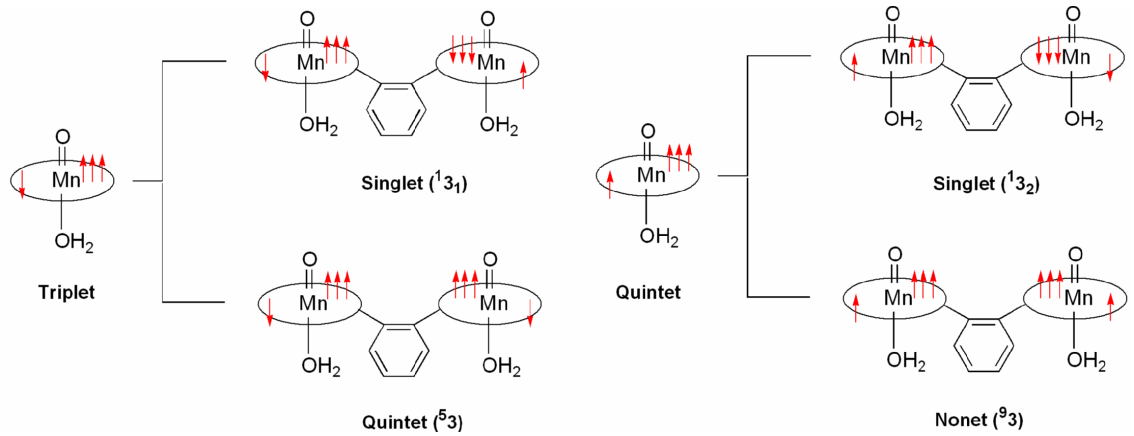

Figure 3.28 Coupling of the key electronic states of $[(H_2O)(Porp)Mn(V)O]^+$ monomer to generate spin states for $[\{(H_2O)(Porp)Mn(V)O\}_2\text{-}(\mu\text{-phe})]^{2+}$ dimer.

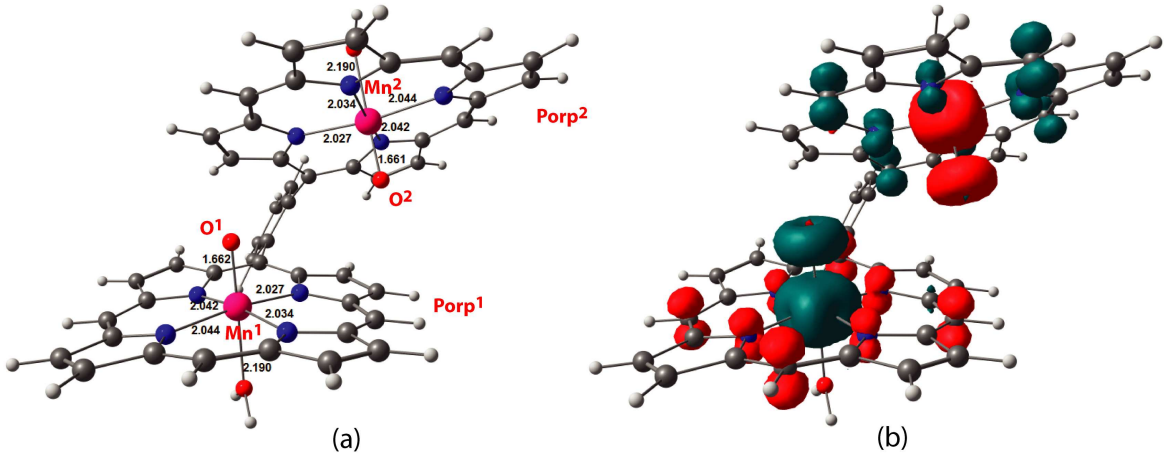

Figure 3.29 (a) Optimised structure with labelling of the fragments and (b) total spin density distribution of the singlet ground state $^1\mathbf{3_1}$.

The second open-shell singlet state, $^1\mathbf{3_2}$, is almost identical both structurally and energetically to that of the ground state $^1\mathbf{3_1}$. The ferromagnetic quintet **(^{5}3)** and nonet **(^{9}3)** states are only 0.5 kcal mol^{-1} and 0.6 kcal mol^{-1} above the ground state respectively. The closed-singlet state **($^1\mathbf{3_{RKS}}$)** is 29 kcal mol^{-1} above the ground state **($^1\mathbf{3_1}$)**, and has relatively shorter Mn-O and bond distances (1.53 Å), consistence with the triple bond character on the Mn-oxo unit in this case. The calculated electronic states of

$[\{(H_2O)(Porp)Mn(V)O\}_2\text{-}(\mu\text{-phe})]^{2+}$ complex confirmed that the most significant electronic property of the stable configurations hold significant porphyrin radical character.

With a description of the limiting electron density distributions in the key electronic states of **1**, **2** and **3** in hand, we are now in a position to interpret the O-O bond formation mechanisms using DFT.

3.4.1.4 The O-O bond formation

If we accept the $[\{(H_2O)(Porp)Mn(V)O\}_2\text{-}(\mu\text{-phe})]^{2+}$ complex **(3)** as the precursor for the oxygen evolution, the O-O bond formation may occur either *via* coupling between the two Mn(V)=O groups (direct mechanism), or by attack of the one Mn(V)=O groups on a solvent water molecule (two-step mechanism). The direct mechanism can be described as a two-electron transfer reaction giving rise to a peroxo intermediate (Figure 3.30a), whereas the two step mechanism involves transfer of two electrons and a proton ($2e^-/H^+$), leading to the formation of a hydroperoxo intermediate (Figure 3.30b). We aim to develop detailed potential energy profiles for the both mechanisms, and compute the active barrier for the O-O bond formation, where we have considered the potential energy surfaces connecting the most stable electronic state(s) of the reactant, intermediate and product complexes.

We have established potential energy profiles for two-electron oxidation of Me_2S, CH_4 and C_2H_4 by $[(H_2O)(Porp)Mn(O)]^+$ in Chapter 2. At long range separations, the reactant complex has dominant $(H_2O)(Porp^{\bullet+})Mn(IV)O$ character ($^3A_{2u}$ or $^5A_{2u}$), where interaction with the incoming nucleophile on the triplet (or quintet) surface is repulsive because oxyl radical character of the oxidant is masked. The oxyl radical character can be 'unmasked' *via* transfer of an electron from oxide to the vacancy in the porphyrin ring, thereby opening up a route for electron transfer from the substrate to the oxide.

The next section describes similar features that emerge in the water oxidation chemistry of the corresponding system $[\{(H_2O)(Porp)Mn(V)O\}_2\text{-}(\mu\text{-phe})]^{2+}$.

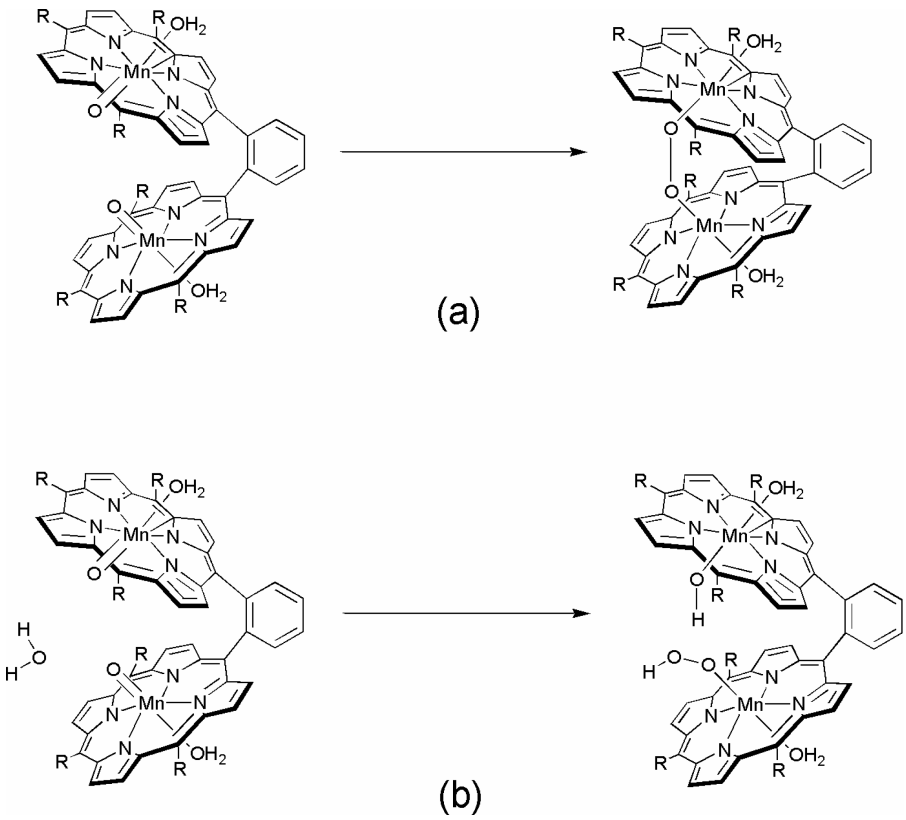

Figure 3.30 Possible O-O bond formation mechanisms; (a) coupling between the two Mn(V)=O groups (direct mechanism), and (b) by attack of the Mn(V)=O groups on a solvent water molecule (two-step mechanism).

3.4.1.4.1 The O-O bond formation: direct mechanism

Detailed electronic structural analysis of the proposed key intermediate **3**, $[\{(H_2O)(Porp)Mn(V)O\}_2\text{-}(\mu\text{-phe})]^{2+}$ complex, shows dominant porphyrin radical character in its open-shell singlet ground state $^1\mathbf{3_1}$ [$\rho(Porp)^1$ = -1.02, $\rho(Porp)^2$ = 1.02], and therefore the Mn(IV)-oxyl character is masked. However, repulsive interactions between the lone pairs on the oxide ligand (as the two Mn=O units approach each other) may drive an electron from the oxide ligand to the vacancy in the porphyrin ring, opening the active channel for the O-O bond formation. Direct coupling of oxide ligands in this way leads to a peroxo species **5** (Figure 3.31). The potential energy

profiles for the O-O bond formation through the direct mechanism are depicted in Figure 3.32.

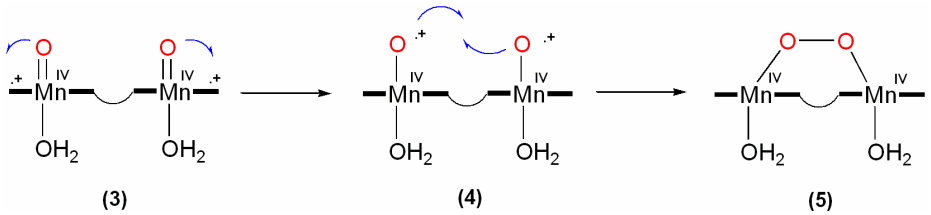

Figure 3.31 O-O bond formation through the coupling of the oxo ligands (direct mechanism).

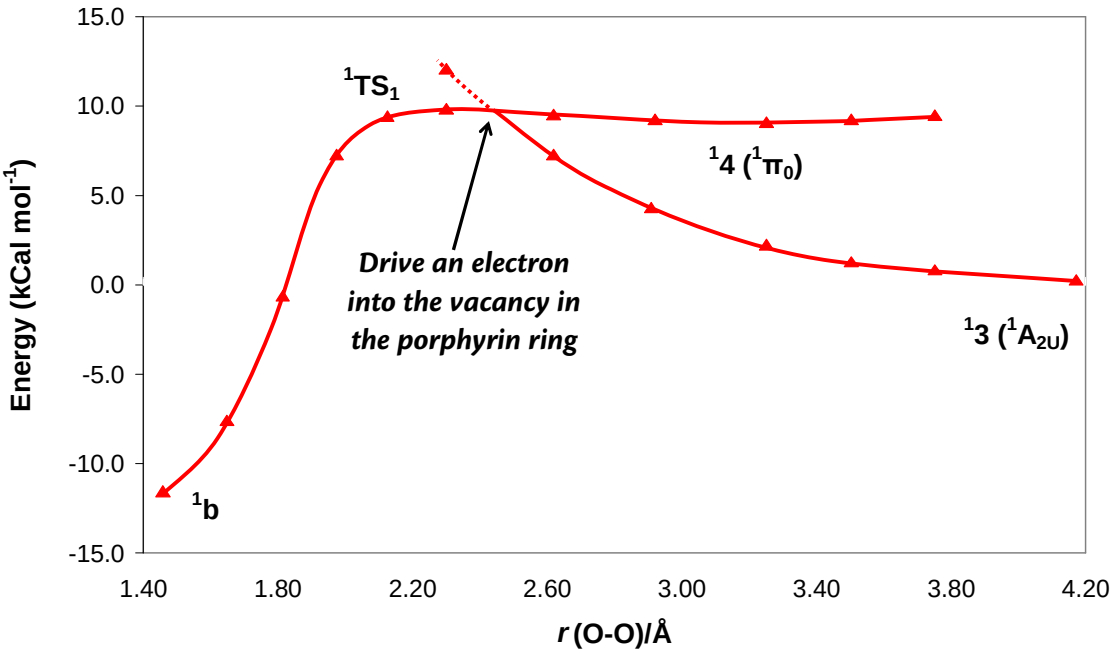

Figure 3.32 Singlet potential energy surfaces for the O-O bond formation *via* coupling between the two Mn(IV)-$O^{\bullet+}$ groups (B3LYP).

At long range separations (> 2.45 Å), the porphyrin radical surface is repulsive as metal-oxyl character is masked ($^1A_{2u}$) (Figure 3.32). In addition to the ground state we have located **(^{1}3$_1$)**, a second stable minimum **^{1}4** with a metal-oxyl radical electronic distribution ($^1\Pi_O$) was found 9.3 kcal mol^{-1} above the entry channel (Figure 3.33a). The open-shell singlet of this oxyl radical system **(^{1}4)** contains spin density on Mn^1 of +3.00, O^1 of -0.91, Mn^2 of -3.01 and O^2 of +0.91 indicating significant metal-oxyl character on

both Mn-oxo units (Table 3.3). Consequently, the singlet metal-oxyl radical potential energy profile ($^1\Pi_O$) is attractive at long range separations (> 2.45 Å), a discontinuity of porphyrin radical ($^1A_{2u}$) and oxyl radical ($^1\Pi_O$) surfaces occurs in the region of *r*(O-O) ~ 2.4 Å, which is 9.5 kcal mol^{-1} above the entry channel. In this region, an electron is transferred from oxide to the vacancy in the Mn sites, 'unmasking' the oxyl radical character. It is important to note that Figure 3.32 represents a one dimensional scan of the potential energy surface, and the discontinuity in the triplet surface does not represent a true transition state, but rather a lower bound to its energy. However, the stationary points we report were obtained without any constraint.

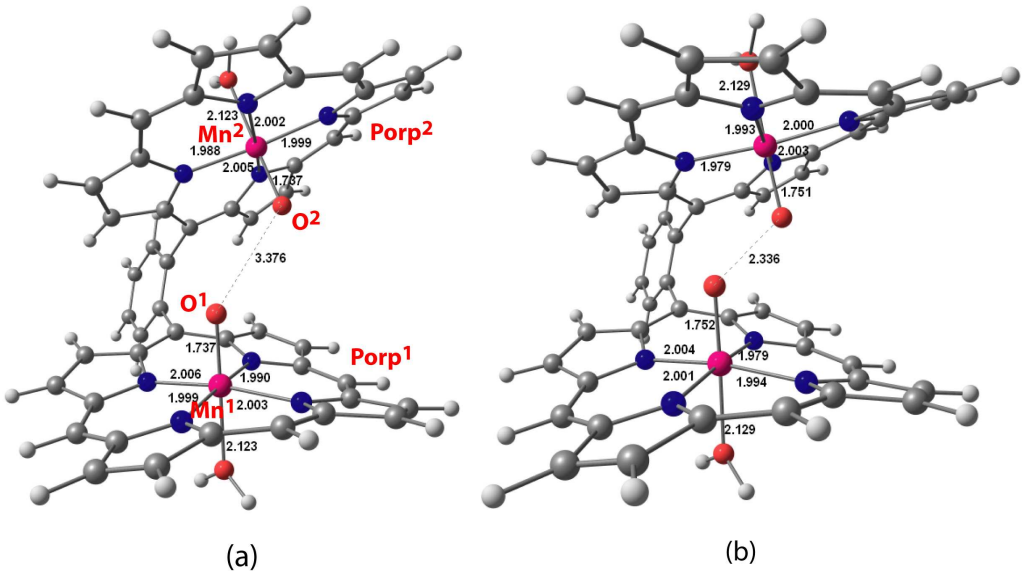

Figure 3.33 Optimised singlet ground state structures with labelling of the fragments of (a) active metal-oxyl radical species **(^{1}4)**, and (b) transition state **^{1}TS$_1$**.

Beyond the discontinuity, coupling of two oxyl radicals of **^{1}4** is almost barrierless, leading to the peroxo product (Figure 3.34a), **(^{1}5)**, *via* a very low-lying transition state, **^{1}TS$_1$** (Figure 3.33b) 9.6 kcal mol^{-1} above the entry channel. Thus the total barrier to the reaction (~9.6 kcal mol^{-1}) is associated almost entirely with the energy required to drive the electron out of the oxide ligand onto the porphyrin. In the resulting singlet peroxo species, **^{1}5,** net spin densities on Mn^1 of +3.07 and Mn^2 of -3.07 are typical of Mn(IV) (S = 3/2), where the individual Mn sites are antiferromagnetically coupled (Table 3.3).

Table 3.3 The optimised structural parameters (Å), spin densities, $<S^2>$ values and relative energies (kcal mol^{-1}) of the key electronic states of the singlet potential energy surfaces.

	Structural parameters			Mulliken Spin density						$<S^2>$	Relative energy
	$r(Mn^1O^1)$	$r(Mn^2O^2)$	$r(O^1O^2)$	$\rho(Mn^1)$	$\rho(Mn^2)$	$\rho(O^1)$	$\rho(O^2)$	$\rho(Porp^1)$	$\rho(Porp^2)$		
$^1\mathbf{3_1}$	1.66	1.66	4.18	2.40	-2.40	0.70	-0.70	-1.02	1.02	4.09	0.0
$^1\mathbf{4}$	1.74	1.74	3.37	3.00	-3.01	-0.91	0.91	-0.01	0.10	3.88	+9.3
$^1\mathbf{TS_1}$	1.75	1.75	2.34	3.01	-3.01	-0.89	0.89	-0.10	0.10	3.85	+9.6
$^1\mathbf{5}$	1.86	1.86	1.45	3.07	-3.06	-0.09	0.09	0.03	-0.02	3.07	-12.8
$^1\mathbf{TS_2}$	1.89	1.89	1.44	3.23	-3.23	-0.15	0.15	-0.09	0.09	3.47	-12.4
$^1\mathbf{6}$	3.66	2.71	1.27	3.95	-3.96	0.00	0.00	0.01	-0.01	4.09	-33.0
$^3\mathbf{6}$	3.75	2.80	1.26	3.96	-3.97	1.01	0.97	0.02	0.00	6.10	-43.5

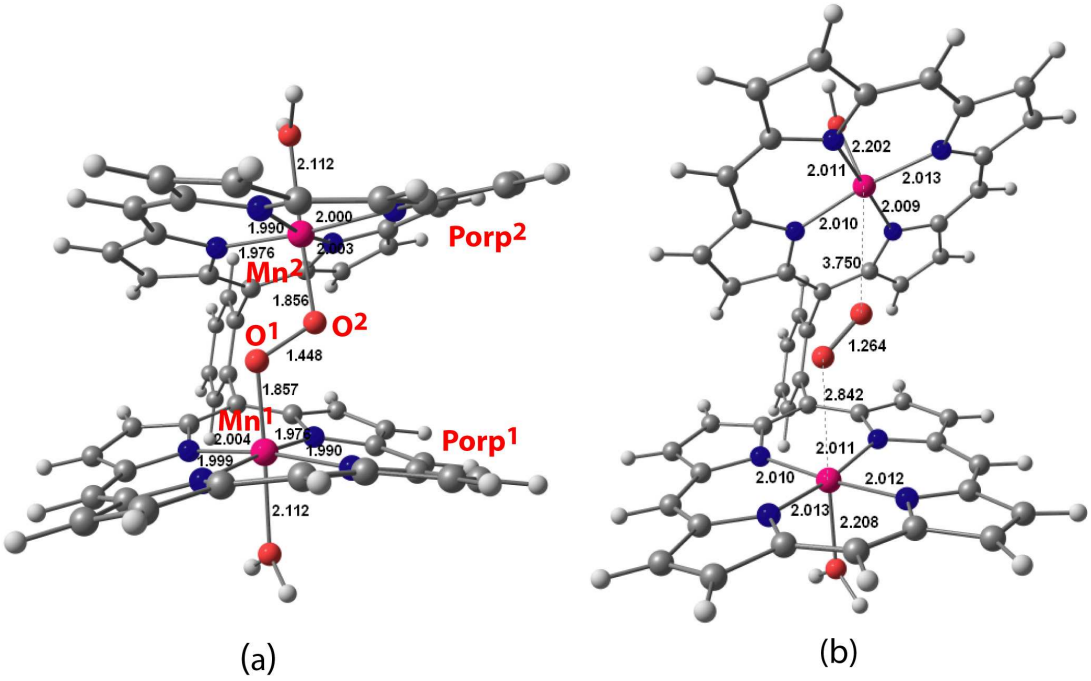

Figure 3.34 Optimised ground state structures with labelling of the fragments of (a) peroxo intermediate **(^{1}5)** and (b) the product complex **(^{3}6)**.

Starting from the peroxo system **(^{1}5)**, the second two-electron transfer process may yield molecular oxygen (Figure 3.35), which is still bound to the catalyst **(6)**. This two

electron transfer process gives rise to **6** *via* a low-lying transition state ^{1}**TS$_2$**, which is only 0.4 kcal mol^{-1} above the peroxo intermediate (**^{1}5**).

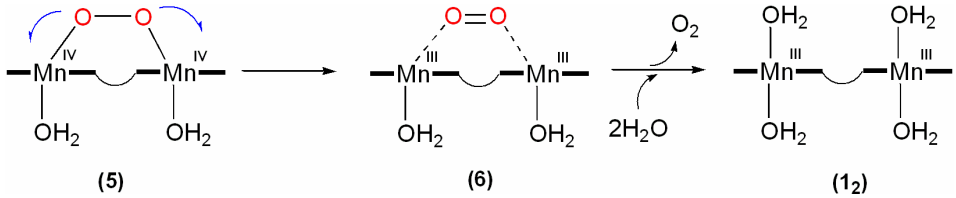

Figure 3.35 The O_2 formation mechanism through the direct coupling of the oxo ligands.

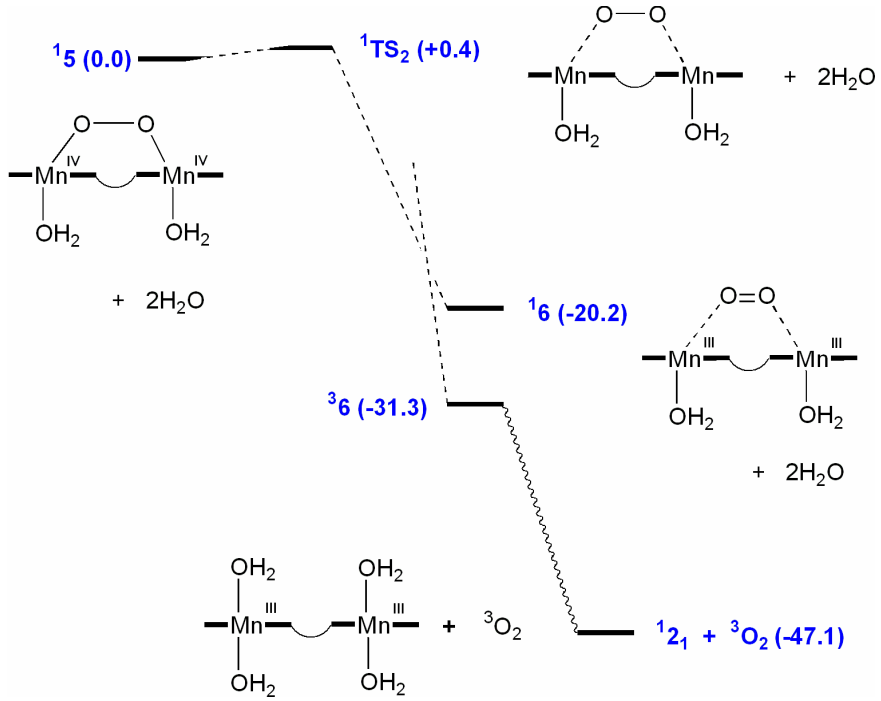

Figure 3.36 Potential energy surfaces for the O_2 formation through the direct coupling of the oxo ligands.

The **^{1}6** state has spin density on Mn^1 of +3.95 and Mn^2 of -3.96 indicating the formation of high spin Mn(III) ions (S = 2). The corresponding triplet state of this system (**^{3}6**) has O_2 in its triplet ground state [$\rho(O^1)$ = 1.01 , $\rho(O^2)$ = 0.97], and is 11.1 kcal mol^{-1} lower than the **^{1}6**, and therefore spin crossover singlet to triplet is required during the second two-electron transfer process. At this stage, association of two solvent water molecules may return the catalyst to its initial state (**^{1}1$_2$**), and yield molecular oxygen (**^{1}1$_2$** + $^{3}O_2$) further 15.8 kcal mol^{-1} lower than **^{3}6**. In summary, the 'direct'

mechanism can be described as a four electron transfer process, where 'unmasking' metal oxyl radical character [Mn(IV)-$O^{\cdot+}$] at both Mn-oxo sites is essential to open the active channel of the catalytic cycle, and the barrier for O-O bond formation is about 9.6 kcal mol^{-1}.

3.4.1.4.2 The O-O bond formation: two-step mechanism

As emphasised above, the isolated $[(H_2O)(Porp)Mn(V)O]^+$ system has porphyrin radical character in its stable spin states, and the key step of the oxidation process again involves 'unmasking' metal oxyl character through spin density transfer from the oxide ligand to the porphyrin ring at the 'discontinuity' region of the potential energy surfaces. In the sulphide oxidation case, the discontinuity region was found at r(O-S) ~ 3.2 Å and about 3.1 kcal mol^{-1} above the entry channel of the porphyrin radical surface. For the oxidation of CH_4, the discontinuity region was found at relatively shorter distance [r(O-H) ~ 1.6 Å], and therefore higher in energy (10.1 kcal mol^{-1}). The two-step mechanism of the Naruta system can be explained by combining the two-electron oxidation of Me_2S and CH_4 (Figure 3.37), where the two-step mechanistic proposal, in principle, has two discontinuity regions, the first of which is for the O-O bond formation and the second is for the O-H bond formation.

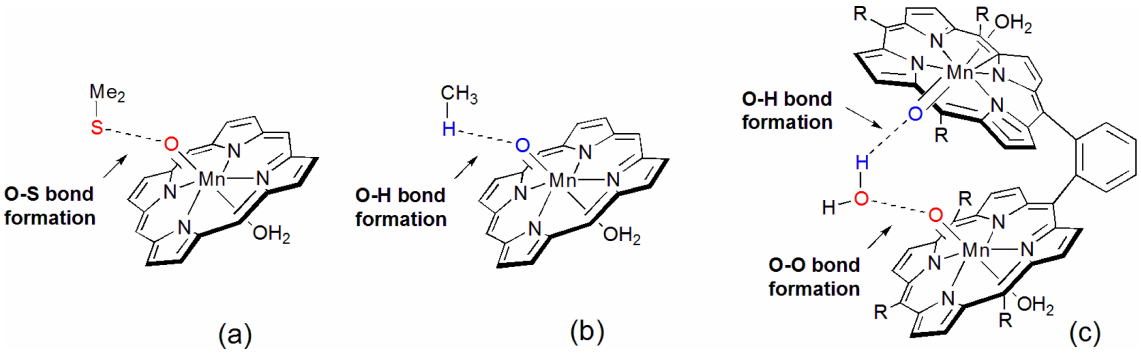

Figure 3.37 Two-electron oxidation of (a) Me_2S (O-S bond formation), (b) CH_4 (O-H bond formation), and (c) four-electron oxidation of water (O-O and O-H bond formation).

Assuming that the interaction between one of the Mn-oxo groups of the $[\{(H_2O)(Porp)Mn(IV)O\}_2\text{-}(\mu\text{-phe})]^{2+}$ complex **(3)** and H_2O leads to O-O bond formation, a molecule of water was incorporated to form an intermediate **3(H_2O)** (Figure 3.38a). Addition of this water molecule between the two Mn=O units does not show a significant influence on the electronic structure, and spin density populations of the open-shell singlet state ^{1}**3(H_2O)** are similar to those in ^{1}**3** (Table 3.4).

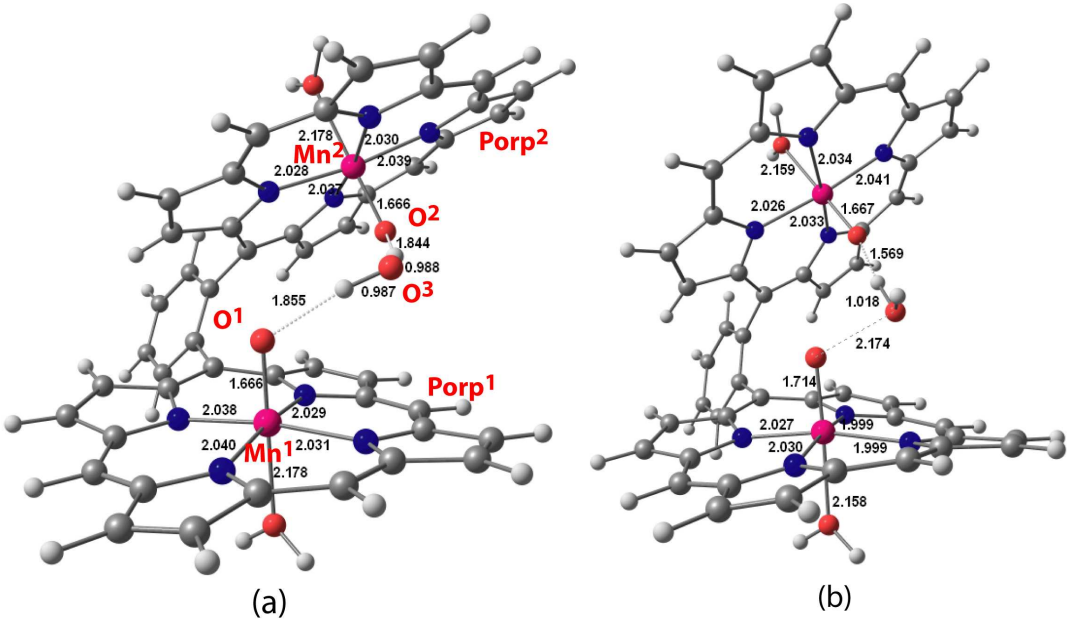

Figure 3.38 Optimised open-shell singlet ground state structures with labelling of the fragments of (a) reactant **[^{1}3(H_2O)]** and (b) oxyl radical intermediate complex **(^{1}7)**.

The optimised structure of ^{1}**3(H_2O)** indicates that the two hydrogen atoms of the water molecule form hydrogen-bonds with the terminal oxo ligand at longer O-O distances (Figure 3.38a). The singlet potential energy surfaces for O-O bond formation are shown in Figure 3.39 and Table 3.4 summarises the fully optimised structural parameters, spin densities, $<S^2>$ values and relative energies of the key stationary points. At long range separations (> 2.4 Å), the singlet potential surface is qualitatively identical to the potential energy profiles of the direct mechanism described in the previous section (i.e. repulsive), and the first discontinuity of the singlet surfaces was found in the same region [r(O-O) ~ 2.4 Å], which is about 4 kcal mol^{-1} above the singlet ground state of the **3(H_2O)** complex. However, in the case of the direct mechanism, both oxo ligands

are bound to the metal sites and due to this constraint the discontinuity region is relatively higher in energy (9.4 kcal mol^{-1}).

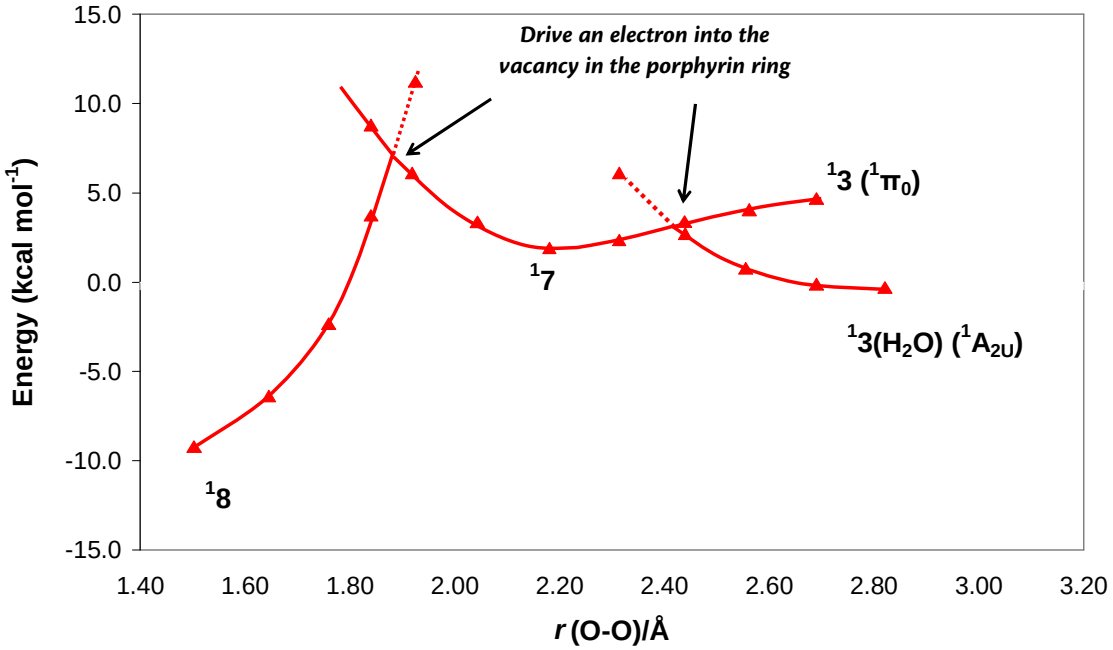

Figure 3.39 Singlet potential energy surfaces for the O-O bond formation or by attack of the one Mn(V)=O groups on a solvent water molecule (B3LYP).

Table 3.4 The optimised structural parameters (Å), spin densities, $<S^2>$ values and relative energies of the key electronic states of the singlet potential energy surface.

	Structural parameters			Mulliken spin density						$<S^2>$	Relative energy
	r(Mn^1O^1)	r(Mn^2O^2)	r(O^1O^3)	ρ(Mn^1)	ρ(Mn^2)	ρ(O^1)	ρ(O^2)	ρ(O^3)	ρ($Porp^1$)	ρ($Porp^2$)		
^{1}3(H$_2$O)	1.67	1.67	2.83	2.47	-2.47	0.62	-0.63	0.00	-1.03	1.03	4.08	0.0
^{1}7	1.71	1.67	2.15	2.97	-2.50	-0.60	-0.63	-0.27	0.02	0.94	3.92	+2.4
^{1}8	2.07	1.77	1.44	3.79	-2.98	-0.37	-0.01	-0.10	0.01	0.08	3.83	-9.7
^{1}TS$_3$	2.27	1.83	1.38	3.93	-3.01	-0.22	-0.08	-0.04	0.02	0.01	3.89	-5.3
^{1}9	2.45	2.22	1.30	3.95	-3.99	0.08	0.02	0.02	0.08	-0.01	4.09	-35.5
^{3}9	2.90	2.27	1.27	3.94	-3.99	0.90	0.03	1.05	0.02	-0.03	6.10	-43.9

In the first discontinuity region of the two-step mechanism, majority spin density of the O^1 transfers to the minority $(Porp)^1$ site, and therefore metal oxyl character is 'unmasked' at the Mn^1-O^1 site. Then the oxyl radical potential energy surface ($^1\Pi_O$) is attractive, and yields a stable intermediate ^{1}**7** (Figure 3.38b). This stable intermediate is however 2.4 kcal mol^{-1} above the entry channel of the porphyrin radical surface ($^1A_{2u}$). The calculated spin densities on Mn^1 of +2.97 and O^1 of -0.60 indicate a triplet Mn(IV)-$O^{\cdot+}$ spin density distribution ($^1\Pi_O$), and therefore Mn^1-O^1 bond length is elongated (1.71 Å). It is important to note that the spin density distribution at the other Mn-oxo-porphyrin site does not significantly change during this process [$\rho(Mn^2)$ = -2.50, $\rho(O^1)$ = -0.63, $\rho(Porp^1)$ = 0.94], which indicate that the second Mn-oxo-porphyrin unit behaves as a spectator during the first spin density transfer process.

The second discontinuity region (for the O^2-H bond formation) was found at about $r(O^1$-$O^3)$ ~ 1.9 Å (Figure 3.39), which represents 'unmasking' Mn(IV)-oxyl character at the Mn^2-O^2 moiety, leading the formation of the hydroperoxo complex ^{1}**8** *via* H atom abstraction. The second discontinuity lies only 6.8 kcal mol^{-1} above the entry channel, which is quite similar to the barrier for the oxidation of CH_4 by the $[(H_2O)(Porp)Mn(V)O]^+$ system we discussed in Chapter 2 (~10 kcal mol^{-1}). The total spin density distribution of the resulting hydroperoxo species ^{1}**8** merits some discussion due to a rather surprising electron density distribution on the Mn^1-O^1-O^3 unit and significant spin contamination $\langle S^2\rangle$ = 3.83 [ideal value is 3.00] (Figure 3.40a). The net spin densities of $\rho(Mn^1)$ = +3.79, $\rho(O^1)$ = -0.37, and $\rho(O^3)$ = -0.10 indicate the formation of Mn(III)-$OO^{\cdot+}$ radical species, whereas the calculated spin density on Mn^2 of -2.98 is typical of Mn(IV) ion (S = 3/2). The elongation of Mn^1-O^1 bond distance (2.07 Å) clearly shows that the Jahn-Teller axis of the high-spin Mn^1(III) ion is along the Mn^1-O^1 direction. In order to gain a better understanding of the electronic structure of ^{1}**8**, the structure optimisation was repeated with the BLYP functional (0% HF). The optimised ^{1}**8** state with BLYP functional yields spin densities on Mn^1 of +2.64, O^1 of 0.02 and O^3 of 0.00 confirming the presence of Mn(IV) ion (S = 3/2), and the calculated $\langle S^2\rangle$ = 3.09 approaches its ideal value (3.00) (Figure 3.40b). As a result, calculated Mn^1-O^1 bond distance decreased to 1.87 Å. Therefore, the electronic structure of the

hydroperoxo intermediate **(8)** appears to depend critically on the identity of the chosen density functional, in particular the amount of HF exchange.

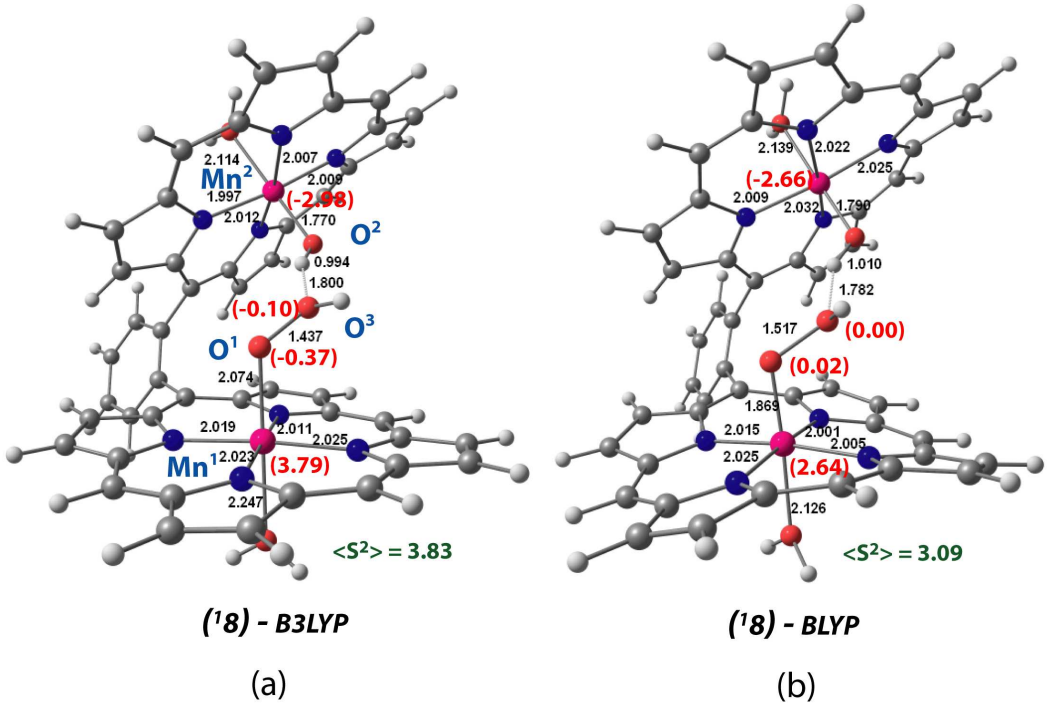

Figure 3.40 Optimised structures of open-shell singlet state of hydroperoxo species **(^{1}8)** with (a) B3LYP (20% HF) and (b) BLYP (0% HF) functionals. Calculated spin densities are in red.

Starting from the stable singlet state of the hydroperoxo species **(^{1}8)**, the next step is a single electron and proton transfer ($1e^-/H^+$) to the Mn^2 site. After accepting an electron, the Mn^2 centre of the resulting complex **(9)** becomes Mn(III) and $^3O_2$ is generated (Figure 3.41).

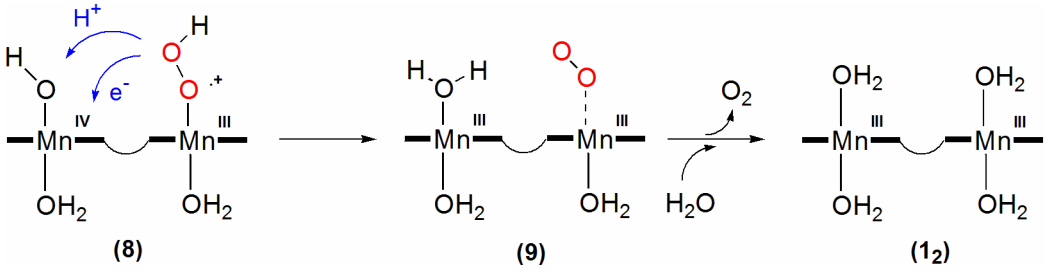

Figure 3.41 Oxygen evolution: attack of the H_2O-Mn(V)O groups on a molecule of water.

The calculated singlet state of this system **(^{1}9)** has spin densities on Mn^1 of +3.95 and Mn^2 of -3.99 indicating the high-spin Mn(III) (S = 2) nature at the both metal cores, and this system is formed through **^{1}TS$_3$**. The corresponding triplet state **(^{3}9)** is further 8.4 kcal mol^{-1} lower in energy (Figure 3.42), where the net spin densities on O^2 of +0.90 and on O^3 of +1.05 confirm the formation of molecular oxygen in its triplet ground state ($^3O_2$), and this state is formed due to spin-crossover from singlet to triplet. As the final step, association of a water molecule to the Mn^1 releases molecular oxygen, and the product [**^{1}1$_2$** + $^3O_2$] is a further 16.0 kcal mol^{-1} lower than **^{3}6**.

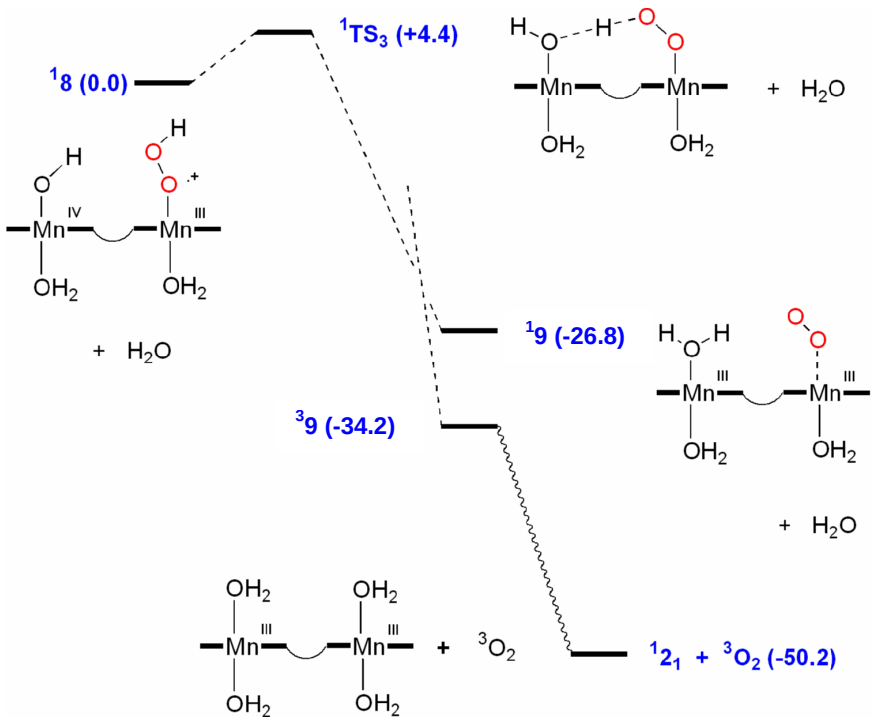

Figure 3.42 Potential energy surfaces for the O_2 formation mechanism through the two-step mechanism.

The overall picture of the two-step mechanism is a four electron and two proton ($4e^-/2H^+$) transfer process [proton coupled electron transfer (PCET)], and there are two important discontinuity regions involved in the O-O bond formation. The overall barrier for the O_2 formation is about 6.8 kcal mol^{-1}, which is lower than the 'direct' mechanism (9.6 kcal mol^{-1}).

3.4.1.5 Conclusions

In summary, our DFT calculations proposed that there are two energetically significant mechanisms, namely the direct mechanism and the two-step mechanism, for oxygen evolution by the Naruta system. The potential energy profiles that connect the key stationery points of the direct (blue) and the two-step (red) mechanisms are summarised in Figure 3.43.

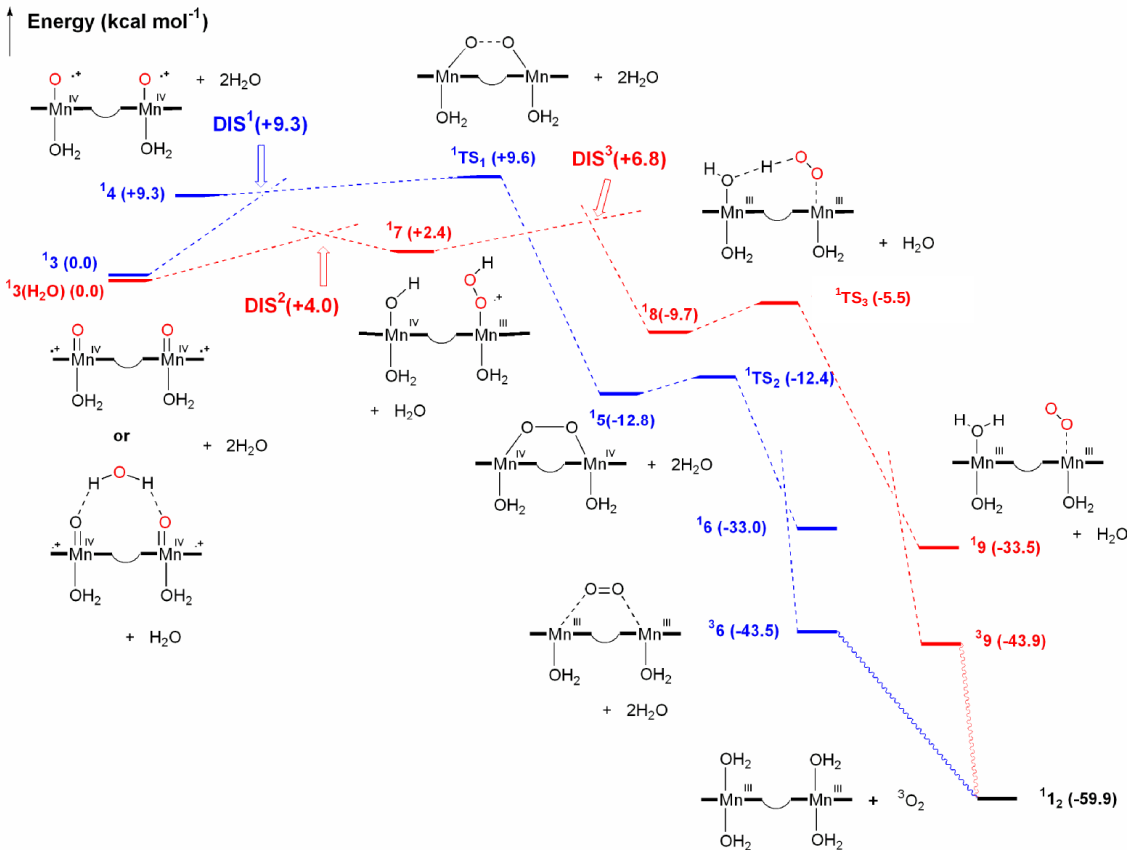

Figure 3.43 Summary of the overall potential energy surfaces for oxygen evolution *via* the both 'direct' (blue) and 'two-step' (red) mechanisms.

The key intermediate ^{1}**3** or ^{1}**3(H$_2$O)** of the proposed reaction pathway has significant porphyrin radical character, and is not reactive for O-O bond formation. Metal-oxyl radical character can be 'unmasked' *via* transfer of an electron from oxide to the vacancy in the porphyrin ring, and opening up a route for electron transfer from the substrate to the oxide, the so-called discontinuity region of porphyrin radical and oxyl

radical surfaces. The O-O bond formation reaction profiles of the Naruta system critically depend on the discontinuity regions of the two singlet potential energy surfaces. For the direct mechanism, the discontinuity region **(DIS^1)** is about 9.3 kcal mol^{-1} above the entry channel **(^{1}3)** and overall barrier for the O-O bond formation is about 9.6 kcal mol^{-1}. In the case of the two-step mechanism, two discontinuity regions exist. The first of these, **(DIS^2)**, is about 4 kcal mol^{-1} above the reactant complex (the O-O bond formation) and the second discontinuity region, **(DIS^3)**, is further 2.8 kcal mol^{-1} higher in energy (O-H bond formation), which is the rate limiting for the two-step mechanism. Therefore, our DFT calculations suggest that the more realistic mechanism for the oxygen evolution of the Naruta system is the two-step mechanism. Further, incorporation of a solvent water molecule is a fundamental chemical step in the two-step mechanism, and therefore this proposal represents a classical biomimetic water oxidation reaction.

3.4.2 Oxygen evolving $[Mn(II)_2(mcbpen)_2(H_2O)_2]^{2+}$ complex

The $[Mn(II)_2(mcbpen)_2(H_2O)_2](ClO_4)_2$ complex developed by McKenzie and co-workers is a well-known biomimetic water oxidation catalyst.[225,226] This system is known to perform water oxidation in the presence of an external oxidant such as *tert*-butylhydroperoxide (TBHP) or cerium nitrate. Membrane inlet mass spectrometry (MIMS) has been used to measure the evolved O_2 concentration in solution, and labelling experiments have revealed that one oxygen atom in the evolved dioxygen comes from water, whereas the second oxygen atom is derived from the oxidant. The proposed mechanism for the water oxidation has been discussed in section 3.1.3.2. The intermediates of the proposed mechanism (Figure 3.44) have been characterised by using electron spin resonance (ESR), UV/Visible, electrospray ionisation-mass spectroscopy (ESI-MS) and electrochemical methods.[225,226] We used DFT to explore possible mechanisms for the catalytic water oxidation reported by McKenzie and co-workers using the available experimental evidence to provide a framework.

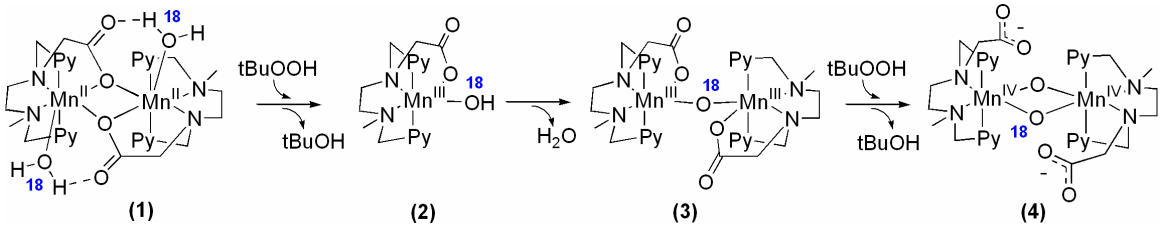

Figure 3.44 The first four intermediates of the proposed reaction mechanism.

The mechanistic hypothesis put forward by McKenzie was based on the premise that the species observed in the ESI-MS spectra are strong candidates in the proposed catalytic cycle, specifically **1**, **2**, **3** and **4** (Figure 3.44). However, it is important to note that the ESI-MS experiment is a gas-phase measurement, while the water oxidation reaction occurs in aqueous solution, although the former may offer important clues to stable species, the participation of these in the reaction chemistry is not certain. Even more fundamentally, the ESI-MS experiment provides the empirical formula of the species present, but no information on structure. Therefore, although the structures shown in Figure 3.44 seem chemically reasonable, it is possible that alternatives isomers with the same formula may exist.

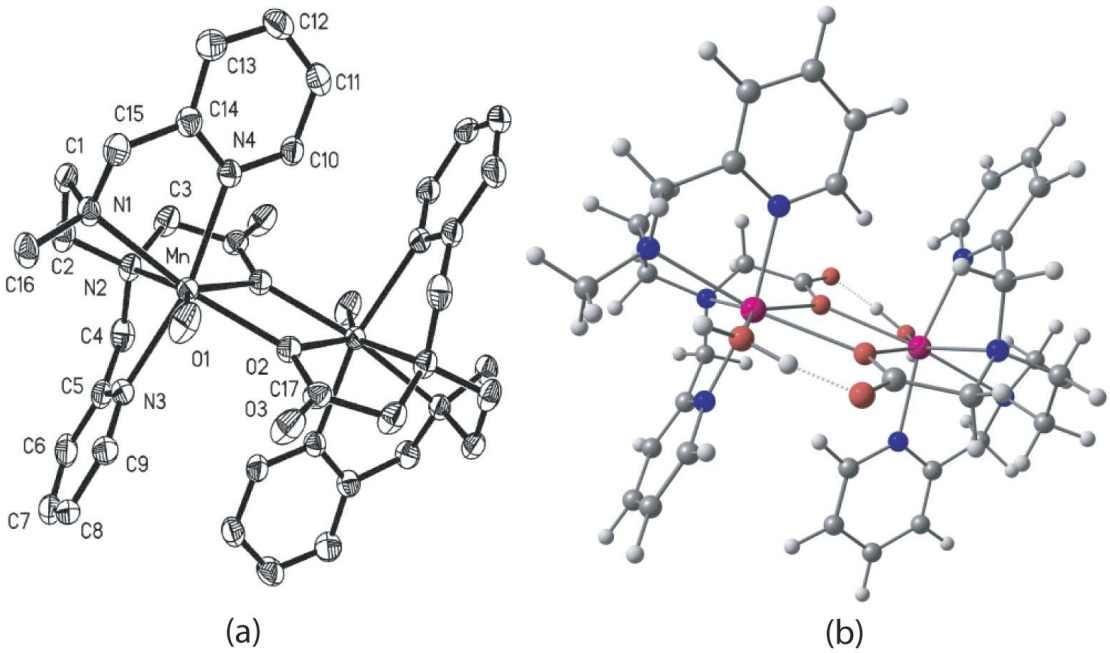

Figure 3.45 (a) Crystal structure of $[Mn(II)_2(mcbpen)_2(H_2O)_2](ClO_4)_2$ **(1)** and (b) optimised open-shell singlet state (**^{1}1)** structure of $[Mn(II)_2(mcbpen)_2(H_2O)_2]^{2+}$.

As a starting point to this investigation, we examined the electronic structures of species **1**, **2**, **3** and **4** in the cycle proposed by McKenzie. Of these, the identity of **1**, the starting compound, is certain as it has been characterised crystallographically (Figure 3.45a), but **2**, **3** and **4** are proposed on the basis of ESI-MS evidence, and therefore their structures are uncertain. We show here that **2** and **3** correspond to stable gas-phase minima, but **4** does not, and we propose alternative formulations for this species. With this information in hand, we then considered possible mechanisms for the water oxidation reaction in aqueous solution.

Table 3.5 The experimental and calculated structural parameters of the $[Mn(II)_2(mcbpen)_2(H_2O)_2]^{2+}$ complex **(1)**.

	Experimental (Å)	**Calculated (Å)**	
		^{1}**1**	^{11}**1**
Mn-Mn	4.0914(9)	4.10	4.11
Mn-O^{2}	2.2313(16)	2.31	2.31
	2.5908(16)	2.56	2.53
Mn-N^{1}	2.419(2)	2.51	2.50
Mn-N^{2}	2.329(2)	2.31	3.31
Mn-N^{3}	2.290(2)	2.28	2.28
Mn-N^{4}	2.246(2)	2.45	2.45

The reactant complex **(1)**, a crystallographically well-characterized $[Mn(II)_2(mcbpen)_2(H_2O)_2](ClO_4)_2$ species holds two seven-coordinate Mn(II) atoms with the carboxylate arms of the 'mcbpen' ligands bridging the metal centres through one of the oxygen atoms. Further, this air stable Mn(II) dimer complex contains non-coordinated carboxylate oxygen atoms, which are hydrogen-bonded to the water ligands on the adjacent Mn ions (Figure 3.45a). The optimised ground state (^{1}**1)** structure is depicted in Figure 3.45b, and calculated structural parameters are summarised in Table 3.5. The crystal structure and the calculated structure contain relatively long metal-ligand bond distances due to the presence of high-spin Mn(II) ions, d^5. Magnetic studies showed a decrease in magnetisation at low temperature, confirming that the exchange coupling interaction is weakly antiferromagnetic.[223,224] Consistent with this,

the ground state of the isolated $[Mn(II)_2(mcbpen)_2(H_2O)_2]^{2+}$ system is an open-shell spin singlet **(^{1}1)**, ($<S^2> = 5.0$) with the net spin densities on Mn ions, ρ(Mn) = -4.89 and +4.89 typical of two antiferromagnetically coupled high-spin Mn(II) ions. The corresponding high-spin state **^{11}1**, ($<S^2> = 30.0$), is structurally and energetically very similar to the singlet ground state, but the net spin densities on Mn ions, ρ(Mn) = +4.89 indicate ferromagnetic coupling.

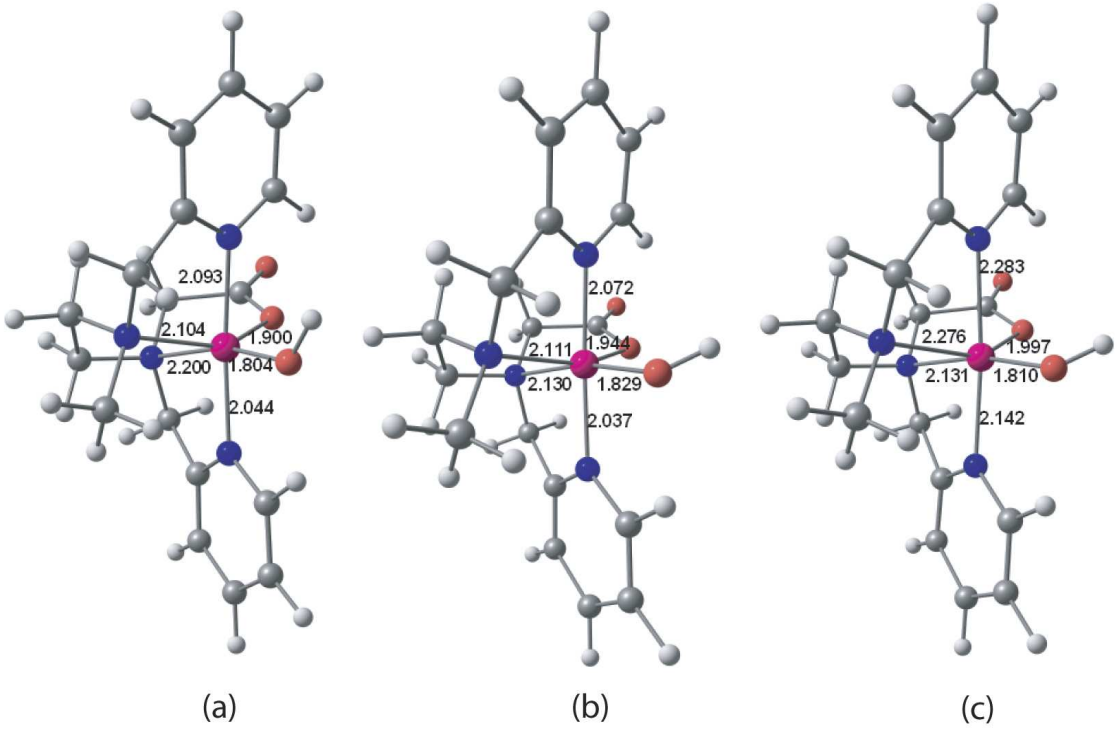

Figure 3.46 Optimised (a) singlet **(^{1}2)** (b) triplet **(^{3}2)** and (c) quintet **(^{5}2)** electronic states of $[Mn(III)(mcbpen)OH]^+$ complex **(2)**.

Oxidation of $[Mn(II)_2(mcbpen)_2(H_2O)_2](ClO_4)_2$ complex with *t*-butyl hydroperoxide (TBHP) gives rise to a mononuclear hydroxide species **2**, $[Mn(III)(mcbpen)OH]^+$, *via* cleaving the bridging carboxylate-O ligands of **1**. ESI-MS studies confirmed that the oxygen atom in **2** is derived from water but not from the oxidant, because the major ions generated with D_2O and $H_2{}^{18}O$ are, $[Mn(III)(mcbpen)OD]^+$ (m/z = 386.5) and $[Mn(III)(mcbpen)^{18}OH]^+$ (m/z = 387.3), respectively. Optimised structural parameters of the singlet, triplet and quintet electronic states of the $[Mn(III)(mcbpen)OH]^+$ are depicted in Figure 3.46 and Table 3.6 summarises calculated spin densities, $<S^2>$ values and relative energies of the key electronic states.

Table 3.6 Structural parameters (Å), spin densities, $<S^2>$ values and relative energies (kcal mol^{-1}) for the optimised structures of $[Mn(III)(mcbpen)OH]^+$ monomer **(2)** and $[Mn(III)_2(mcbpen)_2(O)]^{2+}$ dimer **(3)**.

Multiplicity	ρ(Mn)	$< S^2 >$	Relative energy
$[Mn(III)(mcbpen)OH]^+$			
Singlet **(^{1}2)**	----	0	+26.7
Triplet **(^{3}2)**	1.98	2.01	+6.5
Quintet **(^{5}2)**	3.86	6.06	0.0
$[Mn(III)_2(mcbpen)_2(O)]^{2+}$			
Singlet **(^{1}3)**	-3.78 / 3.78	4.00	0.0
Nonet **(^{9}3)**	3.90 / 3.90	20.13	+4.5

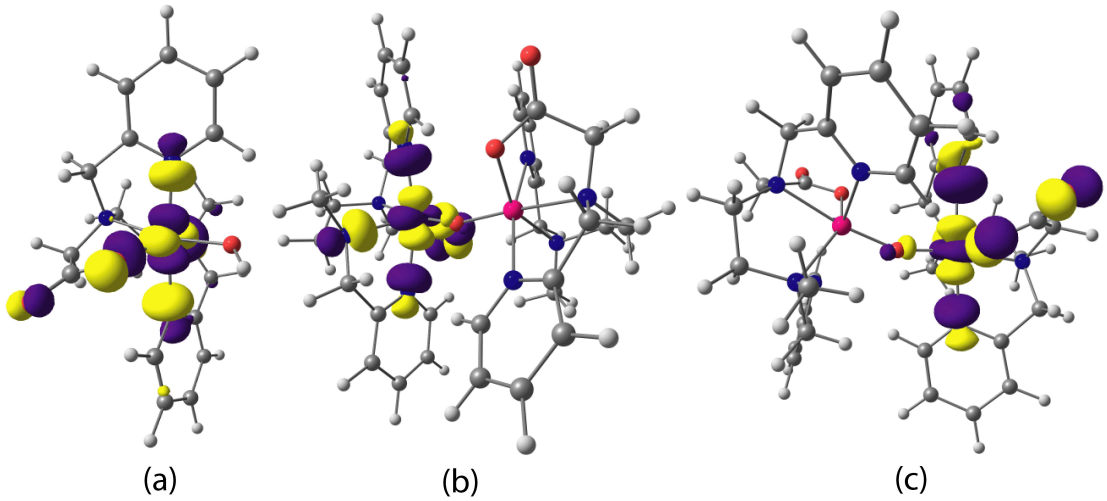

Figure 3.47 (a) Spin-α HOMO of the quintet state **(^{5}2)** of $[Mn(III)(mcbpen)OH]^+$, (b) spin-α HOMO and (c) spin-β LUMO of the singlet ground state **(^{1}3)** of $[Mn(III)_2(mcbpen)_2(O)]^{2+}$.

The calculated electronic states of the $[Mn(III)\text{-}(mcbpen)OH]^+$ system clearly show that the ground state is a quintet, **^{5}2**, with a net spin density on Mn ion, ρ(Mn) = +3.86, is essentially corresponds to the high-spin Mn(III) ion, which has a Jahn-Teller axis orthogonal to the carboxylate arm due to population of the Mn d_{z^2} orbital (α-HOMO) (Figure 3.47a). The corresponding triplet state **(^{3}2)** lies 6.5 kcal mol^{-1} above the quintet ground state, where the net spin density on Mn ion, ρ(Mn) = +1.98, indicates the

presence of low-spin Mn(III) ion. The closed-shell singlet electronic state, ^{1}**2**, is 26.7 kcal mol^{-1} above the quintet ground state.

The next possible step in the catalytic cycle is dehydration of [Mn(III)(mcbpen)OH]$^{+}$ to give a short-lived dinuclear mono-oxo bridged [Mn(III)$_2$(mcbpen)$_2$(O)]$^{2+}$ complex **(3),** which has been identified by using ESI-MS and UV/Visible spectroscopy.[223,224] Labelling experiments suggest that the bridging oxygen atom of this species is also derived from water.

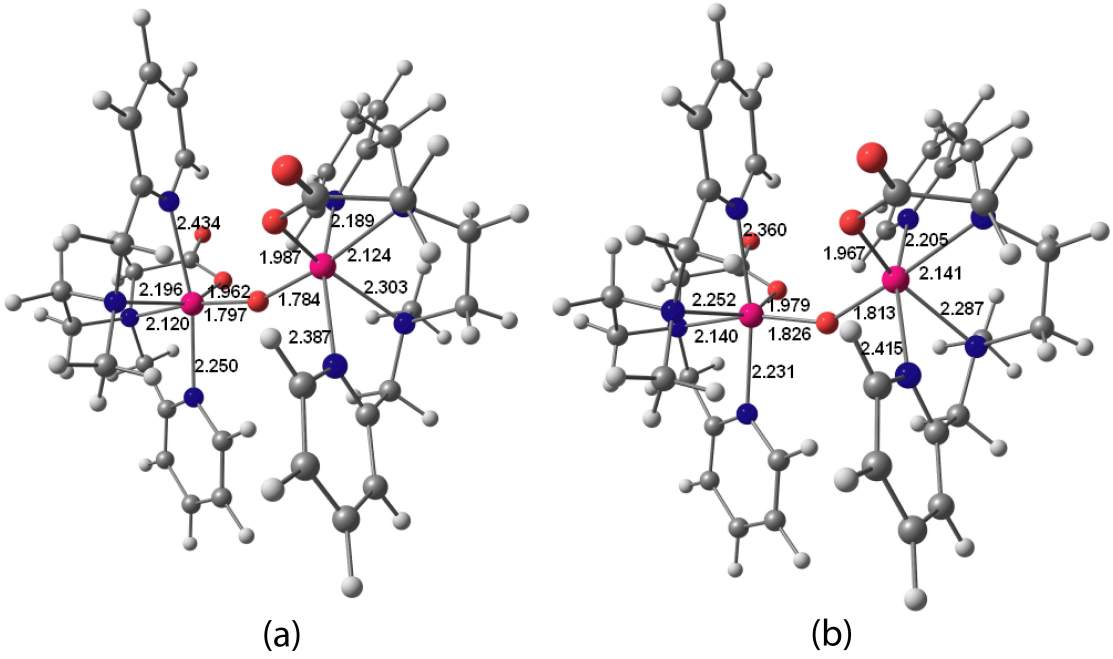

Figure 3.48 Optimised structures of (a) singlet **(**^{1}**3)** and (b) nonet **(**^{9}**3)** electronic states of [Mn(III)$_2$(mcbpen)$_2$(O)]$^{2+}$**(3)**.

For the dinuclear system **3** containing high-spin Mn(III) ions with S = 2 on the individual metal sites, and two distinct configurations, a broken-symmetry singlet and a nonet, are possible (Figure 3.48). In the singlet ground state **(**^{1}**3),** the Mn(III) ions are antiferromagnetically coupled *via* the μ-oxo bridge, and the Jahn-Teller axis remains orthogonal to the carboxylate arm due to population of the d_{z^2} orbitals of both Mn ions (Figure 3.47b and 3.47c). The nonet state (**^{9}3**) with ferromagnetically coupled Mn(III) ions, lies only 4.5 kcal mol^{-1} above the singlet ground state. The computational data presented thus far on species **2** and **3** are therefore fully consistent with the structural

assignments proposed by McKenzie, and both correspond to stable minima on the gas-phase potential energy surface.

3.4.2.1 What is the structure of 4?

According to the proposed catalytic cycle, the next step is oxidation of **3** with TBHP, giving rise to a dimeric $[Mn(IV)_2(O)_2(mcbpen)_2]^{2+}$ complex **(4)** with two 'dangling' carboxylate arms (Figure 3.49). This species was identified in solution of **1-$(ClO_4)_2$** treated with TBHP in acetonitrile, and the basis for the proposed chemical structure of **4** was the ESI-MS evidences (*m*/*z* = 384.2). This diamond-core type complex has been proposed as the precursor for the oxygen evolution through spontaneous collapse of **4** followed by the release of dioxygen *via* a peroxo species **5** (Figure 3.49). However, the structure of **4** immediately raises suspicions, because the overall charge of +2, in combination with two 'dangling' anionic arms, implies a strongly zwitterionic structure with a Mn_2O_4 core carrying a +4 charge. Such a large charge separation is likely to be highly unstable in the gas phase.

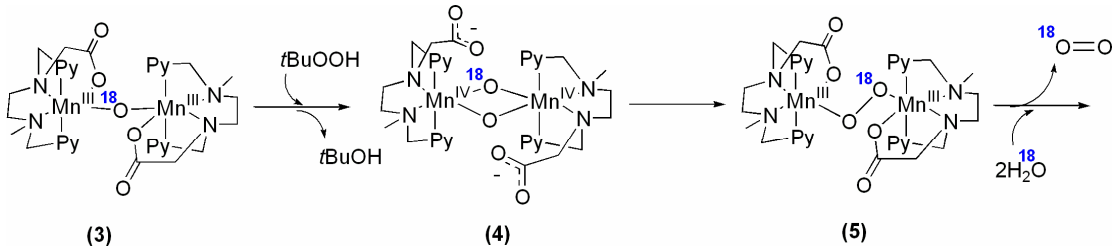

Figure 3.49 Final steps of the proposed reaction mechanism for the oxygen evolution proposed by McKenzie and co-workers.[223]

Magnetic coupling of two Mn(IV) ions in a Mn(IV)(μ-O)$_2$Mn(IV) diamond-core system, in principle, leads to S = 0 (antiferromagnetic) or S = 3 (ferromagnetic) states, with singly occupied non-bonding metal d_{xy}, metal-oxygen π^*_{xz} and π^*_{yz} orbitals. Despite several attempts, we have been unable to locate a minimum for the singlet state ^{1}**4** with the Mn(μ-O)$_2$Mn diamond-core. Instead, the structure converges to an

unsymmetric Mn(III)(μ-O)Mn(IV)-O$^{\cdot+}$ complex **(6)** (Figure 3.50a). The singlet ground state ^{1}**6** of this system has net spin densities on Mn^1 of -2.43 and on O^1 of -0.67 (Table 3.7) highly reminiscent of the Mn(IV)-O$^{\cdot+}$ species described in previous chapter. The net spin density of +3.87 on Mn^2 is characteristic of a Mn(III) ion. Significant spin density on **O**^{3} of -0.41 also indicates that charge transfer from the dangling carboxylate arm to the metal core has occurred (Figure 3.50b).

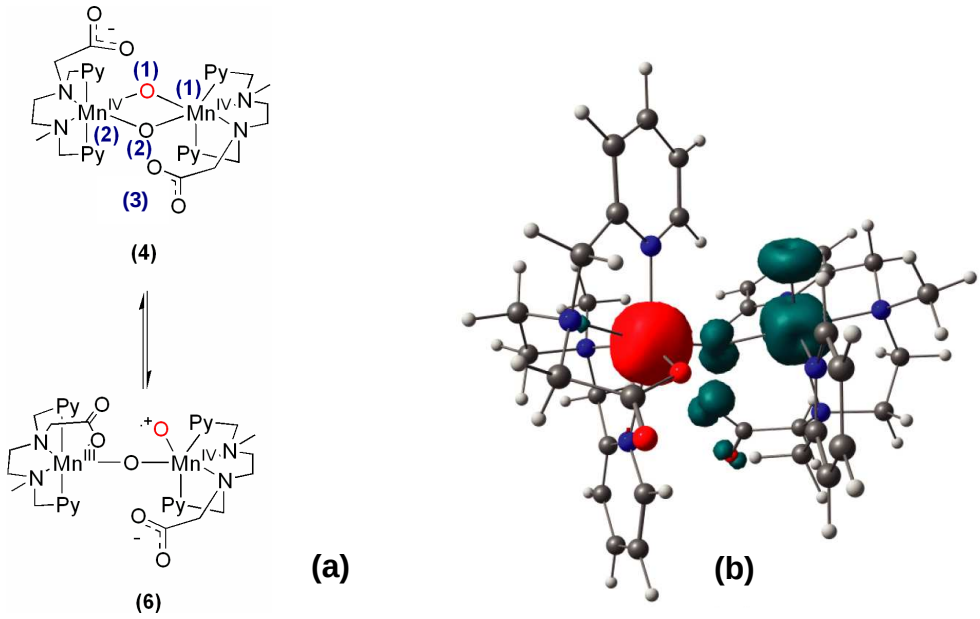

Figure 3.50 (a)'Unmasking' metal oxyl radical character of Mn(IV)-(μ-O)$_2$-Mn(IV) diamond-core **(4)** *via* disproportionation of a Mn-(μ-O) bond, and (b) total spin density plot for the singlet ground state **(**^{1}**6)**.

In light of the work described in the previous chapter, it seems likely that an oxyl radical species, if present in aqueous solution, would be a highly active oxidant towards water.[142-150,167-169] However, the ESI-MS signal corresponding to the empirical formula of **4** [and isomeric **6**] is observed in the gas-phase, where no solvent water is present. It seems rather unlikely that such a potent oxidising species would have a significant lifetime, particularly in the presence of an organic ligand such as mcpben. We have therefore considered alternative structures, isomeric to both **4** and **6**, which might arise from the latter through an intramolecular oxidation reaction. Various isomers for $[Mn_2C_{34}N_8H_{42}O_6]^{2+}$ are shown in Figure 3.51, while optimised structural parameters,

net spin densities, $<S^2>$ values and relative energies of the key electronic states of the possible isomers are summarised in Table 3.7.

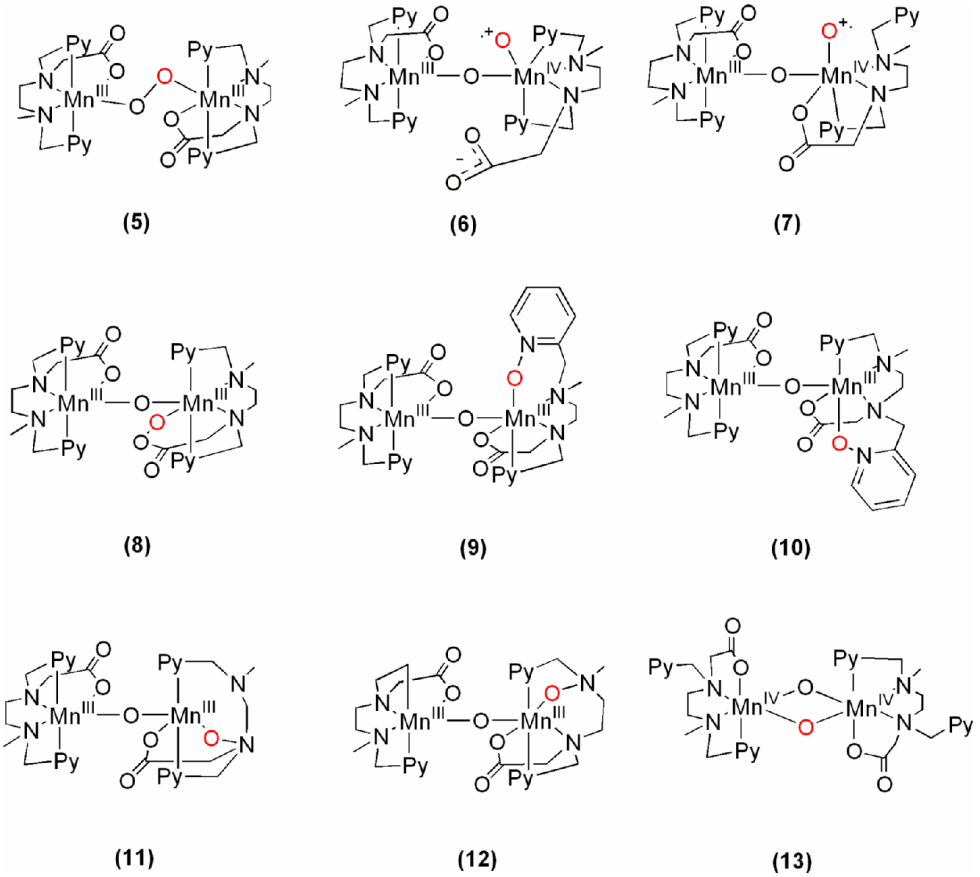

Figure 3.51 Possible isomeric forms for the proposed Mn(IV)-(μ-O)$_2$-Mn(IV) diamond-core **4**.

The first of these alternative structures, **7**, also has a Mn(III)-O-Mn(IV)-O$^{\cdot+}$ oxyl radical core, but in contrast to **6**, the pendant carboxyate arm is now coordinated to the Mn(IV) centre while one of the pyridyl arms has been detached. This alternative isomer relieves some of the unfavourable charge separation, and indeed the singlet ground state of **7** is some 10.7 kcal mol^{-1} lower in energy than **6**. The corresponding diamond-core structure, **13**, which differs from **4** in that two pyridyl arms, rather than anionic carboxylates, are detached, lies a further 7.5 kcal mol^{-1} lower in energy. However, the most stable isomers (a further 20 kcal mol^{-1} higher) correspond not to metal-oxo species (either terminal or bridged) but rather to N-oxides **9**, **10,** and **12** which could, in principle, be formed from oxyl species such as **6** or **7** by nucleophilic attack of the amine or pyridyl lone pair.

Table 3.7 Structural parameters (Å), spin densities, $<S^2>$ values and relative energies (kcal mol^{-1}) for the possible isomeric forms **6**-**14** of the $[Mn_2C_{34}N_8H_{42}O_6]^{2+}$.

Isomer	$r(Mn^1O^1)$	$r(Mn^2O^2)$	$r(Mn^1O^2)$	$r(Mn^1Mn^2)$	Spin densities				$< S^2 >$	Relative energy
					$\rho(Mn^1)$	$\rho(Mn^2)$	$\rho(O^1)$	$\rho(O^2)$		
^{1}**6**	1.68	1.83	1.87	3.51	-2.43	3.87	-0.67	-0.45	3.97	0.0
^{3}**6**	1.67	1.85	1.85	4.36	-2.49	3.87	-0.55	0.26	5.00	+4.1
^{7}**6**	1.67	1.84	1.89	3.49	2.51	3.91	0.58	-0.35	12.01	+1.2
^{9}**6**	1.67	1.87	1.87	3.48	2.48	3.95	0.62	0.40	20.11	+3.2
^{1}**7**	1.78	1.81	1.77	3.58	-2.59	3.83	-0.94	-0.39	3.93	-10.7
^{3}**7**	1.76	1.79	1.76	3.55	-2.73	3.80	0.91	-0.14	4.47	-4.4
^{7}**7**	1.80	1.83	1.80	3.57	2.99	3.88	-0.92	0.20	13.09	-3.6
^{9}**7**	1.79	1.91	1.78	3.67	2.65	3.92	0.94	0.57	20.00	-4.5
^{1}**8**	1.94	1.78	1.82	3.53	-3.85	3.76	0.02	0.02	4.02	-7.5
^{9}**8**	1.94	1.80	1.85	3.50	3.96	3.89	-0.05	0.09	20.13	-5.5
^{1}**9**	2.34	1.78	1.77	3.50	-3.77	3.78	-0.03	0.00	3.99	-40.0
^{9}**9**	2.22	1.80	1.81	3.49	3.89	3.91	0.03	0.09	20.12	-37.2
^{1}**10**	2.22	1.78	1.70	3.52	-3.76	3.76	-0.04	-0.01	3.99	-39.7
^{9}**10**	2.33	1.82	1.80	3.47	3.88	3.90	0.03	0.13	20.11	-36.5
^{1}**11**	1.89	1.79	1.79	3.55	-3.71	3.79	0.01	0.04	3.99	-17.9
^{9}**11**	1.89	1.83	1.81	3.54	3.80	3.90	-0.01	0.16	20.11	-14.5
^{1}**12**	1.98	1.77	1.81	3.44	-3.78	3.76	0.03	0.03	4.01	-37.7
^{9}**12**	1.98	1.79	1.84	3.41	3.88	3.89	0.03	0.04	20.12	-37.0
^{1}**13**	1.87	1.86	2.28	4.49	-3.98	3.96	0.09	0.07	4.18	-18.2
^{9}**13**	1.90	1.90	2.89	4.30	4.08	4.09	-0.17	-0.15	20.23	-25.5
^{1}**5**	1.86	1.86	1.82	2.23	-2.98	2.98	0.01	-0.01	3.12	-20.4
^{7}**5**	1.82	1.82	1.74	2.82	3.04	3.04	0.06	0.07	12.00	-17.6

Nucleophilic attack by a carboxylate ligand is also feasible, leading to peroxycarboxylate species such as **8**, although the weakness of the O-O bond renders these species rather less stable than their N-oxide counterparts. Finally, we have considered the bridging peroxide species, **5**, proposed by McKenzie and co-workers in their original cycle (Figure 3.49). Although more stable than either **6** and **7**, and this structure is considerably less stable than the pyridine-N-oxides. On the basis of these computed energies, we propose that the species responsible for the ESI-MS signal at m/z = 384.2 is not **4**, but rather a pyridine-N-oxide such as **9** or **10**. We noted above that all of the isomeric products shown in Figure 3.51 could, in principle, be derived from oxyl radical intermediates such as **6** or **7**. In the presence of solvent water,

intermolecular O-O bond formation could be competitive with these intramolecular oxidation, leading to water oxidation. This hypothesis requires that the oxyl radical species are present in sufficient concentration to allow the reaction to proceed at a reasonable rate. The oxyl radicals are in equilibrium with (amongst other species) the $Mn(IV)_2O_2$ diamond-core structures, which are well-known stable entities in manganese coordination chemistry, and are generally not noted for their oxidising character. Indeed none of the several hundred such species in the structural database have, to the best of our knowledge, been reported to oxidise water. This observation suggests that the mcpben ligand confers rather unusual activity on the metal core.

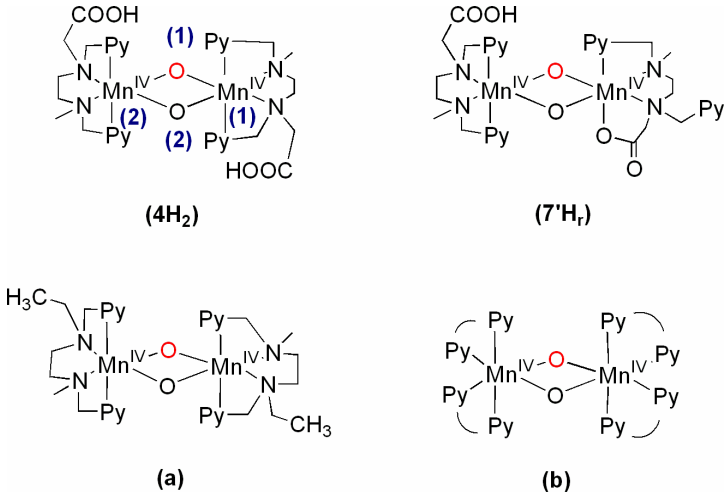

Figure 3.52 Molecular structure of the Mn(IV)(μ-O)$_2$Mn(IV) diamond-core complexes.

To explore this issue, we have compared the disproportionation of the diamond core structure **4H$_2$**, its modified 'open' counterpart **7'H$_r$** (where we protonate the 'dangling' carboxylate arm(s) of **4** and **7** to support convergence) with the corresponding two model ligands shown in Figure 3.52. The first of these models, **(a)**, simply has the two carboxylate arms of mcpben removed by $-CH_3$ while the second **(b)**, is a well-known bipyridine ligand that gives the well-known and stable complex $[(bpy)_2Mn(IV)(\mu\text{-}O)_2Mn(IV)(bpy)_2]^{4+}$, which is not active in water oxidation.

The ground state in each of the diamond Mn(IV)(μ-O)$_2$Mn(IV) core species hold antiferromagnetically coupled Mn(IV) ions. For the bipyridine ligand **(b)**, the corresponding open Mn(III)-O-Mn(IV)-O$^{\cdot+}$ structure (**^{1}b$_p$**) is 14.1 kcal mol^{-1} less stable,

while for the model **^{1}a** the separation is somewhat smaller at +7.5 kcal mol^{-1} respectively. For the full mcpben ligand systems **^{1}7'H** and **^{1}4H$_{2\text{-P}}$** are -4.9 and -5.4 kcal mol^{-1} below the diamond cores (Figure 3.53).

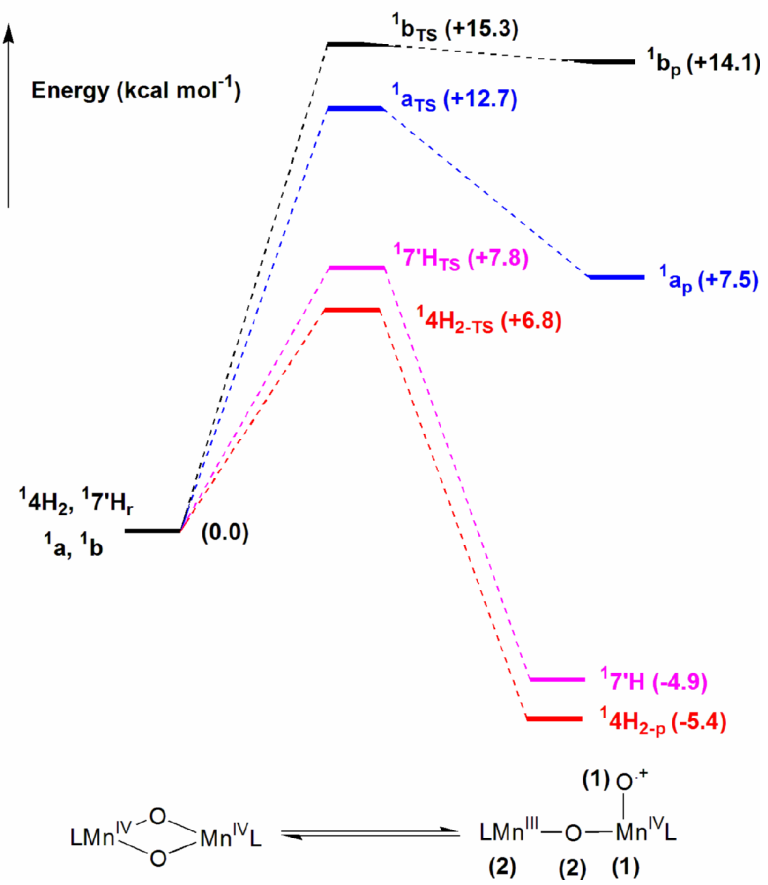

Figure 3.53 Singlet potential energy surfaces for disproportionation of the symmetric Mn(IV)$_2$(μ-O)$_2$ intermediates.

The origin of this difference lies in the presence of the fifth arm in the pentadente mcpben ligand, which can coordinate to the Mn(III) centre to compensate for the loss of one of the oxo ligands, retaining the octahedral geometry about the metal centre. In the model systems **(b)** and **(c)**, stabilisation of the Mn(III) centre is not possible, leading to the highly endothermic disproportionation. The transition states for the disproportionation reaction reflect the thermodynamics, with very 'late' transitions states for both model systems that resemble the products very closely, both structurally and energetically. The transition state for the mcpben ligand system is much earlier (reactant-like), and lies at much lower energy. Optimised structural parameters, net spin

densities, $<S^2>$ values and relative energies of the key stationary points for the singlet potential energy surface are depicted in Table 3.8.

Table 3.8 Optimised structural parameters, net spin densities, $<S^2>$ values and relative energies of the key stationary points.

	r(Mn^{1}O^1)	r(Mn^{2}O^2)	r(Mn^{1}O^2)	r(Mn^{1}Mn^2)	Spin densities				< S^2 >	Relative energy
					ρ(Mn^1)	ρ(Mn^2)	ρ(O^1)	ρ(O^2)		
^{1}**7'H$_r$**	1.91	1.84	1.91	2.87	-3.10	3.11	0.00	0.00	3.10	0.0
^{7}**7'H$_r$**	1.90	1.85	1.91	2.88	3.15	3.10	0.04	0.02	12.20	+3.1
^{1}**7'H$_{TS}$**	1.77	2.13	1.81	3.30	-2.65	3.90	-0.70	-0.50	3.99	+7.8
^{1}**7'H**	1.79	1.81	1.83	3.56	-2.70	3.89	-0.94	-0.30	3.98	-4.9
^{3}**7'H**	1.74	1.87	1.77	3.58	-2.84	3.79	0.83	-0.09	4.88	-3.2
^{1}**4H$_2$**	1.84	1.83	1.87	2.88	-3.11	3.09	0.00	0.00	3.16	0.0
^{7}**4H$_2$**	1.85	1.85	1.88	2.88	3.16	3.18	0.08	0.08	12.23	+2.7
^{1}**4H$_{2\text{-}TS}$**	1.78	2.10	1.83	3.31	-2.67	4.08	-0.72	-0.58	3.99	+6.8
^{1}**4H$_{2\text{-}p}$**	1.75	1.88	1.82	3.54	-2.61	3.97	-0.96	-0.48	4.00	-5.4
^{3}**4H$_{2\text{-}p}$**	1.74	1.87	1.77	3.58	-2.80	3.91	0.84	-0.16	4.87	-3.4
^{1}**a**	1.86	1.86	1.86	2.87	-3.10	3.09	-0.01	-0.01	3.15	0.0
^{7}**a**	1.88	1.87	1.87	2.89	3.17	3.16	0.08	0.08	12.23	+2.4
^{1}**a$_{TS}$**	1.80	1.93	1.82	3.40	-2.76	4.01	-0.88	-0.45	4.02	+12.7
^{1}**a$_p$**	1.78	1.87	1.82	3.62	-2.65	3.93	-1.00	-0.37	3.99	+7.5
^{3}**a$_p$**	1.74	1.86	1.80	3.52	-2.82	3.90	0.79	-0.10	4.82	+5.9
^{1}**b**	1.84	1.84	1.84	2.84	-2.94	2.94	0.00	0.00	3.06	0.0
^{7}**b**	2.06	2.06	2.06	3.82	3.14	3.14	-0.06	-0.06	12.22	+8.8
^{1}**b$_{TS}$**	1.71	1.89	1.81	3.41	-2.60	3.90	-0.95	-0.41	3.97	+15.3
^{1}**b$_p$**	1.78	1.86	1.80	3.59	-2.55	3.85	-1.03	-0.34	3.95	+14.1
^{3}**b$_p$**	1.77	1.84	1.78	3.55	-2.76	3.82	0.87	-0.10	4.88	+15.6

In summary, the coordinative flexibility of the pentadentate *mcbpen* ligand appears to play a key role in this case, where the carboxylate arm of the resultant complexes **^{1}7'H** and **^{1}4H$_{2\text{-}p}$** provides a flexible donor to the Mn^2(III) ion, stabilising the octahedral environment which ultimately lowers the barrier for the disproportionation process. The result is that the open Mn(IV)-oxyl radical form is much more accessible in the mcpben system than in 'standard' $Mn(IV)_2O_2$ diamond cores with tetradentate ligands. The

'carboxylate shift' is a common feature in a variety of coordination modes offered by carboxylate ligands in metal carboxylate proteins in general, where the carboxylate shifts allows for a change in coordination geometry and coordination number.[354-356] It may therefore be important for increasing the accessibility of different redox states (e.g. opening coordination sites for dioxygen binding), which may also play a role in electron transfer events. Based on the analysis of the gas-phase ESI-MS data discussed above, we believe that the species corresponding to structure **4** in the original cycle proposed by Mckenzie and co-workers is in fact a pyridine-N-oxide, formed by intramolecular attack of a pyridyl nitrogen on a transient oxyl radical species such as **6** or **7**. We now turn to the reaction chemistry in aqueous solution, where the key difference is that oxidation of solvent water may compete with the intramolecular processes described above, leading to oxygen evolution.

3.4.2.2 Possible structure of reactive intermediates in aqueous solution

Our gas-phase calculations, guided by ESI-MS data, have identified oxyl radical species such as **6** or **7** as likely intermediates in the process. However, the O_2 evolution was observed not in the gas-phase but rather in aqueous solution at pH 4.75.[223,224] under such conditions, protonation of the carboxylate arms of the mcpben ligand is possible. In this section we consider the electronic structure of the protonated forms of isomers of ^{1}**6** and ^{1}**7**, and compute their p*Ka* values[357-359] (see Appendix A) to establish which are likely to dominate under the given experimental conditions. Calculated structural parameters (Å), spin densities, $<S^2>$ values and relative energies (kcal mol^{-1}) for the possible redox species are depicted in Table 3.9. The electron density distributions of singly protonated **6H** and doubly protonated **6H$_2$** are rather similar to those of isomer **6**, which also contains a Mn(III)-(μ-O)-Mn(IV)-O$^{\cdot+}$ core (Table 3.9). Our DFT calculations confirmed that the ground state of **6, 6H** and **6H$_2$** are all open-shell singlet electronic state. Therefore, we considered the singlet ground state of these systems for our p*Ka* analysis.

Table 3.9 Calculated structural parameters (Å), spin densities, $<S^2>$ values and relative energies (kcal mol^{-1}) for the possible redox species of **6** and **7**.

	r(Mn^1O^1)	r(Mn^2O^2)	r(Mn^1O^2)	r(Mn^1Mn^2)	Spin densities				$< S^2 >$	Relative energy
					ρ(Mn^1)	ρ(Mn^2)	ρ(O^1)	ρ(O^2)		
^{1}**6H**	1.74	1.94	1.80	3.58	-2.50	3.97	-0.95	-0.59	4.03	0.0
^{3}**6H**	1.72	1.95	1.74	3.49	-2.60	3.95	0.76	-0.27	4.80	+0.3
^{7}**6H**	1.71	1.99	1.74	3.50	2.67	3.99	-0.71	0.27	12.83	+2.3
^{9}**6H**	1.73	2.21	1.79	3.84	2.50	3.94	0.91	0.76	20.12	+9.6
^{1}**7H**	1.77	1.86	1.75	3.61	-2.49	3.89	-0.93	-0.50	3.96	+0.2
^{1}**7'H**	1.79	1.81	1.83	3.56	-2.70	3.89	-0.94	-0.30	3.98	+9.4
^{1}**7''H**	1.78	1.83	1.80	3.59	-2.51	3.88	-0.93	-0.46	3.99	+9.1
^{1}**6H$_2$**	1.75	1.88	1.82	3.54	-2.61	3.97	-0.96	-0.48	4.00	0.0
^{3}**6H$_2$**	1.74	1.87	1.77	3.58	-2.80	3.91	0.84	-0.16	4.87	+0.5
^{7}**6H$_2$**	1.74	1.91	1.79	3.55	2.91	4.00	-0.82	0.21	12.96	+3.4
^{9}**6H$_2$**	1.76	1.97	1.82	3.70	2.66	4.00	0.95	0.58	20.13	+4.4

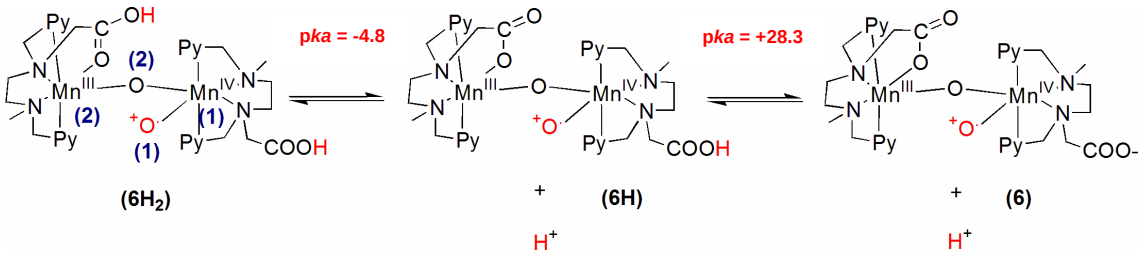

Figure 3.54 Possible redox species for the unsymmetric Mn(III)-(μ-O)-Mn(IV)-$O^{+\cdot}$ complex and calculated p*Ka* values.

The computed pK_a values (Figure 3.54) indicate that the dissociation of the first proton of **6H$_2$** is favourable (pK_a = -4.8), but dissociation of the second proton is not (pK_a = +28.3). Therefore, the most abundant redox species at pH of 4.75 will be the singly protonated Mn(III)-(μ-O)-Mn(IV)-$O^{\cdot+}$ complex **6H**. Total spin density distribution of stable singlet (**^{1}6H**) and triplet (**^{3}6H**) states are depicted in Figure 3.55, and both electronic configurations show marked oxyl radical character.

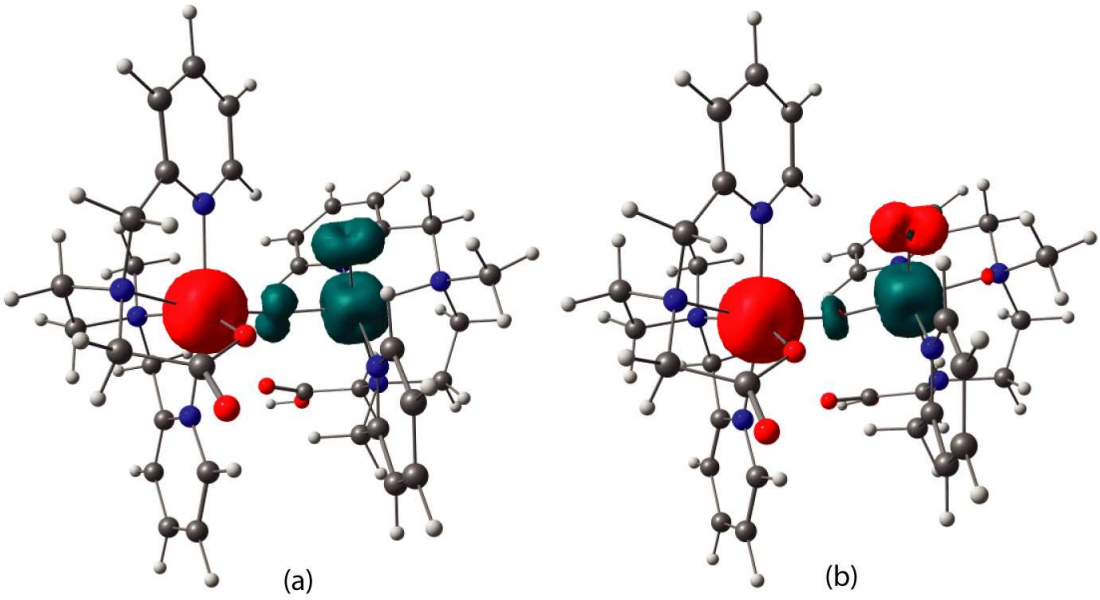

Figure 3.55 Total spin density distributions of the singlet (**^{1}6H**), and the triplet (**^{3}6H**) electronic states of the singly protonated Mn(III)-(μ-O)-Mn(IV)-$O^{+\cdot}$ system.

There are three isomers possible for the analogous singly protonated **7** (Figure 3.56). Calculated open-shell singlet states of these isomers **7H**, **7'H** and **7''H** confirmed the presence of active Mn(IV)-$O^{\cdot+}$ character (Table 3.9), where the most stable isomer is **7H**. Calculated *p*Ka values -1.99 of **7'H** and -2.28 of **7''H** indicated that the dissociation of the proton is favourable. However, **7H**, **7'H** and **7''H** isomers are relatively less stable than **6H**. We therefore use this **6H** as the precursor for our studies of the O-O bond formation pathway.

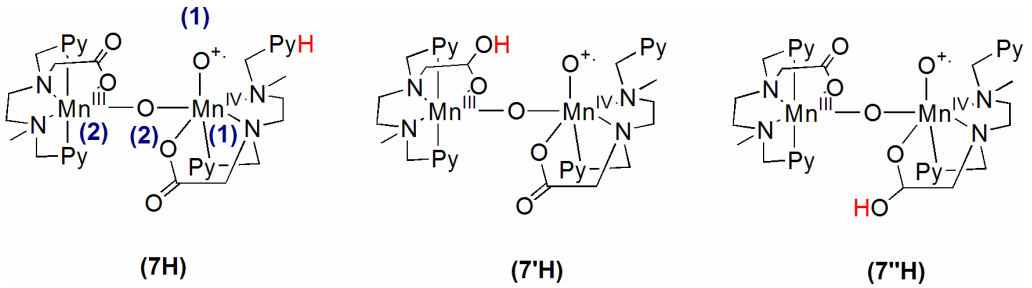

Figure 3.56 Possible isomers for the singly protonated **7**.

3.4.2.3 The O-O bond formation

The active intermediate **6H** has dominant metal-oxyl radical character [Mn(IV)-$O^{+\cdot}$], and therefore interaction with a molecule of H_2O may lead to O-O bond formation. During this process, the water molecule must lose a proton, and so the reaction will be accelerated by the presence of an internal base. In the context of **6H**, this base could be either the bridging oxygen or the carboxylate arm (Figure 3.57).

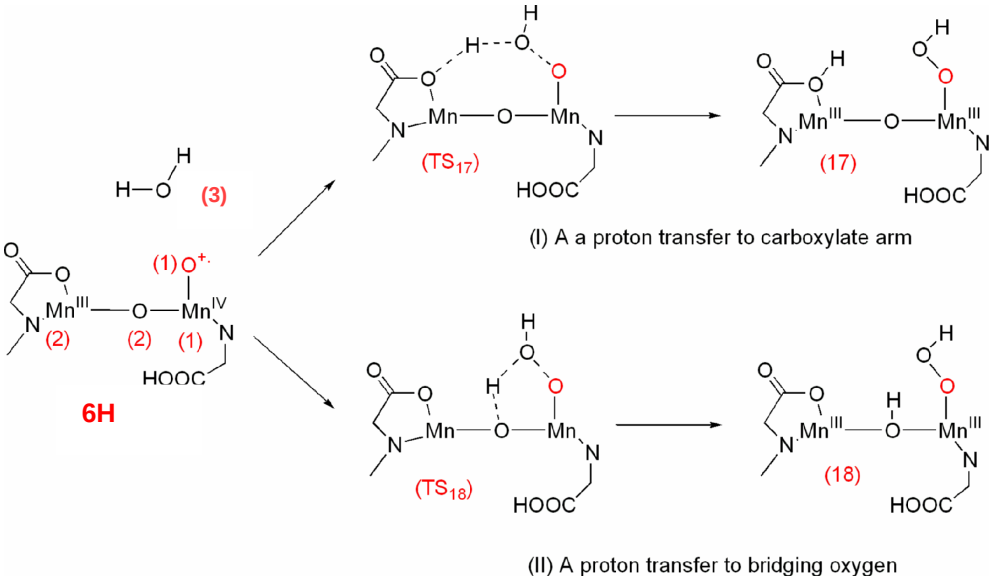

Figure 3.57 Possible O-O bond formation mechanisms involving proton transfer to either to the bridging oxygen or to the carboxylate arm.

In the following section we consider both possibilities, and compute the potential energy profiles for the O-O bond formation in the both cases. We focus on the most stable singlet and triplet electronic states in each case. The optimised structural parameters, net spin densities, $<S^2>$ values and relative energies of the key stationary points for the O-O bond formation mechanisms are summarised in Table 3.10. The addition of a water molecule to the outer coordination sphere at a fixed O^1-O^3 distance of 3.0 Å does not change the electronic structure of the active intermediate **(6H)**, and the open-shell singlet state is still the ground state for the resulting complex **6H(H_2O)**. The energy profiles for the most stable singlet and triplet potential energy surfaces are shown in Figure 3.58 (proton transfer to carboxylate arm in blue, to bridging O in red).

Table 3.10 The optimised structural parameters, net spin densities, $<S^2>$ values and relative energies of the key stationary points of the most stable single and triplet potential energy surfaces for the O-O bond formation step.

	Structural parameters				Mulliken Spin density					$<S^2>$	Relative energy
	$r(Mn^1O^1)$	$r(Mn^2O^2)$	$r(Mn^1O^2)$	$r(O^1O^3)$	$\rho(Mn^1)$	$\rho(Mn^2)$	$\rho(O^1)$	$\rho(O^2)$	$\rho(O^3)$		
^{1}**6H(H$_2$O)**	1.75	1.93	1.8	3.00	-2.50	3.97	-0.96	-0.56	0.00	4.02	0.0
^{3}**6H(H$_2$O)**	1.73	1.92	1.75	3.00	-2.65	3.93	0.80	-0.24	0.00	4.83	+1.1
^{1}**TS$_{17}$**	1.86	1.83	1.80	1.87	-3.27	3.85	-0.34	-0.09	-0.30	4.14	+16.1
^{3}**TS$_{17}$**	1.76	1.81	1.83	1.76	-2.20	3.84	0.01	0.01	0.24	4.21	+14.3
^{3}**TS$_{18}$**	1.70	2.30	1.94	1.87	-2.36	4.00	-0.24	0.01	0.53	4.58	+24.0
^{1}**17**	2.07	1.80	1.82	1.51	-3.83	3.80	0.09	0.06	0.04	4.02	+1.2
^{3}**17**	1.90	1.80	1.85	1.54	-1.96	3.80	0.01	0.04	0.03	3.99	+2.1
^{1}**18**	1.89	1.94	2.38	1.50	-3.96	3.94	0.00	0.01	-0.04	4.13	+3.4
^{3}**18**	1.86	2.23	1.99	1.52	-2.01	4.00	-0.06	0.04	0.00	4.11	+14.1

3.4.2.3.1 Proton migration to the carboxylate arm

This reaction starts at the singlet potential energy surface **^{1}6H(H$_2$O)**, and spin cross-over from singlet to triplet may occur at an early stage of the reaction. As a result, the O-O bond formation proceeds *via* **^{3}TS$_{17}$**, which is 14.3 kcal mol^{-1} above the entry channel of the singlet potential energy surface. The corresponding singlet transition state, **^{1}TS$_{17}$**, is further 1.8 kcal mol^{-1} higher in energy. Then the reaction undergoes a second spin cross-over between the **^{3}TS$_{17}$** and the product **^{1}17**, a Mn(III) hydroperoxide species. Spin-orbit coupling at the metal sites is likely to make both spin crossovers rather facile.[97-102] The fully optimised structure of **^{1}TS$_{17}$**, **^{3}TS$_{17}$**, **^{1}17**, and **^{3}17** are shown in Figure 3.59. The hydroperoxide product, **^{1}17,** has a high-spin Mn^1(III) ion (d^4) [$\rho(Mn^1) = -3.83$] with the Jahn-Teller axis aligned along the Mn^1-O^1 bond (2.07 Å). The second Mn site, Mn^2, has a high-spin d^4 configuration [$\rho(Mn^1) = +3.80$], in this case

with the Jahn-Teller axis along the weakly bound COOH ligand. The key triplet transition state, ^{3}**TS$_{17}$**, is rather product-like, with the proton almost entirely transferred to the carboxylate group (O-H = 1.05 Å) and a substantially formed O-O bond (1.76 Å).

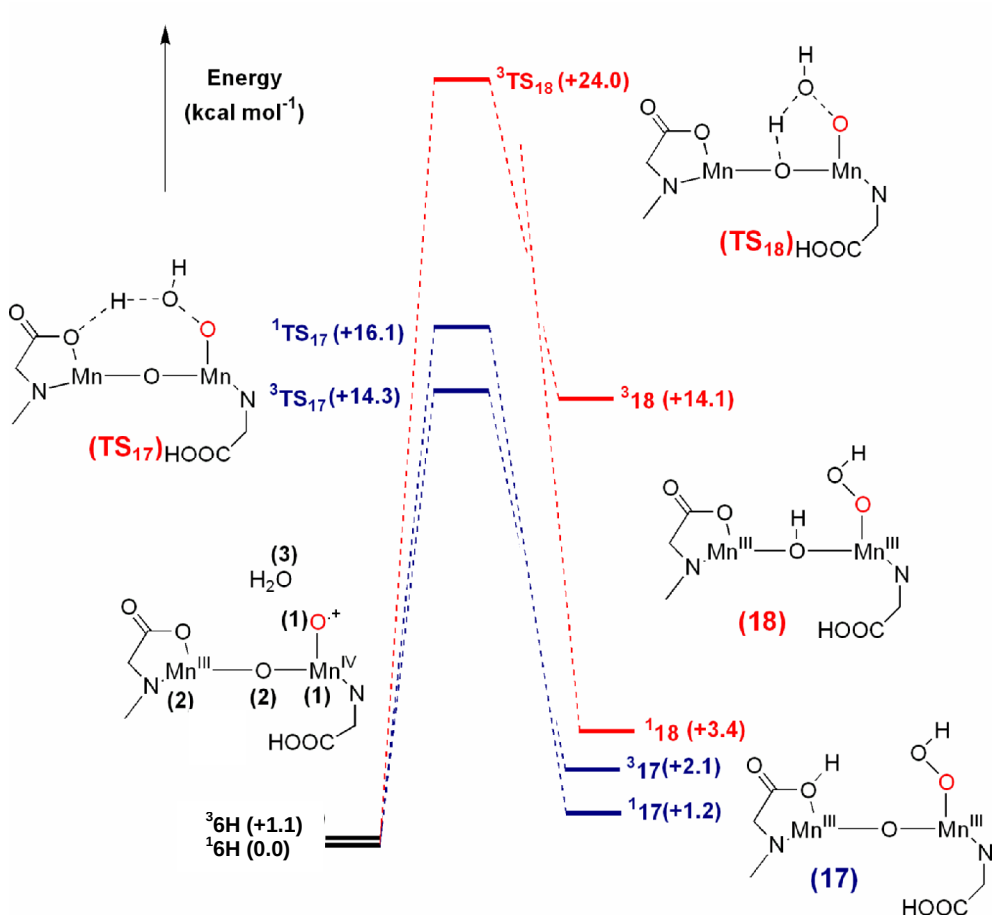

Figure 3.58 Potential energy profile for the O-O bond formation; a proton migration to the carboxylate arm (blue), and a proton migration to the bridging oxygen (red).

3.4.2.3.2 A proton migration to the bridging oxygen

The gross features of the potential energy surfaces are qualitatively similar to that of the proton migration to the bridging carboxylate case, with a low-lying triplet transition state necessitating spin crossover before reaching the hydroperoxide product (Figure 3.58).

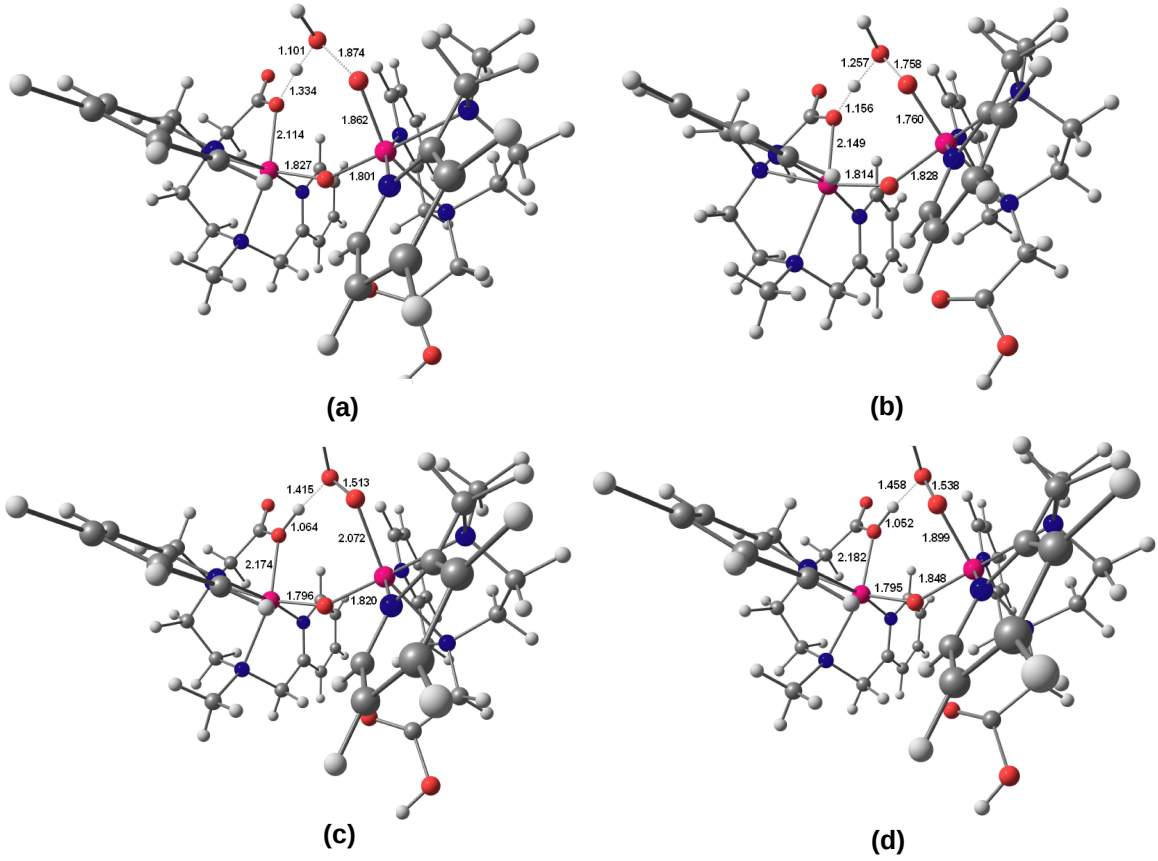

Figure 3.59 Fully optimised structures of (a) ^{1}**TS**$_{17}$, (b) ^{3}**TS**$_{17}$, (c) ^{1}**17**, and (d) ^{3}**17** for the O-O bond formation *via* a proton transfer to the carboxylate arm.

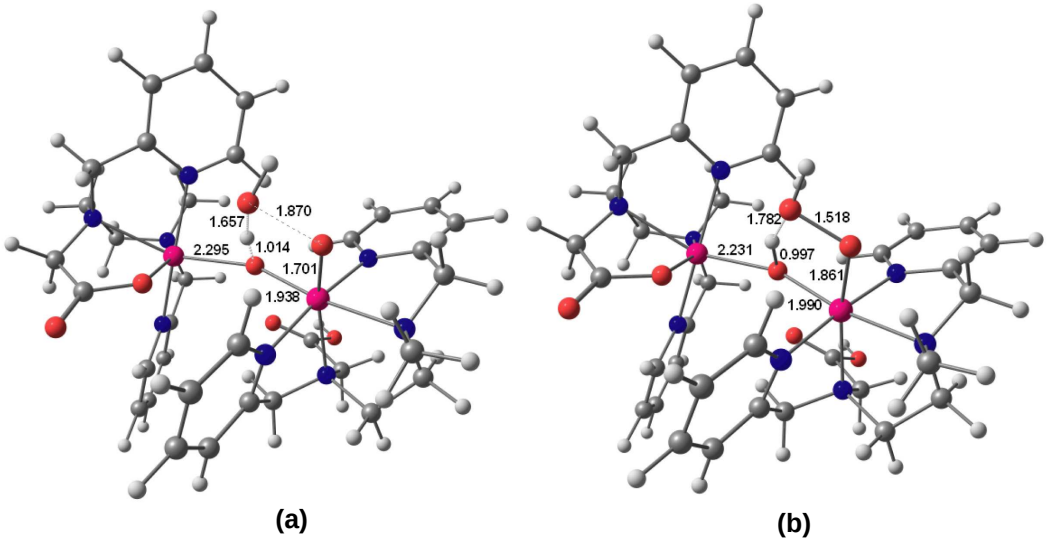

Figure 3.60 Fully optimised structures of (a) ^{3}**TS**$_{18}$ and (b) ^{1}**18** for the O-O bond formation *via* a proton transfer to the bridging oxide.

However, the product is less stable than the isomeric form with a protonated carboxylate ligand, and the corresponding transition state lies 24 kcal mol^{-1} above the entry channel. The relatively low stability of ^{1}**18** can be traced to the rather weak bridging afforded by the μ-OH ligand. In fact, protonation of the bridge causes the Jahn-Teller axis of one of the Mn centres to align along the μ-O bond rather than perpendicular to it (as is always the case for μ-O species), causing a substantial elongation of one of the Mn-O bonds (2.23 Å). The fully optimised structure of ^{3}**TS$_{18}$** and ^{1}**18** are shown in Figure 3.60.

In summary, the gross features of the O-O bond formation are rather similar in the two cases: both involve two electron transfer to the Mn^{1} site and a single proton transfer, either to the carboxylate arm or to the bridging oxide ($2e^{-}/H^{+}$). The barrier in the former case is 14.3 kcal mol^{-1} while in the latter it is over 24.0 kcal mol^{-1}, suggesting that the carboxylate ligands are more likely to act as an intramolecular base. The rather high barrier for protonation of the bridging oxides is similar to the work of Siegbahn on $[(terpy)(H_2O)Mn(IV)(\mu\text{-}O)_2Mn(III)(H_2O)(terpy)]^{3+}$ complex (23.4 kcal mol^{-1} for the triplet surface).[142-145] With a detailed description of the O-O bond formation step in hand, now we are in a position to describe the final oxygen evolution step.

3.4.2.4 Oxygen evolution

The final steps of the catalytic cycle are depicted in Figure 3.61. Starting from ^{1}**17**, a single electron can be transferred to a Mn^{2}(III) ion with concomitant transfer of the hydroperoxide proton to the bridging oxygen, and this $1e^{-}/1H^{+}$ transfer process gives rise to a superoxo intermediate **19**. Then a single electron transfer from OO^{-} to the Mn^{1}(III) ion leads to dissociation of O_2. This scheme is analogous to that proposed for the final stages of oxygen evolution in the diruthenium complex reported by Yang and Baik.[169] The optimised structural parameters, net spin densities, $<S^2>$ values and relative energies of the key stationary points of the potential energy surfaces (Figure 3.62) are

summarised in Table 3.11. This reaction starts at the singlet potential energy surface ^{1}**17**, and $1e^{-}/1H^{+}$ transfer yields to a peroxy species ^{1}**19** through ^{1}**TS$_{19}$**, which is 13.3 kcal mol^{-1} above the ^{1}**17**.

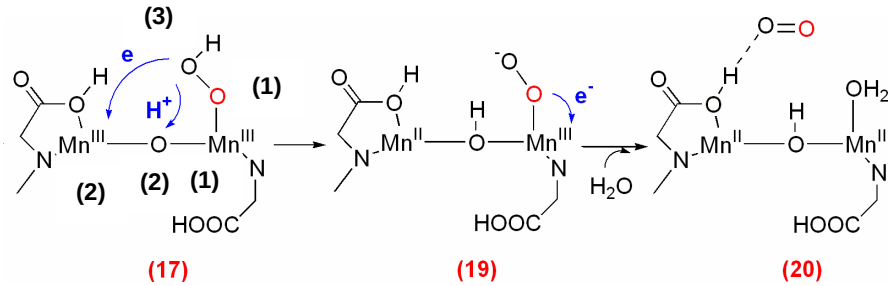

Figure 3.61 Proposed mechanism for the O_2 formation.

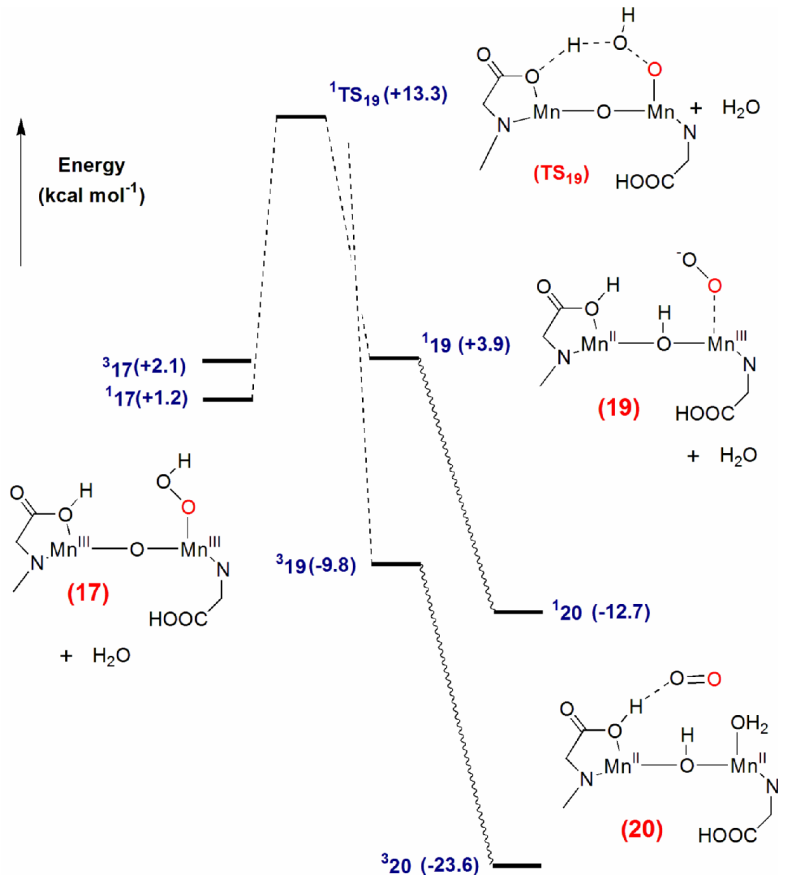

Table 3.62 Potential energy surfaces for the O_2 formation.

The optimised ^{1}**19** has net spin densities of +4.87 on Mn^{2} confirmed the formation of Mn(II) ion (d^{5}), and Mn^{1} ion is still Mn(III) [$\rho(Mn^{2})$ = -3.93]. The computed spin densities on O^{1} of -0.50 and O^{3} of -0.61 on ^{1}**19** imply super-oxo character. However, the

corresponding triplet state, ^{3}**19**, is 13.7 kcal mol^{-1} more stable than ^{1}**19**, and spin densities on O^1 of +0.67 and on O^3 of +0.79 of ^{3}**19** confirm the presence of one unpaired electron on the O_2^- unit, which is antiferromagnetically coupled to Mn^1 site.

Table 3.11 The optimised structural parameters, net spin densities, $<S^2>$ values of the key stationary points of the most stable single and triplet potential energy surfaces for the O_2 formation step.

	Structural parameters				Mulliken Spin density					$<S^2>$
	r(Mn^1O^1)	r(Mn^2O^2)	r(Mn^1O^2)	r(O^1O^3)	ρ(Mn^1)	ρ(Mn^2)	ρ(O^1)	ρ (O^2)	ρ(O^3)	
^{1}**TS$_{19}$**	1.96	1.78	2.31	1.44	-3.82	4.40	-0.33	-0.14	-0.14	4.45
^{1}**19**	2.15	2.27	1.89	1.38	-3.93	4.87	-0.50	0.00	-0.61	5.05
^{3}**19**	2.04	2.16	2.00	1.32	-4.42	4.89	0.67	0.00	0.79	6.40
^{1}**20**	5.77	2.07	2.16	1.26	-4.85	4.87	0.00	0.00	0.00	4.99
^{3}**20**	5.79	2.07	2.16	1.26	-4.85	4.87	0.93	0.00	1.07	7.00

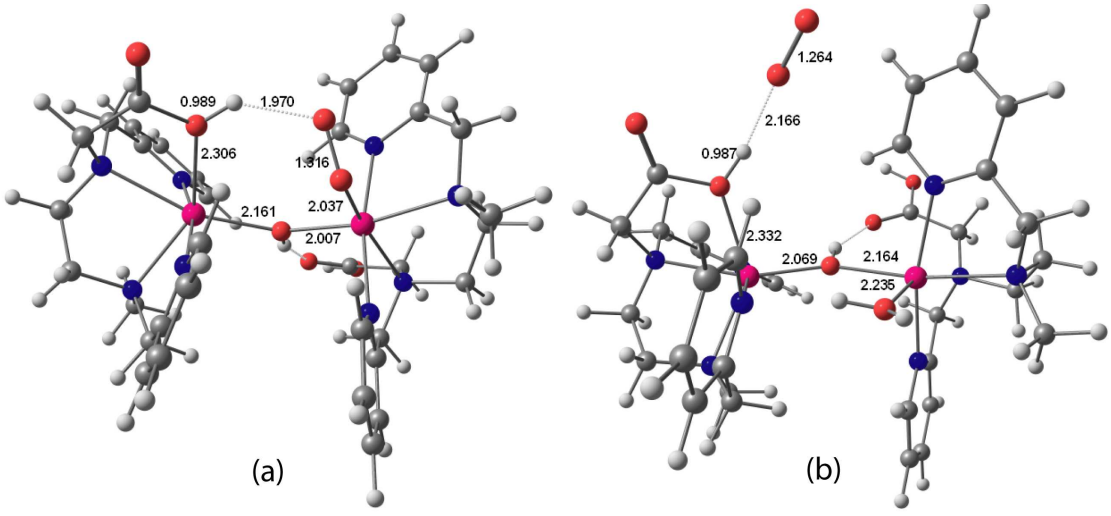

Figure 3.63 Fully optimised structure of (a) ^{3}**19** and (b) ^{3}**20**.

The O-O bond distance 1.38 Å of ^{1}**19** and 1.32 Å of ^{3}**19** are consistent with the experimental value for O_2^- (1.35 Å), and this ^{3}**19** system may form due to spin cross over from singlet to triplet. The calculated spin density on O^2 of 0.93 and O^3 of 1.07 in

^{3}**20** confirmed the formation of an oxygen molecule in its triplet state, and this species is 13.8 kcal mol^{-1} below ^{3}**19**. Optimised structures of ^{3}**19** and ^{3}**20** are shown in Figure 3.63. Finally, condensation of two water molecules and a single deprotonation may return the catalyst to its initial state **(1)** with association of two water molecules.

3.4.2.5 Conclusions

Our DFT calculations indicated that the species responsible for the ESI-MS signal at *m*/*z* = 384.2 (gas phase) is a pyridine-N-oxide **(9** or **10** or **12)**, which may be formed through the intramolecular attack of a pyridyl nitrogen on an oxyl radical species such as **6** or **7** (Figure 3.64), and not the proposed active intermediate **4** in the original cycle of Mckenzie and co-workers.

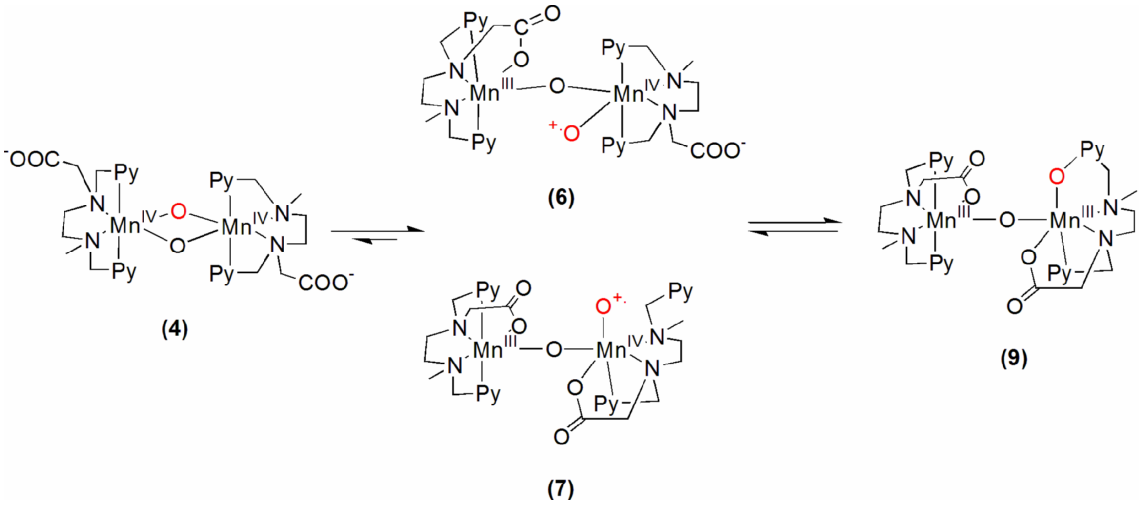

Figure 3.64 Key isomeric forms for the proposed diamond-core system **4**.

The water oxidation, however, occurs in aqueous solution, and thus oxidation of solvent water may compete with the above intramolecular processes, leading to oxygen evolution. This process may proceed *via* oxyl radical intermediates **6H** which are present in sufficient concentration to allow the reaction to proceed because the carboxylate arm of the mcpben ligand provides a flexible donor to the Mn(III) site and stabilises the asymmetric Mn(III)-(μ-O)-Mn(IV)-O$^{\cdot+}$ species. Then the active Mn(IV)-oxyl radical intermediate **(6H)** may react with a molecule of H_2O (solvent), leading to

O-O bond formation through two possible pathways; proton transfer either to the carboxylate arm (barrier of 14.3 kcal mol^{-1}) or to the bridging oxygen (barrier of 24.0 kcal mol^{-1}). The former pathway is more realistic for the O-O bond formation as it has a low barrier, and so the carboxylate arms of the mcbpen ligand have a secondary role as internal base (Figure 3.65).

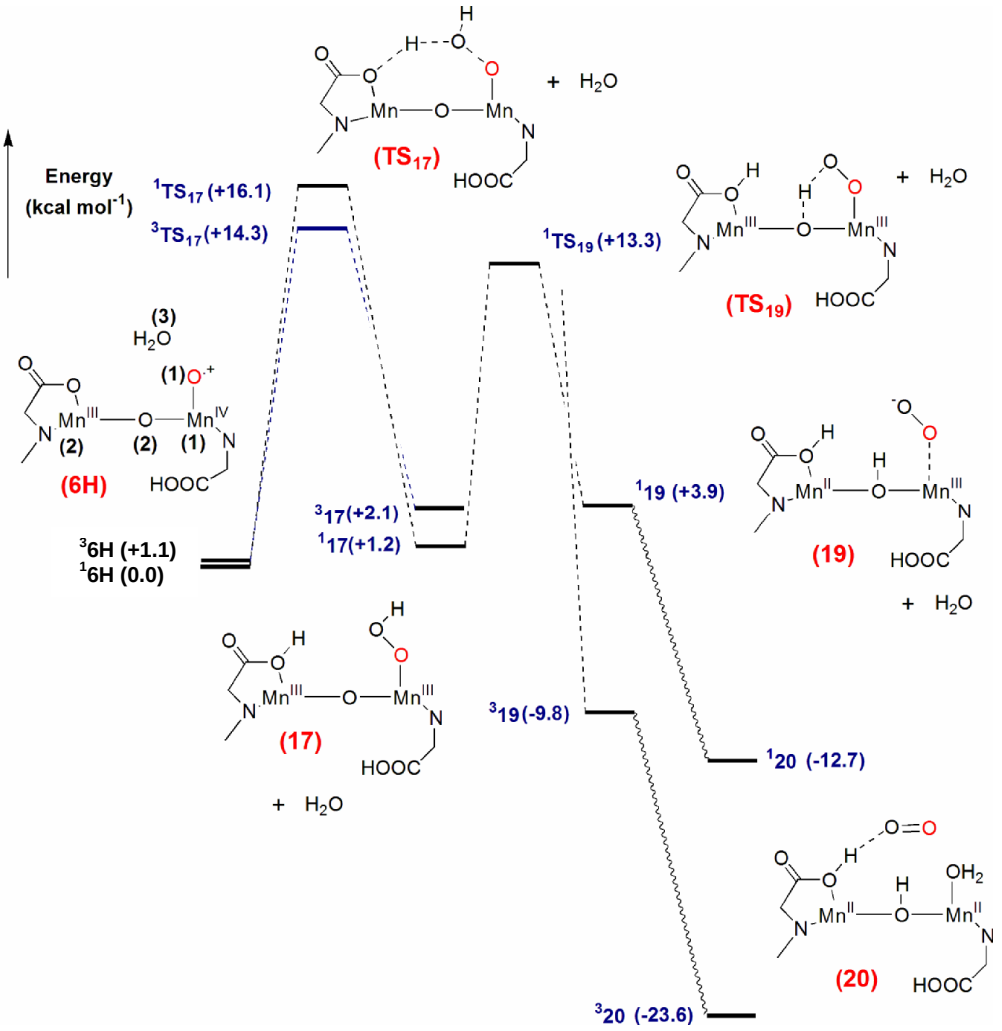

Figure 3.65 Proposed mechanism for the oxygen evolution based on our DFT calculations.

Starting from ^{1}**17**, the hydroperoxo intermediate, a single electron transfer and a proton transfer give rise to a superoxo intermediate ^{1}**19**, with a barrier of 13.3 kcal mol^{-1}. The overall barrier for the oxygen evolution is therefore defined by the first state, the O-O σ bond formation, with a barrier of 14.3 kcal mol^{-1}, which is the same order of magnitude as the model complexes for the OEC by Siegbahn (15.0 kcal mol^{-1}).[142-145] This barrier is relatively smaller than that of the Brudvig oxygen evolving Mn-dimer complex[142-145]

(23.4 kcal mol^{-1}), where the proton transfer occurs to the μ-O unit; in the case of the Mayer oxygen evolving Ru-dimer system[174], the barrier for the O-O bond formation is 26.9 kcal mol^{-1} (proton transfer to the Ru(V)=O unit).[169]

Chapter 4

Copper–Homoscorpionate Complexes as Active Catalysts for Atom Transfer Radical Addition to Olefins

4.1 Introduction

Generation of carbon-carbon bonds is a fundamentally important chemical step in organic synthesis. The Kharasch reaction, the addition of a polyhalogenated saturated hydrocarbon to an alkene, is an efficient way of carbon-carbon σ bond formation,[360-363] which is known to occur in the presence of a free radical precursor as the promoter or a transition metal complex as a catalyst (Figure 4.1).[364-367]

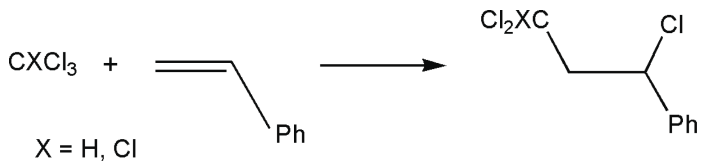

Figure 4.1 Addition of a polyhalogenated saturated hydrocarbon to an alkene substrate to form a 1:1 adduct.

For the metal-based catalysts, two types of mechanism have been proposed; atom transfer radical addition (ATRA) and atom transfer radical polymerisation (ATRP).[368-370] The ATRA targets the formation of 1:1 adducts of alkyl halides and alkenes catalysed by transition metal complexes. The key steps involved in the ATRA are depicted in Figure 4.2. The reaction proceeds *via* a metal induced homolytic cleavage of the carbon-halogen bond, which gives rise to a metal-halide complex and a carbon-centered radical. Then the latter species interacts with the olefin to form the second radical species, which induces the abstraction of halogen from the metal-halide complex. The metal catalyst therefore participates in both initiation and chain propagation steps. Over the past few decades, a number of metal-based synthetic catalysts have been proposed for the ATRA, including ruthenium-, nickel- and copper-based systems.[371-375]

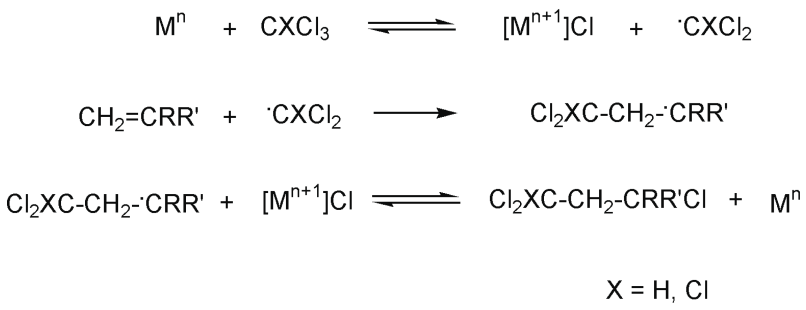

Figure 4.2 Key steps involved in the atom transfer radical addition (ATRA) of a polyhalogenated saturated hydrocarbon to an alkene.

Tp^x	R^1	R^2	R^3
Tp*	Me	H	Me
$Tp^{tBu, Me}$	Me	H	tBu
$Tp^{Cy,Br}$	H	Br	C_6H_{11}
Tp^{Br3}	Br	Br	Br
Tp^{Ms}	H	H	$C_6H_2Me_3$

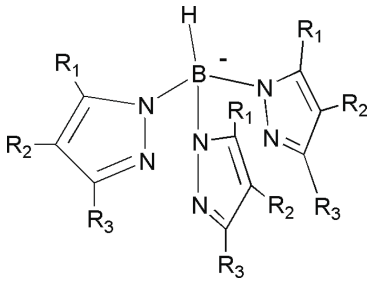

Figure 4.3 Homoscorpionate ligands (Tp^x).

In the present study, we focused on the role of the polypyrazolylborate-copper family of complexes (Tp^xCu) in ATRA reactions (Kharasch addition),[376] where the availability of a number of Tp^x ligands offers an opportunity to gain a better understanding of mechanistic details and to tune such systems for synthetic purposes (Figure 4.3). The catalytic activity of these systems has been proposed to be enhanced in the presence of bulky and electron donating Tp^x ligands.[376] A recent study by Pérez and co-workers provided some kinetic and mechanistic details for addition of CCl_4 and $CHCl_3$ to olefins catalysed by the Tp^xCu family of complexes in the presence of a donor ligand such as MeCN, which induces ATRA.[376] The best conversions have been observed for the catalysts containing $Tp^{tBu,Me}$ and $Tp^{Cy,Br}$ ligands. In contrast, Tp* or Tp^{Ms} ligands provided low conversions and the $Tp^{Br3}Cu$ system was ineffective even at higher temperatures. The nature of the Tp^x ligands appears to play a significant role on catalytic activity either for donor or steric reasons. The presence of electron donor groups, in principle, increases the electron density at the metal site and such species may easily be oxidised. At the same time, the steric bulk of the substituents at the Tp^x ligand may prevent the formation of dinuclear $Tp^x{}_2Cu$ species. Therefore, electronic and steric effects of the Tp^x ligands may dramatically control the catalytic activity of Tp^xCu complexes.[377-379]

Pérez and co-workers have proposed a catalytic cycle for the ATRA of CCl_4 or $CHCl_3$ to olefins catalysed by $Tp^xCu(I)$ complexes in the presence of an added donor MeCN (Figure 4.4). In this cycle, the homolytic cleavage of the carbon-halogen bond gives rise to a carbon-centered radical ($^{\cdot}CXCl_2$), and concomitant oxidation of Cu(I) to Cu(II) generates a metal-halide complex $Tp^xCu(II)Cl$, which is believed to be the rate determining step. In the presence of the donor MeCN, the $Tp^xCu(II)Cl$ intermediate may give rise to a $Tp^xCu(II)Cl(MeCN)$ species. The carbon-centered radical interacts with the olefin to form the second radical species ($Cl_2XCCH_2C^{\cdot}HR$), which may abstract the halogen from either $Tp^xCu(II)Cl$ or $Tp^xCu(II)Cl(MeCN)$. Subsequently, the metal is reduced to the initial oxidation state and the addition product is formed. There are, however, still uncertainties concerning the detailed chemical steps involved in the proposed catalytic cycle, in

particular the rate determining step, role of the Tp^x ligands and proposed metal-halide complexes $Tp^xCu(II)Cl$ and $Tp^xCu(II)Cl(MeCN)$.

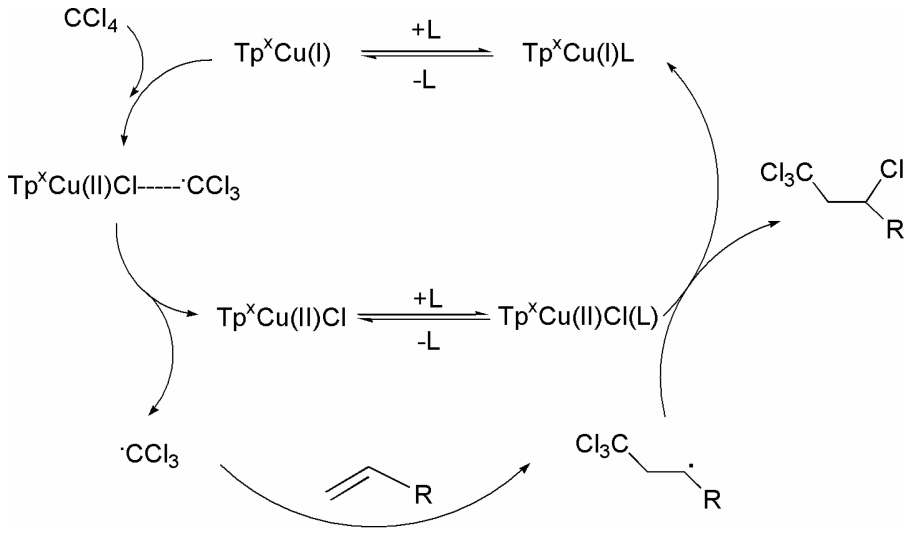

Figure 4.4 Proposed catalytic cycle for the ATRA of CCl_4 or $CHCl_3$ to olefins catalysed by Tp^xCu complexes in the presence of an added donor L.[376]

4.2 Objectives

In the present study, we use DFT in conjunction with a quantum mechanics/molecular mechanics (QM/MM) approach[380-385] to explore the electronic structure of Tp^xCu complexes in the proposed catalytic cycle (Figure 4.4). With a description of the key electronic features of the Tp^xCu systems in hand, we compare the potential energy surfaces for ATRA of CCl_4 to C_2H_4 by $Tp^HCu(I)$ and $Tp^{tBu,Me}Cu(I)$ complexes with the added donor MeCN. The intrinsic tuneability of Tp^x ligands provide an ideal platform for establishing structure/function relationships of Tp^xCu complexes in ATRA (Kharasch addition) reactions, and also opens up new synthetic pathways.

4.3 Computational methodology

Gas phase optimisations were carried out using DFT and hybrid ONIOM(QM:MM) approach[386-388] as implemented in the Gaussian03[73] package with the B3LYP functional.[46-48] The LanL2DZ basis set and associated effective core potential was employed for Cu[77,80-82] and 6-31G(d) for the other atoms. All geometry optimisations were full with no restrictions and vibrational frequency calculations were also performed in order to establish that the stationary points were minima or transition states. In the ONIOM(QM:MM) approach, the full system, $Tp^{tBu,Me}$Cu(II), is divided into two different regions, each of them with a different computational description. The electronically sophisticated environment is treated with DFT, while the interactions related to the bulk of the $Tp^{tBu,Me}$ ligand , –*t*Bu and –Me, are treated with much more affordable MM approach, where UFF[389] was employed in the MM region. The total energy of the QM/MM model [E_{Tot}(QM,MM)] can be obtained by the following formula;

$$E_{Tot}(QM,MM) = E_{QM}(QM) + E_{MM}(QM,MM) - E_{MM}(QM) \quad (4.1)$$

where the first term, E_{QM}(QM), represents the total energy of the model system (QM). The next two terms consider the MM contribution within the MM region and between the QM and MM regions.

4.4 Results and discussion

In the present work, we considered the ATRA of CCl_4 to C_2H_2 catalysed by Tp^xCu complexes in the presence of MeCN (L). Two types of ligand systems for the Tp^x were considered, namely Tp^H ligand, where we replaced all the bulky substituants of Tp^x by H for simplicity, and the $Tp^{tBu,Me}$ ligand (Figure 4.5).

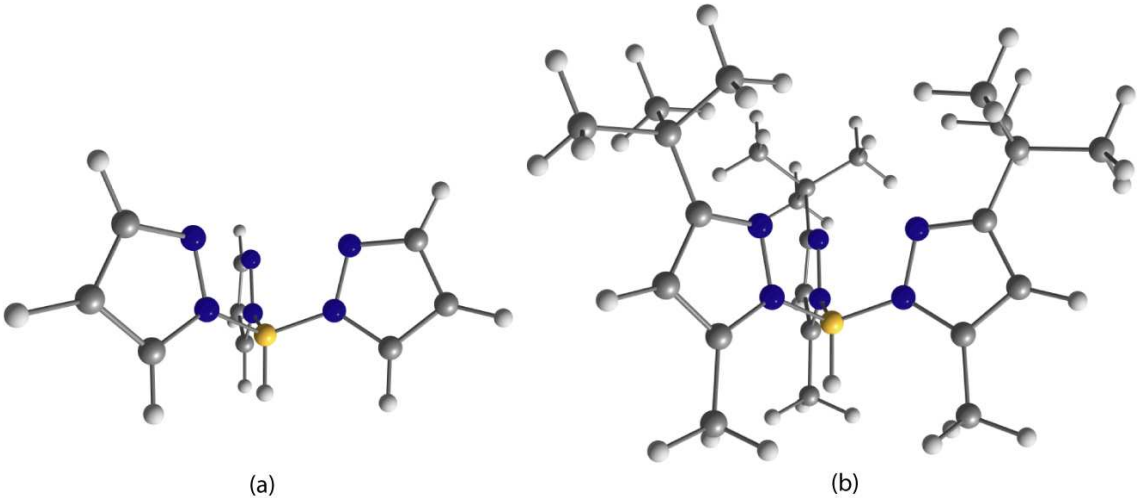

Figure 4.5 The Tp^{x} ligands considered in this work; (a) simplified Tp^{H} and (b) $Tp^{tBu,Me}$.

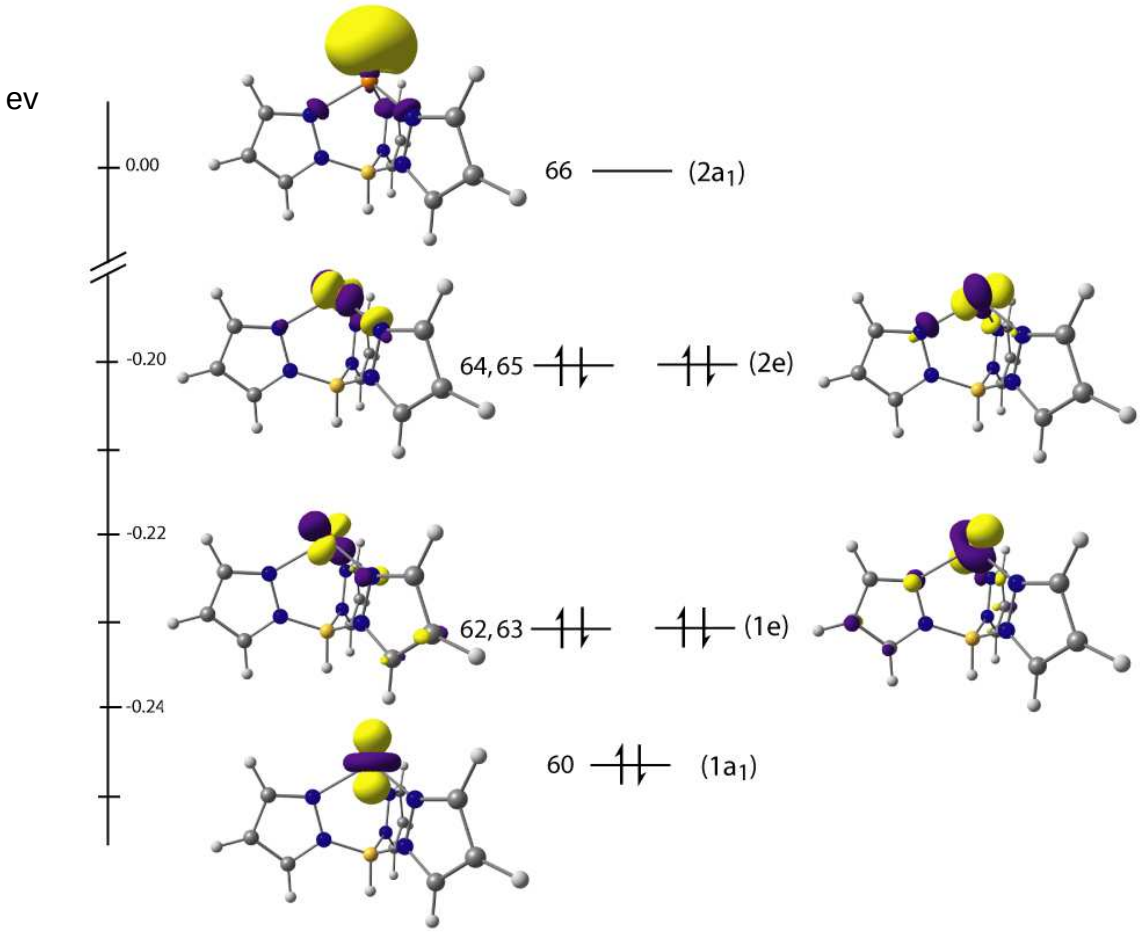

Figure 4.6 Kohn–Sham orbitals for the singlet electronic state of $Tp^{H}Cu(I)$ (orbitals are labelled according to the C_{3V} point group).

4.4.1 Electronic structure of $Tp^{x}Cu(I)$ and $Tp^{x}Cu(I)(MeCN)$

Both $Tp^{x}Cu(I)$ and $Tp^{x}Cu(I)(MeCN)$ complexes hold fully occupied metal *d* orbitals (d^{10}), and therefore the electronic structure of these systems can be described by using the spin-restricted Kohn–Sham formalism (RKS). The Kohn–Sham orbitals for the singlet state of the pyramidal $Tp^{H}Cu(I)$ complex are summarised in Figure 4.6. Under C_{3V} symmetry, the metal d_{z2} orbital of this system has a_1 symmetry while the four other *d* orbitals form degenerate orbitals of *e* symmetry (1e and 2e). The empty non-bonding p_z orbital of the metal centre forms the LUMO.

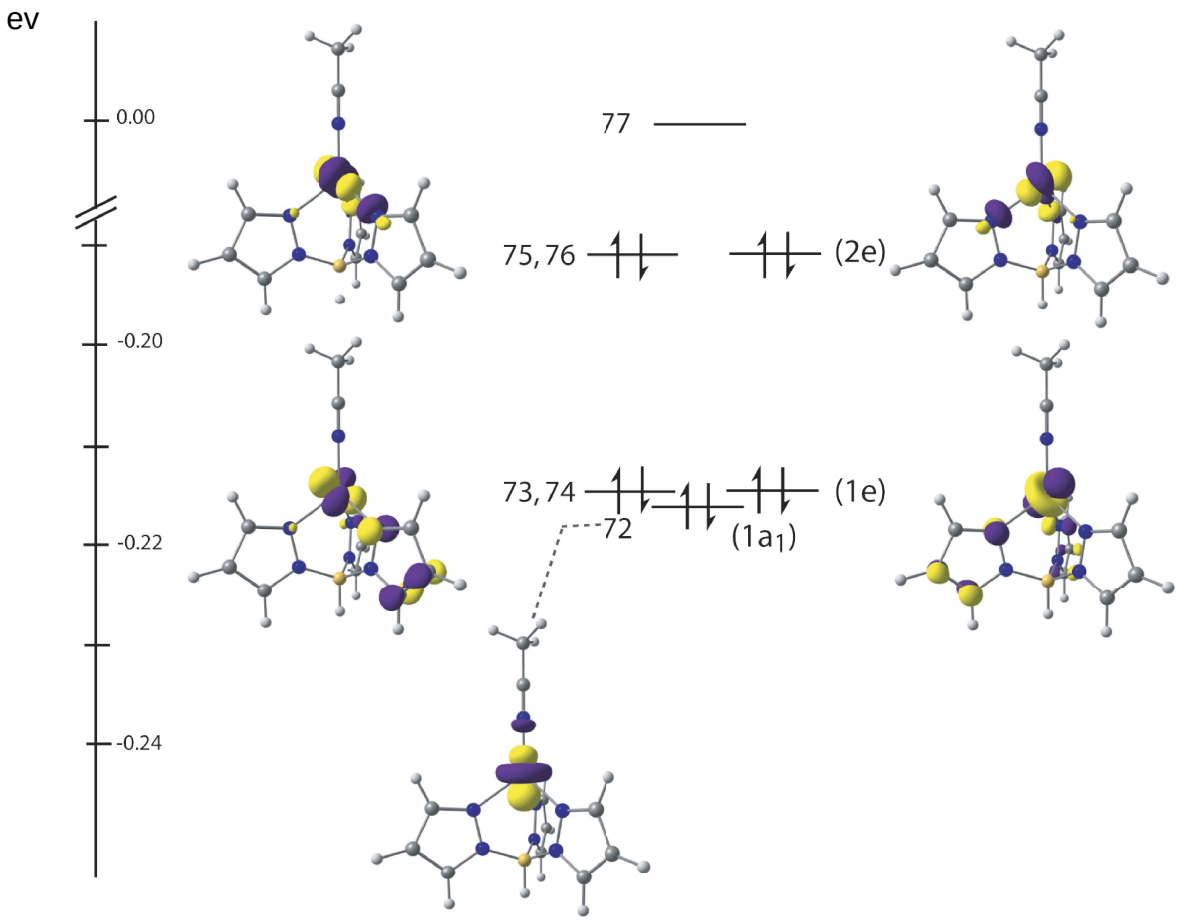

Figure 4.7 Kohn–Sham orbitals for the singlet electronic state of $Tp^{H}Cu(I)(MeCN)$ (orbitals are labelled according to the C_{3V} point group).

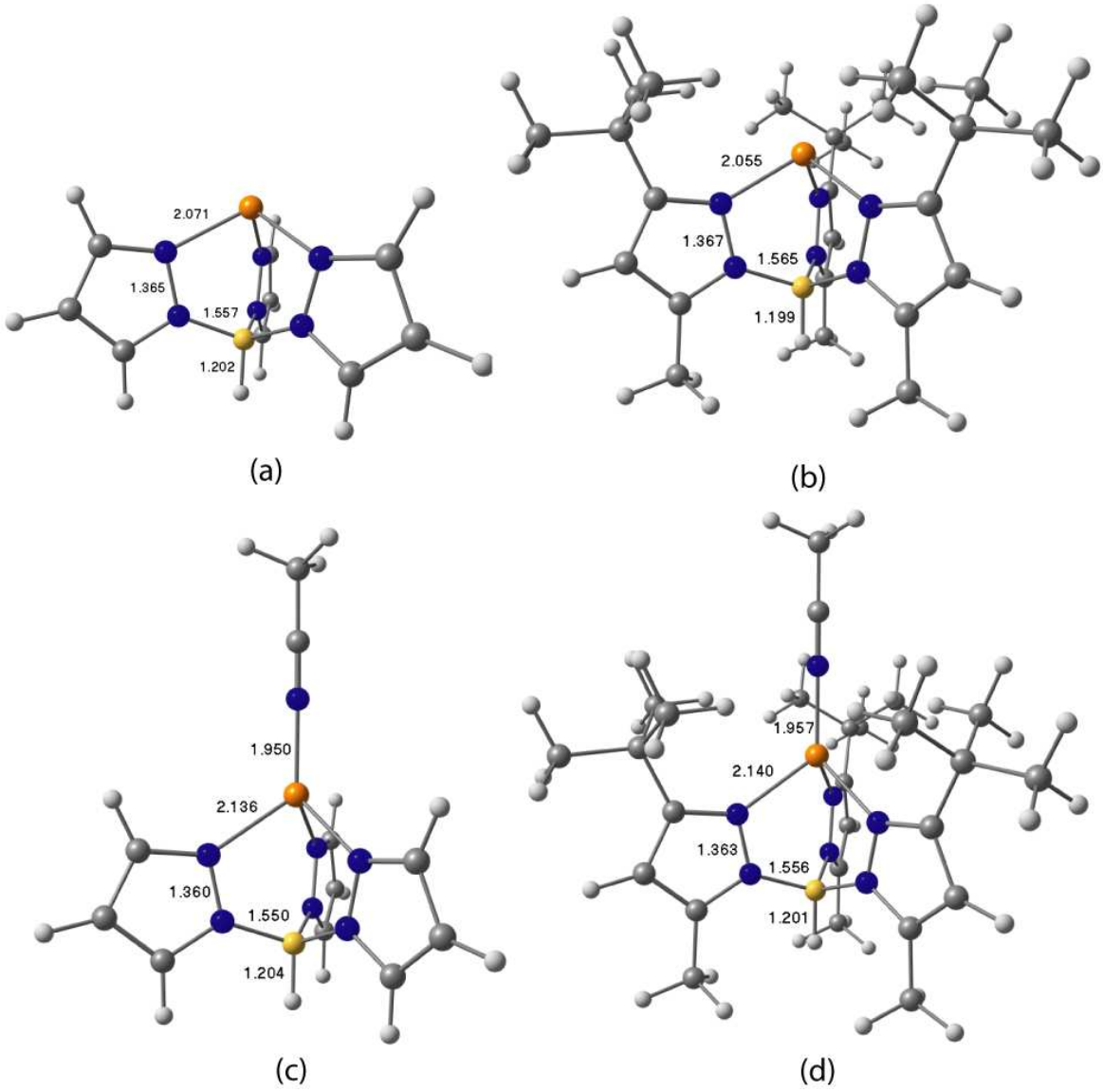

Figure 4.8 Optimised structures of (a) $Tp^{H}Cu(I)$, (b) $Tp^{tBu,Me}Cu(I)$, (c) $Tp^{H}Cu(I)(MeCN)$ and (d) $Tp^{tBu,Me}Cu(I)($ MeCN) (structural parameters are in Å).

Coordination of the MeCN ligand on the $Tp^{H}Cu(I)$ complex gives rise to a tetrahedral $Tp^{H}Cu(I)(MeCN)$ species, and the electronic structure of this system is quite similar to that of the $Tp^{H}Cu$ (Figure 4.7), where the metal d_{z^2} orbital ($1a_1$) and the degenerate metal *d* orbitals (1e) are closer in energy. In the presence of a stronger ligand such as Cl^-, $[Tp^{H}Cu(I)Cl]^-$ complex (d^{10}) for instance, the metal d_{z^2} orbital ($1a_1$) may approach the

HOMO (2e). In the presence of the MeCN ligand, optimised $Tp^{x}Cu(I)(MeCN)$ systems have slightly longer Cu-N bonds (Figure 4.8). The calculated Cu-N(L) bond length of $Tp^{tBu,Me}Cu(I)(MeCN)$ complex (1.96 Å) is relatively higher than that of $Tp^{H}Cu(I)(MeCN)$ system (1.95 Å), which indicates steric effects of the tBu groups of the $Tp^{tBu,Me}$ ligand. In the presence of MeCN (in solution), $Tp^{x}Cu(I)$ complex is in equilibrium with the $Tp^{x}Cu(I)(MeCN)$. The former species is believed to be the active component for the catalytic activity.

4.4.2 Electronic structure of $Tp^{x}Cu(II)Cl$ and $Tp^{x}Cu(II)Cl(MeCN)$

Transition metal ions with d^9 configuration, notably Cu(II) ion, are Jahn-Teller active and the structural distortion of the metal coordination sphere is severe. In general, ML_4 type complexes containing d^9 configuration are in between square-planer (diamagnetic d^8) and tetrahedral (paramagnetic d^8 or d^{10}) shape. For the $Tp^{x}Cu(II)Cl$ complex (d^9), three doublet electronic states can be generated by removing a single electron either from the doubly degenerate metal *d* orbitals (2e) or from the metal d_{z^2} orbital ($1a_1$) of the $[Tp^{H}Cu(I)Cl]^{-}$ (anionic form).

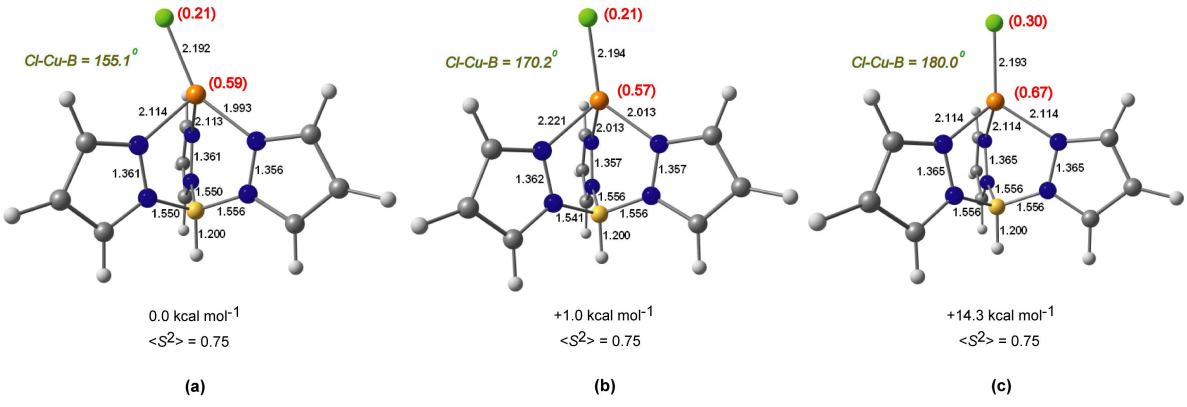

Figure 4.9 Optimised doublet electronic states (a) $^{2}A'$ (b) $^{2}A''$ and (c) $^{2}A'''$ of $Tp^{H}Cu(II)Cl$ complex.

We optimised three possible doublet electronic states for the $Tp^{H}Cu(II)Cl$ complex (Figure 4.9). In the first doublet state $^{2}A'$ (Figure 4.9a), the ground state, holds the B-Cu-Cl angle of 155.1º, which indicates a highly distorted tetrahedral coordination sphere at the metal centre. The net spin densities ρ(Cu) = 0.59 and ρ(Cl) = 0.21 suggests that the radical character is mainly on the metal. The Kohn–Sham orbitals for the $^{2}A'$ state are summarised in Figure 4.10, where the orbitals are separated into spin-α and spin-β manifolds. One of the 2e orbitals, **73** of spin-α and **72** of spin-β, are doubly occupied, and therefore Cu-N antibonding character of this orbital leads to two long Cu-N bonds (2.11 Å) and one short Cu-N bond (1.99 Å) (Figure 4.9a).

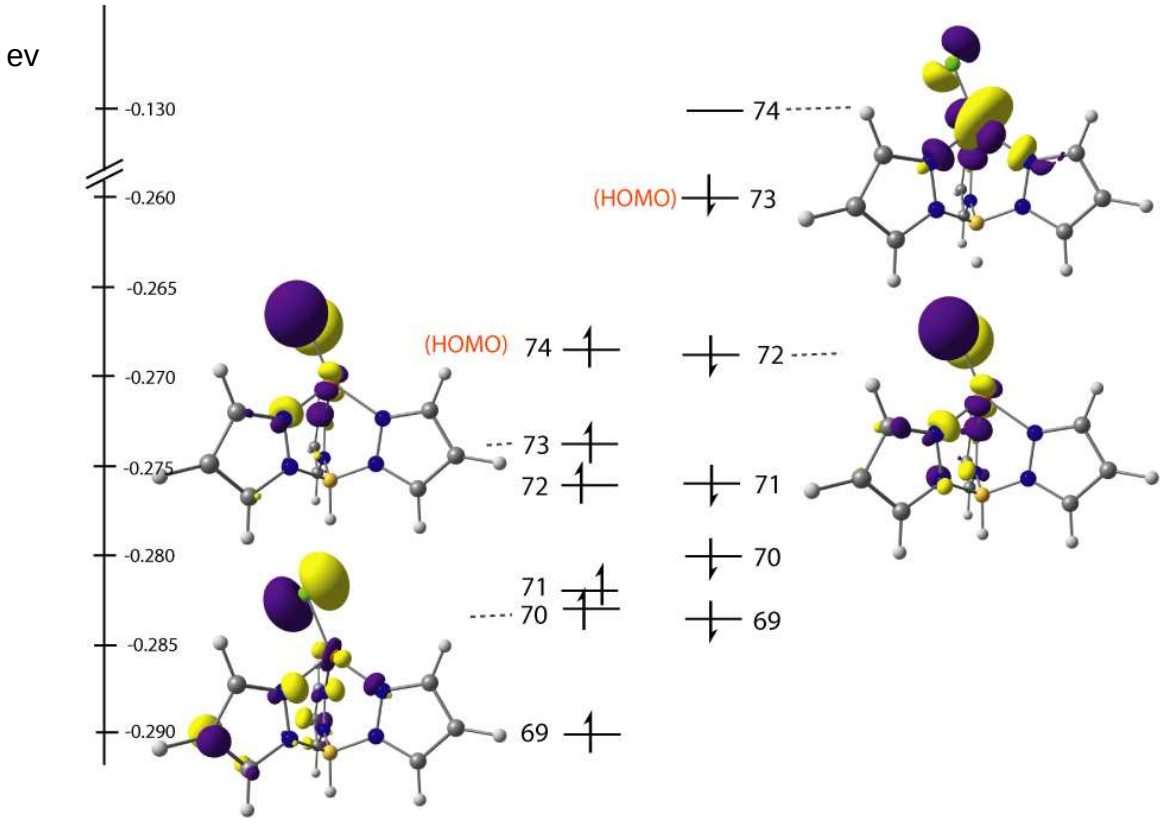

Figure 4.10 Kohn–Sham orbitals for the optimised $^{2}A'$ electronic state of $Tp^{H}Cu(II)Cl$.

The second doublet electronic state, $^{2}A''$, was obtained by altering the occupation of the spin-β manifold of the $^{2}A'$ state (**72** and **74** orbitals), and the optimised $^{2}A''$ is only 1.0 kcal mol^{-1} above the ground state $^{2}A'$ (Figure 4.9b). Kohn–Sham orbitals of the $^{2}A''$ state are

depicted in Figure 4.11, where the doubly occupied one of 2e orbitals [**73** of spin-α and **72** of spin-β], has significant Cu-N antibonding character at a single Cu-N bond, which leads to one long Cu-N bond (2.22 Å) and two short Cu-N bonds (2.01 Å). The B-Cu-Cl angle of the optimised ^{2}A" state is 170.2º, indicating a distorted tetrahedral metal coordination sphere (Figure 4.9b).

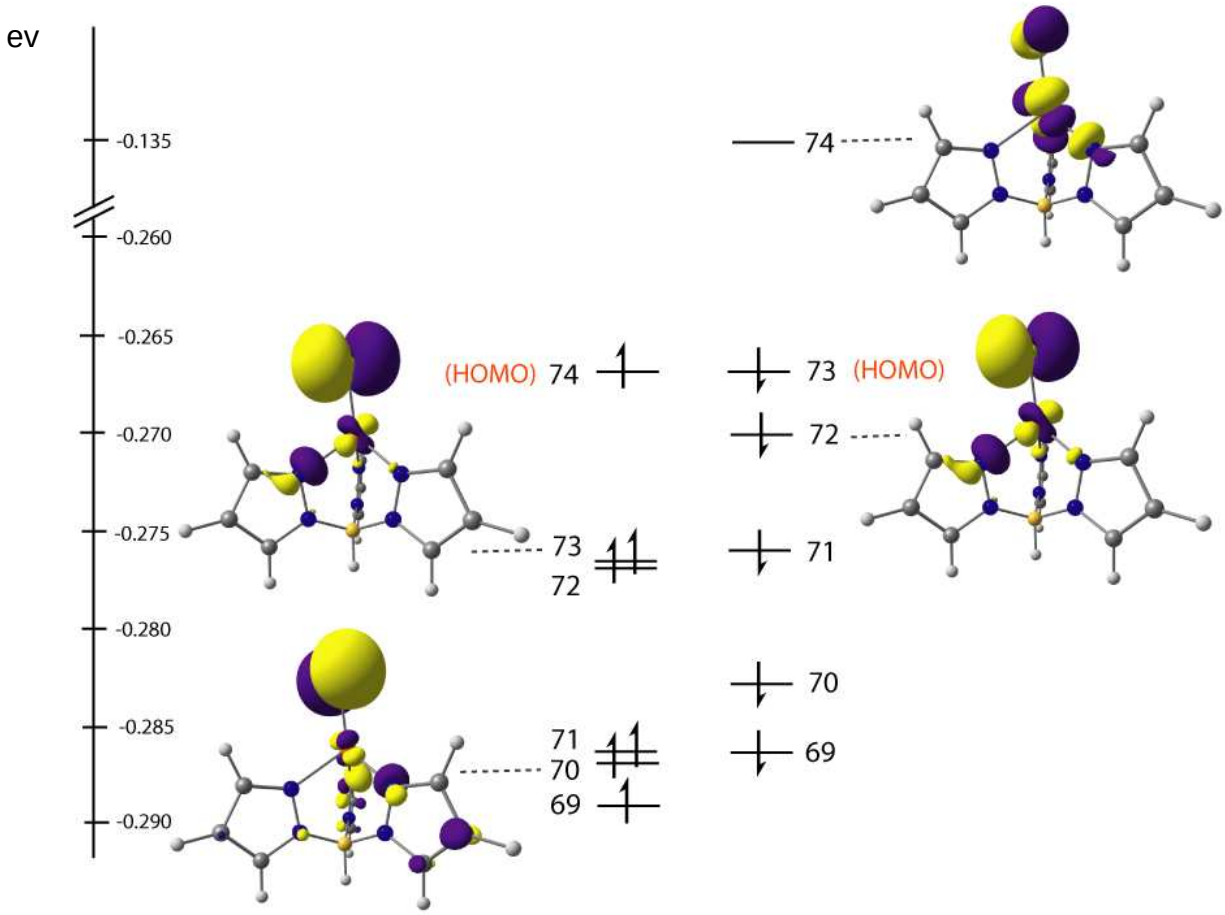

Figure 4.11 Kohn–Sham orbitals for the optimised ^{2}A" electronic state of Tp^{H}Cu(II)Cl.

The optimised third doublet electronic state of the Tp^{H}Cu(II)Cl complex, ^{2}A"', has Cl-Cu-B angle of 180^0, and is symmetric (C_{3V}) (Figure 4.9c). The Kohn–Sham orbitals for the optimised ^{2}A"' state are summarised in Figure 4.12, where the metal d_{z^2} orbital of the spin-β manifold **(74)** is unoccupied. However, this doublet electronic state is 14.3 kcal mol^{-1} above the ground state ^{2}A'.

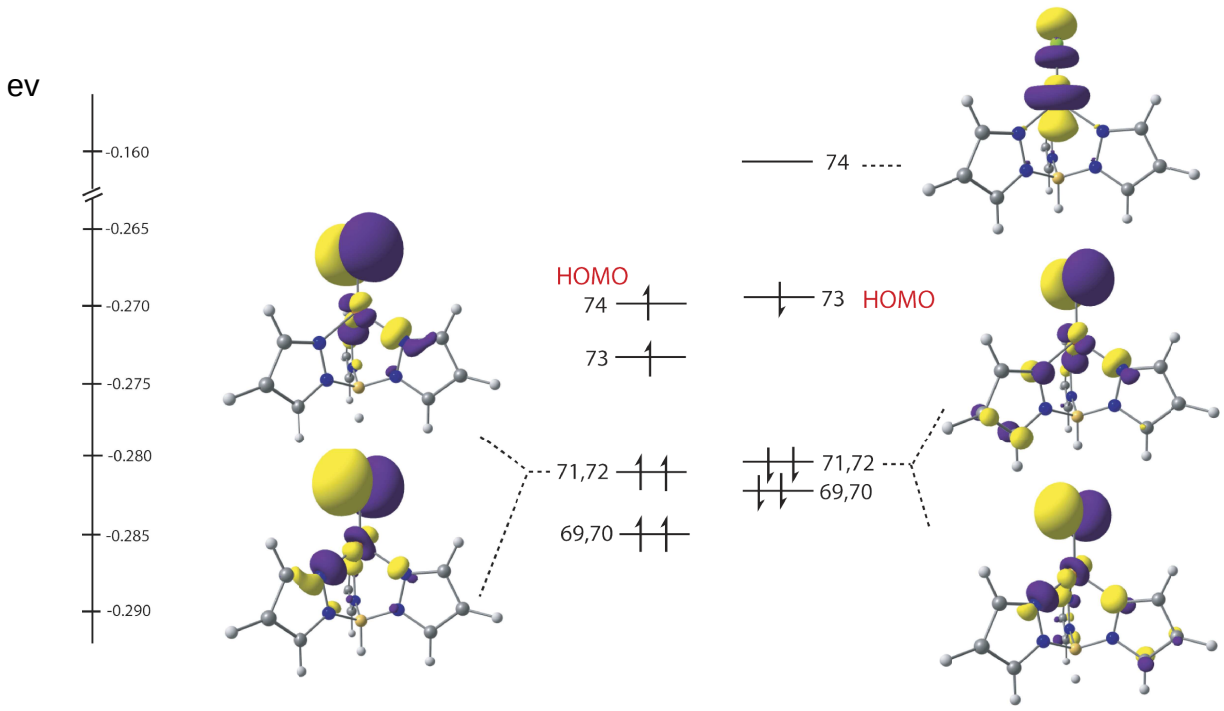

Figure 4.12 Kohn–Sham orbitals for the optimised ^{2}A''' electronic state of Tp^{H}Cu(II)Cl.

The optimised doublet electronic states of the Tp^{tBu,Me}Cu(II)Cl complex are shown in Figure 4.13. In the computed geometries, the pattern of two long and one short Cu-N bond distances (2.13, 2.12, and 1.97 Å) are clearly present in the ^{2}A' state (Figure 4.13a), whereas one long and two short Cu-N distances pattern (2.27 and 2.04 Å) is found in the ^{2}A" state. The X-ray structure of Tp^{tBu,Me}Cu(II)Cl has Cu-N bond distances of 2.07, 2.07, and 1.93 Å corresponds to the calculated ^{2}A' state. The calculated Cu-Cl bond length 1.19 Å of the ^{2}A' state agrees with the X-ray structure (1.18 Å). Both ^{2}A' and ^{2}A" states hold rather equivalent Cl-Cu-B angles (172.3^{o} and 171.8^{o}), which deviate from the X-ray structure (159.3^{o}). The optimised ^{2}A''' state holds a symmetric metal coordination sphere (Cl-Cu-B = 179.5^{o}), and this state is 12.2 kcal mol^{-1} above the energetically equivalent ^{2}A' and ^{2}A" states. Despite the recording of two stable doublet electronic states (^{2}A' and ^{2}A") in the solid state, a mixture of both should occur in solution, and the complex may convert from one doublet state to the other.

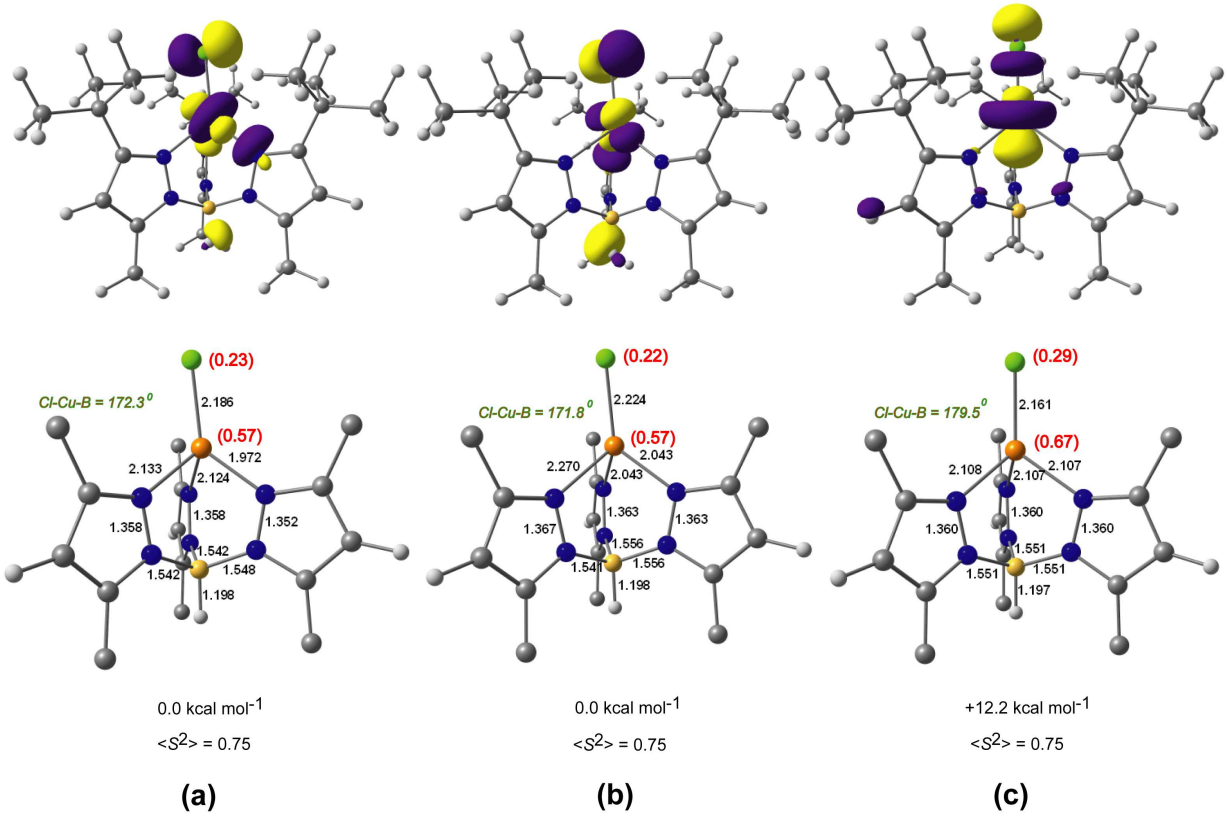

Figure 4.13 Optimised doublet electronic states (a) ^{2}A' (b) ^{2}A" and (c) ^{2}A'" of Tp^{tBu,Me}Cu(II)Cl and the corresponding unoccupied metal *d* orbital at the spin-*β* manifold.

Coordination of MeCN to the Tp^{x}Cu(II)Cl species gives rise to penta-coordinated Tp^{x}Cu(II)Cl(MeCN) (d^9). Kohn–Sham orbitals for the doublet state of Tp^{H}Cu(II)Cl(MeCN) are summarised in Figure 4.14. Most noticeably, the metal d_{z^2} orbital of the spin-*β* manifold **(85)** is unoccupied in this case, and leads a longer Cu-Cl bond distance (2.31 Å) (Figure 4.14). The net spin densities on the Cu-Cl site remain very similar to those in the ^{2}A' state of Tp^{H}Cu(II)Cl.

In the corresponding full model, Tp^{tBu,Me}Cu(II)Cl(MeCN), the metal d_{z^2} orbital of the spin-*β* manifold is still unoccupied (Figure 4.15b), and yields a longer Cu-Cl bond distance (2.38 Å) in this system (Figure 4.15a).

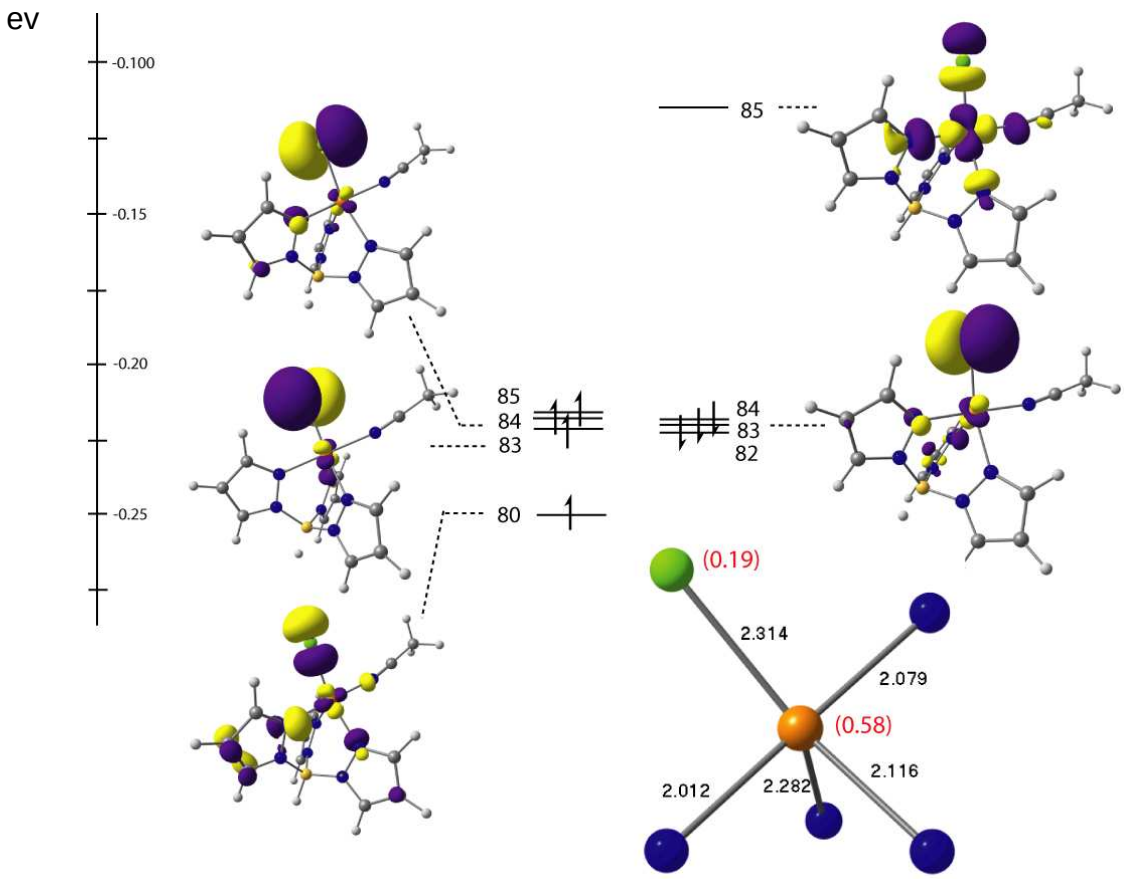

Figure 4.14 Kohn–Sham orbitals for the doublet electronic state, key structural parameters (Å) and spin densities of $Tp^{H}Cu(II)Cl(MeCN)$.

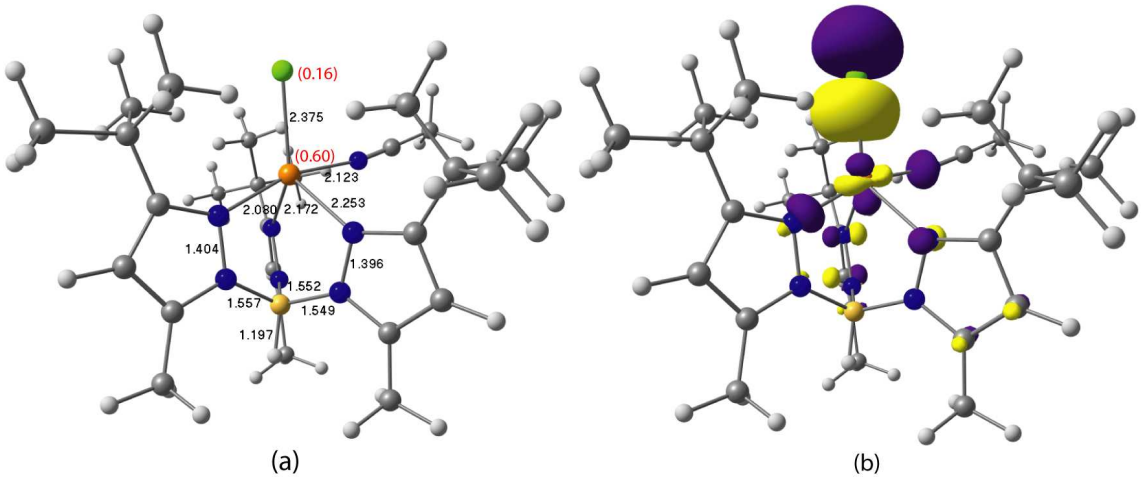

Figure 4.15 (a) Structural parameters (Å) and spin densities (red) of the optimised structure, and (b) unoccupied metal d_{z^2} orbtal of the spin-β manifold in the doublet state of $Tp^{tBu,Me}Cu(II)Cl(MeCN)$.

4.4.3 Catalytic cycle

With a description of the detailed electronic structure of $Tp^{x}Cu(I)$ and $Tp^{x}Cu(II)$ systems in hand, this section compares potential energy surfaces for ATRA of CCl_4 to C_2H_4 by $Tp^{H}Cu(I)$ and $Tp^{tBu,Me}Cu(I)$ complexes with the added donor MeCN.

4.4.3.1 Atom transfer radical addition of CCl_4 to C_2H_4 by $Tp^{H}Cu(I)$

The potential energy diagram for the ATRA of CCl_4 to C_2H_4 by $Tp^{H}Cu(I)$ is shown in Figure 4.16. The active component for the catalytic activity is believed to be the $Tp^{H}Cu(I)$ complex, which is in equilibrium with the $Tp^{H}Cu(I)(MeCN)$. Our calculations indicated that the former species is 17 kcal mol^{-1} higher in energy. Therefore, the first step of the catalytic cycle is to remove MeCN from the $Tp^{H}Cu(I)(MeCN)$ species, which opens the active channel of the ATRA process. The $Tp^{H}Cu(I)$ complex has a closed-shell singlet ground state (RKS), which interacts with CCl_4 to form a neutral $Tp^{H}Cu(I)Cl\text{-}CCl_3$ intermediate, only 3.7 kcal mol^{-1} below the $Tp^{H}Cu(I)$. Then the homolytic cleavage of the C-Cl bond gives rise to a $[Tp^{H}Cu(II)Cl]\ldots[\dot{C}Cl_3]$ species at the C-Cl bond dissociation limit, which is 12.5 kcal mol^{-1} above the $Tp^{H}Cu(I)Cl\text{-}CCl_3$ intermediate.

At the beginning of the C-Cl bond cleavage, the spin density on each metal centre must be zero as dictated by the closed-shell singlet (RKS) electronic state, and this constraint remains as the C-Cl bond lengthens if the RKS scheme is retained. However, it is clear that each of the fragments $Tp^{H}Cu(II)Cl$ and $\dot{C}Cl_3$ have a single unpaired electron (non-zero spin density), so the calculations at the bond dissociation limit is preferred with the UKS method. For the $[Tp^{H}Cu(II)Cl]\ldots[\dot{C}Cl_3]$ limit, two energetically and structurally similar spin states, a singlet (UKS) and a triplet, are possible depending on ferro- or antiferromagnetic coupling of the individual $Tp^{H}Cu(II)Cl$ and $\dot{C}Cl_3$ fragments. The singlet

potential energy surface lies lower than the highly repulsive triplet profile at shorter C-Cl separations.

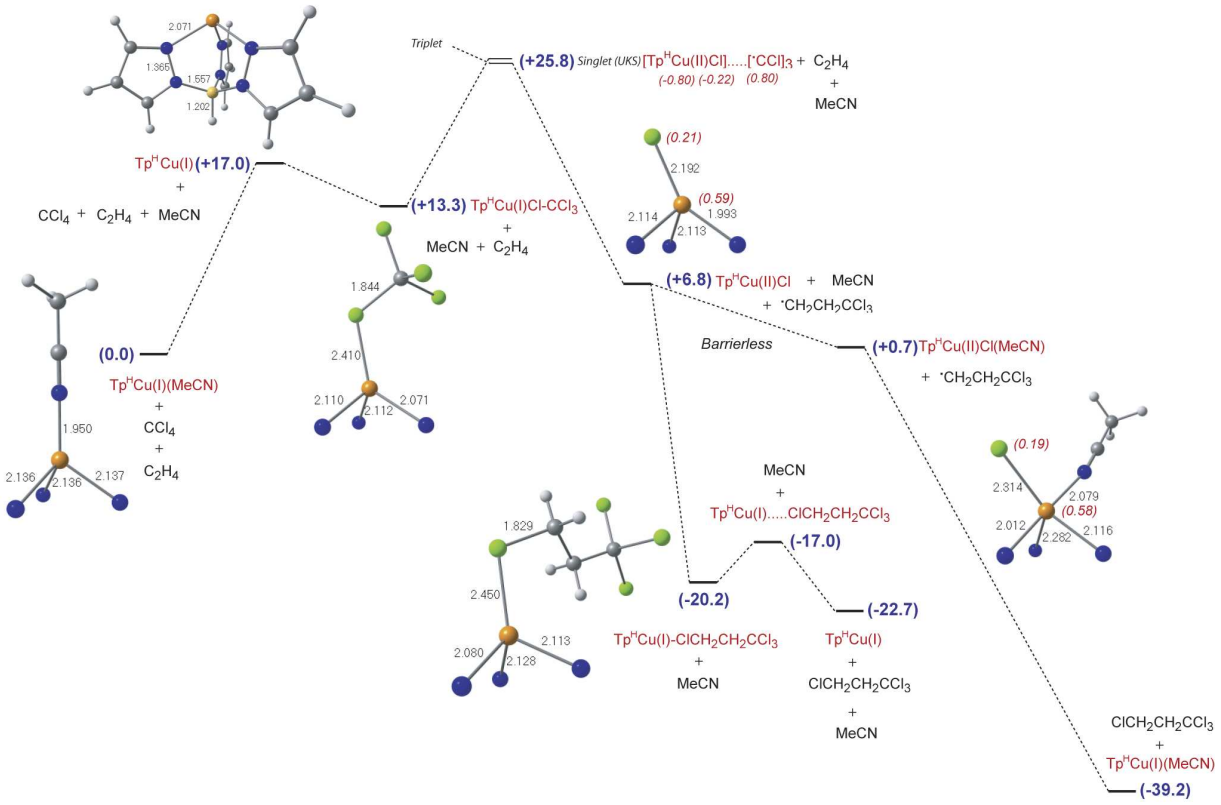

Figure 4.16 Potential energy diagram for the ATRA of CCl_4 to C_2H_4 by $Tp^HCu(I)$ complex. (energy values are in kcal mol^{-1} and spin densities are shown in italics).

The radical characteristics of the $^{\bullet}CCl_3$ fragment appear at a rather early stage of the singlet (UKS) surface. Therefore, transfer of the α-spin density from $^{\bullet}CCl_3$ to the C_2H_4 leads to the second radical species $^{\bullet}CH_2CH_2CCl_3$ *via* a low-lying transition state, only 5.7 kcal mol^{-1} above the carbon-centered radical (Figure 4.17). The resulting $Tp^HCu(II)Cl$ species is 6.8 kcal mol^{-1} above the entry channel, and the distorted tetrahedral Cu coordination sphere of this complex provides more space for the ligand (MeCN) association, which is therefore barrierless and yields $Tp^HCu(II)Cl(MeCN)$ species only 6.1 kcal mol^{-1} below the $Tp^HCu(II)Cl$ (both systems can be described with the UKS formalism).

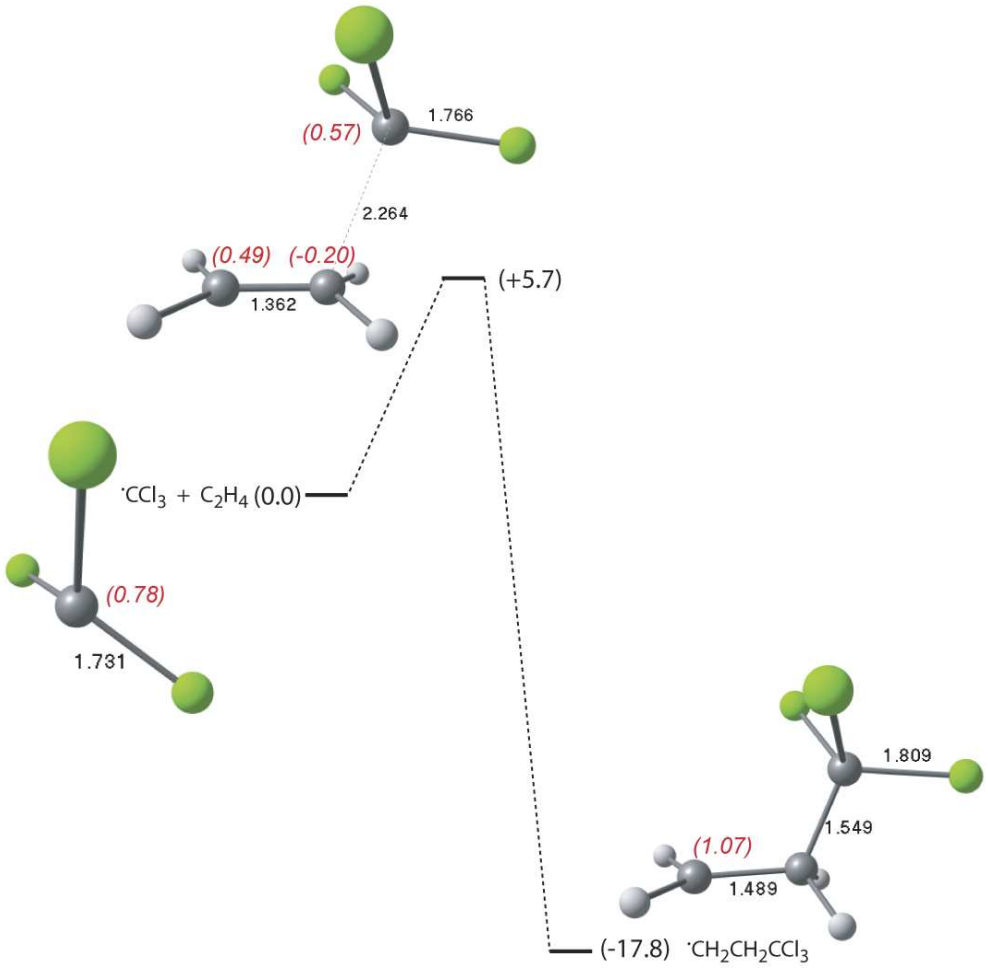

Figure 4.17 Potential energy diagram for the reaction of $^{\cdot}CCl_3$ with C_2H_4 to form the second radical species $^{\cdot}CH_2CH_2CCl_3$ (energy values are in kcal mol^{-1} and spin densities are shown in italics).

In the presence of the active $^{\cdot}CH_2CH_2CCl_3$ radical, a halogen atom can be abstracted from both $Tp^{H}Cu(II)Cl$ and $Tp^{H}Cu(II)Cl(MeCN)$. For $Tp^{H}Cu(II)Cl$, the addition product is formed *via* a stable intermediate $Tp^{H}Cu(I)$-$ClCH_2CH_2CCl_3$, a closed-shell system found 20.2 kcal mol^{-1} below the entry channel. Then, Cu-Cl bond dissociation yields the product $ClCH_2CH_2CCl_3$ with a barrier of 5.2 kcal mol^{-1}. In the case of the $Tp^{H}Cu(II)Cl(MeCN)$ system, despite several attempts, we have been unable to locate a minimum for the

corresponding (MeCN)Tp^{H}Cu(I)-$ClCH_2CH_2CCl_3$ intermediate, and this system dissociates spontaneously into $ClCH_2CH_2CCl_3$ and Tp^{H}Cu(I)(MeCN). In terms of the overall reaction, the dissociation of the MeCN ligand from Tp^{H}Cu(I)(MeCN) to form the active Tp^{H}Cu(I) complex has a barrier of 17 kcal mol^{-1}, and the C-Cl bond dissociation limit is further 8.8 kcal mol^{-1} higher in energy. These steps lead to the highest point of the potential energy surface (Figure 4.16), and therefore both contribute to the overall barrier of the ATRA process.

4.4.3.2 Atom transfer radical addition of CCl_4 to C_2H_4 catalysed by $Tp^{tBu,Me}$Cu(I)

The computed potential energy profile for the ATRA of CCl_4 to C_2H_4 catalysed by the $Tp^{tBu,Me}$Cu(I) complex is depicted in Figure 4.17. In qualitative terms, the overall reaction pathway is similar to that of the simplified Tp^{H}Cu(I) system. The MeCN ligand dissociation from $Tp^{tBu,Me}$Cu(I)(MeCN) to form the active $Tp^{tBu,Me}$Cu(I) complex has a barrier of 19 kcal mol^{-1} (experimental ΔH = 20.1 kcal mol^{-1}),[390] and the C-Cl dissociation limit of the neutral $Tp^{tBu,Me}$Cu(I)Cl-CCl_3 intermediate is further 9.7 kcal mol^{-1} higher in energy, leading to the $Tp^{tBu,Me}$Cu(II)Cl species.

The most interesting differences occur in the coordination of MeCN to the $Tp^{tBu,Me}$Cu(II)Cl intermediate, which has a barrier of 6.9 kcal mol^{-1}, and the resulting $Tp^{tBu,Me}$Cu(II)Cl(MeCN) species is 5.5 kcal mol^{-1} above the $Tp^{tBu,Me}$Cu(II)Cl. This indicates the importance of the steric effects of the $Tp^{tBu,Me}$ ligand on the approaching ligand (MeCN). Consequently, the Cl abstraction process will occur preferably from the tetrahedral $Tp^{tBu,Me}$Cu(II)Cl complex, and the corresponding closed-shell $Tp^{tBu,Me}$Cu(I)-$ClCH_2CH_2CCl_3$ intermediate lies 20.9 kcal mol^{-1} below the entry channel. Due to the steric hindrance of the bulky tBu groups of the $Tp^{tBu,Me}$ ligand, the Cu-Cl bond length of the intermediate is 2.64 Å, which is significantly longer than the analogous Tp^{H}Cu(I)-

$ClCH_2CH_2CCl_3$ species (2.45 Å). Therefore, dissociation of Cu-Cl bond is quite easy in this case (barrier is 3.1 kcal mol^{-1}).

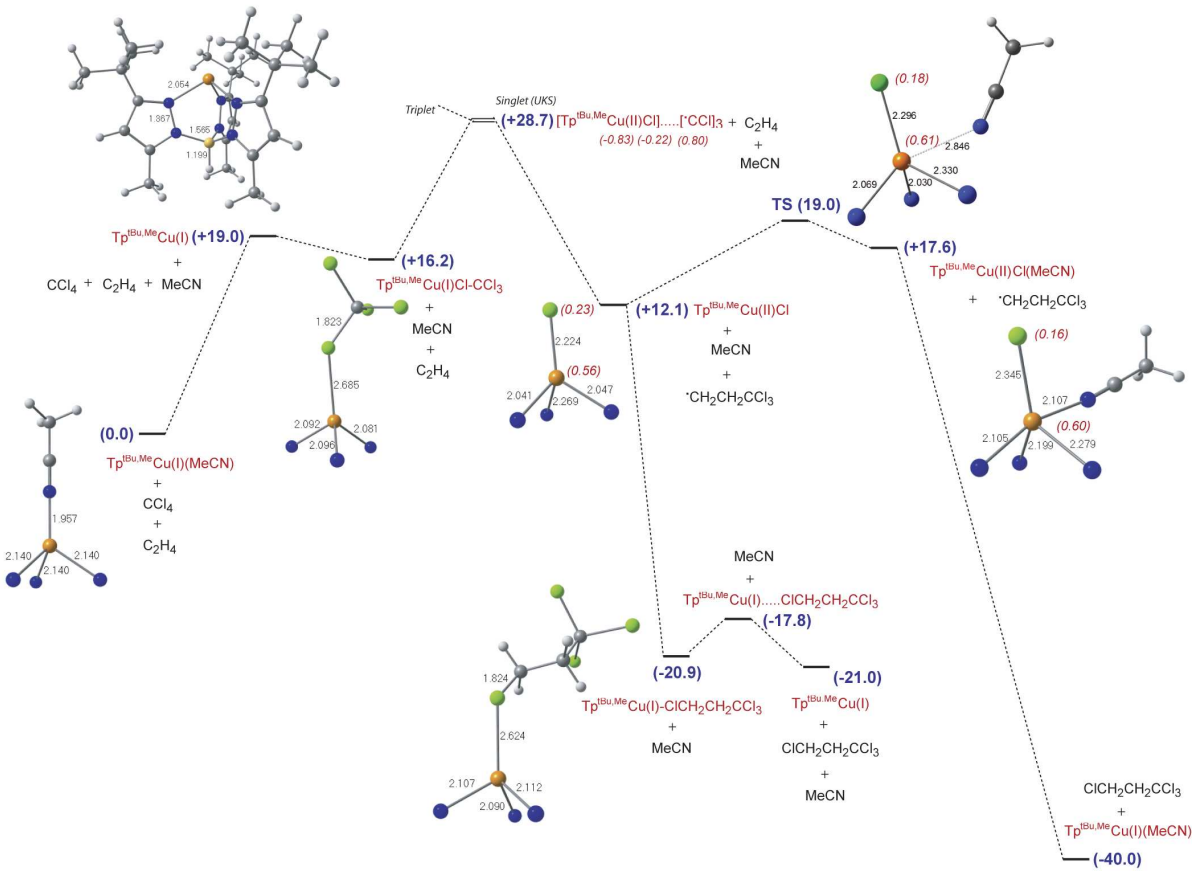

Figure 4.17 Potential energy diagram for the ATRA of CCl_4 to ethylene by $Tp^{tBu,Me}Cu$ model complex (energy values are in kcal mol^{-1} and spin densities are shown in italics).

If the Cl abstraction starts from the penta-coordinate system, $Tp^{tBu,Me}Cu(II)Cl(MeCN)$, product formation is again barrierless, and we have not been able to find a minimum for the $(MeCN)Tp^{tBu,Me}Cu(II)$-$ClCH_2CH_2CCl_3$ intermediate. The most important feature, however, is that the overall barrier for the ATRA process is still the initial MeCN ligand dissociation from $Tp^{tBu,Me}Cu(I)(MeCN)$ to form the active $Tp^{tBu,Me}Cu(I)$ complex (19 kcal mol^{-1}) and the C-Cl bond dissociation limit (further 9.7 kcal mol^{-1}).

4.5 Conclusions

We have presented extensive use of hybrid QM/MM techniques to model the electronic structural features and mechanistic information of homoscorpionate-Cu complexes in ATRA of CCl_4 to C_2H_4. Our survey of the electronic structure of $Tp^xCu(I)$ and $Tp^xCu(II)Cl$ complexes confirmed that the former species are symmetric (C_{3V}) and the latter species hold three distinct spin doublet electronic states.

In the overall reaction profile for the ATRA of CCl_4 to C_2H_4, the dissociation of MeCN from $Tp^xCu(I)(MeCN)$ to form the active $Tp^xCu(I)$ complex and the C-Cl bond dissociation lead to the highest point of the potential energy surface, and therefore these steps contribute to the overall barrier of the ATRA process. For the simplified system Tp^H, the overall barrier is 25.8 kcal mol^{-1}, and for the full system $Tp^{tBu,Me}$, the overall barrier is 28.7 kcal mol^{-1}. Both metal-halide complexes $Tp^xCu(II)Cl$ and $Tp^xCu(II)Cl(MeCN)$ may participate in the Cl abstraction process of the proposed catalytic cycle. In the case of the $Tp^HCu(II)Cl$, coordination of MeCN is barrierless, and the resultant $Tp^xCu(II)Cl(MeCN)$ is 6.1 kcal mol^{-1} lower in energy. Therefore, the Cl abstraction step may be prefered for the $Tp^xCu(II)Cl(MeCN)$ species. In contrast, coordination of MeCN to the $Tp^{tBu,Me}Cu(II)Cl$ has a barrier of 5.9 kcal mol^{-1}. Consequently, Cl abstraction may be prefered for the $Tp^{tBu,Me}Cu(II)Cl$ species, which may imply the active role of the $Tp^{tBu,Me}$ ligand and the added ligand MeCN in ATRA reactions.

Chapter 5

Electronic Structure of Pyrazolate-supported $Fe_3(\mu_3\text{-}O)$ Complexes: Prediction of Mössbauer Parameters and Exchange Coupling Constants using Broken-symmetry DFT.

5.1 Introduction

Magnetically coupled iron clusters have been extensively studied due to their relevance to biology: the iron−sulfur cubane complexes (Fe_4S_4) are well-known in biological electron-transfer processes, and therefore the study of model complexes containing Fe_4S_4-cubane cores has been one of the central themes of bioinorganic chemistry.[391-394] In the study of redox activity, spin or charge density distributions of these synthetic metal clusters are very useful in probing our understanding of structure-function relationships of Fe-based clusters in electron-transfer proteins. The magnetic properties of transition metal clusters have been important in the development of the field of single molecular magnets (SMM).[395-399] SMMs are proposed as the key candidates for future technological applications such as high-density information storage at the molecular level and quantum computing.[400-402] This chapter focuses on the electronic structure of pyrazolate-supported $Fe_3(\mu_3\text{-}O)$ systems, in particular $[Fe_3(\mu_3\text{-}O)(\mu\text{-}4\text{-}O_2N\text{-}pz)_6X_3]^{2-}$ complexes (where pz = pyrazolato, X = Cl, Br) prepared by Raptis and co-

workers.[403,404] Crystal structures of the both $[Fe_3(\mu_3\text{-}O)(\mu\text{-}4\text{-}O_2N\text{-}pz)_6Cl_3]^{2-}$ and $[Fe_3(\mu_3\text{-}O)(\mu\text{-}4\text{-}O_2N\text{-}pz)_6Br_3]^{2-}$ systems are given in Figure 5.1. These model systems have been shown to be precursors for the synthesis of higher nuclearity Fe clusters.[405-407]

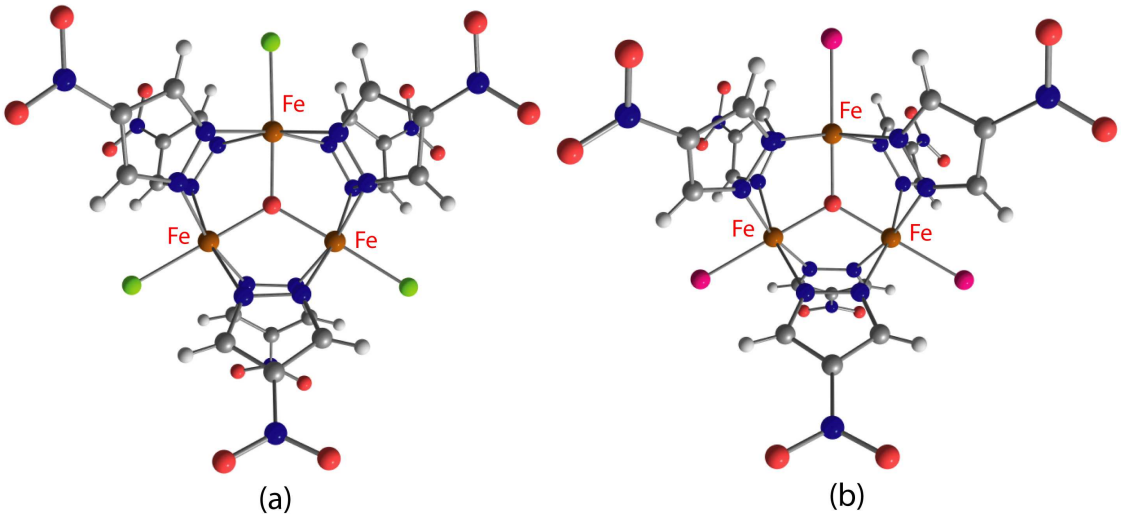

Figure 5.1 Crystal structure of (a) $[Fe_3(\mu_3\text{-}O)(\mu\text{-}4\text{-}O_2N\text{-}pz)_6Cl_3]^{2-}$ and (b) $[Fe_3(\mu_3\text{-}O)(\mu\text{-}4\text{-}O_2N\text{-}pz)_6Br_3]^{2-}$ complexes.[403,404]

The Fe_3 clusters of interest here have been characterised using spectroscopic methods such as X-ray, infrared, electron paramagnetic resonance (EPR), Mössbauer (MB) and electro chemical methods.[403,404] The purpose of the work in this chapter is to compute the electronic structure of $[Fe_3(\mu_3\text{-}O)(\mu\text{-}4\text{-}O_2N\text{-}pz)_6X_3]^{2-}$ clusters, and use this as a basis to enhance the information content of the physical measurements, particularly the magnetic susceptibility data and the Mössbauer spectra. In both contexts, the nature of the interactions between Fe ions and their chemical environment are the key issues. Theoretical exploration of magnetic phenomena has been largely focused on dinuclear transition metal complexes, although extensions to larger clusters have emerged in recent years.[397-399,408-412] The Mössbauer parameters can be used for investigating the mixed-valent nature of Fe-based systems, and a number of studies have recently emerged, where Mössbauer parameters of single Fe centres have been calculated with some success.[413-420] The problem of extending these ideas to polynuclear systems is that the broken-symmetry wave functions typically used to describe the electronic structure

are not eigenvalues of the spin Hamiltonian. It is not therefore clear that they form an adequate basis for comparison of spectroscopic parameters. Our goal here is to compute Mössbauer parameters for two exchange coupled $[Fe_3(\mu_3\text{-}O)(\mu\text{-}4\text{-}O_2N\text{-}pz)_6X_3]^{2-}$ complexes for a variety of electronic configurations to establish the extent of which the computed values are sensitive to the chosen configuration. In this way we can evaluate different models of electronic structure against experiments.

5.2 Computational details

All the gas phase single point energy calculations or structure optimisations were performed using the ORCA programme[76] with the hybrid B3LYP functional,[46-48] and geometry optimisations were full, with no restrictions. The TZVP basis set was considered for Fe and for all atoms bonded to the metal, and TZV basis functions were employed for the remaining atoms.[83-86] Mössbauer parameters for the crystal structure or the optimised structures were computed with CP(PPP) basis set[421] for Fe and TZVP for the remaining atoms.

5.3 Results and discussion

5.3.1 Electronic structure of $[Fe_3(\mu_3\text{-}O)(\mu\text{-}4\text{-}O_2N\text{-}pz)_6X_3]^{2-}$

The crystal structures of $[Fe_3(\mu_3\text{-}O)(\mu\text{-}4\text{-}O_2N\text{-}pz)_6X_3]^{2-}$ complexes considered in this work contain one short [Fe(1)-Fe(3)] and two longer almost identical [Fe(1)-Fe(2) and Fe(2)-F(3)] metal-metal bond distances (Figure 5.2). It is important to note that the halogen substituent does not affect the Fe-Fe bond distances, which are equivalent for chlorinated or brominated species.

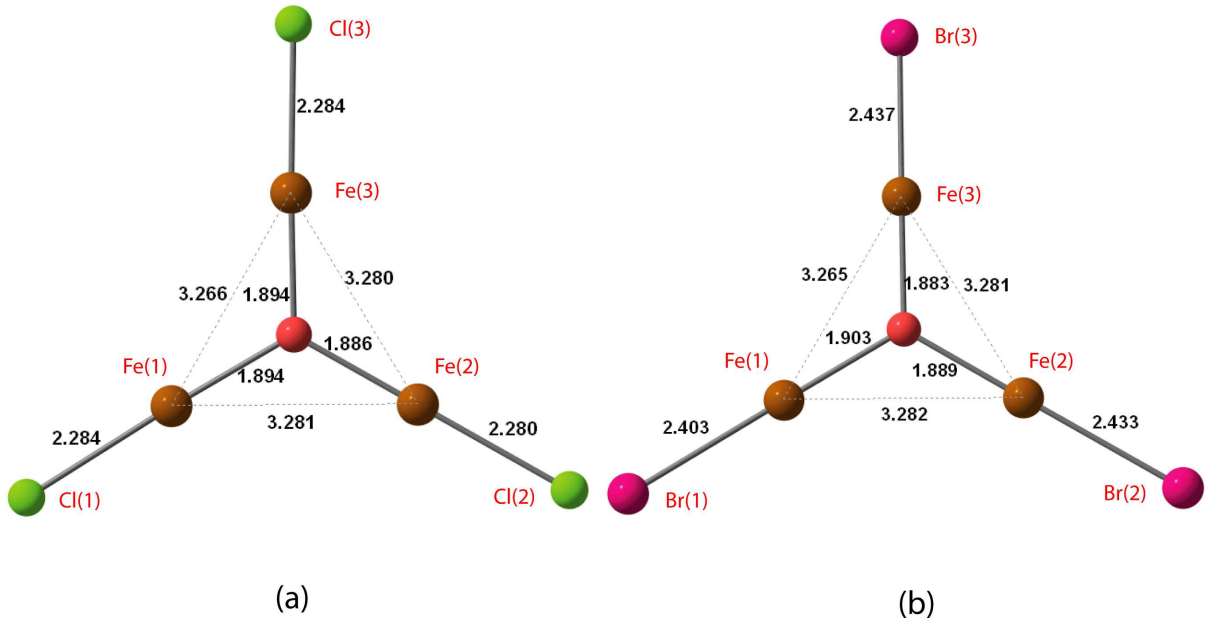

Figure 5.2 Key structural parameters (Å) of the crystal structures of (a) $[Fe_3(\mu_3\text{-}O)(\mu\text{-}4\text{-}O_2N\text{-}pz)_6Cl_3]^{2-}$ and (b) $[Fe_3(\mu_3\text{-}O)(\mu\text{-}4\text{-}O_2N\text{-}pz)_6Br_3]^{2-}$ complexes.

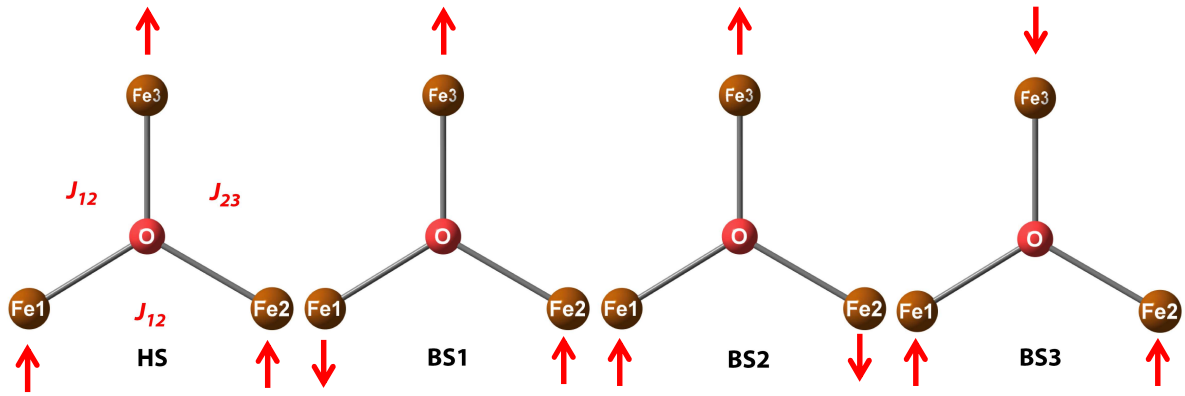

$$\text{HS: } |5/2\rangle|5/2\rangle|5/2\rangle = |\alpha\alpha\alpha\rangle$$

$$\text{BS1: } |-5/2\rangle|5/2\rangle|5/2\rangle \equiv |\beta\alpha\alpha\rangle$$

$$\text{BS2: } |5/2\rangle|-5/2\rangle|5/2\rangle \equiv |\alpha\beta\alpha\rangle$$

$$\text{BS3: } |5/2\rangle|5/2\rangle|-5/2\rangle \equiv |\alpha\alpha\beta\rangle$$

Figure 5.3 Possible spin configurations (M_S = 15/2 and M_S = 5/2) for $[Fe_3(\mu_3\text{-}O)(\mu\text{-}4\text{-}O_2N\text{-}pz)_6X_3]^{2-}$ complexes containing three Fe^{3+} (d^5) ions (C_1-symmetry).

The most striking difference is the metal-halide bond lengths, where the Fe-Cl bond lengths (average length is 2.282 Å) are relatively shorter than the Fe-Br bond distances (average length is 2.424 Å), and these changes of the metal coordination sphere may significantly affect the Mössbauer parameters (*vide infra*). We have considered four possible spin configurations for each of the two clusters, namely HS [M_S = 15/2], and BS1, BS2 and BS3 states, each of which has [M_S = 5/2] (Figure 5.3). The M_S = 15/2 state can be written as $HS = |\alpha\alpha\alpha\rangle$ while the M_S = 5/2 states are: $BS1 = |\beta\alpha\alpha\rangle, BS2 = |\alpha\beta\alpha\rangle$, and $BS3 = |\alpha\alpha\beta\rangle$. Computed net spin densities, $<S^2>$ values and total energies of HS, BS1, BS2, and BS3 states are depicted in Table 5.1.

Table 5.1 Computed net spin densities, $<S^2>$ values and total energies of HS, BS1, BS2, and BS3 states for the crystal structures of $[Fe_3(\mu_3\text{-}O)(\mu\text{-}4\text{-}O_2N\text{-}pz)_6Cl_3]^{2-}$ and $[Fe_3(\mu_3\text{-}O)(\mu\text{-}4\text{-}O_2N\text{-}pz)_6Br_3]^{2-}$ complexes.

Multiplicity	Computed net spin densities							$<S^2>$	Energy (eV)
	ρ[Fe(1)]	ρ[Fe(2)]	ρ[Fe(3)]	ρ[O]	ρ[Cl(1)]	ρ[Cl(2)]	ρ[Cl(3)]		
$[Fe_3(\mu_3\text{-}O)(\mu\text{-}4\text{-}O_2N\text{-}pz)_6Cl_3]^{2-}$									
HS (M_S = 15/2)	4.25	4.25	4.25	0.61	0.21	0.21	0.21	63.77	-212971.4633
BS1 (M_S = 5/2)	-4.18	4.21	4.21	0.18	-0.19	0.18	0.20	13.58	-212971.7936
BS2 (M_S = 5/2)	4.21	-4.18	4.21	0.18	0.20	-0.19	0.20	13.58	-212971.7989
BS3 (M_S = 5/2)	4.25	4.25	-4.17	0.20	0.20	0.19	-0.19	13.58	-212971.7939
$[Fe_3(\mu_3\text{-}O)(\mu\text{-}4\text{-}O_2N\text{-}pz)_6Br_3]^{2-}$									
HS (M_S = 15/2)	4.22	4.22	4.22	0.62	0.24	0.23	0.23	63.77	-385535.8198
BS1 (M_S = 5/2)	-4.16	4.19	4.19	0.20	-0.21	0.22	0.22	13.57	-385536.1434
BS2 (M_S = 5/2)	4.19	-4.16	4.19	0.19	0.23	-0.20	0.22	13.57	-385536.1540
BS3 (M_S = 5/2)	4.18	4.19	-4.16	0.18	0.23	0.22	-0.21	13.57	-385536.1555

The HS state of $[Fe_3(\mu_3\text{-}O)(\mu\text{-}4\text{-}O_2N\text{-}pz)_6Cl_3]^{2-}$ features the majority spin-α density on all three Fe centres, ρ(Fe) = 4.25, which is typical for high-spin Fe^{3+} ions (S = 5/2), and the metal cores are ferromagnetically coupled through the μ_3-O atom (Figure 5.4a).

Moreover, the coordinating atoms, in particular Cl and (μ_3-O) also hold significant positive spin densities, demonstrating the spin delocalisation from metal to the ligands. In the broken symmetry state BS1, the net spin densities on Fe, [ρ(Fe1) = -4.18, ρ(Fe2) = 4.21, ρ(Fe3) = 4.21], indicate anti-ferromagnetic nature (Figure 5.4b). Calculated $<S^2>$ values for the HS state of 63.77 and the BS states of 13.58 are close to the ideal values ferromagnetic ($<S^2>$ = 63.75) and anti-ferromagnetic ($<S^2>$ ≈ 13.75) respectively. The single point energy calculations on the crystal structure clearly identify the BS states as being more stable than the HS state.

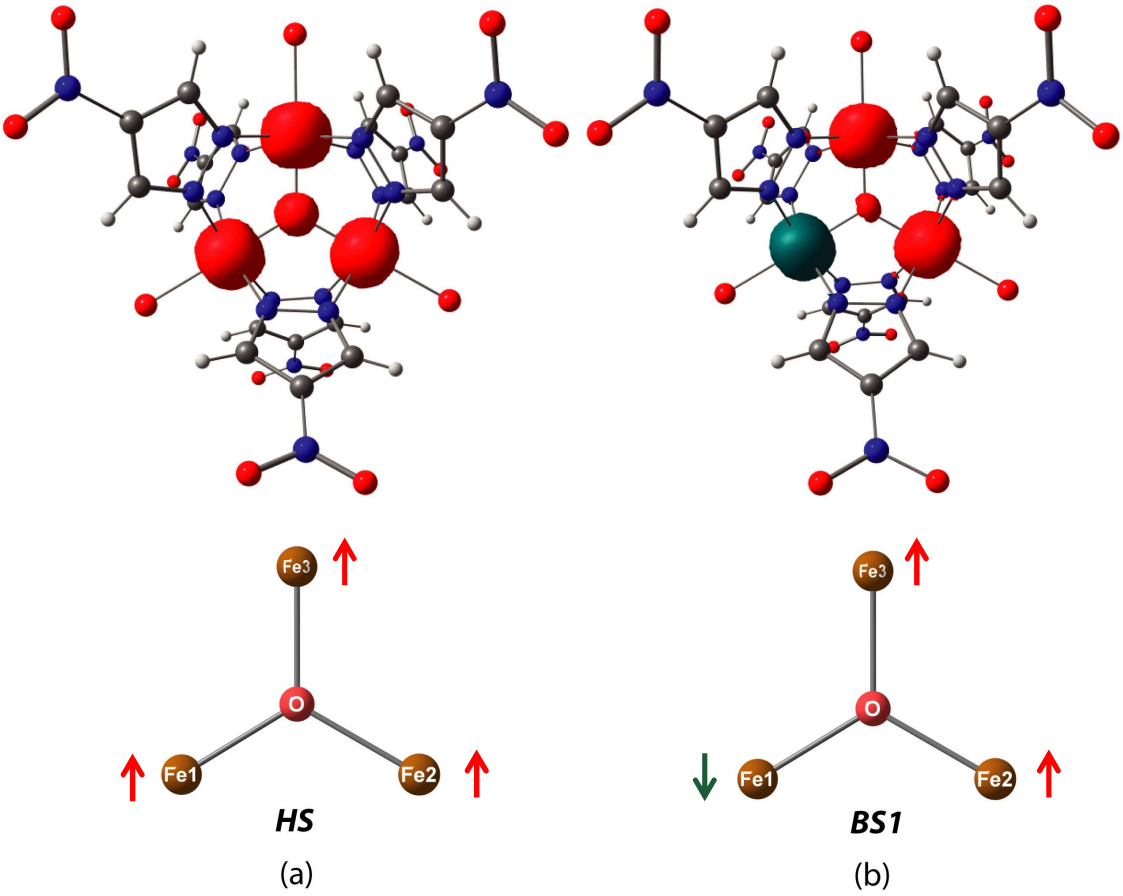

Figure 5.4 Total spin density distributions in the (a) HS state (M_S = 15/2) and the (b) BS1 state (M_S = 5/2) for the crystal structure of $[Fe_3(\mu_3\text{-}O)(\mu\text{-}4\text{-}O_2N\text{-}pz)_6X_3]^{2-}$.

One important question that we wish to address later in this chapter is how sensitive the calculated Mössbauer parameters are to changes in geometry. In particular, we wish to establish the degree of error that could be introduced if we had to rely on optimised rather than X-ray coordinates. To that end, we have optimised the structure of the HS

and BS1 states of the two clusters. Optimised structural parameters are compared to the crystal structure in Table 5.2. Optimisation of the HS states (with 15 unpaired electrons) of both complexes give rise to highly symmetric (C_{3V}) structures, which feature relatively longer metal-ligand and metal-metal bond distances. In contrast, the optimised BS1 state of $[Fe_3(\mu_3\text{-}O)(\mu\text{-}4\text{-}O_2N\text{-}pz)_6X_3]^{2-}$ complexes exhibit relatively shorter Fe(1)-(μ_3-O) bonds due to the antiferromagnetic nature of the Fe(1)-Fe(2) and Fe(1)-Fe(3) interactions, which gives rise to C_{2V} symmetry.

Table 5.2 Key structural parameters of the crystal structures[403,404] and the optimised HS (M_S = 15/2), BS1 (M_S = 5/2) states for $Fe_3(\mu_3\text{-}O)(\mu\text{-}4\text{-}O_2N\text{-}pz)_6X_3]^{2-}$ complexes.

	Crystal structure	**Optimised structures**	
		HS (M_S = 15/2)	**BS1 (M_S = 5/2)**
$[Fe_3(\mu_3\text{-}O)(\mu\text{-}4\text{-}O_2N\text{-}pz)_6Cl_3]^{2-}$			
Fe…Fe	3.267(1), 3.280(1)	3.35	3.32, 3.33
Fe-O	1.885(4), 1.894(2)	1.94	1.93, 1.89
Fe-N	2.129(3)-2.152(4)	2.16-2.17	2.15-2.16
Fe-Cl	2.280(2), 2.284(2)	2.36	2.36, 2.46
Fe-O-Fe	120.4(1), 119.1(2)	120	119.0, 120.5
O-Fe-Cl	177.7(1), 180.0(1)	179.9	179.8
$[Fe_3(\mu_3\text{-}O)(\mu\text{-}4\text{-}O_2N\text{-}pz)_6Br_3]^{2-}$			
Fe…Fe	3.27(1), 3.28(1)	3.35	3.32, 3.33
Fe-O	1.88(5), 1.90(5)	1.95	1.89, 1.93
Fe-N	2.11(8), 2.14(8)	2.18-2.19	2.15-2.16
Fe-Br	2.43(1), 2.44(2)	2.48	2.49, 2.50
Fe-O-Fe	119.6(3)-120.3(3)	120	118.8, 120.5
O-Fe-Br	177.4(16), 178.3(18)	179.9	179.6

5.3.2 Evaluation of exchange coupling constants

Theoretical and experimental studies of the magnetic properties of polynuclear transition metal clusters have received much attention over recent years due to their

critical role in designing new molecular magnetic materials.[397-399,408-412] The interaction between the localised single particle magnetic moments of the majority of these systems can be described by an effective Hamiltonian containing a number of terms [Equation (5.1)].[408]

$$\hat{H} = \hat{H}_{\text{Heisenberg}} + \hat{H}_{\text{Anisotropy}} + \hat{H}_{\text{Zeeman}} \tag{5.1}$$

$$\hat{H}_{\text{Heisenberg}} = -\sum_{ij} J_{ij}\, \mathbf{S}_i \cdot \mathbf{S}_j \tag{5.2}$$

$$\hat{H}_{\text{Anisotropy}} = \sum_{ij} \mathbf{S}_i \cdot \mathbf{D}_{ij} \cdot \mathbf{S}_j + \sum_{ij} \mathbf{d}_{ij} \cdot \mathbf{S}_i \times \mathbf{S}_j \tag{5.3}$$

$$\hat{H}_{\text{Zeeman}} = g\mu_B \sum_i \mathrm{B} \cdot \mathrm{S_i} \tag{5.4}$$

The simplest effective Hamiltonian contains only the Heisenberg operator [Heisenberg–Dirac–van Vleck (HDVV) spin Hamiltonian - Equation (5.2)], and is isotropic, where J_{ij} is the exchange parameter between spins at sites *i* and *j*, which measures the 'strength' of the interactions between local spins. Positive J_{ij} indicates ferromagnetic coupling, while the negative sign represents antiferromagnetic coupling. The vector operators $\mathbf{S}_i$ and $\mathbf{S}_j$ in Equation (5.2) are single-particle spin operators. Anisotropic terms (non-Heisenberg exchange interactions) in the total Hamilton operator [Equation (5.3)] contain the asymmetric (pseudodipolar) interaction $\mathbf{(D}_{ij}\mathbf{)}$ and the antisymmetric interaction $\mathbf{(d}_{ij}\mathbf{)}$. Finally, the Zeeman term [Equation (5.4)], describes the interactions with the external magnetic field B. Experimentally, exchange coupling constants are typically estimated by fitting simultaneously the temperature and field dependence of the magnetisation to an effective Hamiltonian of the type described above. In the analysis of the $[Fe_3(\mu_3\text{-}O)(\mu\text{-}4\text{-}O_2N\text{-}pz)_6X_3]^{2-}$ systems, the fitting was done with the following constraints:[403,404]

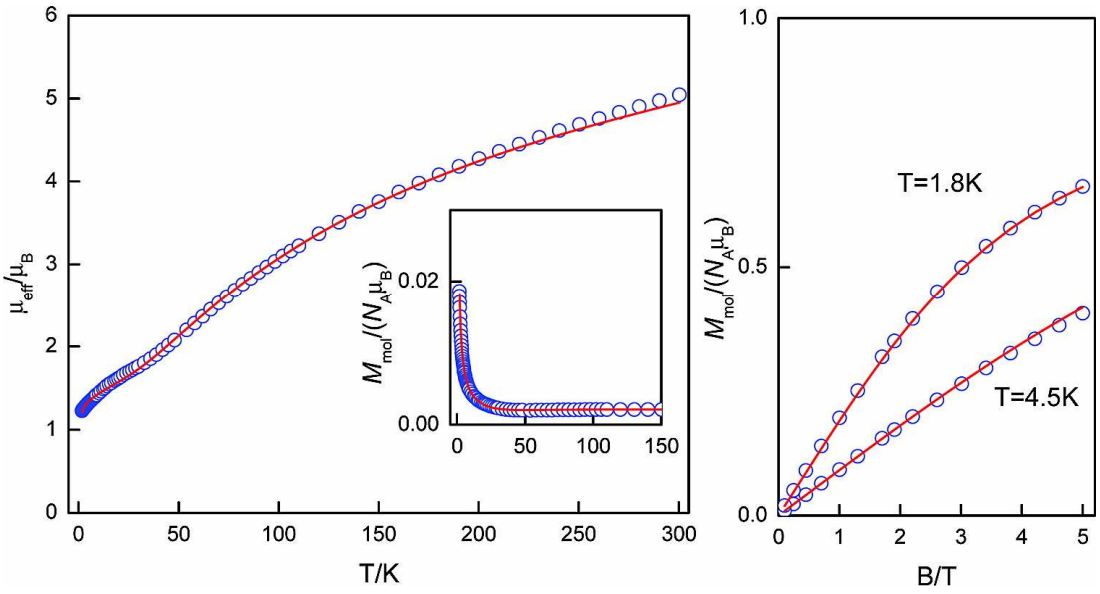

(a) The best-fit for J_{12}/hc = J_{23}/hc = -80.1 cm^{-1} and J_{13}/hc = -72.4 cm^{-1}.

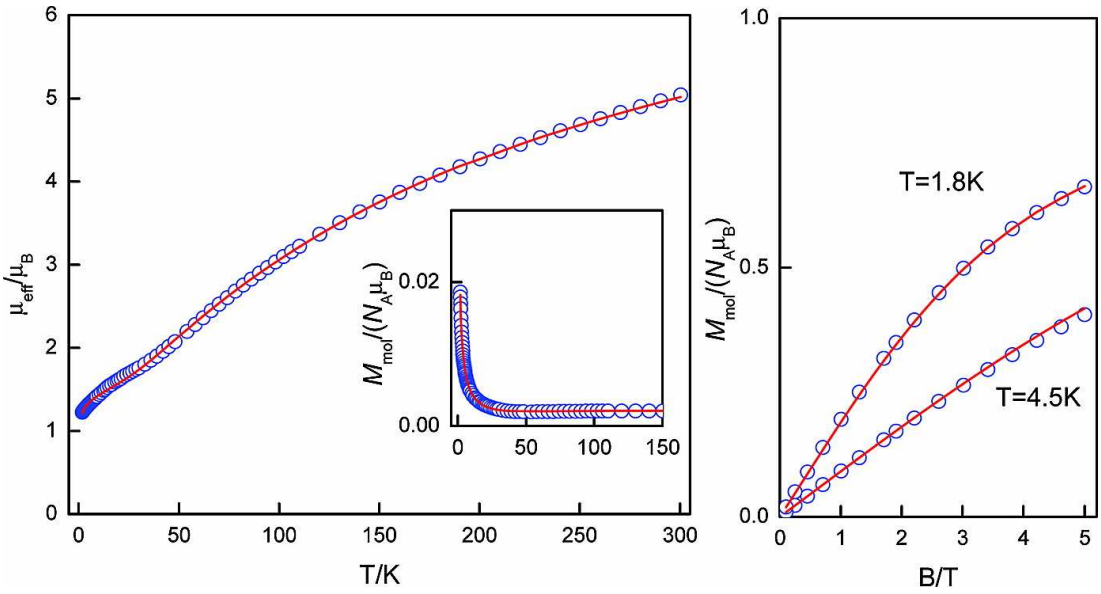

(b) The best-fit for J_{12}/hc = J_{23}/hc = -70.6 cm^{-1} and J_{13}/hc = -80.8 cm^{-1}.

Figure 5.5 Temperature dependence of the effective magnetic moment and magnetisation for $[Fe_3(\mu_3\text{-}O)(\mu\text{-}4\text{-}O_2N\text{-}pz)_6Cl_3](Bu_4N)_2$. The open circles represent experimental data and solid line shows the best-fit for (a) $|J_{12}| = |J_{23}| > |J_{13}|$ and (b) $|J_{12}| = |J_{23}| < |J_{13}|$.

(1) Based on the symmetry (C_{2V}) of the $[Fe_3(\mu_3\text{-}O)(\mu\text{-}4\text{-}O_2N\text{-}pz)_6X_3]^{2-}$ systems, Fe(1)-Fe(2) and Fe(2)-Fe(3) bond distances are almost identical, and therefore $|J_{12}| = |J_{23}| \neq |J_{13}|$.

(2) The g factors for Fe(III) are fixed at $g_x = g_y = g_z = 2.0$.

(3) Asymmetric exchange is neglected, $\mathbf{(D_{ij} = 0)}$.

(4) The antisymmetric exchange vector is equal for each pair, $\mathbf{d_{12} = d_{23} = d_{31} = d}$, and only the z-component was assumed to be non-zero, i.e. $d_x = d_y = 0$.

The experimental exchange coupling constants for $[Fe_3(\mu_3\text{-}O)(\mu\text{-}4\text{-}O_2N\text{-}pz)_6Cl_3]^{2-}$ were estimated by considering the temperature dependence of the magnetisation at an applied field of B = 0.1 T and the field dependence of the magnetisation at 1.8 and 4.5 K (Figure 5.5).

Table 5.3 Experimental and calculated exchange coupling constants (experimental data shows the best-fit for $|J_{12}| = |J_{23}| > |J_{13}|$ and $|J_{12}| = |J_{23}| < |J_{13}|$).

Experimental fits	**Computed J_{ij}**	**Computed J'_{ij}**
$[Fe_3(\mu_3\text{-}O)(\mu\text{-}4\text{-}O_2N\text{-}pz)_6Cl_3]^{2-}$		
J_{12}/hc = -80.1 cm^{-1} J_{23}/hc = -80.1 cm^{-1} J_{13}/hc = -72.4 cm^{-1}	J_{12}/hc = -108.1 cm^{-1} J_{23}/hc = -108.7 cm^{-1} J_{13}/hc = -104.9 cm^{-1}	J_{12}/hc = -90.1, cm^{-1} J_{23}/hc = -90.1 cm^{-1} J_{13}/hc = -87.4 cm^{-1}
J_{12}/hc = -70.6 cm^{-1} J_{23}/hc = -70.6 cm^{-1} J_{13}/hc = -80.8 cm^{-1}		
$[Fe_3(\mu_3\text{-}O)(\mu\text{-}4\text{-}O_2N\text{-}pz)_6Br_3]^{2-}$		
J_{12}/hc = –82.7 cm^{-1} J_{23}/hc = –82.7 cm^{-1} J_{13}/hc = –79.7 cm^{-1}	J_{12}/hc = -103.8 cm^{-1} J_{23}/hc = -102.8 cm^{-1} J_{13}/hc = -105.2 cm^{-1}	J_{12}/hc = -86.6 cm^{-1} J_{23}/hc = -85.7 cm^{-1} J_{13}/hc = -87.6 cm^{-1}
J_{12}/hc = –80.8 cm^{-1} J_{23}/hc = –80.8 cm^{-1} J_{13}/hc = –97.5 cm^{-1}		

It is important to emphasise that the presence of four parameters leaves the system over-parameterised, and it is often possible to identify more than one set that provides a good fit to the data. In the $Fe_3(\mu_3\text{-O})$ clusters of interest here, two quite different parameter sets were found for both X = Cl and X = Br (Table 5.3).[403] In one case, $|J_{12}| = |J_{23}| > |J_{13}|$ while in the other $|J_{12}| = |J_{23}| < |J_{13}|$. In terms of the interactions between metal ions, the difference has important implications: for $|J_{12}| = |J_{23}| > |J_{13}|$, the coupling between irons Fe(1) and Fe(3) is less antiferromagnetic than between Fe(1) and Fe(2) and between Fe(2) and Fe(3), while for $|J_{12}| = |J_{23}| < |J_{13}|$ the opposite is true. Given that the Fe(1)-Fe(3) distance is smaller than Fe(1)-Fe(2) and Fe(2)-Fe(3), it is important to establish which of these two sets of values is correct. In this section, we calculated exchange coupling constants (J_{ij}) as defined through the Heisenberg Hamiltonian [Equation (5.2)]. Recent computational studies of dinuclear and polynuclear complexes, in particular with DFT using hybrid functionals, indicated that this is a good approximation to predict exchange coupling constants and magnetic properties with a reasonable level of accuracy. The HDVV spin Hamiltonian for the $[Fe_3(\mu_3\text{-O})(\mu\text{-4-}O_2\text{N-pz})_6X_3]^{2-}$ systems can be written as;

$$\hat{H}_{\text{Heisenberg}} = -J_{12}\,\mathbf{S}_1 \cdot \mathbf{S}_2 - J_{23}\,\mathbf{S}_2 \cdot \mathbf{S}_3 - J_{13}\,\mathbf{S}_1 \cdot \mathbf{S}_3 \qquad (5.5)$$

The parameters describing the interactions between localised electron spins namely J_{12}, J_{23}, and J_{13}, can be estimated by using the broken symmetry (BS) approach developed by Noodleman and co-workers.[413-416] This method establishes the one-to-one mapping between diagonal elements of the HDVV spin Hamiltonian matrix computed in products of single-centre spin functions and diagonal elements of the exact non-relativistic Hamiltonian matrix computed in single determinant wave functions for a state with HS (M_S = 15/2) and a BS (M_S = 5/2) state. The energies of the HS, BS1, BS2, and BS3 spin configurations (Figure 5.3) are relatively straightforward to compute with DFT. The diagonal elements of the HDVV Hamiltonian can be computed as follows:

$$\text{HS: } |5/2\rangle\,|5/2\rangle\,|5/2\rangle = |\alpha\alpha\alpha\rangle$$

$$E_{HS} = \left(-25/4\right)\left[J_{12} + J_{23} + J_{13}\right] \tag{5.6}$$

$$BS1: \left|-5/2\right\rangle \left|5/2\right\rangle \left|5/2\right\rangle = \left|\beta\alpha\alpha\right\rangle$$

$$E_{BS1} = \left(-25/4\right)\left[-J_{12} + J_{23} - J_{13}\right] \tag{5.7}$$

$$BS2: \left|5/2\right\rangle \left|-5/2\right\rangle \left|5/2\right\rangle = \left|\alpha\beta\alpha\right\rangle$$

$$E_{BS2} = \left(-25/4\right)\left[-J_{12} - J_{23} + J_{13}\right] \tag{5.8}$$

$$BS3: \left|5/2\right\rangle \left|5/2\right\rangle \left|-5/2\right\rangle = \left|\alpha\alpha\beta\right\rangle$$

$$E_{BS3} = \left(-25/4\right)\left[J_{12} - J_{23} - J_{13}\right] \tag{5.9}$$

Then, the differences between these energies can be related directly to exchange coupling constants:

(5.6) – (5.7)

$$E_{HS} - E_{BS1} = \left(-50/4\right)\left[J_{12} + J_{13}\right] \tag{5.10}$$

(5.6) – (5.8)

$$E_{HS} - E_{BS2} = \left(-25/4\right)\left[J_{12} + J_{23}\right] \tag{5.11}$$

(5.6) – (5.9)

$$E_{HS} - E_{BS3} = \left(-25/4\right)\left[J_{23} + J_{13}\right] \tag{5.12}$$

The exchange coupling constants J_{12}, J_{23}, and J_{13} can be calculated by solving Equations (5.10), (5.11), and (5.12). It is important to notice that the projection implicit in the Noodleman scheme typically overestimates the calculated exchange coupling constants. Ruiz and co-workers have suggested that this is because the spin-projection implied in

the mapping of BS-state energies onto the diagonal elements of the isotropic exchange Hamiltonian accounts for non-dynamical electron correlation[417-423], which is already accounted for to some extent in the UDFT-BS solutions. Based on this idea, Ruiz proposed an alternative expression [Equation (5.13)] to obtain exchange coupling constants for dinuclear systems. This method have been shown to yield much better agreement between calculated (in particular DFT with the B3LYP functional) and experimental values of exchange coupling constants. This empirical approach can be extended to polynuclear systems by considering interactions between metal ions in a pairwise manner.[424]

$$E_{HS} - E_{BS} = -J'_{ij}(2S_iS_j + S_j) \tag{5.13}$$

In the Noodleman approach described above, the corresponding expression for a pair of interacting centres is;

$$E_{HS} - E_{BS} = -J_{ij}(2S_iS_j) \tag{5.14}$$

Then, a relationship between J'_{ij} and J_{ij} can be established by combining equation (5.13) and (5.14).

$$J'_{ij}(2S_iS_j + S_j) = J_{ij}(2S_iS_j)$$

$$J'_{ij} = J_{ij}\,\frac{(2S_iS_j)}{(2S_iS_j + S_j)} \tag{5.15}$$

In the case of $[Fe_3(\mu_3\text{-}O)(\mu\text{-}4\text{-}O_2N\text{-}pz)_6X_3]^{2-}$ complexes containing Fe^{3+} (d^5) core ions $S = 5/2$, and substituting this value to the above equation yields,

$$J'_{ij} = (5/6)\,J_{ij} \tag{5.16}$$

Therefore, J'_{ij} values using the Ruiz approach can easily be generated from those using Noodleman's model, and in this work, we compare both J'_{ij} and J_{ij}. Calculated and experimental exchange coupling constants are summarised in Table 5.3. It is important to notice that the experimental fits considered C_{2V} symmetry of both chlorinated and brominated complexes, and therefore $J_{12} = J_{23}$. In contrast, we made no assumptions about symmetry in our UBS-DFT approach. The calculated values confirm the dominant antiferomagnetic nature of the Fe centres of the both $[Fe_3(\mu_3\text{-}O)(\mu\text{-}4\text{-}O_2N\text{-}pz)_6X_3]^{2-}$ complexes. The absolute values obtained with Noodleman's approach [Equation (5.14)] were significantly higher than the experimental fits, but the suppression of long-range correlation effects of the B3LYP functional in the Ruiz approach [Equation (5.13)] results in a good agreement with the experimental results. Therefore, we continue the discussion with the calculated *Js* from Ruiz's method.

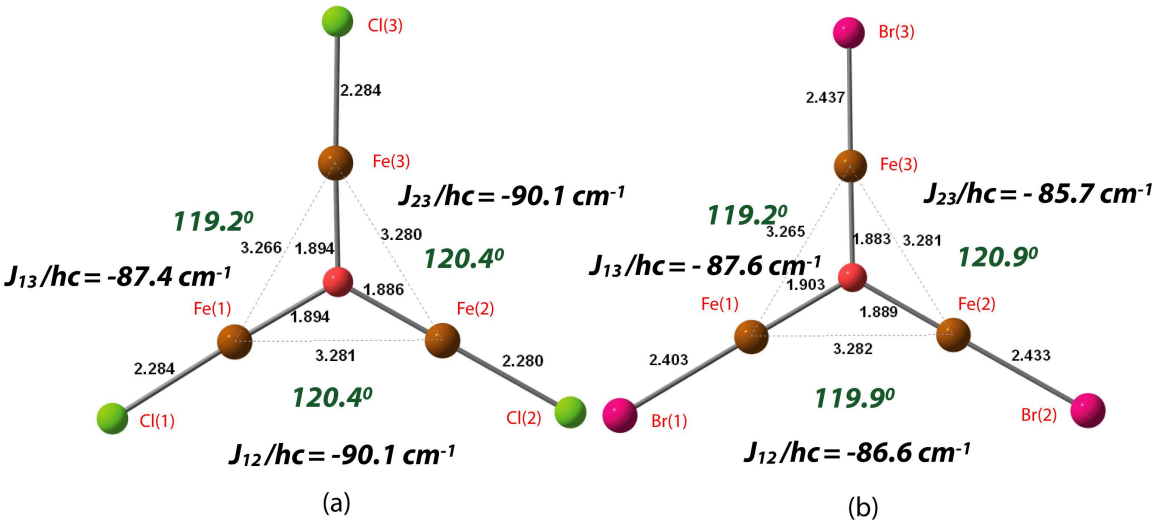

Figure 5.6 Calculated exchange coupling constants and key structural parameters (Å) of the crystal structures of (a) $[Fe_3(\mu_3\text{-}O)(\mu\text{-}4\text{-}O_2N\text{-}pz)_6Cl_3]^{2-}$ and (b) $[Fe_3(\mu_3\text{-}O)(\mu\text{-}4\text{-}O_2N\text{-}pz)_6Br_3]^{2-}$ complexes.

The symmetry of the crystal structure of $[Fe_3(\mu_3\text{-}O)(\mu\text{-}4\text{-}O_2N\text{-}pz)_6Cl_3]^{2-}$ leads to identical Fe(1)-(μ_3-O)-Fe(2) and Fe(2)-(μ_3-O)-Fe(3) angles of 120.4^0 (Figure 5.6), as a result of which the calculated J_{12} and J_{23} are equivalent [J_{12}/hc = J_{23}/hc = -90.1 cm^{-1}]. The coupling between Fe(1) and Fe(3) is rather smaller (J_{13}/hc = -87.4 cm^{-1}), so our

calculated exchange coupling constants support the experimental fitting where $|J_{12}| = |J_{23}| > |J_{13}|$. At first sight, this seems surprising as the Fe(1)-Fe(3) distance is the shortest of the three. However, the magnetic coupling between Fe *d* electrons in these systems does not occur directly 'through space' but rather *via* superexchange mediated by the μ_3-O *p* of $[Fe_3(\mu_3\text{-}O)(\mu\text{-}4\text{-}O_2N\text{-}pz)_6X_3]^{2-}$. This superexchange is highly dependent on the Fe-(μ_3-O)-Fe angles: according to the Goodenough-Kanamori rules,[434,435] antiferromagnetic exchange is favoured in linear Fe-O-Fe geometries, while ferromagnetic coupling is favoured where the Fe-(μ_3-O)-Fe angle is 90^0. Thus the marginally smaller Fe(1)-O-Fe(3) angle reduces the antiferromagnetic exchange between these centres. The situation is less clear-cut for the $[Fe_3(\mu_3\text{-}O)(\mu\text{-}4\text{-}O_2N\text{-}pz)_6Br_3]^{2-}$ complex, where the absence of symmetry elements means that all three coupling constants are different. In this case, the three calculated J_{ij} are rather similar, and it is difficult to establish a clear magneto-structural correlation.

5.3.3 Evaluation of ^{57}Fe Mössbauer parameters

Mössbauer spectroscopy is associated with the resonant emission or absorption of a gamma photon by the atomic nucleus, where the energy of gamma radiation causes energy level transitions in the atomic nucleus itself. These energy levels can be influenced by both the electronic and magnetic environment of the atomic nucleus, and such changes in the energy levels can provide information about the local environment within a system.[433,435] Therefore, Mössbauer spectroscopy is a very useful spectroscopic technique to explore interactions between the nucleus and its environment. Mössbauer spectra of $[Fe_3(\mu_3\text{-}O)(\mu\text{-}4\text{-}O_2N\text{-}pz)_6X_3](Bu_4N)_2$, recorded in the 4.2-300 K range and zero magnetic field, are shown in Figure 5.7. Each spectrum contains a symmetric quadrupole doublet with $\delta = 0.43(1)$ mm s^{-1} and $\Delta E_Q = 1.02(2)$ mm s^{-1} at 78 K.[403,404] At higher temperature, 293 K, the isomer shift is reduced to $\delta = 0.32(1)$ mm s^{-1}, but there is no significant change observed for ΔE_Q. Changes in the isomer shift upon oxidation or reduction have been used extensively to establish the nature (localised/delocalised) of

mixed valent systems. However, these methods rely entirely on the existence of unambiguous assignment of the peaks in the precursors where all iron centres have the same oxidation state. In the systems of interest here the assignments are indeed unambiguous, but this is not the case in, for example, the Fe_8 cluster reported by Raptis and co-workers,[403] where two chemically distinct types of iron centres are present.

Our purpose here is to establish the accuracy of DFT methods in computing Mössbauer parameters in exchange-coupled clusters, with a view of using DFT to establish definitive assignments of peaks in cases where there is such ambiguity. Over the last few years DFT has been used for predicting Mössbauer parameters in a range of mononuclear iron complexes, but has not yet been applied to clusters.[425-432] In the previous section we emphasised that the broken-symmetry wavefunctions are not eigen states of the full spin Hamiltonian, and as such it is not obvious that they provide a good foundation for the computation of spectroscopic parameters. Thus we particularly aim to establish the extent to which the parameters depend on the coupling between the metal centres.

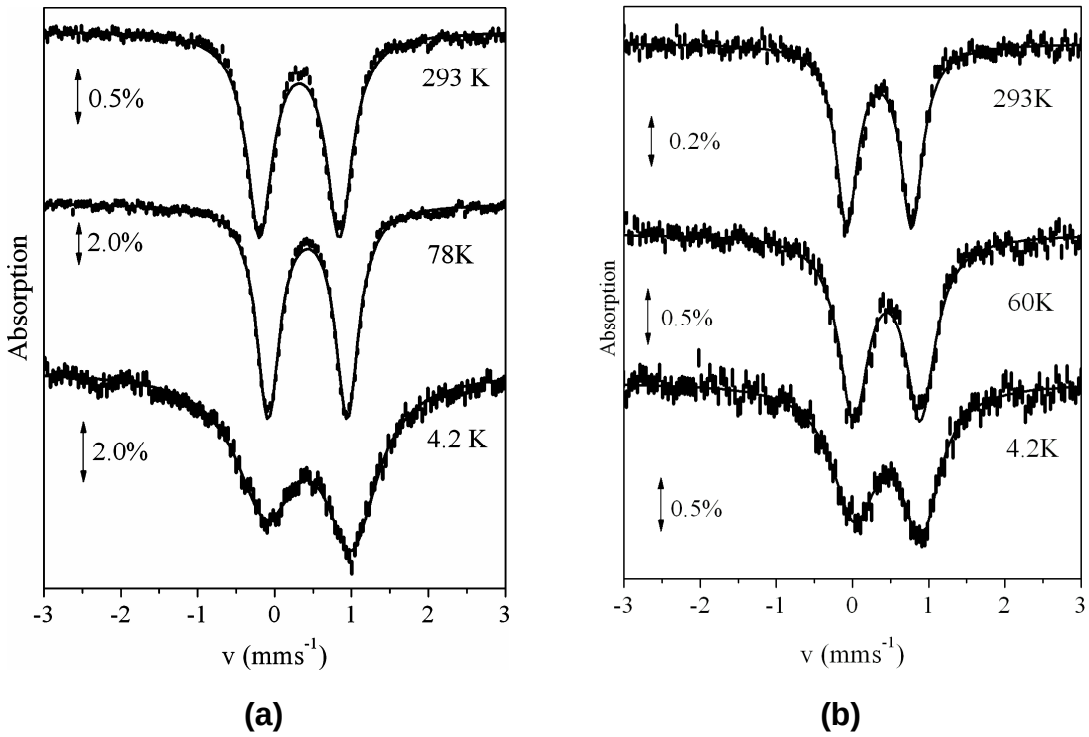

Figure 5.7 Mössbauer spectra of (a) $[Fe_3(\mu_3\text{-}O)(\mu\text{-}4\text{-}O_2N\text{-}pz)_6Cl_3](Bu_4N)_2$ and (b) $[Fe_3(\mu_3\text{-}O)(\mu\text{-}4\text{-}O_2N\text{-}pz)_6Br_3](Bu_4N)_2$ at 293, 78, and 4.2 K.

5.3.3.1 The Mössbauer effect

Mössbauer spectra are described by three important parameters, namely isomer shift (IS or δ), quadrupole splitting (QS or ΔE_Q) and hyperfine splitting (for magnetic materials only) (Figure 5.8).[433] In the transmission spectrum for the simplest case (blue), the shift away from zero velocity is due to the fact that the source and the absorber atoms are in different local environments and this shift is generally called isomer shift (δ). Interaction of the nuclear quadrupole moment with the electric field gradient splits the transmission spectrum of ^{57}Fe into doublets (red), where the 1/2 and 3/2 labels represent the nuclear spin quantum numbers **I** (or intrinsic angular momentum), and the separation between the two component peaks of a doublet is defined as the quadrupole splitting (QS or ΔE_Q).

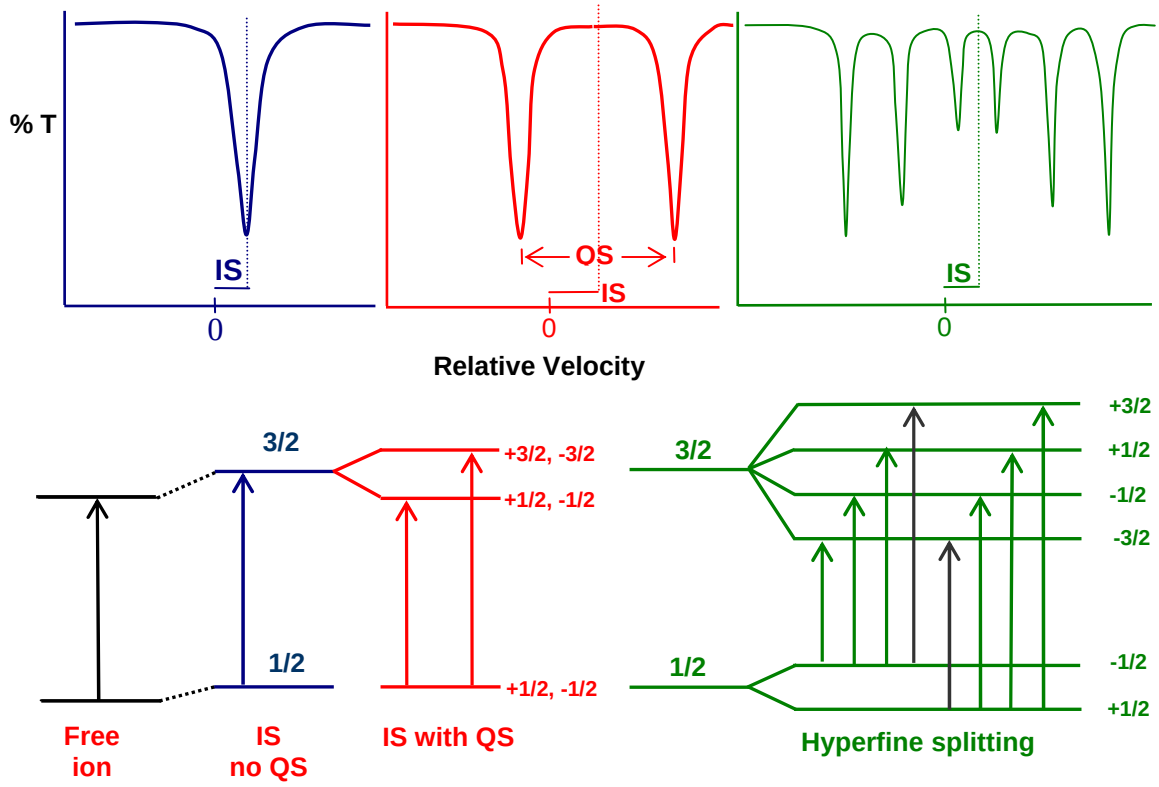

Figure 5.8 The three important parameters, namely isomer shift (IS or δ), quadrupole splitting (QS or ΔE_Q) and hyperfine splitting (for magnetic materials only).

In the presence of a magnetic field, Zeeman splitting is possible, which gives rise to a sextet pattern (green) with the line ratio 3:2:1:1:2:3. Moreover, this hyperfine splitting is caused by the electrons around the Fe atom(s), which create a magnetic field, and then the energy levels in the Fe nucleus split into six possible nuclear transitions. It is important to note that the transitions shown in gray, m_I = -1/2 to +3/2 and m_I = +1/2 to -3/2, are forbidden as they do not follow the selection rule ($|\Delta m_I| \leq 1$). The positions of the peaks in the sextet are defined as the hyperfine splitting of the nuclear energy levels. Under zero applied magnetic field, the Mössbauer parameters, specifically isomer shift (δ) and the quadrupole splitting (ΔE_Q) of a given iron centre are related to the total electron density of a given iron centre itself.[433,434] Therefore, Mössbauer spectroscopy reveals valuable information about the electron shielding, bond hybridisation and symmetry (structure) of ^{57}Fe complexes.[433] The isomer shift critically depends on the local environment of the Fe nucleus in the absorber and is shown to be proportional to the electron density at a Fe nucleus (ρ_0), and which can be expressed as,

$$\delta = \frac{4}{5}\pi Z S(Z) e_0^2 R^2 \left(\frac{\delta R}{R}\right)\left[\rho_0^A(0) - \rho_0^S(0)\right] \tag{5.17}$$

where Z is the nuclear charge of the Mössbauer absorber, *S(Z)* is the relativistic correlation factor, e_0 is the elementary charge, *R* is one-half of the sum of the radii of the Mössbauer nucleus in the ground and the excited states, δR is the difference of the two radii, $\rho_0^A(0)$ is the non-relativistic electron density at the nucleus for the Mössbauer absorber, $\rho_0^S(0)$ is the same quantity for a given standard. The above equation can be simplified as,

$$\delta = a\left[\rho_0^A(0) - C\right] + b \tag{5.18}$$

The constants *a* and *b* can be estimated by plotting calculated values of $\rho_0^A(0)$ versus experimental isomer shifts. The fit parameters *a* and *b* can the be used to estimate isomer shifts for calculated $\rho_0^A(0)$ values. Neese and co-workers have established suitable fit parameters for Fe using the hybrid B3LYP functional.[427]

$$\Delta E_Q = \frac{1}{2} eQV_z \sqrt{1+\frac{1}{3}\eta^2} \quad (5.19)$$

The second important quantity, quadrupole splitting (ΔE_Q) provides information about the asymmetry of the electron density in the vicinity of the MB atom (^{57}Fe). ΔE_Q can be calculated from the electric field gradient V_i (i = x, y, z) and asymmetry parameter η = $(V_X - V_Y)/V_Z$, where V_X, V_Y and V_Z are the principal components of the electric field gradient tensors in a coordinate system, and e is the electric charge, and Q(^{57}Fe) is defined as the nuclear quadrupole moment. The quadrupole splitting derives from the asymmetric occupations of *p*-, *d*-, and *f*-electron orbitals, and therefore ΔE_Q is related directly to the geometry of the compound.[433] Many studies demonstrated that the sign and the magnitude of quadrupole splitting can be calculated accurately at the B3LYP level.[425-431]

5.3.3.2 Calculated Mössbauer parameters

In Table 5.4 we compare experimental Mössbauer parameters for $[Fe_3(\mu_3\text{-}O)(\mu\text{-}4\text{-}O_2N\text{-}pz)_6X_3]$ with computed values. The calculations have been performed for the HS (M_S = 15/2) and the BS1 (M_S = 5/2) states. We have also compared values for the crystal structure and optimised structure in order to establish the magnitude of the possible error if we had to rely solely on a computed geometry. The calculated isomer shifts for the HS (average 0.39 mm s^{-1}) and BS1 (0.40 mm s^{-1}) states of the crystal structure of $[Fe_3(\mu_3\text{-}O)(\mu\text{-}4\text{-}O_2N\text{-}pz)_6Cl_3]^{2-}$ system are very similar, and both are in good agreement with the experimental value (0.43 cm^{-1}) reported at 78 K. The calculated isomer shifts for the brominated system $[Fe_3(\mu_3\text{-}O)(\mu\text{-}4\text{-}O_2N\text{-}pz)_6Br_3]$ are rather similar to those for chlorinated species, whereas the experimental values are rather different (0.47 and 0.43 mm s^{-1}). This may reflect inadequacies in the computational strategy but it is important to note that the experimental values are strongly temperature dependent, which complicates comparisons with computed values. Most importantly, our results indicate that the isomer shift is not strongly dependent on the chosen configuration. This is

perhaps unsurprising as the isomer shift depends on electron density at the nucleus, which should be rather similar for both configurations.

Table 5.4 Comparison of experimental and calculated Mössbauer parameters of the $[Fe_3(\mu_3\text{-}O)(\mu\text{-}4\text{-}O_2N\text{-}pz)_6X_3]^{2-}$ complexes.

	Experimental			Calculated parameters			
				Crystal structure		Optimised structures	
	78 K	293 K		HS (M_S = 15/2)	BS1 (M_S = 5/2)	HS (M_S = 15/2)	BS1 (M_S = 5/2)
$[Fe_3(\mu_3\text{-}O)(\mu\text{-}4\text{-}O_2N\text{-}pz)_6Cl_3]^{2-}$							
δ (mm s^{-1})	0.43(1)	0.32(1)	Fe(1)	0.39	0.39	0.43	0.43
			Fe(2)	0.39	0.39	0.43	0.43
			Fe(3)	0.39	0.40	0.44	0.43
			Average	0.39	0.40	0.43	0.43
$\|\Delta E_Q\|$ (mm s^{-1})	1.02(2)	1.02(2)	Fe(1)	0.99	1.00	1.08	1.25
			Fe(2)	1.10	1.04	1.06	0.95
			Fe(3)	0.99	0.92	1.08	0.96
			Average	1.03	0.99	1.07	1.05
$[Fe_3(\mu_3\text{-}O)(\mu\text{-}4\text{-}O_2N\text{-}pz)_6Br_3]^{2-}$							
δ (mm s^{-1})	0.47(1)	0.35(1)	Fe(1)	0.39	0.39	0.44	0.44
			Fe(2)	0.39	0.39	0.44	0.44
			Fe(3)	0.39	0.39	0.44	0.44
			Average	0.39	0.39	0.44	0.44
$\|\Delta E_Q\|$ (mm s^{-1})	0.87(2)	0.85(2)	Fe(1)	0.93	0.92	0.94	1.10
			Fe(2)	0.93	0.91	0.95	0.83
			Fe(3)	0.96	0.95	0.93	0.81
			Average	0.95	0.93	0.93	0.91

The computed isomer shifts for the corresponding optimised HS and BS1 states were slightly higher (difference is ~ 0.03 mm s^{-1}), but again no significant differences between the configurations emerged. Calculated ΔE_Q values for the crystal structure of the chlorinated system (HS or BS1 states) are also strikingly similar to the experimental values (78 K). However, computed ΔE_Q values for the optimised structure showed

stronger deviations from the experimental values. The average value is ~0.1 mm s^{-1} larger in the optimised structures, and the individual values show a much greater spread. The variation within each set is a direct consequence of the much shorter Fe(1)-O distance in BS1. As we noted previously, this shortening simply reflects the fact that BS1 is not a true eigen state, and the real structure represents an average of the three broken-symmetry states, BS1, BS2 and BS3, where the contraction occurs along different bonds. The variation is therefore an artefact arising from the use of a broken-symmetry wavefunction to optimise the geometries.

5.4 Conclusions

Detailed electronic structure analysis of $[Fe_3(\mu_3\text{-}O)(\mu\text{-}4\text{-}O_2N\text{-}pz)_6X_3]^{2-}$ complexes revealed that there are four key spin configurations namely HS, BS1, BS2 and BS3, where the HS (M_S = 15/2) state contains five spin-α electrons on each Fe centre, while the BS (M_S = 5/2) states contain five spin-β electrons mostly localised on one iron centre and the remaining 10 spin-α electrons on the other two Fe sites. In the presence of C_{2V} symmetry there are only two unique broken symmetry states (i.e. the BS2 and BS3 states are almost identical), and these BS states are clearly more stable than the HS configuration.

Calculation of the exchange coupling constants for $[Fe_3(\mu_3\text{-}O)(\mu\text{-}4\text{-}O_2N\text{-}pz)_6X_3]^{2-}$ complexes employed an extension of the computational strategies proposed by Noodleman and co-workers or Ruiz and co-workers, where we considered the isotropic Heisenberg Hamiltonian for calculating J_{ij} (or J'_{ij}) values through the UBS-DFT approach. Even with this approximation, calculated exchange coupling constants are in good agreement with the experimental fits, in particular with Ruiz's approach. Our calculated exchange coupling constants for $[Fe_3(\mu_3\text{-}O)(\mu\text{-}4\text{-}O_2N\text{-}pz)_6Cl_3]^{2-}$ system confirmed that $|J_{12}| = |J_{23}| > |J_{13}|$. In contrast, for the brominated systems $|J_{12}| \sim |J_{23}| < |J_{13}|$.

Theoretical prediction of Mössbauer parameters with the B3LYP hybrid method for the $[Fe_3(\mu_3\text{-}O)(\mu\text{-}4\text{-}O_2N\text{-}pz)_6X_3]^{2-}$ systems showed accurate estimation of both the isomer shifts (δ) and the nuclear quadrupole splitting (ΔE_Q). Our DFT results clearly indicate that different spin density distributions, in particular M_S = 15/2 and M_S = 5/2 configurations have no significant impact on the calculated Mössbauer parameters for a given structure. However, structure optimisations of various electronic configurations significantly affect the geometry of metal coordination spheres, as a result of which the calculated ΔE_Q values can deviate substantially from the experimentally predicted parameters, in particular for the optimised broken symmetry states. This condition may be a significant challenge in computing ΔE_Q in cases where the geometry is unknown.

Appendix A

The pK_a values reported in this thesis were calculated by considering the acid (AH) dissociation process as a sum of several intermediate steps as shown in the following thermodynamic cycle.[357-359]

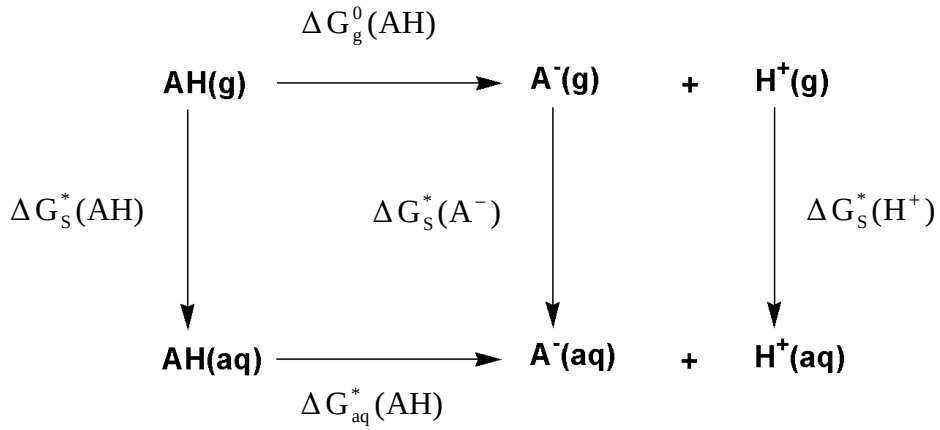

All calculated gas-phase free energies employed an ideal gas at 1 atm as the reference state, which is denoted by the superscript degree symbol. Free energies that employ in the standard-state definition are denoted by a superscript asterisk.[358] The free energy of acid dissociation in solution, $\Delta G_{aq}^*(AH)$, can be calculated by considering the Hess's law;

$$\Delta G_{aq}^*(AH) = \Delta G_g^0(AH) + \Delta G_S^*(A^-) + \Delta G_S^*(H^+) - \Delta G_S^*(AH) - \Delta G_S^{*\to 0} \quad (1)$$

Then, *K*a and p*K*a can be obtained through the following thermodynamic relationships;

$$\Delta G_{aq}^*(AH) = - RT \ln(K_a) \quad (2)$$

$$\Delta G_{aq}^*(AH) = 2.303\, RT\, (pK_a) \quad (3)$$

The $\Delta G_g^0(AH)$ of the Equation (1) was obtained by performing gas phase optimisations followed by frequency calculations for **AH** and $\mathbf{A}^-$. Solvation free energies of **AH** [$\Delta G_S^*(AH)$] and $\mathbf{A}^-$ and [$\Delta G_S^*(A^-)$] were calculated by a self-consistent reaction field (SCRF) approach,[436-438] where these calculations were performed at the gas phase optimised geometries with dielectric constant (ε) value of 78.35 (water). We have used solvation free energy of the proton, $\Delta G_S^*(H^+)$ = - 265.9 kcal mol^{-1}, reported by Tissandier *et al.* [439] and $\Delta G_S^{*\rightarrow 0}$ has been reported to be 1.9 kcal mol^{-1}.[358]

References

[1] E. Merzbacher, *Quantum Mechanics*, Wiley, New York, 2nd edition, 1970.

[2] I. N. Levine, *Quantum Chemistry*, Prentice Hall, Englewood Cliffs, NJ, 4th edition, 1991.

[3] A. Szabo and N. S. Ostlund, *Modern Theoretical Chemistry*, MacMillan Pub. Inc., New York, 1982.

[4] R. McWeeny, *Methods of Molecular Quantum Mechanics*, Academic Press, London, 1992.

[5] M. Born and R. Oppenheimer, *Annalen der Physik*, 1927, **389**, 457.

[6] M. Massimi, *Pauli's Exclusion Principle*, Cambridge University Press, 2005.

[7] J. C. Slater, *Phys. Rev.*, 1929, **34**, 1293.

[8] J. C. Slater, *Phys. Rev.*, 1930, **35**, 509.

[9] V. Fock, *Z. Phys.*, 1930, **61**, 126.

[10] W. Pauli, *Z. Phys.*, 1925, **31**, 765.

[11] N. M. Hugenholtz, *Phys. Rev.*, 1954, **96**, 1158.

[12] P. Löwdin, *Phys. Rev.*, 1955, **97**, 1509.

[13] J. Quintanilla and C. Hooley, *Physics World*, 2009, **22**, 37.

[14] C. J. Cramer, *Essentials of Computational Chemistry*, Chichester, John Wiley & Sons, Ltd., 2002, pp. 191.

[15] R. McWeeny, *Coulson's Valence*, Oxford University Press, 1979, pp. 124.

[16] F. Jensen, *Introduction to Computational Chemistry*, Chichester, England, John Wiley and Sons, 2007, pp. 133.

[17] R. McWeeny, Methods of Molecular Quantum Mechanics, Academic Press, London, 1992.

[18] R. J. Bartlett, *Ann. Rev. Phys. Chem.*, 1981. **32**, 359.

[19] C. Møller and M. S. Plesset, *Phys. Rev.*, 1934, **46**, 618.

[20] M. L. Leininger, W. D. Allen, H. F. Schaefer and C. D. Sherrill, *J. Chem. Phys.*, 2000, **112** , 9213.

[21] J. Cizek, *J. Chem. Phys.*, 1966, **45,** 4256.

[22] J. Cizek, *Adv. Chem. Phys.*, 1969, **14**, 35.

[23] J. A. Pople, M. H. Gordon and K. Raghavachari, *J. Chem. Phys.*, 1987, **87**, 5968.

[24] G. E. Scuseria, C. L. Janssen and H. F. Schaefer, *J. Chem. Phys.*, 1988, **89**, 7382.

[25] G. E. Scuseria and H. F. Schaefer, *J. Chem. Phys.*, 1989, **90,** 3700.

[26] W. Koch and M. C. Holthausen, *A Chemist's Guide to Density Functional Theory*, Wiley-VCH, Weinheim, 2nd edition, 2002.

[27] R. G. Parr and W. Yang, *Density Functional Theory of Atoms and Molecules*, Oxford University Press, New York, 1989.

[28] J. N. Harvey, *Annu. Rep. Prog. Chem., Sect. C.*, 2006, **102**, 203.

[29] F. Neese, *Coord. Chem. Rev.*, 2009, **253**, 526.

[30] P. Hohenberg and W. Kohn, *Phys. Rev.*, 1964, **136**, B864.

[31] W. Kohn and L. J. Sham, *Phys. Rev.*, 1965, **140**, A1133.

[32] D. M. Ceperley and B. J. Alder, *Phys. Rev. Lett.*, 1980, **45**, 566.

[33] J. C. Slater, *Phys. Rev.*, 1951, **81**, 385.

[34] D. M. Ceperley and B. J. Alder, *Phys. Rev. Lett.*, 1980, **45**, 566.

[35] S. H. Vosko, L. Wilk and M. Nusair, *Can. J. Phys.*, 2000, **58**, 1200.

[36] J. P. Perdew, K. Burke and M. Ernzerhof , *Phys. Rev. Lett.*, 1996, **77**, 3865.

[37] A. D. Becke, *Phys. Rev. A*, 1988, **38**, 3098.

[38] J. P. Perdew, *Phys. Rev. B*, 1986, **33,** 8822.

[39] J. P. Perdew, *Electronic Structure of Solids*, P. Ziesche and H. Eschrig (Ed.), Akademie Verlag, Berlin, 1991.

[40] J. P. Perdew, J. A. Chevary, S. H. Vosko, K. A. Jackson, M. R. Pederson, D. J. Singh and C. Fiolhais, *Phys. Rev. B*, 1992, **46**, 6671.

[41] A. D. Becke, *J. Chem. Phys.*, 1996, **104,** 1040.

[42] C. Lee, W. Yang and R. G. Parr, *Phys. Rev. B*, 1988, **37**, 785.

[43] B. Miehlich, A. Savin, H. Stoll and H. Preuss, *Chem. Phys. Lett.*, 1989, **157**, 200.

[44] J. P. Perdew, A. Ruzsinszky, J. Tao, V. N. Staroverov, G. E. Scuseria and G. I. Csonka, *J. Chem. Phys.*, 2005, **123**, 62201.

[45] J. Tao, J. P. Perdew, V. N. Staroverov and G. E. Scuseria, *Phys. Rev. Lett*., 2003, 91, 146401.

[46] A. D. Becke, *J. Chem. Phys*., 1996, **140**, 1040.

[47**]** A. D. Becke, *J. Chem. Phys*., 1993, **98**, 5648.

[48] A. D. Becke, *Phys. Rev. A*., 1997, **107**, 8554.

[49] J. P. Perdew, J. A. Chevary, S. H. Vosko, K. A. Jackson, M. R. Pederson, D. J. Singh and C. Fiolhais, *Phys. Rev. B*, 1992, **46**, 6671.

[50] V. N. Staroverov, G. E. Scuseria, J. Tao and J. P. Perdew, *J. Chem. Phys*., 2003, **119**, 12129.

[51] C. Adamo and V. Barone, *J. Chem. Phys.*, 1999, **110**, 6158.

[52] Y. Zhao and D. G. Truhlar, *Theor. Chem. Acc.*, 2008, **120**, 215.

[53] Y. Zhao and D. G. Truhlar, *J. Phys. Chem. A*, 2006, **110**, 13126.

[54] Y. Zhao and D. G. Truhlar, *J. Phys. Chem.*, 2006, **110**, 5121.

[55] Y. Zhao, N. E. Schuitz and D. G. Truhlar, *J. Chem. Theory and Comput*, 2006, **2**, 364.

[56] Y. Zhao, N. E. Schuitz and D. G. Truhlar, *J. Chem. Phys.*, 200, **123**, 1.

[57] A. D. Becke, *J. Chem. Phys.*, 1993, **98**, 1372.

[58] S. Grimme, *J. Chem. Phys.*, 2006, **124**, 34108.

[59] T. Benighaus, R. A. Distasio, Jr., R. C. Lochan, J. D. Chai and M. H. Gordan, *J. Phys. Chem. A*, 2008, **112**, 2702.

[60] T. Schwabe and S. Grimme, *Phys. Chem. Chem. Phys.*, 2006, **8**, 4398.

[61] T. Schwabe and S. Grimme, *Phys. Chem. Chem. Phys.*, 2007, **9**, 3397.

[62] J. C. Slater, *Phys. Rev.*, 1930, **36**, 57.

[63] S. F. Boys, *Proc. R. Soc. London Ser. A*, 1950, **200**, 542.

[64] W. J. Hehre, R. F. Stewart and J. A. Pople, *J. Chem. Phys.*, 1980, **51,** 2657.

[65] M. Dolg, *Modern Methods and Algorithms of Quantum Chemistry*, Proceedings, 2nd edition, J. Grotendorst (Ed.), John von Neumann Institute for Computing, Julich, NIC Series, 2000, **3**, pp. 507.

[66] W. R. Wadt and P. J. Hay, *J. Chem. Phys*., 1985, **82**, 284.

[67] L. F. Pacios and P. A. Christiansen, *Ab initio relativistic effective potentials with spin-orbit operators, I. Li through Ar*, 1985.

[68] A. Szabo and N. S. Ostlund, *Modern Quantum Chemistry: Introduction to Advanced Electronic Structure Theory*, MacMillan Publishing Co., New York, 1989.

[69] J. Alml and P. R. Taylor, *J. Chem. Phys.*, 1997, **86**, 4070.

[70] T. Hashimoto, K. Hirao and H. Tatewaki, *Chem. Phy. Lett*., 1995, **243**, 190.

[71] T. H. Dunning. *J. Chem. Phys.*, 1989, **90**, 1007.

[72] S. K. Min, E. C. Lee, H. M. Lee, D. Y. Kim, D. Kim and K. S. Kim, *J Comput. Chem.*, 2008, **29**, 1208.

[73] M. J. Frisch, G. W. Trucks, H. B. Schlegel, G. E. Scuseria, M. A. Robb, J. R. Cheeseman, J. A. Montgomery, T. Vreven, K. N. Kudin, J. C. Burant, J. M. Millam, S. S. Iyengar, J. Tomasi, V. Barone, B. Mennucci, M. Cossi, G. Scalmani, N. Rega, G. A. Petersson, H. Nakatsuji, M. Hada, M. Ehara, K. Toyota, R. Fukuda, J. Hasegawa, M. Ishida, T. Nakajima, Y. Honda, O. Kitao, H. Nakai, M. Klene, X. Li, J. E. Knox, H. P. Hratchian, J. B. Cross, V. Bakken, C. Adamo, J. Jaramillo, R. Gomperts, R. E. Stratmann, O. Yazyev, A. J. Austin, R. Cammi, C. Pomelli, J. Ochterski, P. Y. Ayala, K. Morokuma, G. A. Voth, P. Salvador, J. J. Dannenberg, V. G. Zakrzewski, S. Dapprich, A. D. Daniels, M. C. Strain, O. Farkas, D. K. Malick, A. D. Rabuck, K. Raghavachari, J. B. Foresman, J. V. Ortiz, Q. Cui, A. G. Baboul, S. Clifford, J. Cioslowski, B. B. Stefanov, G. Liu, A. Liashenko, P. Piskorz, I. Komaromi, R. L. Martin, D. J. Fox, T. Keith, M. A. Al-Laham, C. Y. Peng, A. Nanayakkara, M. Challacombe, P. M. W. Gill, B. G. Johnson, W. Chen, M. W. Wong, C. Gonzalez and J. A. Pople, *GAUSSIAN 03 (Revision D.02)*, Gaussian, Inc., Wallingford, CT, 2004.

[74] M. J. Frisch, G. W. Trucks, H. B. Schlegel, G. E. Scuseria, M. A. Robb, J. R. Cheeseman, G. Scalmani, V. Barone, B. Mennucci, G. A. Petersson, H. Nakatsuji, M.

Caricato, X. Li, H. P. Hratchian, A. F. Izmaylov, J. Bloino, G. Zheng, J. L. Sonnenberg, M. Hada, M. Ehara, K. Toyota, R. Fukuda, J. Hasegawa, M. Ishida, T. Nakajima, Y. Honda, O. Kitao, H. Nakai, T. Vreven, J. A. Montgomery, J. E. Peralta, F. Ogliaro, M. Bearpark, J. J. Heyd, E. Brothers, K. N. Kudin, V. N. Staroverov, R. Kobayashi, J. Normand, K. Raghavachari, A. Rendell, J. C. Burant, S. S. Iyengar, J. Tomasi, M. Cossi, N. Rega, J. M. Millam, M. Klene, J. E. Knox, J. B. Cross, V. Bakken, C. Adamo, J. Jaramillo, R. Gomperts, R. E. Stratmann, O. Yazyev, A. J. Austin, R. Cammi, C. Pomelli, J. W. Ochterski, R. L. Martin, K. Morokuma, V. G. Zakrzewski, G. A. Voth, P. Salvador, J. J. Dannenberg, S. Dapprich, A. D. Daniels, O. Farkas, J. B. Foresman, J. V. Ortiz, J. Cioslowski, and D. J. Fox, *Gaussian 09, Revision A.02*, Gaussian, Inc., Wallingford CT, 2009.

[75] Jaguar 7.5v, Schrödinger, LLC, New York, NY, 2008.

[76] F. Neese, *ORCA-an ab initio, Density Functional and Semiempirical Program Package,* 2.6-35, University of Bonn: Bonn, Germany, 2008.

[77] T. H. Dunning and P. J. Hay, *Modern Theoretical Chemistry*, H. F. Schaefer (Ed.), Vol. 3, Plenum, New York, 1976, 1.

[78] P. Fuentealba, H. Preuss, H. Stoll and L. V. Szentpaly, *Chem. Phys. Lett.*, 1992, **89**, 418.

[79] P. Fuentealba, H. Stoll, L. V. Szentpaly, P. Schwerdtfeger and H. Preuss, *J. Phys. B*, 1983, **16**, L323.

[80] P. J. Hay and W. R. Wadt, *J. Chem. Phys.*, 1985, **82**, 270.

[81] W. R. Wadt and P. J. Hay, *J. Chem. Phys.*, 1985, **82**, 284.

[82] P. J. Hay and W. R. Wadt, *J. Chem. Phys.*, 1985, **82**, 299.

[83] R. Ditchfield, W. J. Hehre and J. A. Pople, *J. Chem. Phys.*, 1971, **54**, 724.

[84] W. J. Hehre, R. Ditchfield and J. A. Pople, *J. Chem. Phys.*, 1972, **56**, 2257.

[85] A. Schaefer, H. Horn and R. Ahlrichs, *J. Chem. Phys.*, 1992, **97**, 2571.

[86] A. Schaefer, C. Huber and R. Ahlrichs, *J. Chem. Phys.*, 1994, **100**, 5829.

[87] S. Shaik, D. Kumar, S. P. de Visser, A. Altun and W. Thiel, *Chem. Rev.*, 2005, **105**, 2279.

[87] S. Shaik, D. Kumar, S. P. de Visser, A. Altun and W. Thiel, *Chem. Rev.*, 2005, **105**, 2279.

[88] B. Meunier, S. P. de Visser and S. Shaik, *Chem. Rev.*, 2004, **104**, 3947.

[89] E. I. Solomon, *Inorg. Chem.*, 2001, **40**, 3656.

[90] F. Neese, J. M. Zaleski, K. L. Zaleski and E. I. Solomon, *J. Am. Chem. Soc.*, 2000, **122**, 11703.

[91] K. Yoshizawa, Y. Kagawa and Y. Shiota, *J. Phys. Chem. B*, 2000, **104**, 12365.

[92] C. M. Bathelt, L. Ridder, A. J. Mulholland and J. N. Harvey, *J. Am. Chem. Soc.*, 2003, **125**, 15004.

[93] C. M. Bathelt, J. Zurek, A. J. Mulholland and J. N. Harvey, *J. Am. Chem. Soc.*, 2005, **127**, 12900.

[94] M. Radon and E. Broclawik, *J. Chem. Theory Comput.*, 2007, **3**, 728.

[95] I. Wasbotten and A. Ghosh, *Inorg. Chem.*, 2006, **45**, 4910.

[96] K. P. Ravindranathan, E. Gallicchio, R. A. Friesner, A. E. McDermott and R. M. Levy, *J. Am. Chem. Soc.*, 2006, **128**, 5786.

[97] D. E. Clemmer, Y. M. Chen, F. A. Khan and P. B. Armentrout, *J. Phys. Chem.*, 1994, **98**, 6522.

[98] D. Schroder and H. Schwarz, *Angew. Chem., Int. Ed. Engl.*, 1995, **34**, 1973.

[99] M. Filatov and S. Shaik, *J. Phys. Chem. A*, 1998, **102**, 3835.

[100] S. P. de Visser, F. Ogliaro, N. harris and S. Shaik, *J. Am. Chem. Soc.*, 2001, **123**, 3037.

[101] F. Oligaro, S. P. de Visser, J. T. Groves and S. Shaik, *Angew. Chem., Int. Ed. Engl.*, 2001, **40**, 2874.

[102] P. K. Sharma, S. P. de Visser and S. Shaik, *J. Am. Chem. Soc.*, 2003, **125**, 8698.

[103] J. T. Groves and G. A. McClusky, *J. Am. Chem. Soc.*, 1976, **98**, 859.

[104] J. T. Groves, *J. Chem. Educ.*, 1985, **62**, 928.

[105] D. Kumar, S. P. de Visser and S. Shaik, *J. Am. Chem. Soc.*, 2003, **125**, 13024.

[106] J. P. McEvoy and G. W. Brudvig, *Chem. Rev.*, 2006, **106**, 4455.

[107] V. L. Pecoraro and W. Y. Hsieh, *Inorg. Chem.*, 2008, **47**, 1765.

[108] M. Palucki, N. S. Finney, P. J. Pospisil, M. L. Guler, T. Ishida and E. N. Jacobsen, *J. Am. Chem. Soc.*, 1998, **120**, 948.

[109] F. M. MacDonnell, N. L. P. Fackler, C. Stern and T. V. O'Halloran, *J. Am. Chem. Soc.*, 1994, **116**, 7431.

[110] T. J. Collins, R. D. Powell, C. Sledobnick and E. S. Uffelman, *J. Am. Chem. Soc.*, 1990, **112**, 899.

[111] T. J. Collins and S. W. Gordon-Wylie, *J. Am. Chem. Soc.*, 1989, **111**, 4511.

[112] B. S. Mandimutsira, B. Ramdhanie, R. C. Todd, H. L.Wang, A. A. Zareba, R. S. Czemuszewicz and D. P. Goldberg, *J. Am. Chem. Soc.*, 2002, **124**, 15170.

[113] E. Tangen and A. Ghosh, *J. Am. Chem. Soc.*, 2002, **124**, 8117.

[114] E. M. McGarrigle and D. G. Gilheany, *Chem. Rev.*, 2005, **105**, 1563.

[115] W. Zhang, J. L. Loebach, S. R. Wilson and E. N. Jacobsen, *J. Am. Chem. Soc.*, 1990, **112**, 2801.

[116] R. Irie, K. Noda, Y. Ito, N. Matsumoto and T. Katsuki, *Tetta. Lett.*, 1990, **31**, 7345.

[117] K. Srinivasan, P. Michaud and J. K. Kochi, *J. Am. Chem. Soc.*, 1986, **108**, 2309.

[118] M. Palucki, P. Hanson and E. N. Jacobsen, *Tetrahedron Lett.*, 1992, **33**, 7111.

[119] J. Brinksma, R. La Crois, B. L. Feringa, M. I. Donnoli and C. Rosini, *Tetrahedron Lett.*, 2001, **42**, 4049.

[120] J. Brinksma, L. Schmieder, G. van Vliet, R. Boaron, R. Hage, D. E. De Vos, P. L. Alsters and B. L. Feringa, *Tetrahedron Lett.*, 2002, **43**, 2619.

[121] G. B. Shulpin, G. V. Nizove, Y. N. Kozlov and I. G. Pechenkina, *New J. Chem.*, 2002, **26**, 1238.

[122] G. B. Shulpin, G. S. Fink and J. R. Lindsay Smith, *Tetrahedron*, 1999, **55**, 5345.

[123] R. Hage, J. E. Iburg, J. Kerschner, J. H. Koek, E. L. M. Lempers, R. J. Martens, U. S. Racheria, S. W. Russell, T. Swarthoff, M. R. P. van Vilet, J. B.Warnaar, L. van der Wolf and B. Krijnen, *Nature*, 1994, **369**, 637.

[124] R. Hage and A. Lienke, *J. Mol. Catal. A*, 2006, **251**, 150.

[125] J. R. L. Smith, J. Murray, P. H. Walton and T. R. Lowdon, *Tetrahedron Lett.*, 2006, **47**, 2005.

[126] J. R. L. Smith, B. C. Gilbert, A. M. Payeras, J. Murray, T. R. Lowdon, J. Oakes, R. P. Prats and P. H. Walton, *J. Mol. Catal. A*, 2006, **251**, 114.

[127] Z. Gross, G. Golubkov and L. Simkhovich, *Angew. Chem., Int. Ed. Engl.*, 2000, **39**, 4045.

[128] B. Meunier, *Chem. Rev.*, 1992, **92**, 1411.

[129] J. T. Groves, J. Lee and S. S. Marla, *J. Am. Chem. Soc.*, 1997, **119**, 6269.

[130] N. Jin and J. T. Groves, *J. Am. Chem. Soc.*, 1999, **121**, 2923.

[131] R. Zhang and M. Newcomb, *J. Am. Chem. Soc.*, 2003, **125**, 12419.

[132] R. Zhang, J. H. Horner and M. Newcomb, *J. Am. Chem. Soc.*, 2005, **127**, 6573.

[133] W. Nam, I. Kim, M. H. Lim, H. J. Choi, J. S. Lee and H. G. Jang, *Chem. Eur. J.*, 2002, **8**, 2067.

[134] F. De Angelis, N. Jin, R. Car and J. T. Groves, *Inorg. Chem.*, 2006, **45**, 4268.

[135] J. T. Groves, Y. Watanabe and T. J. McMurry, *J. Am. Chem. Soc.*, 1983, **105**, 4489.

[136] N. Jin and J. T. Groves, *J. Am. Chem. Soc.*, 1999, **121**, 2923.

[137] W. J. Song, M. S. Seo, S. DeBeer George, T. Ohta, R. Song, M. J. Kang, T. Tosha, T. Kitagawa, E. I. Solomon and W. Nam, *J. Am. Chem. Soc.*, 2007, **129**, 1268.

[138] J. Ning, M. Ibrahim, T. G. Spiro and J. T. Groves, *J. Am. Chem. Soc.*, 2007, **129**, 12416.

[139] Z. Gross, *Angew. Chem., Int. Ed. Engl.*, 2008, **47**, 2737.

[140] Y. Shimazaki, T. Nagano, H. Takesue, B. H. Ye, F. Tani and Y. Naruta, *Angew. Chem., Int. Ed. Engl.*, 2004, **43**, 98.

[141]. Y. Gao, J. Liu, M. Wang, Y. Na, B. Akermark and L. Sun, *Tetrahedron*, 2007, **63**, 1987.

[142] P. E. M. Siegbahn and R. H. Crabtree, *J. Am. Chem. Soc.*, 1999, **121**, 117.

[143] P. E. M. Siegbahn, *Inorg. Chem.*, 2000, **39**, 2923.

[144] M. Lundberg, M. R. A. Blomberg and P. E. M. Siegbahn, *Inorg. Chem.*, 2004, **43**, 264.

[145] M. Lundberg and P. E. M. Siegbahn, *Phys. Chem. Chem. Phys.*, 2004, **6**, 4772.

[146] P. E. M. Siegbahn and M. R. A. Blomberg, *Philos. Trans. R. Soc. London, Ser. A*, 2005, **363**, 847.

[147] M. Lundberg and P. E. M. Siegbahn, *Photochem. Photobiol. Sci.*, 2005, **4**, 1035.

[148] P. E. M. Siegbahn, *Chem. Eur. J.*, 2006, **12**, 9217.

[149] M. Lundberg, M. A. Blomberg and P. E. M. Siegbahn, *Inorg. Chem.*, 2004, **43**, 264.

[150] S. P. de Visser, D. Kumar, R. Neumann and S. Shaik, *Angew. Chem., Int. Ed. Engl.*, 2004, **43**, 5661.

[151] D. Feichtinger and D. A. Plattner, *Chem. Eur. J.*, 2001, **7**, 591.

[152] P. O. Norrby, C. Linde and B. Å. Kermark, *J. Am. Chem. Soc.*, 1995, **117**, 11035.

[153] C. Linde, B. Å. Kermark, P. O. Norrby and M. Svensson, *J. Am. Chem. Soc.*, 1999, **121**, 5083.

[154] P. Brandt, P. O. Norrby, A. M. Daly and D. G. Gilheany, *Chem. Eur. J.*, 2002, **8**, 4299.

[155] Y. G. Abashkin and S. K. Burt, *Inorg. Chem.*, 2005, **44**, 1425.

[156] L. Cavallo and H. Jacobsen, *J. Org. Chem.*, 2003, **68**, 6202.

[157] L. Cavallo and H. Jacobsen, *Eur. J. Inorg. Chem.*, 2003, 892.

[158] L. Cavallo and H. Jacobsen, *J. Phys. Chem. A*, 2003, **107**, 5466.

[159] L. Cavallo and H. Jacobsen, *Inorg. Chem.*, 2004, **43**, 2175.

[160] H. Jacobsen and L. Cavallo, *Organometallics*, 2006, **25**, 177.

[161] I. V. Khavrutskii, D. G. Musaev and K. Morokuma, *Inorg. Chem.*, 2003, **42**, 2606.

[163] A. Ghosh and E. Gonzalez, *Isr. J. Chem.*, 2000, **40**, 1.

[164] F. de Angelis, N. Jin, R. Car and J. T. Groves, *Inorg. Chem.*, 2006, **45**, 4268.

[165] S. P. de Visser, F. Oligaro, Z. Gross and S. Shaik, *Chem. Eur. J.*, 2001, **7**, 4954.

[166] A. Gosh and P. R. Taylor, *Curr. Opin. Chem. Biol.*, 2003, **7**, 113.

[167] E. Steene, T. Wondimagegn and A. Ghosh, *J. Phys. Chem. B*, 2001, **105**, 11406.

[168] T. Privalov, L. Sun, B. A. kermark, J. Liu, Y. Gao and M. Wang, *Inorg. Chem.*, 2007, **46**, 7075.

[169] X. Yang and M. H. Baik, *J. Am. Chem. Soc.*, 2006, **128**, 7476.

[170] D. Balcells, C. Raynaud, R. H. Crabtree and O. Eisenstein, *Chem. Commun.*, 2008, 744.

[171] A. E. Anastasi, P. H. Walton, J. R. Lindsay Smith, W. M. C. Sameera and J. E. McGrady, *Inorg. Chim. Acta*, 2008, **361**, 1079.

[172] N. S. Venkataramanan, G. Kuppuraj and S. Rajagopal, *Coord. Chem. Rev.*, 2005, **249**, 1249.

[173] A. Chellamani, N. I. Alhaji, S. Rajagopal, R. Sevvel and C. Srinivasan, *Tetrahedron*, 1995, **51**, 12677.

[174] A. Chellamani, P. Kulanthaipandi and S. Rajagopal, *J. Org. Chem.*, 1999, **64**, 2232.

[175] A. Chellamani, N. M. I. Alhaji and S. Rajagopal, *J. Chem. Soc., Perkin Trans.*, 1997, 299.

[176] A. D. Becke, *Phys. Rev. A*,1988, **38**, 3098.

[177] C. Lee, W. Yang and R. G. Parr, *Phys. Rev.*, 1988, **37**, 785.

[178] B. Miehlich, A. Savin, H. Stoll and H. Preuss, *Chem. Phys. Lett.*,1989, **157**, 200.

[179] M. S. Gebhard, S. A. Koch, M. Millar, F. J. Devlin, P. J. Stephens and E. I. Solomon, *J. Am. Chem. Soc.*, 1991, **113**, 1640.

[180] D. Dai and M. H. Whangbo, *J. Chem. Phys.*, 2001, **114**, 2887.

[181] D. Dai and M. H. Whangbo, *J. Chem. Phys.*, 2003, **118**, 29.

[182] J. N. Harvey, *Struct. Bonding*, 2004, **112**, 151.

[183] D. V. Behere, *Inorg. Chem.*, 1980, **19**, 992.

[184] H. M. Goff and A. P. Hansen, *Inorg. Chem.*, 1984, **23**, 321.

[185] R. J. Cheng, S. H. Chang and K. C. Hung, *Inorg. Chem.*, 2007, **46**, 1948.

[186] J. Krzystek, J. Telser, L. A. Pardi, D. P. Goldberg, B. M. Hoffman and L. C. Brunel, *Inorg. Chem.*, 1999, **38**, 6121.

[187] C. J. Cramer, A. Kinal, M. Wloch, P. Piecuch and L. Gagliardi, *J. Phys. Chem. A*, 2006, **110**, 11557.

[188] L. Cavallo and H. Jacobsen, *Angew. Chem., Int. Ed. Engl.*, 2000, **39**, 589.

[189] A. E. Shilov and G. B. Shulpin, *Chem. Rev*., 1997, **97**, 2879.

[190] J. T. Groves, *J. Inorg. Biochem.*, 2006, **100**, 434.

[191] T. G. Spiro, R. S. Czernuszewicz and X. Y. Li, *Coord. Chem. Rev.*, 1990, **100**, 541.

[192] P. K. Sharma, S. P. de Visser, F. Ogliaro and S. Shaik, *J. Am. Chem. Soc.*, 2003, **125**, 2291.

[193] S. N. Dhuri, M. S. Seo, Y. M. Lee, H. Hirao, Y. Wang, W. Nam and S. Shaik, *Angew. Chem., Int. Ed.*, 2008, **47**, 3356.

[194] C. L. Hill and B. C. Schardt, *J. Am. Chem. Soc.*, 1980, **102**, 6374.

[195] D. Mansuy, *Coord. Chem. Rev.*, 1993, **125**, 129.

[196] J. T. Groves, *J. Chem. Educ.*, 1985, **62**, 928.

[197] J. T. Groves, *J. Porphyrins Phthalocyanines*, 2000, **4**, 350.

[198] T. Strassner and K. N. Houk, *J. Am. Chem. Soc.*, 2000, **122**, 7821.

[199] J. P. Collman, A. S. Chien, T. A. Eberspacher and J. I. Brauman, *J. Am. Chem. Soc.*, 1998, **120**, 425.

[200] P. R. O. de Montellano, *Acc. Chem. Res.*, 1987, **20**, 289.

[201] M. Sono, M. P. Roach, E. D. Coulter and J. H. Dawson, *Chem. Rev.*, 1996**,** 2841.

[202] P. R. O. de Montellano (Ed.), *Cytochrome P450: Structure, Mechanism and Biochemistry*, 3rd edition, Plenum Press, NewYork, 2004.

[203] J. T. Groves and R. Quinn, *Inorg. Chem.*, 1984, **23**, 3846.

[204] J. T. Groves and R. Quinn, *J. Am. Chem. Soc.*, 1985, **107**, 5790.

[205] J. T. Groves and K. H. Ahn, *Inorg. Chem.*, 1987, **26**, 3831.

[206] J. T. Groves and W. J. Jr. Kruper, *J. Am. Chem. Soc.*, 1979, **101**, 7613.

[207] J. T. Groves and R. C. Haushaulter, *J. Chem. Soc., Chem. Commun.*, 1981, 1163.

[208] J. T. Groves, W. J. Jr. Kruper, R. C. Haushaulter and W. M. Butler, *Inorg. Chem.*, 1982, **21**, 1363.

[209] J. E. Penner-Hahn, M. Benfatto, B. Hedman, T. Takahashi, D. Sebastian, J. T. Groves and K. O. Hodgson, *Inorg. Chem.*, 1986, **25**, 2255.

[210] J. T. Groves, R. C. Haushaulter, M. Nakamura, T. E. Nemo and B. J. Evans, *J. Am. Chem.Soc.*, 1981, **103**, 2884.

[211] B. Boso, L. Lang, T. J. McMurry and J. T. Groves, *J. Chem. Phys.*, 1983, **79**, 1122.

[212] J. E. Penner-Hahn, K. S. Elbe, T. J. McMurry, M. R. Renner, A. L. Balch, J. T. Groves, J. H. Dawson and K. O. Hodgson, *J. Am. Chem. Soc.*, 1986, **108**, 7819.

[213] D. H. Chin, A. L. Balch and G. N. La Mar, *J. Am. Chem. Soc.*, 1980, **102**, 1446.

[214] D. H. Chin, G. N. La Mar and A. L. Balch, *J. Am. Chem. Soc.*,1980, **102**, 4344.

[215] A. L. Balch, G. N. La Mar, L. L. Grazynski, M. W. Renner and V. Thanabal, *J. Am. Chem. Soc.*, 1985, **107**, 3003.

[216] J. T. Groves and R. Quinn, *Inorg. Chem.*, 1984, **23**, 3846.

[217] J. T. Groves and R. Quinn, *J. Am. Chem. Soc.*, 1985, **107**, 5790.

[218] C. María, Curet-Arana, G. A. Emberger, L. J. Broadbelt and R. Q. Snurr, *J. Mol. Catal. A Chem.*, 2008, **285**, 120.

[219] D. Ostovic and T. C. Bruice, *Acc. Chem. Res.*, 1992, **25**, 314.

[220] L. C.Yuan and T. C. J. Bruice, *Chem. Soc. Chem. Commun.*, 1985, 868,

[221] A. J. Castellino and T. C. Bruice, *J. Am. Chem. soc.*, 1988, **110**, 158.

[222] J. T. Groves and M. K. Stern, *J. Am. Chem. Soc.*, 1987, **109**, 3812.

[223] Y. Shimazaki, N. Nagano, H. Takesue, B. H. Ye, F. Tani and Y. Naruta, *Angew. Chem.*, 2004, **116**, 100.

[224] Y. Naruta, M. Sasayama and T. Sasaki, *Angew. Chem. Int. Ed. Engl.*, 1994, **33**, 1839.

[225] A. K. Poulsen, A. Rompel and C. J. McKenzie, *Angew. Chem. Int. Ed.*, 2005, **44**, 6916.

[226] C. Baffert, M. N. Collomb, A. Deronzier, S. K Knudsen, J. M. Latour, K. H. Lund, C. J. McKenzie, M. Mortensen, L. P. Nielsen and N. Thorup, *Dalton Trans.*, 2003,1765.

[227] J. B. Howard and D. C. Rees, *Chem. Rev*., 1996, **96**, 2965.

[228] J. Kim and C. D. Rees, *Science*, 1992, **257**, 1677.

[229] J. Kim and C. D. Rees, *Nature*, 1992, **360**, 553.

[230] L. Que and A. E. True, *Prog. Inorg. Chem.*, 1990, **38**, 97.

[231] G. C. Dismukes, *Chem. Rev*., 1996, **96**, 2909.

[232] R. M Fronko, J. E. Penner-Hahn and C. J. Bender, *J. Am. Chem. Soc.*, 1988, **110**, 7554.

[233] W. F. Beyer and I. Fridovich, *Biochemistry*, 1985, **24**, 6460.

[234] A. C. Rosenzweig, C. A. Frederick, S. J. Lippard and P. Nordlund, *Nature*, 1993, **366**, 537.

[235] A. C. Rosenzweig and S. J. Lippard, *Acc. Chem. Res.*, 1994, **27**, 229.

[236] K. A. Magnus, B. Hazes, H. Thon-That, G. Bonaventura, J. Bonaventura and W. G. J. Hol, *Proteins*, 1994, **19**, 302.

[237] A. Volbeda and W. G. J. Hol, *J. Mol. Biol*., 1989, **209**, 249.

[238] K. N. Ferreira, T. M. Iverson, K. Maghlaoui, J. Barber and S. Iwata, *Science*, 2004, **303**, 1831.

[239] G. M. Cheniae and I. F. Martin, *Biochim. Biophys. Acta*, 1970, **197**, 219.

[240] K. Sauer, *Acc. Chem. Res.*, 1980, **13**, 249.

[241] C. F. Yocum, C. T. Yerkes, R. E. Blankenship, R. R. Sharp and G. T. Babcock, *Proc. Natl. Acad. Sci. U.S.A.*, 1981, **78**, 7507.

[242] R. E. Blankenship, *Molecular Mechanisms of Photosynthesis*, Blackwell Science Ltd., Oxford, 2002.

[243] T. J. Wydrzynski and K. Satoh, *Photosystem II. The Light-Driven Water: Plastoquinone Oxidoreductase*, T. J. Wydrzynski and K. Satoh (Ed.), Advances in Photosynthesis and Respiration, Springer, Dordrecht, 2005.

[244] J. Yano, Y. Pushkar, P. Glatzel, A. Lewis, K. Sauer, J. Messinger, U. Bergmann and V. K. Yachandra, *J. Am. Chem. Soc.*, 2005, **127**, 14974.

[245] K. Han and S. Katoh, *Plant Cell Physiol.*, 1993, **34**, 585.

[246] P. Ådelroth, K. Lindberg and L. E. Andreasson, *Biochemistry*, 1995, **34**, 9021.

[247] A. Boussac, J. L. Zimmermann and A. W. Rutherford, *Biochemistry*, 1989, **28**, 8984.

[248] M. Sivaraja, J. Tso and G. C. Dismukes, *Biochemistry*, 1989, **28**, 9459.

[249] T. A. Ono and Y. Inoue, *Arch. Biochem. Biophys.*, 1989, **275**, 440.

[250] H. J. van Gorkom and C. F. Yocum, *Photosystem II: The Light-Driven Water:Plastoquinone Oxidoreductase*; T. J. Wydrzynski, K. Satoh, Eds., Springer: Dordrecht, The Netherlands, 2005, pp 307.

[251] B. J. Hallahan, J. H. A. Nugent, J. T. Warden and M. C. W. Evans, *Biochemistry*, 1992, **31**, 4562.

[252] M. L. Gilchrist, J. A. Ball, D. W. Randall and R. D. Britt, *Proc. Natl. Acad. Sci. U.S.A.*, 1995, **92**, 9545.

[253] N. Lydakis-Simantiris, P. Dorlet, D. F Ghanotakis and G. T. Babcock, *Biochemistry*, 1998, **37**, 6427.

[254] L. E. Andreasson, I. Vass, S. Styring, *Biochim. Biophys. Acta*, 1995, 155.

[255] P. H. Homann, *Photosynth. Res.*, 2002, **73**, 169.

[256] P. O. Sandusky and C. F. Yocum, *Biochim. Biophys. Acta*, 1984, **766**, 603.

[257] P. M. Kelley and S. Izawa, *Biochim. Biophys. Acta*, 1978, **502**, 198.

[258] T. A. Ono, H. Nakayama, H. Gleiter, Y. Inoue and A. Kawamori, *Arch. Biochem. Biophys.*, 1987, **256**, 618.

[259] P. H. Homann, *Plant Physiol.*, 1988, **88**, 194.

[260] B. Kok, B. Forbush and M. McGloin, *Photochem. Photobiol*., 1970, **11**, 457.

[261] G. C. Dismukes and Y. Siderer, *Proc. Natl. Acad. Sci. U. S. A.*, 1981, **78**, 274.

[262] J. Messinger, J. H. A. Nugent and M. C. W. Evans, *Biochemistry*, 1997, **36**, 11055.

[263] J. M. Peloquin, K. A. Campbell, D. W. Randall, M. A. Evanchik, V. L. Pecoraro, W. H. Armstrong and R. D. Britt, *J. Am. Chem. Soc.*, 2000, **122**, 10926.

[264] L. V. Kulik, B. Epel, W. Lubitz and J. Messinger, *J. Am. Chem. Soc.*, 2005, **127**, 2392.

[265] L. V. Kulik, B. Epel, W. Lubitz and J. Messinger, *J. Am. Chem. Soc.*, 2007, **129**, 13421.

[266] J. H. Su, W. Lubitz and J. Messinger, *J. Am. Chem. Soc.*, 2008, **130**, 786.

[267] M. Haumann, C. Müller, P. Liebisch, L. Iuzzolino, J. Dittmer, M. Grabolle, T. Neisius, W. Meyer-Klaucke and H. Dau, *Biochemistry*, 2005, **44**, 1894.

[268] W. C. Liang, T. A. Roelofs, R. M. Cinco, A. Rompel, M. J. Latimer, W. O. Yu, K. Sauer, M. P. Klein and V. K. Yachandra, *J. Am. Chem. Soc.*, 2000, **122**, 3399.

[269] M. Haumann, C. Müller, P. Liebisch, L. Iuzzolino, J. Dittmer, M. Grabolle, T. Neisius, W. Meyer-Klaucke and H. Dau, *Biochemistry*, 2005, **44**, 1894.

[270] J. P. McEvoy and G. W. Brudvig, *Chem. Rev.*, 2006, **106**, 4455.

[271] J. Kern and G. Renger, *Photosynth. Res.*, 2007, **94**, 183.

[272] G. Renger, *Photosynth. Res.*, 2007, **92**, 407.

[273] F. A. Armstrong, *Philos. Trans.*, 2008, **363**, 1263.

[274] J. B. Vincent and G. Christou, *Inorg. Chim. Acta*, 1987, **136**, 41.

[275] W. F. Ruettinger, M. Yagi, K. Wolf, S. Bernasek and G. C. Dismukes, *J. Am. Chem. Soc.*, 2000, **122**, 10353.

[276] R. Tagore, H. Chen, R. H. Crabtree and G. W. Brudvig, *J. Am. Chem. Soc.*, 2006, **128**, 9457.

[277] W. Hillier and T. Wydrzynski, *Biochemistry*, 2000, **39**, 4399.

[278] W. Hillier, J. Messinger and T. Wydrzynski, *Biochemistry*, 1998, **37**, 16908.

[279] W. Hillier and T. Wydrzynski, *Biochim. Biophys. Acta*, 2001, 197.

[280] V. L. Pecoraro and M. J. Baldwin, M. T. Caudle, W. Y. Hsieh and N. A. Law, *Pure Appl. Chem.* 1998, **70**, 925.

[281] J. S. Vrettos, J. Limburg and G. W. Brudvig, *Biochim. Biophys. Acta*, 2001, 229.

[282] J. Limburg, V. A. Szalai and G. W. Brudvig, *J. Chem. Soc., Dalton Trans.*, 1999, 1353.

[283] G. Hendry and T. Wydrzynski, *Biochemistry*, 2003, **42**, 6209.

[284] C. W. Hoganson and G. T. Babcock, *Science*, 1997, **277**, 1953.

[285] M. R. A. Blomberg, P. E. M.Siegbahn, S. Styring, G. T. Babcock, B. Akermark and P. Korall, *J. Am. Chem. Soc.*, 1997, **119**, 8285.

[286] C. W. Hoganson, N. Lydakis-Simantiris, X. S. Tang, C. K Tommos, K. Warncke, G. T. Babcock, B. A. Diner, J. McCracken and S. Styring, *Photosynth. Res.*, 1995, **46**, 177.

[287] C. Tommos and G. T. Babcock, *Acc. Chem. Res.*, 1998, **31**, 18.

[288] M. L. Gilchrist, J. A. Ball, D. W. Randall and R. D. Britt *Proc. Natl. Acad. Sci. U.S.A.* 1995, **92**, 9545.

[289] B. A. Diner, *Biochim. Biophys. Acta*, 2001, 147.

[290] X. S. Tang, B. A. Diner, B. S. Larsen, M. L. Gilchrist, G. A. Lorigan and R. D. Britt, *Proc. Natl. Acad. Sci. U.S.A.*, 1994, **91**, 704.

[291] R. D. Britt, X. S. Tang, M. L. Gilchrist, G. A. Lorigan, B. S. Larsen and B. A. Diner, *Biochem. Soc. Trans.*, 1994, **22**, 343.

[292] R. J. Debus, K. A. Campbell, W. Gregor, Z. L. Li, R. L. Burnap and R. D. Britt, *Biochemistry*, 2001, **40**, 3690.

[293] R. J. Debus, K. A. Campbell, J. M. Peloquin, D. P. Pham and R. D. Britt, *Biochemistry*, 2000, **39**, 470.

[294] M. R. A. Blomberg, P. E. M. Siegbahn, S. Styring, G. T. Babcock, B. Akermark and P. Korall, *J. Am. Chem. Soc.*, 1997, **119**, 8285.

[295] C. W. Hoganson, N. Lydakis-Simantiris, X. S. Tang, C. Tommos, K. Warncke, G. T. Babcock, B. A. Diner, J. McCracken and S. Styring, *Photosynth. Res.*, 1995, **46**, 177.

[296] J. H. Robblee, R. M. Cinco and V. K. Yachandra, *Biochim. Biophys. Acta.*, 2001, **1503**, 7.

[297] V. K. Yachandra, K. Sauer and M. P. Klein, *Chem. Rev.*, 1996, **96**, 2927.

[298] E. A. Lewis and W. B. Tolman, *Chem. Rev.*, 2004, **104,** 1047.

[299] H. Dau and L. Iuzzolino Dittmer, *J. Biochim. Biophys. Acta*, 2001, 1503.

[300] J. Messinger, *Phys. Chem. Chem. Phys.*, 2004, **6**, 4764.

[301] J. H. Robblee, J. Messinger, R. M. Cinco, K. L. McFarlane, C. Fernandez, S. A. Pizarro, K. Sauer and V. K. Yachandra, *J. Am. Chem. Soc.*, 2002, **124**, 7459.

[302] C. P. Aznar and R. D. Britt, *Philos. Trans. R. Soc. London Ser. B*, 2002, **357**, 1359.

[303] G. Hendry and T. Wydrzynski, *Biochemistry*, 2003, **42**, 6209.

[304] M. J. Baldwin, T. L. Stemmler, P. J. Riggs-Gelasco, M. L. Kirk, J. E. Penner-Hahn and V. L. Pecoraro, *J. Am. Chem. Soc.*, 1994, **116**, 11349.

[305] J. N. Harvey, M. Aschi, H. Schwarz and W. Koch, *Theor. Chem. Acc.*, 1998, **99**, 95.

[306] E. M. Sproviero, J. A. Gascon, J. P. McEvoy, G. W. Brudvig and V. S. Batista, *J. Am. Chem. Soc.*, 2008, **130**, 3428.

[307] W. D. Cornell, P. Cieplak, C. I. Bayly, I. R. Gould, K. M. Merz, D. M. Ferguson, D. C. Spellmeyer, T. Fox, J. W. Caldwell and P. A. Kollman, *J. Am. Chem. Soc.*, 1995, **117**, 5179.

[308] H. Dau, P. Liebisch and M. Haumann, *Phys. Chem. Chem. Phys*., 2004, **6**, 4781.

[309] M. Haumann, C. Muller, P. Liebisch, L. Iuzzolino, J. Dittmer, M. Grabolle, T. Neisius and W. H. Meyer, *Biochemistry* 2005, **4**, 1894.

[310] A. Gonis, *Green Functions for Ordered and Disordered Systems*; North Holland: Amsterdam, 1992.

[311] A. L. Ankudinov, C. Bouldin, J. J. Rehr, J. Sims and H. Hung, *Phys. Rev. B*, 2002, **65**, 104107.

[312] S. W. Gersten, G. J. Samuels and T. J. Meyer, *J. Am. Chem. Soc.*, 1982, **104**, 4029.

[313] J. A. Gilbert, D. S. Eggleston, J. Wyatt, R. Murphy, D. A. Geselowitz, S. W. Gersten, D. J. Hodgson and T. J. Meyer, *J. Am. Chem. Soc.*, 1985, **107**, 3855.

[314] J. K. Hurst, J. Zhou and Y. Lei, *Inorg. Chem.*, 1992, **31**, 1010.

[315] E. L. Lebeau, S. A. Adeyemi and T. J. Meyer, *Inorg. Chem.*, 1998, **37**, 6476.

[316] E. L. Lebeau and T. J. Meyer, *Inorg. Chem.*, 1999, **38**, 2174.

[317] W. J. Vining and T. J. Meyer, *Inorg. Chem.*, 1986, **25**, 2023.

[318] C. W. Chronister, R. A. Binstead, J. Ni and T. J. Meyer, *Inorg. Chem.*, 1997, **36**, 3814.

[319] F. Liu, T. Cardolaccia, B. J. Hornstein, J. R. Schoonover and T. J. Meyer, *J. Am. Chem. Soc.*, 2007, **129**, 2446.

[320] R. A. Binstead, C. W. Chronister, J. Ni, C. M. Hartshorn and T. J. Meyer, *J. Am. Chem. Soc.*, 2000, **122**, 8464.

[321] D. Geselowitz and T. J. Meyer, *Inorg. Chem.*, 1990, **29**, 3894.

[322] H. Yamada, W. F. Siems, T. Koike and J. K. Hurst, *J. Am. Chem. Soc.*, 2004, **126**, 9786.

[323] X. Yang, M. H. Baik, *J. Am. Chem. Soc.*, 2004, **126**, 13222.

[324] E. L. Lebeau, S. A. Adeyemi and T. J. Meyer, *Inorg. Chem.*, 1998, **37**, 6476.

[325] M. Rodriquez, I. Romero, C. Sens and A. Llobet, *J. Mol. Catal. A*, 2006, **251**, 215.

[326] C. Sens, I. Romero, M. Rodriguez, A. Llobet, T. Parela and J. Benet-Buchholz, *J. Am. Chem. Soc.*, 2004, **126**, 7798.

[327] T. Wada, K. Tsuge and K. Tanaka, *Inorg. Chem.*, 2001, **40**, 329.

[328] T. Wada and K. Tanaka, *Eur. J. Inorg. Chem.*, 2005, 3832.

[329] T. Wada, K. Tsuge and K. Tanaka, *Angew. Chem. Int. Ed.*, 2000, **39**, 74.

[330] R. Zong and R. P. Thummel, *J. Am. Chem. Soc.*, 2005, **127**, 2802.

[331] J. P. Collins, J. P. Sauvage, *Inorg. Chem.*, 1986, **25**, 135.

[332] P. Kühn, J. Pieper, O. Kaminskaya, H. G. Eckert, R. E. Lechner, V. Shuvalov and G. Renger, *Photosynthesis Research*, 2005, **84**, 317.

[333] J. Z. Wu, E. Sillitto, G. P. A. Yap, J. Sheats and G. C. Dismukes, *Inorg. Chem.*, 2004, **43**, 5795.

[334] J. Z. Wu, F. D. Angelis, T. G. Carrell, G. P. A. Yap, J. Sheats, R. Car and G. C. Dismukes, *Inorg. Chem.*, 2006, **45**, 189.

[335] W. Rüttinger, M. Yagi, K. Wolf, S. Bernasek and G. C. Dismukes, *J. Am. Chem. Soc.*, 2000, **39**, 2021.

[336] M. Yagi, K. Wolf, P. J. Baesjou, S. Bernasek and G. C. Dismukes, *Angew. Chem.*, 2001, **113**, 3009.

[337] W. Rüttinger, C. Campana and G. C. Dismukes, *J. Am. Chem. Soc.*, 1997, **119**, 6670.

[338] S. Mukhopadhyay, S. K. Mandal, S. Bhaduri and W. H. Armstrong, *Chem. Rev.*, 2004, **104**, 3981.

[339] W. Rüttinger and G. C. Dismukes, *Chem. Rev.*, 1997, **97**, 1.

[340] J. Limburg, J. S. Vrettos, L. M. Liable-Sands, A. L. Rheingold, R. H. Crabtree and G. W. Brudvig, *Science*, 1999, **283**, 524.

[341] J. Limburg, J. S. Vrettos, H. Chen, J. C. D. Paula, R. H. Crabtree and G. W. Brudvig, *J. Am. Chem. Soc.*, 2001, **123**, 423.

[342] H. Chen, R. Tagore, G. Olack, J. S. Vrettos, T. C. Weng, J. Penner-Hahn, R. H. Crabtree and G. W. Brudvig, *Inorg. Chem.*, 2007, **46**, 34.

[343] M. Lundberg, R. A. Blomberg and P. E. M. Siegbahn, *Inorg. Chem.*, 2004, **43**, 264.

[344] M. Yagi and M. Kaneko, *Chem. Rev.*, 2001, **101**, 21.

[345] A. R. Howelles, A. Sankarraj and C. Shannon, *J. Am. Chem. Soc.*, 2004, **126**, 12258.

[346] Y. Ebina, N. Sakai and T. Sasaki, *J. Phys. Chem. B*, 2005, **109**, 17212.

[347] V. Y. Shafirovich, N. K. Khannonov and A. E. Shilov, *J. Inorg. Biochem.*, 1981, **15**, 113.

[348] M. Yagi, S. Tokita, K. Nagoshi, I. Ogino and M. Kaneko, *J. Chem. Soc., Faraday Trans.*, 1996, **92**, 2457.

[349] M. Yagi, N. Sukegawa and M. Kaneko, *J. Phys. Chem. B*, 2000, **104**, 4111.

[350] K. Kinoshita, M. Yagi and M. Kaneko, *Macromolecules*, 1998, **31**, 6042.

[351] L. Noodleman, T. Lovell, W. G. Han, J. Li and F. Himo, *Chem. Rev.*, 2004, 104, 459.

[352] L. Noodleman, *J. Chem. Phys.*, 1981, **74**, 5737.

[353] K. Ichhara and Y. Naruta, *Chem. Lett.*, 1988, 185.

[354] R. L. Rardin, W. B. Tolman and S. J. Lippard, *New J. Chem.* 1991, **15**, 417.

[355] M. E. Andersson, M. H. Gbom, A. R. Matthis, K. K. Andersson, B. M. Sjöberg and P. Nordlund, *J. Am. Chem. Soc.*, 1999, **121**, 2346.

[356] P. Nordlund and H. Eklund, *Curr. Opin. Struct. Biol.* 1995, **5**, 758.

[357] J. Ho and M. L. Coote, *J. Chem. Theory Comput.*, 2009, **5**, 295.

[358] C. P. Kelly, C. J. Cramer and D. G. Truhlar, *J. Phys. Chem. A*, 2006, **110**, 2493.

[359] J. Pratuangdejkul, W. Nosoongnoen, G. A. Guérin, S. Loric, M. Conti, J. M. Launay and P. Manivet, *Chem. Phy. Lett.*, 2006, **420**, 538.

[360] M. S Kharasch, H. Engelmann F. R. and Mayo, *J. Org., Chem.*, 1938, **2**, 288.

[361] M. S. Kharasch, E. V. Jensen and W. H. Urry, *Science*, 1945, **102**, 169.

[362] M. S. Kharasch, E. V. Elwood and W. H. Urry, *J. Am. Chem. Soc.*, 1947, **69**, 1100.

[363] M. S. Kharasch and H. N. Friedlander, *J. Org. Chem.*, 1949, **14**, 239.

[364] M. Hájek, P. Silhavy and J. Málek, *Collect. Czech. Chem. Commun.*, 1980, **45**, 3488.

[365] K. Maruoka, H. Sano, Y. Fukutani and H. Yamamoto, *Chem. Lett.*, 1985, 1689.

[366] R. Grigg, J. Devlin, A. Ramasubbu, R. M. Scott and P. Stevenson, *J. Chem. Soc., Perkin Trans.*, 1987, **1**, 1515.

[367] R. Kh. Friedlina and F. K. Velichko, *Synthesis*, 1977, 145.

[368] J. S.Wang, K. Matyjaszewski, *J. Am. Chem. Soc.*, 1995, **117**, 5614.

[369] K. L. Matyjaszewski, *Curr. Org. Chem.*, 2002, **6**, 67.

[370] L. A. van de Kuil, D. M. Grove, R. A. Gossage, J. W. Zwikker, L. W. Jenneskens, W. Drenth and G. van Koten, *Organometallics*, 1997**, 16**, 4985.

[371] K. Maruoka, H. Sano, Y. Fukutani and H. Yamamoto, *Chem. Lett.*, 1985, 1689.

[372] K. Matyjaszewski and J. Xia, *Chem. Rev.*, 2001, **101**, 2921.

[373] R. Kh. Friedlina and F. K. Velichko, *Synthesis*, 1977, 145.

[374] L. Quebatte, K. Thommes and K. Severin, *J. Am. Chem. Soc*., 2006, **128**, 7440.

[375] R. A. Gossage, L. A. V. de Kuil and G. van Koten, *Acc. Chem. Res.*, 1998, **31**, 1.

[376] J. M. M. Molina, A. Caballero, M. M. Daz-Requejo, S. Trofimenko, T. R. Belderran and P. J. Pérez, *Inorg. Chem.*, 2007, **46**, 7725.

[377] S. Trofimenko, *Scorpionates: The Coordination Chemistry of Polypyrazolylborate Ligands*, Imperial College Press: River Edge, NJ, 1999.

[378] L. M. L. Chia, S. Radojevic, I. J. Scowen, M. McPartlin and M. A. Halcrow, *J. Chem. Soc., Dalton Trans.* 2000, 133.

[379] A. Warshel and M. Levitt, *J. Mol. Biol.*, 1976, **103**, 227.

[380] U. C. Singh and P. A. Kollman, *J. Comput. Chem.*, 1986, **7**, 718.

[381] M. J. Field, P. A. Bash and M. Karplus, *J. Comput. Chem.*, 1990, **11**, 700.

[382] H. M. Senn and W. Thiel, *Angew. Chem. Int. Ed.* 2009, **48**, 3065.

[383] F. Maseras, *Top. Organomet. Chem.*, 1999, **4**, 166.

[384] F. Maseras, *Computational Organometallic Chemistry*, T. Cundari, M. Dekker (Ed.), New York, 2001,159.

[385] F. Maseras and K. Morokuma, *J. Comput. Chem.*, 1995, **16**, 1170.

[386] M. Svensson, S. Humbel, R. D. J. Froese, T. Matsubara, S. Sieber and K. Morokuma, *J. Phys. Chem.*, 1996, **100**, 19357.

[387] T. Vreven, K. Morokuma, O. Farkas, H. B. Schlegel and M. J. Frisch, *J. Comput. Chem.*, 2003, **24**, 760.

[388] T. Vreven, K. S. Byun, I. Komaromi, S. Dapprich, J. A. Montgomery, K. Morokuma and M. J. Frisch, *J. Chem. Theory Comput.*, 2006, **2**, 815.

[389]. A. K. Rappé, C. J. Casewit, K. S. Colwell, W. A. Goddard and W. M. Skiff, *J. Am. Chem. Soc.* 1992, **114**, 10024.

[390] W. M. C. Sameera, F, Maseras, and P. J. Pérez, *Inorg. Chem.*, (In preparation).

[391] A. J. Thomson, *Iron-sulphur proteins in Metalloproteins*, Verlag Chemie, Weinheim, 1985, 79.

[392] F. R. Salemme, *Annu. Rev. Biochem.*, 1977, **46**, 299.

[393] R. Cammack, *Adv. Inorg. Chem.*, 1992, **38**, 281.

[394] P. V. Rao and R. H. Holm, *Chem. Rev.*, 2004, **104**, 527.

[395] K. Wieghardt, K. Pohl, I. Jibril and G. Huttner, *Angew. Chem. Int. Ed. Engl.*, 1984, **23**, 77.

[396] R. Caciuffo, G. Amoretti, A. Murani, R. Sessoli, A. Caneschi, and D. Gatteschi, *Phys. Rev. Lett.*, 1998, **81**, 4744.

[397] A. V. Postnikov, J. Kortus and M. R. Pederson, *phys. stat. sol.*, 2006, **243**, 2533.

[398] M. Verdaguer, *Polyhedron*, 2001, **20**, 1115.

[399] B. Barbara, *Physics World*, 1999, 35.

[400] C. J. Milios, S. Piligkos and E. K. Brechin, *Dalton Trans.*, 2008, 1809.

[401] S. R. Sessoli, D. Gatteschi, A. Caneschi and M. A. Novak, *Nature*, 1993, **365**, 141.

[402] W. Wernsdorfer and R. Sessoli, *Science*, 1999, **284**, 133.

[403] D. Pinero, P. Baran, R. Boca, R. Herchel, M. Klein, R. G. Raptis, F. Renz, and Y. Sanakis, *Inorg. Chem.*, 2007, **46**, 10981.

[404] W. M. C. Sameera, John. E. McGrady, Ekaterina M. Zueva, Dalice Piñero, Radovan Herchel, Yannis Sanakis and Raphael G. Raptis. *Eur. J. Inorg. Chem.* (In preparation).

[405] H. Yao, J. Wang, Y. Ma, O. Waldmann, W. Du, Y. Song, Y. Li, L. Zheng, S. Decurtins and X. Xin, *Chem. Commun.*, 2006, 1745.

[406] C. Benelli, S. Parsons, G. A. Solan and R. E. P. Winpenny, *Angew. Chem. Int. Ed. Engl.*, 1996, **35**, 1825.

[407] M. Taft, W. Wernsdorfer, K. Folting, M. Pink and G. Christou, *J. Am. Chem. Soc*., 2004, **126**, 2156.

[408] J. Schnack, *Lect. Notes Phys*., 2004, **645**, 155.

[409] A. K. Boudalis, Y. Sanakis, F. Dahan, M. Hendrich and J. P. Tuchagues, *Inorg. Chem.*, 2006, **45**, 443.

[410] C. Stadler, J. Daub, J. Köhler, R. W. Saalfrank, V. Coropceanu, V. Schünemann, C. Ober, A. X. Trautwein, S. F. Parker, M. Poyraz, T. Inomata and R. D. Cannon, *J. Chem. Soc., Dalton Trans.*, 2001, 3373.

[411] K. S. Gavrilenko, A. Addison, L. Thompson and V. V. Pavlishchuk, *Theor. Exp. Chem.*, 2004, **40**, 214.

[412] C. T. Dziobkowski, J. T. Wrobleski and D. B. Brown, *Inorg. Chem.*, 1981, **20**, 671.

[413] L. Noodleman and J. G. Jr. Norman, *J. Chem. Phys.*, 1979, **70**, 4903.

[414] L. Noodleman, *J. Chem. Phys.*, 1981, **74**, 5737.

[415] L. Noodleman and E. R. Davidson, *Chem. Phys.*, 1986, **109**, 131.

[416] L. Noodleman and D. A. Case, *Adv. Inorg. Chem.*, 1992, **38**, 423.

[417] E. Ruiz, J. Cano, S. Alvarez and P. Alemany, *J. Comput. Chem.*, 1999, **20**, 1391.

[418] E. Ruiz, P. Alemany, S. Alvarez and J. Cano, *J. Am. Chem. Soc.*, 1997, **119**, 1297.

[419] E. Ruiz, P. Alemany, S. Alvarez and J. Cano, *Inorg. Chem.*, 1997, **36**, 3683.

[420] E. Ruiz, J. Cano, S. Alvarez and P. Alemany, *J. Am. Chem. Soc.*, 1998, **120**, 11122.

[421] E. Ruiz, C. Graaf, P. Alemany and S. Alvarez, *J. Phys. Chem. A*, 2002, **106**, 4938.

[422] A. Rodriguez-Fortea, P. Alemany, S. Alvarez and E. Ruiz, *Eur. J. Inorg. Chem.*, 2004, 143.

[423] E. Ruiz, S. Alvarez, J. Cano and V. Polo, *J. Chem. Phys.*, 2005, **123**, 164110.

[424] J. Kanamori, *J. Phys. Chem. Solids*, 1959, **10**, 87.

[425] A. X. Trautwein, E. Bill, E. L. Bominaar and H. Winkler, *Struc. Bonding*, 1991, **7**, 8.

[426] F. Neese, *J. Biol. Inorg. Chem.*, 2006, **11**, 702.

[427] M. Römelt, S. Ye and F. Neese, *Inorg. Chem.*, 2009, **48**, 784.

[428] J. F. Berry, G. S. DeBeer and F. Neese, *Phys. Chem. Chem. Phys*., 2008, 4361.

[429] M. Shoji, T. Saito, R. Takeda, Y. Kitagawa, T. Kawakami, S. Yamanaka, M. Okumura and K. Yamaguchi, *Chem. Phy. Lett.*, 2007, **446**, 228.

[430] J. C. Schoneboom, F. Neese and W. Thiel , *J. Am. Chem. Soc.* 2005, **27**, 5840.

[431] F. Neese, *Inorg. Chim. Acta.*, 2002, **337**, 181.

[432] G. J. Long (Ed.), *Mössbauner Spectroscopy Applied to Inorganic Chemistry*, 1984-1989, **1-3**, Plenum Press, New York.

[433] M. D. Dyar, D. G. Agresti, M. W. Schaefer, C. A. Grant and E. C. Sklute, *Annu. Rev. Earth Planet. Sci.*, 2006, **34**, 83.

[434] T. C. Gibb, *Principles of Mössbauner Spectroscopy*, John Wiley & sons, NY, 1976.

[435] J. B. Goodenough, *Magnetism and the Chemical Bond*, Interscience, New York, 1963.

436. S. R. Edinger, C. Cortis, P. S. Shenkin and R. A. Friesner, *Phys. Chem. B*, 1997, **101**, 1190.

437. C. M. Cortis and R. A. Friesner, *J. Comput. Chem.*, 1997, **18**, 1570.

438. C. M. Cortis and R. A. Friesner, *J. Comput. Chem.*, 1997, **18**, 1591.

439. M. D. Tissandier, K. A. Cowen, W. Y. Feng, E. Gundlach, M. H. Cohen, A. D. Earhart, J. V. Coe and T. R. Tuttle, *J. Phys. Chem. A*, 1998, **102**, 7787.